Modélisation micromécanique de matériaux hétérogènes contenant des microfissures avec la Méthode des Eléments Discrets (MED)

Farid Asadi

HAL Id: tel-03420983
https://theses.hal.science/tel-03420983

Submitted on 9 Nov 2021

University of Limoges

ED 609 - Sciences et Ingénierie des Matériaux, Mécanique, Énergétique (SIMME)

Institut de Recherche sur les CERamiques (IRCER)

Thesis submitted for the degree of
Doctor of Philosophy of Limoges University

Presented by
Farid ASADI

Defence date: 22/June/2021

Micro-Mechanical Modelling of Heterogeneous Materials Containing Microcracks with Discrete Element Method (DEM)

(In the framework EU Horizon 2020 Marie Skłodowska-Curie ATHOR project)

Thesis supervisors: M. Marc Huger, M. Damien André, M. Pascal Doumalin

JURY:

President of the jury
M. Olivier Castelnau, Professor, PIMM, Arts et Metiers Institute of Technology Paris (France)

Reviewers
M. Frederic Victor Donzé, Professor, ISTerre, Université de Grenoble Alpes (France)
M. Mohamed Guessasma, Professor, LTI, Université de Picardie Jules Verne (France)

Examiners
M. Olivier Castelnau, Professor, PIMM, Arts et Metiers Institute of Technology Paris (France)
M. Dietmar Gruber, Associate Professor, Chair of Ceramics, Montanuniversität Leoben (Austria)
M. Marc Huger, Professor, IRCER, University of Limoges (France)
M. Damien André, Associate Professor, IRCER, University of Limoges (France)
M. Pascal Doumalin, Associate Professor, PPRIME, University of Poitiers (France)

Guests
M. Sacha Emam, Research Engineer/Project Manager, ITASCA Consultants S.A.S. (France)
M. Laurent Brochard, Associate Professor, Navier, École des Ponts ParisTech (France)
M. Hugues Lemaistre, Research Engineer, IMERYS / CALDERYS (France)

<u>Acknowledgements</u>

I first express my deepest gratitude to *Prof. Marc Huger*, my supervisor and coordinator of the ATHOR project, for his scientific guidance, precious support, and being an inspiring idol for developing my soft skills. My sincere thanks to *Dr. Damien André*, my other supervisor, for his invaluable scientific advice, unconditional help, and enthusiasm for discussing DEM. Special thanks to *Dr. Pascal Doumalin*, my other supervisor, for his availability and insightful criticism.

Also, special regards to *Dr. Sacha Emam*, my mentor from the ITASCA company, for his advice and support, especially for PFC and FLAC software. I would like to thank *Dr. Dietmar Gruber*, as I was delighted to work with him during my visiting period at the University of Leoben in Austria. Many thanks to *Dr. Hugues Lemaistre* for hosting my secondment in Imerys company.

I would also like to thank all jury members: *Prof. Olivier Castelnau, Prof. Frederic Victor Donzé, Prof. Mohamed Guessasma,* and *Dr. Laurent Brochard*. I highly appreciated their constructive comments and views on my work.

It was an immense honour and privilege to be an Early-Stage Researcher (ESR) in the ATHOR project and as part of a dynamic team alongside fourteen other ATHOR ESRs. For the past three years, apart from the fruitful scientific exchanges, we have created many unforgettable memories together all around the globe (Germany, Japan, Italy...). I think this was a unique experience to be a part of such a fantastic international community. I enjoyed the close cooperation of all fourteen talented ESRs, and I must mention those to which I was closest and extend to them my warmest regards and affection: To *Diana* (punctual mama of ATHOR), *Robert* (my office/table football partner), *Sina* (my journey mate), *Soheil* (my talented mate) and *Hung* (my athletic mate).

I owe acknowledgement to all my friends and colleagues from IRCER laboratory, ENSIL-ENSCI national engineering school and the University of Limoges for making this journey so sweet, especially: *Daria*, *Glyn*, *Imad*, *Thi*, *Aliz*, *Siham* and *Andrezj*.

Last but not least, I have to thank my family: my mother, *Farideh*, who always encouraged me to follow my path; my father, *Hamid*, who always stood beside me on my journey. My sister, *Maryam*, and her husband, *Majid*, who've always wished for my good health and happiness. Finally and most importantly, to my beloved wife, *Bahar*, for her pure love, care, constant support, and all the beautiful moments that we've shared together. Thank you all from the bottom of my heart.

General introduction

Refractories are mineral materials able to sustain high temperatures, typically above 1000°C, required for many industrial processes. These materials should usually tolerate extreme conditions such as thermal and mechanical stresses as well as corrosion and erosions. The main applications of refractory materials are in steelmaking, cement making, ceramics, and glass production. The steelmaking industry is for sure the primary consumer of refractory materials (more than 70% of annual production) and refractories, are a vital element for all steps of steel processing.

Since the industrial revolution in Europe, the steelmaking industry remains a backbone of economic growth and manufacturing development for European countries. This notion might not be tangible until knowing the fact that, even now, each European Union citizen consumes an average of 320 kilograms of steel per year, which highlights its importance in everyday life. In fact, steel is used in every aspect of our surroundings, from mobility (cars, trains…), structures (towers, bridges, …) even the culinary uses (kitchen sinks, cookware…). To keep this essential industry productive, the continuous process of supplying refractories should be guaranteed. In this way, constant engineering and innovations in refractories are needed to deal with new and more challenging steelmaking requirements. Therefore, it has been more than 15 years that the FIRE[1] network (Federation for International Refractory Research and Education) gathered academic and industrial partners to promote refractory research programs and train skilled researchers and engineers for the next generations of this domain. Thanks to these collaborations, a significant experience has been acquired, which led to the creation of the ATHOR[2] Marie Curie project (Advanced THermomechanical multi-scale mOdelling of Refractory linings), which is an Innovative European Training Network supported by the European Commission[3]. The ATHOR project aims to train 15 highly skilled early-stage researchers through PhD studies, and its consortium is consisting of seven academic poles (University of Limoges, University of Aachen, University of Leoben…) and eight industrial partners (Saint-Gobain, Safran, Imerys…). This project is focused on the thermomechanical investigation and behaviour prediction of refractory linings: from the grain scale to the whole steel ladle structure. This is due to the fact that the steel ladle is at the core of the steelmaking process and is the major refractory using structure in the whole steel production chain.

In steel ladle, refractories face severe thermal shocks (rapid variation of temperature) due to the filling and emptying of melted steel. These thermal shocks induce stresses, which could weaken the refractory linings and potentially leads to complete failure of the ladle (breakthrough). When such a breakthrough occurs, it involves enormous cost, significant production loss, environmental pollution, and most importantly, huge risks for personals' safety.

---

[1] http://fire-refractory.org/
[2] https://www.etn-athor.eu/
[3] https://ec.europa.eu/research/mariecurieactions/actions/research-networks_en

As a part of the ATHOR project, this PhD aims to take advantage of advanced numerical tools to study the thermomechanical behaviour of refractory materials related to their microstructure design. To go in this way, it should be highlighted that the thermal shock resistance of refractories is closely related to the material ability to resist against crack propagation. Thus, in many cases, previous experimental studies already demonstrate that a voluntary introduction of a large number of microcracks within the microstructure of refractories during processing could strongly improve their thermal shock resistance, thanks to the promotion of a high non-linear tensile behaviour. From this experimental fact, the present PhD aims to better understand the relationship between microstructure design and macroscopic thermomechanical behaviour (non-linearity of stress-strain curves in tension and associated fracture energy). Thus, it is in particular targeted to model such fracturing behaviours, which involves a high number of microcracks, and the effect of these microcracks on the macroscopic thermomechanical behaviour. To tackle these general points, the Discrete Element Method (DEM) numerical approach is assigned for this PhD, thanks to its strong ability to manage a high number of cracks simultaneously during simulations.

In fact, the development of DEM to better understand the microstructure effects on thermomechanical behaviour of refractory materials started just a couple of years ago at IRCER[4] (recruitment of Dr. Damien André in 2014, the first PhD on this subject between 2016 and 2019). Hence, there were no extensive previous experiences in this new domain at the starting point of this PhD. Therefore, in line with the ATHOR project, this PhD follows a pre-defined general goal to develop numerical tools based on the DEM approach to investigate the relationships between microstructure and thermomechanical properties of heterogeneous materials containing microcracks.

The chosen DEM model of this study is the Flat Joint Model (FJM), thanks to its ability to mimic the microstructure of angular and interlocked grains, including fracturing processes in quasi-brittle materials. The framework of the FJM model is Particle Flow Code (PFC3D) from ITASCA[5] company (partner of this PhD), which is different from GranOO workbench, developed and previously used at IRCER. To go in this way, this dissertation is organised into five chapters, and a brief insight into these chapters will be given here.

Chapter I: This chapter will be dedicated to state of the art in line with the purpose of this PhD. It is divided into three main parts. Firstly, an introduction to the thermal shock resistance in refractories will be given. Then, a review about phenomenological fracture mechanics, dedicated to such heterogenous materials, will be provided. At the end of this first chapter, different numerical methods will be reviewed regarding their abilities for simulating fracture propagation and damaged materials.

Chapter II: This chapter will be dedicated to the Flat Joint Model (FJM), which has been chosen as the main DEM contact model for the present study. At first, the PFC3D framework, where the FJM model is implemented, will be introduced. Then, a description of FJM and its related input parameters will be presented in detail. Afterwards, due to the necessity of calibration of input parameters in discrete models, sensitivity studies about the FJM input parameters influence on the apparent simulated properties will be

---

[4] https://www.ircer.fr/
[5] https://www.itascacg.com/

conducted. It is aimed here to obtain a rationalised calibration algorithm in order to precisely and efficiently reproduces, by FJM, the targeted macroscopic mechanical behaviour of the material.

Chapter III: This chapter will be dedicated to proposing a DEM periodic homogenisation approach by using the notion of the Representing Volume Element (RVE) for modelling a pseudo infinite media. In this way, the multi-scale purpose of this study for upscaling the local properties (coming from heterogeneous microstructures) to the apparent elastic behaviour (macroscopic mechanical response) will be addressed. Implementing such a periodic homogenisation approach in DEM will allow working on a pseudo-infinite small domain, thus with a limited number of discrete elements. Such kind of homogenisation for a continuum media in DEM is not as robust as in FEM. In this chapter, the proposed model will investigate the quantitative prediction of macroscopic properties for bi-phase and porous materials by comparing to experimental data, analytical Hashin and Shtrikman model and numerical Finite Element Method (FEM).

Chapter IV: This chapter will be dedicated to proposing a model for mimicking the non-linear mechanical behaviour by considering microcracking process in a continuum media. In fact, as previously mentioned, numerous microcracks can be intentionally induced within the microstructure of refractories to increase their thermal shock resistance. The presence of such microcracks usually induces a non-linear quasi-brittle mechanical behaviour. To numerically reproduce this phenomenon, a DEM model will be proposed based on the randomisation of local fracture criteria following a Weibull distribution. The results of the proposed model will be compared to reference Alumina Spinel experimental data. Subsequently, a meta-algorithm will be proposed to calibrate potentially any DEM model quantitatively for simulating such non-linear behaviour. This aims to tune the fracture energy and brittleness of the material in DEM simulations by promoting diffused damages and crack branching into the microstructure.

Chapter V: This chapter will be dedicated to the applicability of the proposed numerical model of chapter IV to mimic the Wedge Splitting Test (WST), which is commonly used to quantify the brittleness of refractories. WST could be, in fact, an index for characterising the quasi-brittle behaviour of refractories. Again, this behaviour is closely linked to the presence of the mentioned pre-existing microcracks and their ability to promote crack branching during loading. Therefore, this chapter aims to examine the ability of the proposed statistical numerical approach to reproduce this fundamental phenomenon. The results of such simulations will be qualitatively compared to two model materials with different fracturing behaviour: a highly brittle pure Magnesia and a quasi-brittle Magnesia Hercynite. Besides, the obtained crack branching from these simulations will be qualitatively compared to the experimental cracking, captured by Digital Image Correlation (DIC). In the end, a discrete/continuous hybrid model will be proposed to optimise the WST simulations in order to save computational time. To go further in the optimisation way, rigid discrete blocks elements will be introduced to act as large aggregates within the microstructure.

Finally, this dissertation will be close by concluding the overall achievements of this study, and the proposition of potential prospective studies, based on the obtained experience and results.

Chapter I: State of art and context

I.1. Thermal shock resistance

Based on the literature, thermal shock resistance is the ability of materials to tolerate thermal stresses, caused by rapid changes in temperature, without any failure (Schacht 2004). Refractories are continually exposed to these thermal shocks during their service life, and these thermal cycles could induce stresses which could weaken the materials in application and potentially leads to complete failure. Therefore, to improve this very practical aspect, different authors have continuously developed theoretical concepts to quantify the thermal shock resistance of materials. Since more than half a century ago, different key approaches have been thus set up to quantify thermal shock resistance of ceramics.

I.1.1. Key physical properties from Kingery's approach

In 1955, Kingery proposed a thermo-elastic approach to analyse the thermal shock resistance for undamaged materials (Kingery 1955). This approach was proposed for a simplified case of homogeneous and continuous material with a linear elastic mechanical behaviour. He assumed an infinite slab with an initial temperature of T_1, suddenly exposed to the temperature of T_2 which leads to a thermal gradient inside the slab. This thermal gradient will induce thermal stresses. If these thermal stresses become equal to the material's strength, then the minimum temperature difference for crack initiation is reached. For a high rate of heat transfer (for example, cooling by a high flux of water), the first thermal shock resistance parameter, called R (in °C), can be written as:

$$R = \frac{\sigma_t \, (1 - \nu)}{E \, \alpha}$$

Eq. I-1

where σ_t is tensile strength, ν, E and α are Poisson's ratio, Young's modulus and thermal expansion coefficient of the material, respectively.

This parameter is corresponding to the maximum temperature difference that the material could withstand without initiating any fracturing process.

On the other hand, this temperature difference could depend on the thermal conductivity of the material for a low rate of heat transfer (for example, cooling by a low flux of air).

Therefore, a second thermal shock resistance parameter R' (in W/m), has been introduced by considering the thermal conductivity:

$$R' = \frac{\lambda \, \sigma_t \, (1 - \nu)}{E \, \alpha}$$

Eq. I-2

where λ is the thermal conductivity of the material.

As interesting indicators, by increasing R and R', the thermal shock resistance of the materials will increase, which means the material could tolerate a higher temperature difference without any failure. Taking into account Eq. I-1 and Eq. I-2, the most common influential factors on the thermal shock resistance from Kingery's point of view are listed below (Askeland *et al.* 2016):

- thermal expansion coefficient (α), low thermal expansion coefficient decreases dimensional changes and increases the ability to withstand thermal shock;
- thermal conductivity (λ), high thermal conductivity helps to transfer heat and reduce temperature gradients within the material;
- Young's modulus (E), a low Young's modulus reduces the stress level for a given strain generated by the temperature gradients and thus reduce the risk of failure;
- tensile strength (σ_t), a high value of the tensile strength is commonly recommended since it allows larger thermal strains before failure.

Considering these points, to obtain a material with high thermal shock resistance, α and E values should be low, while the λ and σ_t values should be high. Thus, the first step to finding such material with the mentioned desired macroscopic parameters is to check the property databases of the potential candidates. One of the most common charts, which considers these points to compare thermal shock resistance of different materials, has been proposed by Ashby (Ashby 1999). Based on Ashby's approach, the mentioned influential parameters have been plotted specifically for the refractory materials well-documented in the GRANTA software. The normalised tensile strength σ_t/E, has been plotted against thermal expansion coefficient α in Fig. I-1 (a) and against the normalised thermal expansion coefficient α/λ in Fig. I-1 (b). It should be mentioned that certain refractories groups in the plotted charts had slightly different σ_t or E values. However, here, the strongest properties were intentionally considered, in order to be as close as possible to pure compositions and/or to grains properties. Besides, such customised plots are mainly pedagogical, and to be more practical, it could be necessary to test other potential materials in order to build a suitable dedicated database.
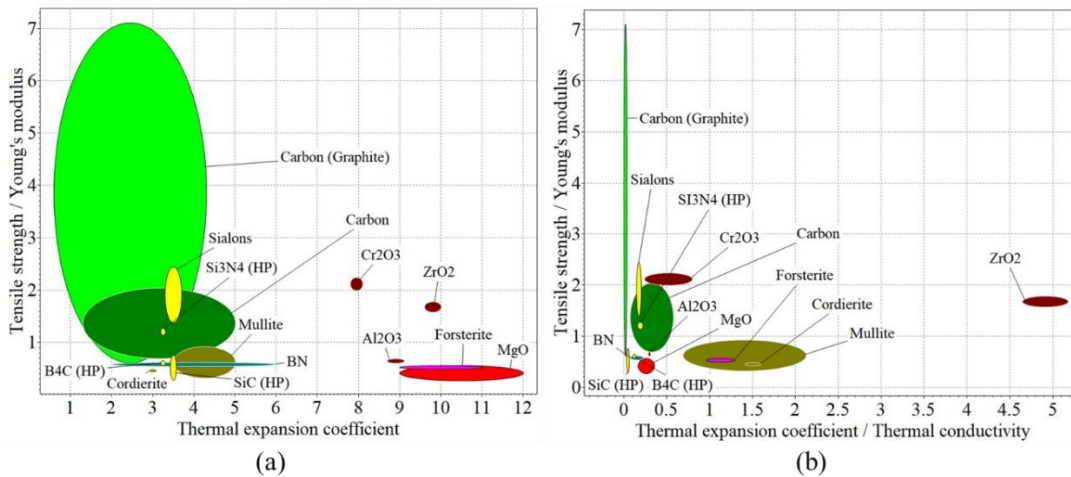
Fig. I-1. Simplified thermal shock resistance comparison chart for refractories:
(a) normalised tensile strength σ_t/E against thermal expansion coefficient α, and (b) against the normalised thermal expansion coefficient α/λ.

In agreement with R and R' Kingery's parameters, the thermal expansion coefficient α and the normalised thermal expansion coefficient α/λ, presented in Fig. I-1 (a) and (b) should be low to decrease the thermal expansion gradient. On the other hand, the

normalised tensile strength σ_t/E should be high to allow large strains without failure. Therefore, the top left-handed side of the charts is the region for thermal shock resistant materials. Comparing Fig. I-1 (a) and (b), it can be seen that, in both charts, Graphite exhibits a very good thermal shock resistance, which can explain why Graphite is commonly added to certain refractories. Also, at first glance, on Fig. I-1 (a), it appears that Magnesia (MgO) is not an appropriate candidate to be used in refractories (for thermal shock); however, by considering the normalised thermal expansion coefficient α/λ in Fig. I-1 (b), MgO is placed in a reasonable position among the others, showing the importance of considering the normalised thermal expansion coefficient too.

After such comparisons (from intrinsic properties), if the desired material with specific macroscopic properties was not found in materials databases, it could also be possible to mix different constituents to design a specific microstructure in order to achieve the targeted macroscopic properties.

I.1.2. Microstructure influence on critical physical properties

It is quite common to mix different constituents to achieve the desired macroscopic behaviour for a given refractory material. For industrial applications, one of the critical aspects is also resistance against corrosion, especially for refractories, which are in contact with slags. Therefore, at this stage, refractory engineers must introduce corrosion-resistant large grains such as Magnesia (MgO). On the other hand, although using these types of large grains will increase the corrosion resistance of the material, it will undesirably decrease its tensile strength. Depending on the microstructure (grain size, compacity…), other properties like Young's modulus and strain at rupture, even thermal expansion, could be affected. Hence, a compromise between the different required properties should be found.

If this approach (mixing the constituents) is not enough to achieve the targeted properties, it is also possible to modify or tune the microstructure of the material. For example, by introducing microcracks at the local scale, the macroscopic properties of the refractories will change due to the induced internal damages, and this could positively affect the thermal shock resistance of the material. In fact, the presence of local discontinuities will lead to a decrease of Young's modulus (Hasselman 1969) and of the thermal expansion coefficient of the material (Chotard *et al.* 2008). Based on previous Kingery's formulation (Eq. I-2), decreasing these two parameters can improve the thermal shock resistance of the material.

Commonly, refractories are heterogeneous materials consisting of large grains within a bonding matrix. A microcracking process within the microstructure can be controlled by adding inclusions during the fabrication of the refractories in order to obtain the required macroscopic properties. Such microcracking process within the microstructure can be tuned, either during heating or cooling, through adjusting the Coefficient of Thermal Expansion (CTE) mismatch between the different constituents of the material.

To simplify this complex media, let us assume a bi-phase model material composed of a continuum matrix and spherical inclusions. Such a system has been studied by Tessier-Doyen *et al.* (Nicolas Tessier-Doyen 2003). For such a system, three different scenarios could happen during the cooling stage after sintering by exhibiting different

thermal expansion coefficients. The thermal coefficient of the matrix (α_{matrix}) could be smaller, equal or bigger than the thermal expansion coefficient of inclusion ($\alpha_{inclusion}$). These three cases are described in the Fig. I-2:

a) when $\Delta\alpha < 0$, the matrix has a lower thermal expansion coefficient; therefore, it has a slower contraction during cooling in comparison to the inclusion, which leads to radial tensile and circumferential compressive stresses. If these stresses reach the debonding threshold, debonding of inclusion will occur. An example of this behaviour can be seen in the Cordierite Mullite refractories in Fig. I-2 (d). This refractory is mostly used for tiles making purposes, and the Cordierite matrix exhibits a lower thermal expansion coefficient in comparison to the Mullite inclusions.

b) when $\Delta\alpha = 0$, there will be no induced thermal stress; therefore, no cracks or deboning. This theoretical concept is relatively rare to be observed in reality while mixing different constituents.

c) when $\Delta\alpha > 0$, the matrix has a higher thermal expansion coefficient; therefore, it has a faster contraction during cooling in comparison to the inclusion, which leads to circumferential tensile and radial compressive stresses. If these stresses reach the fracturing threshold of the matrix, networks of the microcracks within the matrix will form (starting from the interface). An example of this behaviour can be seen in Magnesia Spinel refractories in Fig. I-2 (f). These refractories are mainly used in rotary kilns of the cement industry, and the Magnesia matrix exhibits a higher thermal expansion coefficient in comparison to the Spinel inclusions, which lead to microcrack within the matrix in the vicinity of the Spinel grains.
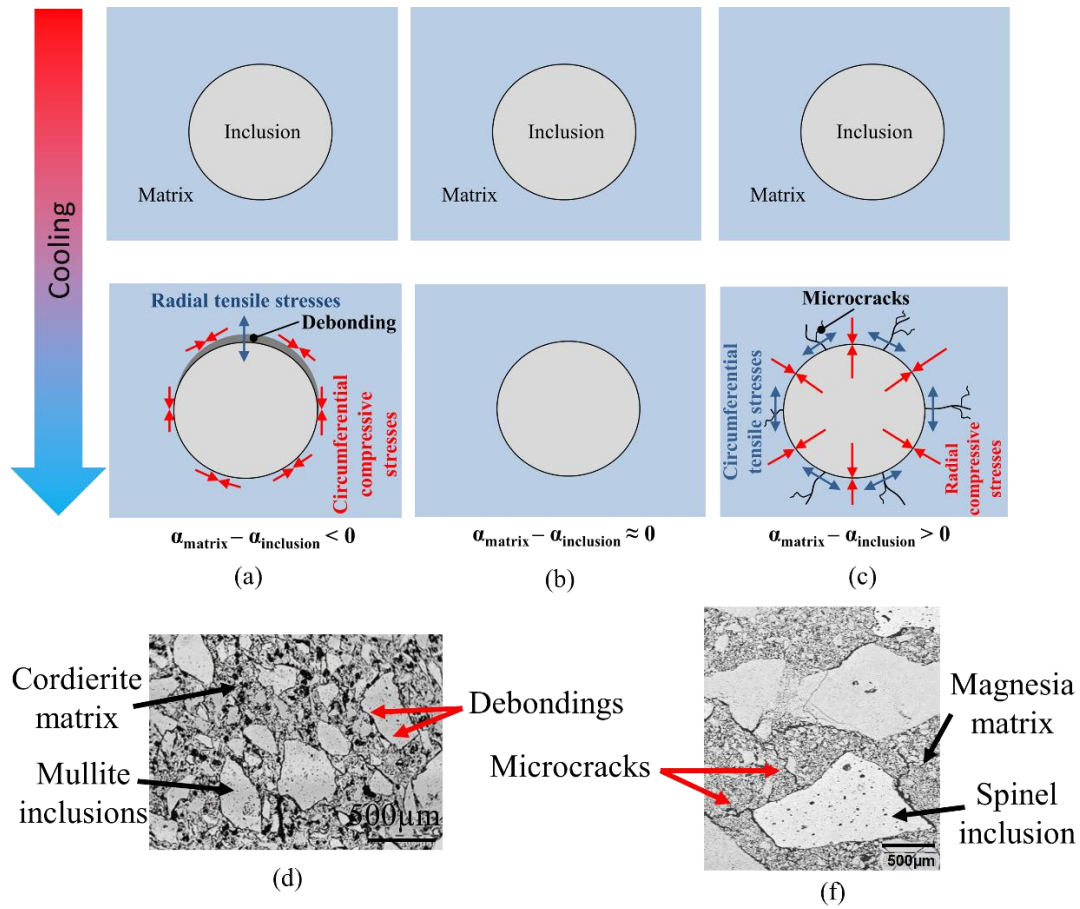
Fig. I-2. Three scenarios for CTE mismatches and corresponding stress development around inclusions: (a) matrix CTE smaller than inclusion, (b) matrix CTE equal to inclusion (c) matrix CTE bigger than inclusion. (d) the real case for Cordierite Mullite (Chotard *et al.* 2008) and (f) the real case for Magnesia Spinel (Renaud Grasset-Bourdel 2011).

This controlled network of microcracks could also improve materials thermal shock resistance and directly affect Kingery's key parameters. In fact, such an initial microcracks network could allow the material to exhibit significant residual mechanical properties after thermal shock. This critical point is not taken into account by Kingery's approach. Indeed, the severity of the damage arising from thermal shock determines the loss in mechanical properties. Hence, in order to quantify the thermal shock resistance of such damageable materials, a dedicated, energetic approach was introduced by Hasselman, which is explained in the next section.

I.1.3. An energetical approach by Hasselman

Hasselman introduced the energetic approach during the 1960s and 1970s (Hasselman 1963, Hasselman 1969, Hasselman and Youngblood 1978). In this approach, the microcracks stability is studied by considering the induced thermal stresses. It is assumed that in the initial state, the material contains microcracks, and these microcracks are homogenously distributed; also, the stress field interactions of neighbouring cracks and stress relaxation are not considered. It was assumed that crack propagation is controlled

by the minimisation of the total energy of the system. This total energy E_{total}, is the sum of elastic energy and the surface energy of the cracks (Hasselman 1969):

$$E_{total} = E_{elastic} + E_{surface}$$
Eq. I-3

where $E_{elastic}$ is the stored energy in the case of linear elasticity and $E_{surface}$ is the surface energy, which corresponds to energy to create crack surfaces within the system.

Later on, Hasselman proposed two parameters for thermal shock resistance. Firstly, as a measure to compare the damage level of different materials, the thermal shock damage resistance parameter R'''' was introduced, which is defined as:

$$R'''' = \frac{E\,\gamma_s}{\sigma_t^2}$$
Eq. I-4

where E is Young's modulus, σ_t is the tensile strength, and γ_s is the fracture surface energy (in J/m^2).

By increasing this parameter, it is expected that unstable crack propagation within the sample decrease. It leads to promote a more quasi-brittle behaviour, rather than a highly brittle behaviour. Afterwards, Hasselman introduced a parameter to address the resistance against the growth of initial rather large cracks. This parameter was called thermal stress crack stability R_{st}:

$$R_{st} = \sqrt{\frac{\gamma_s}{E\,\alpha^2}}$$
Eq. I-5

By increasing this parameter, it is expected that fracture propagation will be more difficult. Considering R'''' and R_{st}, these two parameters depend on Young's modulus, fracture surface energy and tensile strength. By using a simple approximation of elastic energy, it can be assumed that $E\,\alpha^2 \cong \sigma^2/E$. Hence, both parameters will be inversely proportional to σ^2/E, which is related to the stored elastic strain energy (Popov 1998). Indeed, this energy is the primary source of force for initiating and propagating cracks within the material. Hence, considering the Hasselman parameters, this energy should be decreased in order to increase the thermal shock resistance of the material; in other words, a low value of strength should be targeted by introducing some internal defects.

To sum up, a high strength potentially leads to a low thermal shock resistance of refractories. In fact, the thermal shock resistance decreases proportionally to the square of the strength. That is why the refractory industry is not focusing on developing high-strength refractories (Schacht 2004).

I.1.4. Crack growth in refractories

After introducing the potential microcracking process and its influences on the thermal shock resistance of the materials, the crack growth process itself is a vital aspect to investigate. As mentioned, high thermal shock resistance is strongly connected to the material's ability to resist against crack propagation through large energy dissipation by creating new surfaces and friction mechanisms. As shown in Fig. I-3, this dissipation process could occur within the fracture process zone (FPZ) in front of the growing crack or in following wake region, that follows the growing crack front (Schacht 2004).
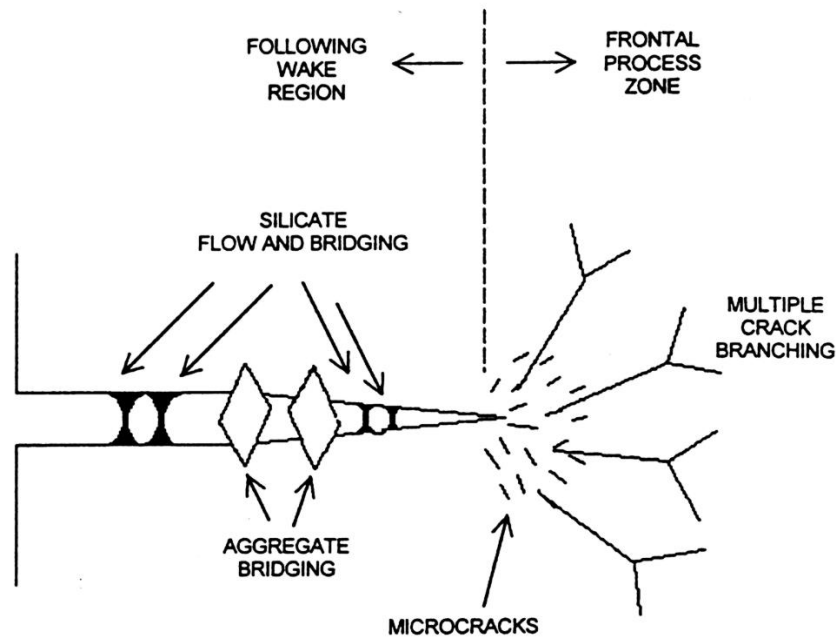
Fig. I-3. Scheme of fracture propagation mechanism (Schacht 2004).

In the crack's tip, a large microcracking process should happen to promote crack branching. In the wake region (behind the advancing crack), the aggregate bridging should happen to increase crack opening resistance (Steinbrech *et al.* 1983). These points will have a crucial impact on the macroscopic mechanical behaviour of the material as it could lead to non-linear behaviour and will be explained more in details in the following section.

I.1.5. Aggregates role in thermal shock resistance and non-linear behaviour

Aggregates could have a positive influence on the thermal shock resistance of refractories. In fact, refractory producers use this point for a long time to increase the thermal shock damage resistance of fireclays by adding large hard aggregates as "*thermal shock crack stoppers*" (Schacht 2004). As mentioned in the previous section, aggregate bridging in the wake region of the crack could increase the fracture propagation resistance and, consequently, the thermal shock resistance. The other function of large aggregates is to induce microcracks within the refractory's microstructure, reducing the overall strength of materials, and leading to increased thermal shock resistance, as mentioned in the Hasselman approach (see section I.1.3). Thus, it is preferred to have multi-phase refractories by introducing aggregates, as the aggregates (Schacht 2004):

- increase microcracks level by introducing crack deviation around them and;
- consume energy through bridging phenomena following the crack.

Although adding aggregates to microstructure could positively impact the thermal shock resistance of refractories, it will have a considerable impact on macroscopic mechanical behaviour. In this regard, in a study by Grasset-Bourdel, this impact of

introducing aggregates on the thermal-induced microcracks and, consequently, on the mechanical behaviour of two-phase refractories was investigated (Renaud Grasset-Bourdel *et al.* 2013). In the mentioned study, Magnesia Spinel refractories with different content of Spinel grains were tested. Due to the CTE mismatch between the two phases (Spinel grains and Magnesia matrix), radial microcracks around the inclusions were generated during the cooling phase, as shown in Fig. I-2 (see section I.1.2). It was shown that the amount of microcracks was correlated to the Spinel grains content. Afterwards, the macroscopic mechanical behaviour of these refractories was characterised by using the uniaxial tensile test. Fig. I-4 is showing the stress-strain curves with different Spinel grains content within the microstructure.
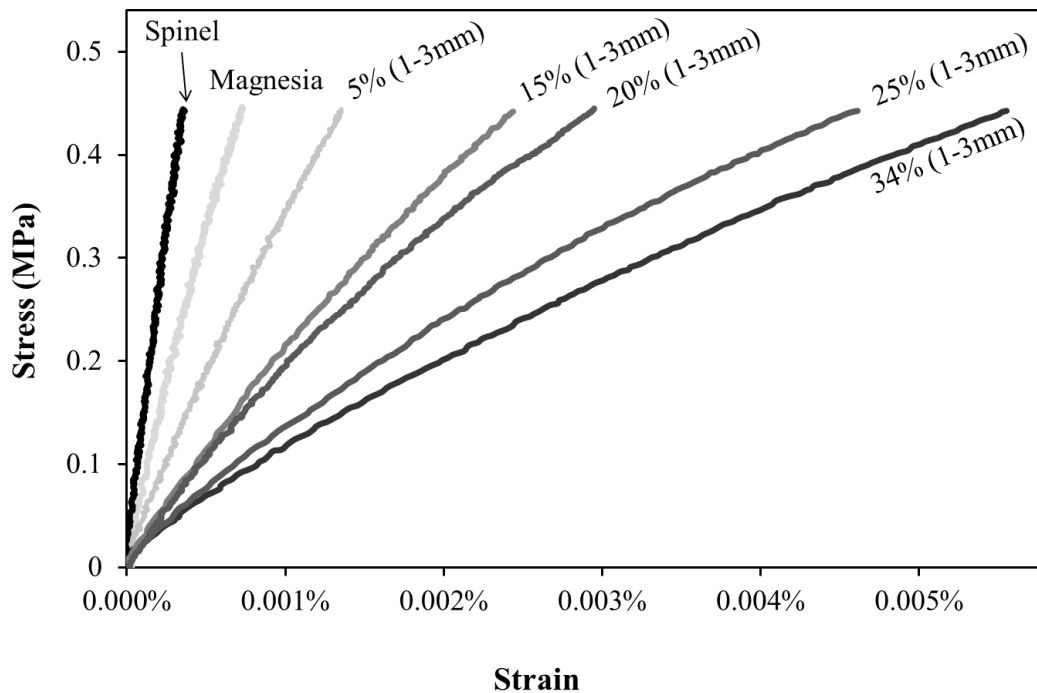
Fig. I-4. The stress-strain curves with different Spinel grains contents within a Magnesia matrix (Renaud Grasset-Bourdel *et al.* 2013)

As shown in Fig. I-4, pure Magnesia itself shows a relatively linear behaviour; however, by introducing and increasing the Spinel grains content, the two-phase refractories exhibit a considerable non-linear behaviour. This non-linearity increases as the Spinel grain contents increases. This increase is related to the amount of thermal-induced microcracks.

To sum up, it is evident that for improving the thermal shock resistance of refractories, it is essential to optimise the non-linearity of their mechanical behaviour (by inducing microcracks) and obtain an equilibrium between strength value and quasi-brittle behaviour. This point can be achieved by tailoring and designing suitable microstructures. Hence, designing and testing such new microstructures will require a combination of theoretical fracture mechanics basis, experimental approaches and numerical simulations in order to predict the efficiency of designed microstructures. These topics will be explained more in the following sections.

I.2. Phenomenological approach of fracture mechanics

I.2.1. Linear fracture mechanics

The general first approach to fracture mechanics is Linear Elastic Fracture Mechanics (LEFM), proposed by Griffith, which simply considers an elliptical crack propagating in an elastic, isotropic media (Griffith *et al.* 1921). The Griffith work was an energetic approach that describes fracture based on the balance between elastic energy and energy dissipation due to the creation of new crack surfaces. Hence, the parameter G_c, which is the critical energy release rate, was introduced. For an infinite plate under uniform axial tensile stress, containing a straight crack of length 2a, perpendicular to the stress, it can be written:

$$G_c = \frac{\sigma_r^2 \, \pi \, a}{E}$$

<div align="right">Eq. I-6</div>

where σ_r is the strength, E is the Young´s modulus, and a is the crack size.

This Griffith approach is only valid for highly brittle materials such as glass and some fine grain ceramics due to the absence of other energy dissipating mechanisms (Griffith *et al.* 1921). Later in 1957, Irwin proposed a local asymptotic approach, which relies on singular stresses associated with a sharp crack by using the stress intensity factor. In this approach, the stress can be formulated according to the crack tip position and its vicinities for an isotropic linear elastic material, as shown in Fig. I-5 (Irwin 1957).
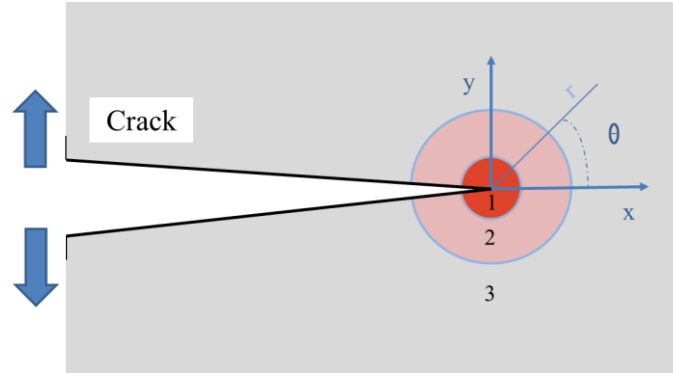
Fig. I-5. Polar coordinate axis ahead of a crack tip adopted from (Anderson 2017).

The stress fields ahead of a crack tip can be written as:

$$\sigma_{ij} = \frac{K}{\sqrt{2 \, \pi \, r}} f_{ij}(\theta)$$

<div align="right">Eq. I-7</div>

where, σ_{ij} is the stress, K is the stress intensity factor, r and θ are the polar coordinates from the crack tip, and f_{ij} is the dimensionless function depends on the geometry of the sample and test configurations.

Regarding the Eq. I-7, theoretically, the stress in the immediate region around the crack tip (area 1) is infinite. Area 2 is a stress singularity zone, where the singularity near

the crack tip is proportional to $1/\sqrt{r}$ and area 3, is the far-field stress zone. In this way, by focusing on area 2 and using stress singularities in the asymptotic local approach, Irwin introduced a crack propagation criterion called critical stress intensity factor or fracture toughness:

$$K_{IC} = \sigma_r \, Y \sqrt{\pi \, a}$$

<div align="right">Eq. I-8</div>

where, K_{IC} is the toughness, and Y is a geometrical factor.

By assuming the crack in an infinite media, the geometrical factor, Y, will be equal to one (for plane stress). Then, taking into account Eq. I-6, Eq. I-8 and it can be written that:

$$G_c = \frac{K_{IC}^2}{E}$$

<div align="right">Eq. I-9</div>

This equation shows that fracture toughness is related to fracture energy; therefore, fracture toughness is considered as an index for the resistance of the material against crack propagation. However, both Griffith and Irwin approaches are considered as part of Linear Elastic Fracture Mechanics (LEFM), which mostly suits for purely brittle materials. Indeed, LEFM is mostly involved for materials with negligible non-linear behaviour (potentially resulting from diffused damage or plastic deformations). Thus, the linear elastic assumption is not suitable for refractories, as this class of materials can exhibit significant non-linear behaviour even at room temperature (see section I.1.5). This non-linear behaviour has been firstly studied in the case of metal alloys to consider the development of plasticity in the vicinity of crack (Rice 1968). The non-linear fracture mechanics coming from damages zones produced by microcracks within refractory microstructures will be introduced in the following section.

I.2.2. Non-linear fracture mechanics

The Elastic-Plastic Fracture Mechanics (EPFM) has been specifically developed for materials with non-linear behaviour resulting from plastic deformations in front of the crack tip, as shown in Fig. I-6 in the case of a compact tension test. In this test, a plate containing a single-edge notch undergoes tensile forces. ASTM standardised this test for measuring fracture toughness in metallic alloys (Slepetz *et al.* 1975).
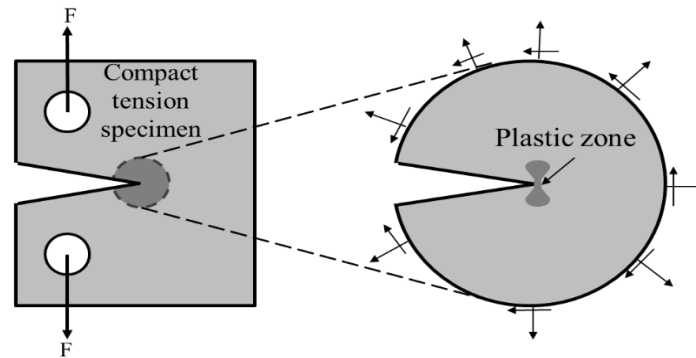
Fig. I-6. The schematic of the compact tension test, adopted from (Anderson 2017)

It should be mentioned that, although the EPFM models were initially proposed for metals, they can be extended for quasi-brittle materials, which are promoting the same macroscopic non-linear behaviour. In fact, such a mechanical behaviour could have two different phenomenological local reasons; firstly, the plastic zone ahead of the advancing crack, which is the case for metal alloys as mentioned earlier. Secondly, this non-linearity could also be observed in quasi-brittle materials such as refractories, where diffused microcracks are developing within the damaged fracture process zone (FPZ), as explained in section I.1.4.

The most popular elastic-plastic parameter in EPFM for fracture criterion in non-linear materials is *J* counter integral, proposed by Rice (Rice 1968). In this approach, the plastic deformation has been taken into account to analyse fracturing in a quasi-brittle material. Rice proposed that the non-linear energy release rate, *J*, could be written as a path-independent line integral. Indeed, the *J* integral can be viewed as both an energy parameter and a stress intensity parameter, as *J* uniquely could characterise crack tip stresses and strains (Anderson 2017). Therefore, a higher *J* value will ultimately lead to higher energy for crack initiation in a stationary crack, which means a tougher material.

A relationship was established between energy release rate and *J-integral*; for opening fracture, it can be written:

$$G_c = \frac{K_{IC}^2}{E} = J \qquad \text{Eq. I-10}$$

In the case of quasi-brittle materials, the area around the crack tip (area 2 in Fig. I-5) generates most of the non-linear phenomena, which deals with the release of elastic energy during crack propagation through the FPZ. For refractories, in particular, Sakai *et al.*, investigated this non-linear fracture behaviour (Sakai *et al.* 1986). Based on the mentioned study, the free energy (ΔG) corresponds to the energy balance during a crack extension over the area of *Δa* (as shown in Fig. I-7(a)) and can be described as:

$$\Delta G = \Delta \pi + \Delta \Gamma + \Delta U_{ir} \qquad \text{Eq. I-11}$$

where, *Δπ* corresponds to the potential energy change, which is, in fact, negative during the test. The term *ΔΓ* corresponds to the energy required to produce the new fracture surfaces area (*ΔA*), which is a linear function of cracked surface area, and can be written as:

$$\Delta \Gamma = 2 \gamma_S \Delta A \qquad \text{Eq. I-12}$$

where, as a reminder, the γ_S, is the materials surface energy (see section I.1.3.). Finally, ΔU_{ir} corresponds to additional energy consumption by irreversible processes. Now, as a quasi-static condition for a stable crack advancement, the free energy should be zero ($\Delta G = 0$) and by considering Eq. I-11, it can be written that (Sakai *et al.* 1986):

$$-\Delta \pi = \Delta \Gamma + \Delta U_{ir} \qquad \text{Eq. I-13}$$

In the same way, in order to normalise by the surface of the fracture, it can be written:

$$-\frac{\Delta\pi}{\Delta A} = \frac{\Delta\Gamma}{\Delta A} + \frac{\Delta U_{ir}}{\Delta A}$$

Eq. I-14

This relation highlights that the change in the system's potential energy during fracturing will be consumed in two ways; to produce new fracture surfaces and for additional irreversible processes (such as local plasticity, friction, interlocking aggregates and heat…). The schematic force-displacement response of such a quasi-brittle refractory is shown in Fig. I-7 (b).
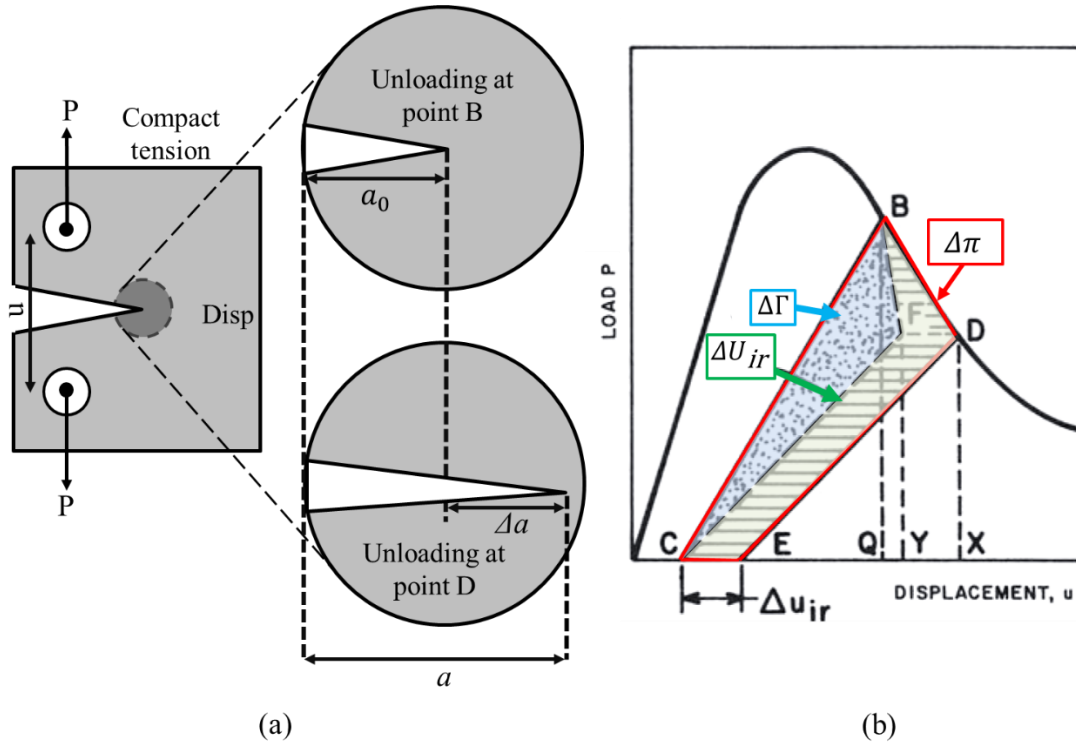
Fig. I-7. Conceptual aspects around compact tension test: (a) a schematic view of the crack advancement (Δa) under tensile loading, and (b) the load-displacement curve with areas corresponding to the energy consumed by surfaces creation ($\Delta\Gamma$) and to energy consumed by other irreversible processes (ΔU_{ir}), adapted from (Sakai *et al.* 1986).

To break down the shown load-displacement curve of Fig. I-7 (b), the total area of the BDEC ($\Delta\pi$) is related to the total energy consumption (work of fracture), while loading the sample from B to D. The CBF area ($\Delta\Gamma$) is the energy associated with fracture advancement (surfaces creation) in elastic and reversible conditions. This means that if the material would be unloaded in such a condition, the unloading curve would go back to point C, with no additional residual deformations (reversible). However, in reality, the unloading curve will go back to point E, because of other energy dissipation mechanisms which lead to the additional terms (ΔU_{ir}), corresponding to irreversible processes. Now, the triangle CBQ and EDX are showing the stored energy for point B and D, respectively. Considering the line CF drown in parallel with ED, its intersection with the value of the force for point D, will be the point F. Now, the two triangles of CFY and EDX are equal,

and the area BDECF correspond in fact to energy consumption by irreversible processes (ΔU_{ir}).

This configuration was showing a stable fracture propagation process within a refractory. Nevertheless, compact tension configuration is not very suitable for refractories as it requires drilling holes to apply the load, which induce stress concentration, potentially leading to an unpredictable rupture. Therefore, later on, Wedge Splitting Test (WST), which is more adapted to characterise brittle materials such as concretes and refractories, has been introduced by Tschegg (Tschegg 1986). Compared to the compact tension test, WST is easier to manage, as there is no stress concentration, and it can produce a relatively big fracture area compared to the size of the sample (Brühwiler et al. 1990). In the next section, WST is explained more in detail.

I.2.3. Fracture energy quantification of refractories by Wedge Splitting Test (WST)

The principle of WST is to break a brick in the opening mode of fracturing by applying a vertical force and its transformation in horizontal forces to produce a stable crack, as shown in Fig. I-8 (a). The typical force-displacement curve for the WST is also shown in Fig. I-8 (b).
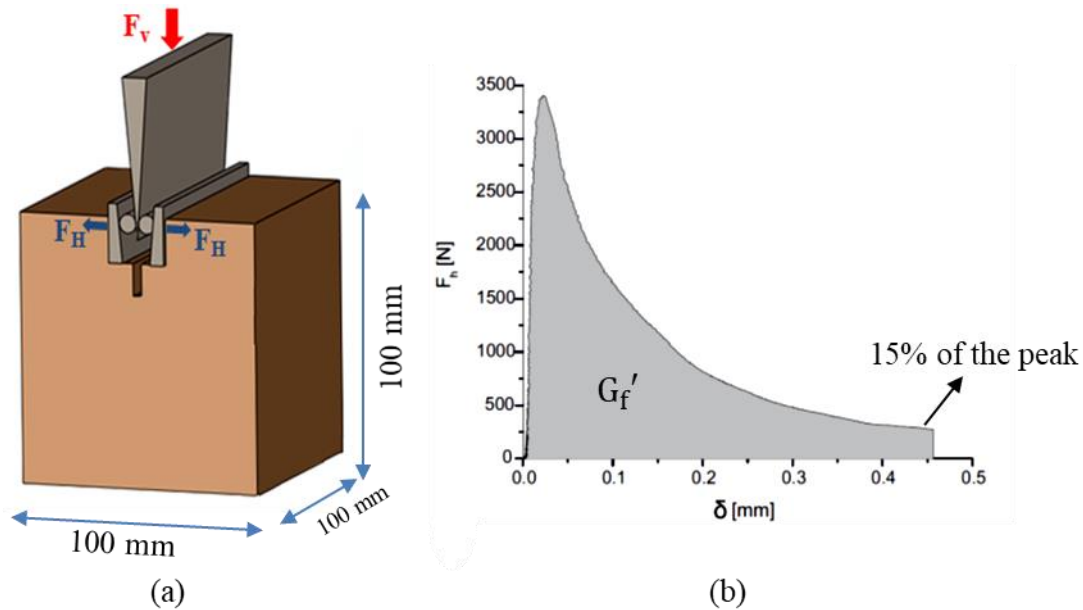
Fig. I-8. Wedge Splitting Test (WST): (a) schematic view of the device, (b) typical force-displacement curve. From (Belrhiti 2015).

WST aims to obtain specific fracture energy (G_f) and brittleness number (B) of materials (Tschegg 1986). Specific fracture energy is the amount of energy necessary to create a one-unit area of a crack, which is commonly determined by the area under of strain-softening curve. In order to calculate the specific fracture energy of materials, based on the obtained force-displacement curve, the following relationship was introduced by Harmuth *et al.* (Harmuth *et al.* 1997a):

$$G'_f = \frac{1}{A} \int_0^{\delta F_{max}15\%} F_h d\delta \qquad \text{Eq. I-15}$$

where G'_f, A and F_h, are the specific fracture energy (J/m^2), the fracture surface (m^2) and the horizontal force (N), respectively. In such an experimental test, to avoid the loading wedge touches the sample while it is moving downward, the test is usually stopped at 15% of the force peak. Thus, the full value of G_f cannot be precisely determined. This restriction to 15% of the force peak leads to introduce G'_f, instead of G_f. That is why in the case of WST, the term *specific fracture energy* is preferred to *fracture energy*.

To evaluate the brittleness of the refractories, one of the earliest concepts was introduced by Gogotsi in 1973 (Gogotsi 1973). He introduced parameter *X* as a criterion for brittleness, which was defined on the stress-strain curve of a sample under mechanical loading. It can be written as:

$$X = \frac{linear\ elastic\ energy}{total\ energy\ of\ rupture} \qquad \text{Eq. I-16}$$

Later, in 1988 in the case of concretes, Bazant proposed a first brittleness number (*B*) as a shape-independent and size-independent index in order to characterise fracturing behaviour (Bazant *et al.* 1988). Afterwards, Harmuth *et al.* used a refined and adapted WST to obtain the Brittleness number (*B*) for refractories (Harmuth *et al.* 1997a). In this context, the Brittleness number (*B*) is proportional to energy stored elastically at crack initiation over total fracture energy:

$$B \propto \frac{energy\ stored\ elastically\ at\ crack\ initiation}{fracture\ energy\ for\ total\ fracture} = \frac{W_{Elastic}}{W_{Fracture}}$$

and, it was defined as:

$$B = \frac{f_t^2 . l}{G_f . E} \qquad \text{Eq. I-17}$$

where *ft, l, E* are the tensile strength (Pa), the sample length (m), and Young's modulus (Pa), respectively.

As mentioned, WST results could be an index for characterising the fracture behaviour of quasi-brittle refractories. As an example of WST for such an application for refractories, in a study by Grasset-Bourdel *et al.*, two refractory model materials have been compared using WST (Renaud Grasset-Bourdel *et al.* 2013). The first one was a pure Magnesia, which is a relatively brittle material, and the second one was a Magnesia Spinel with 15% of the spinel content, which exhibits a quasi-brittle behaviour. Their WST force-displacement curves are shown in .
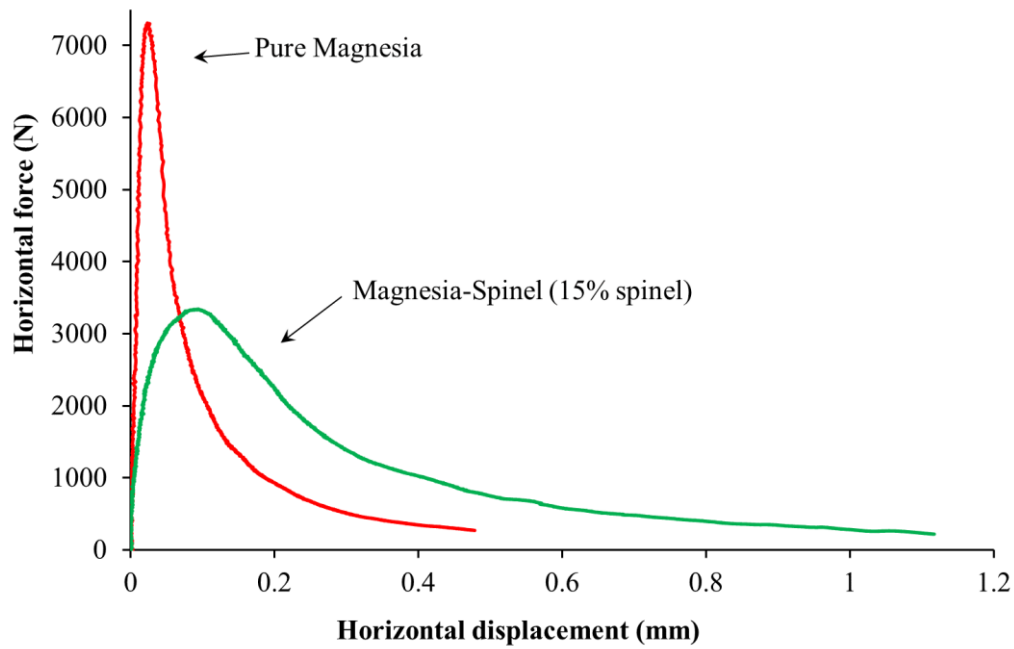
Fig. I-9. WST force-displacement curves for Magnesia and Magnesia Spinel
(Renaud Grasset-Bourdel 2011).

As explained in section I.1.2 and I.1.5, such a quasi-brittle behaviour of Magnesia Spinel is due to the presence of thermally induced microcracks within the material microstructure, resulting from introducing Spinel grains into a pure Magnesia matrix. Ultimately, WST force-displacement curves can be used to obtain the fracture energy and brittleness number of these refractories. In Table I-1, these two parameters have been compared.

Table I-1. The fracture energy and brittleness number for Magnesia and Magnesia Spinel
(Renaud Grasset-Bourdel 2011)

Refractory Model Material	Fracture Energy (G_f, J/m^2)	Brittleness Number (B, -)
Pure Magnesia	196	0.47
Magnesia Spinel (15% Spinel)	326	0.15

As it can be seen, the fracture energy in the quasi-brittle Magnesia Spinel is higher than in pure Magnesia, which results in having a lower brittleness number. This point leads to higher resistance of Magnesia Spinel against fracture propagation thanks to the introduction of Spinel inclusions, which generates a network of microcracks within the Magnesia Spinel microstructure. However, the presence of such microcracks within a ceramic material is well-known to have a significant impact on strength values, and this impact is commonly studied through statistical approaches.

I.2.4. Contribution of the statistical approaches to the fracture mechanics

In the case of ceramic materials, in order to account for the influence of the size of defects within the microstructure on the global strength of materials, the most famous statistical approach has been developed by Weibull, and it is based on the *weakest link* concept. It will be explained more in detail in the following section.

I.2.4.1. Weibull statistical distribution

Waloddi Weibull introduced this statistical distribution function in 1939 (Weibull 1939), and later, he proposed a better summarisation of his work in 1951 (Weibull 1951). Afterwards, this distribution became widely used for different mechanical applications. By using Weibull distribution, the probability of failure for a solid material under a tensile load $P_f (\sigma)$ is given as (Weibull 1951):

$$P_f(\sigma) = 1 - e^{-\left(\frac{\sigma}{\sigma_0}\right)^m}$$
Eq. I-18

where σ, m and σ_0 are the tensile stress (MPa), the Weibull modulus, and the scaling parameter, respectively.

The Weibull statistical distribution is commonly used as a macroscopic concept to describe the occurrence of random homogenised defects inside a 3D solid sample, which could cause a variation in the macroscopic tensile strength of the different specimens of a given material. In the field of ceramics, the Weibull modulus can have a wide range, typically below 30; the value of *m* for some ceramics is presented in Table I-2 (Tinschert *et al.* 2000).

Table I-2. Weibull modulus (*m*) for certain ceramics (Tinschert *et al.* 2000)

Ceramic	Weibull modulus (m)
Feldspathic porcelain	13.6
Glass-infiltrated alumina	5.5
Alumina-reinforced feldspathic porcelain	13
zirconia ceramic	18.4

I.2.4.2. Application of Weibull distribution to describe quasi-brittle behaviour

As mentioned in section I.1.5, a very interesting quasi-brittle behaviour of refractories could be obtained when a suitable network of microcracks (numerous small discontinuities) is voluntarily introduced within the microstructure of materials. From already available experimental work reported in the literature, few authors recently started to develop numerical modelling approaches that could account for these numerous discontinuities. Even if such numerical approaches will be detailed in section I.3, developing a model that could accurately represent the influence of all these numerous discontinuities, up today, is still a challenging aspect. Nevertheless, in this way, Dai *et al.*

used a local Weibull approach for introducing such local stochastic defects. Indeed, the local Weibull approach brings the statistical distribution for local tensile strengths within each FEM simulation element (Dai *et al.* 2017). Such a model was applied to WST in order to examine the influence of local variability of strength on the global WST force-displacement curve, trying to mimic the obtained experimental results using a reverse approach. In addition to the Weibull distribution of local strengths, Dai *et al.* used a simplified bilinear strain-softening behaviour, as shown in Fig. I-10 to simulate the material's local microstructure behaviour during the WST.
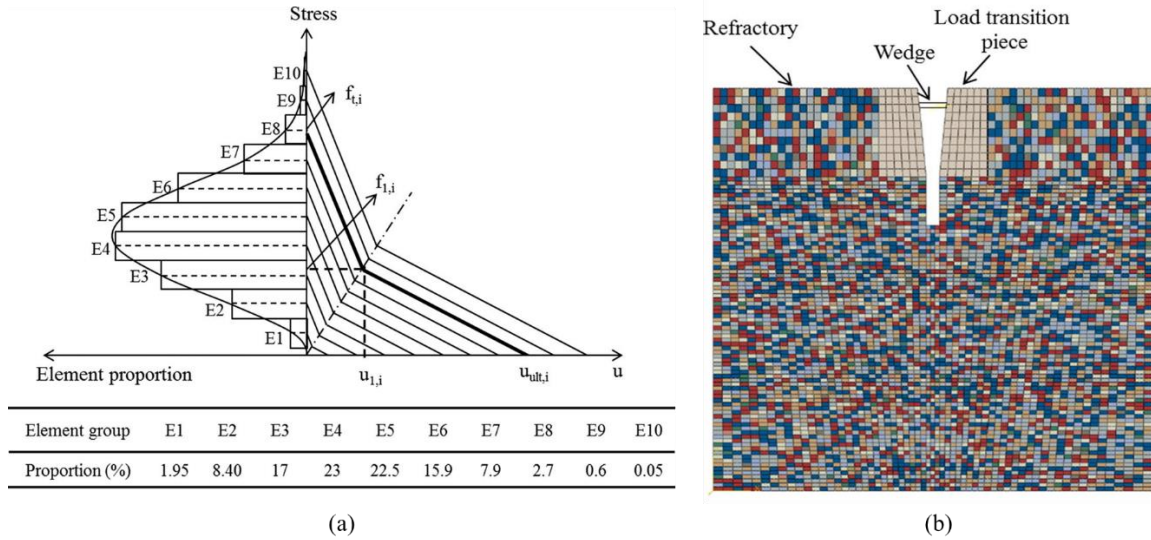
Fig. I-10. WST simulation in FEM: (a) the schematic diagram for strength distribution and assigned strain-softening behaviour for different groups of finite elements, and (b) the heterogeneous continuum model for WST; each set of colour is showing a group of the tensile strength (Dai *et al.* 2017).

As shown in Fig. I-10 (a), ten classes (E1, E2, …, E10) of elements with different tensile strengths were assigned. The proportion of finite elements belonging to each class was following a Weibull distribution with a modulus of 3. Moreover, each of these classes follows a dedicated pre-defined bi-linear strain-softening behaviour. These elements were randomly distributed in the model geometry, as shown in Fig. I-10 (b). By using such a FEM model, including the Weibull approach, bi-linear strain-softening behaviour and optimisation loops, it was possible to successfully reproduce an experimental non-linear curve of WST for Magnesia Spinel refractory, as shown in Fig. I-11.
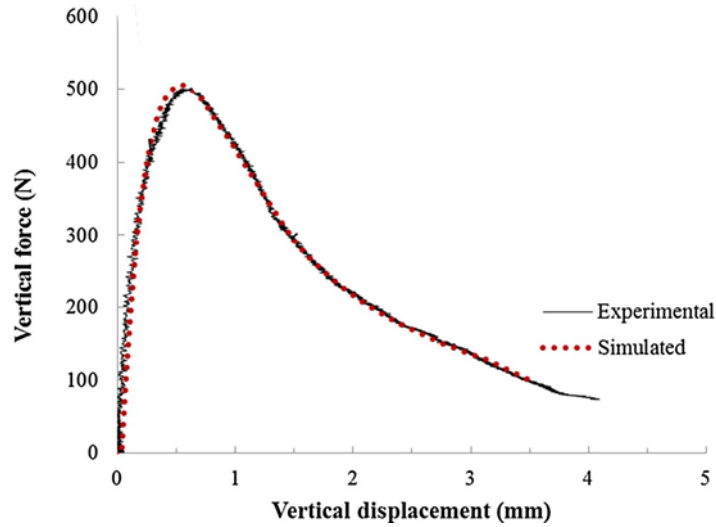
Fig. I-11. The non-linear curve of WST of Magnesia Spinel refractory: simulation vs experiment (Dai *et al.* 2017).

Combining the fracture mechanics basis and numerical simulations could be a robust tool to virtually test and predict the thermo-mechanical performance of refractory material, accounting for their complex microstructures. Eventually, such an approach could help to design optimised microstructures. The next section will be dedicated to potential numerical tools that could be suitable for simulating such material containing numerous discontinuities.

I.3. Different numerical models to simulate damaged materials and fracture propagation

Empowering calculation computers and tools enables engineers to use numerical simulations for bigger (higher degrees of freedom) and/or more complicated problems (thermo-mechanics, multi-scale problems…), consequently increasing the calculation accuracy. This means by having high-performance calculation tools nowadays, it is possible to decrease the simplifying assumptions, and at the same time, to simulate complex problems with conditions much closer to reality.

In this regard, the ATHOR project has taken advantage of numerical approaches in different scales to investigate further and predict thermomechanical behaviour of refractory linings: from the grain scale to the whole steel ladle structure. The simplified hierarchy of this multi-scale approach is shown in Fig. I-12. As mentioned before, this PhD study aimed to investigate the microstructure of refractories, which means that it will be focused on the grain scale, up to a single refractory brick scale. The numerical tools, which will be discussed later in this section, are mostly reviewed by considering their performances in such scales.
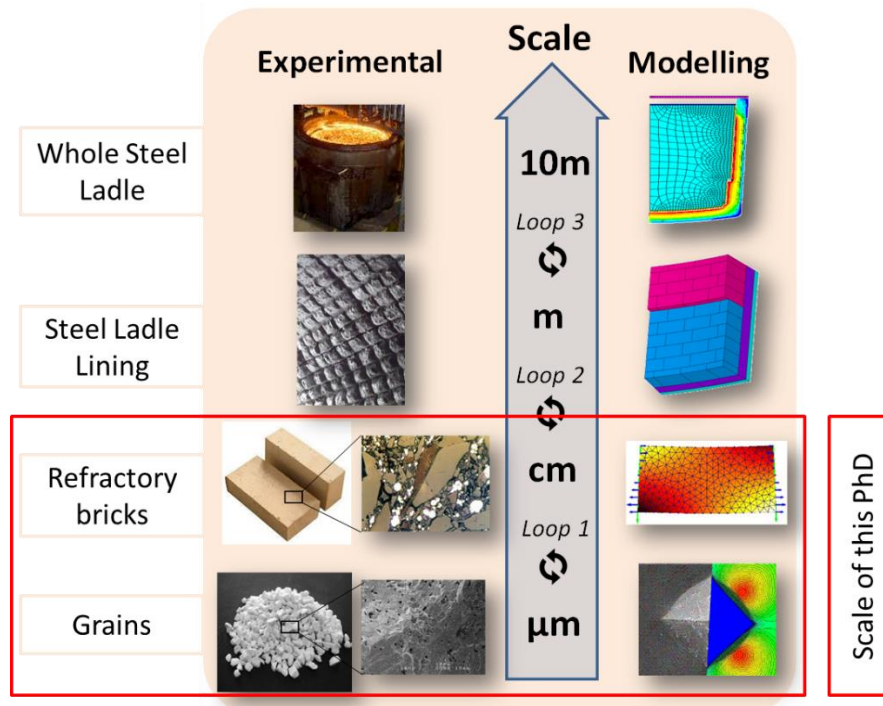
Fig. I-12. The simplified hierarchy of trans-scale modelling approach in the ATHOR project.

There are many different numerical approaches previously proposed to simulate and solve complex engineering problems. Each numerical model has its own limitations and advantages. Considering this fact, an appropriate numerical model should be chosen and implemented to suit a particular engineering and scientific problem. Despite their differences, most numerical simulations follow a certain meta-algorithm to solve a targeted problem, as shown in Fig. I-13 (Jebahi 2013).
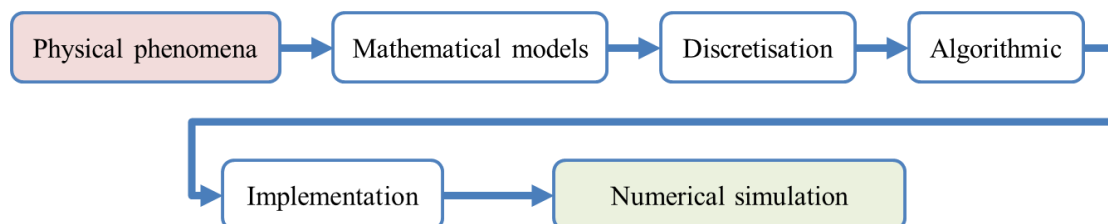
Fig. I-13. General numerical simulations meta-algorithm (Jebahi 2013)

There are many mathematical models for modelling a physical phenomenon, from continuous approaches to discrete ones. Depending on the nature of the physical phenomenon, each of these two general approaches could be used. An overview of the main numerical approaches is given in Fig. I-14. In the following sections, each of these numerical models will be introduced.

FEM: Finite Element Method
XFEM: Extended Finite Element Method
FVM: Finite Volume Method
EFGM: Element Free Galerkin Method

NSCD: None-Smooth Contact Dynamic Method
DEM: Discrete Element Method
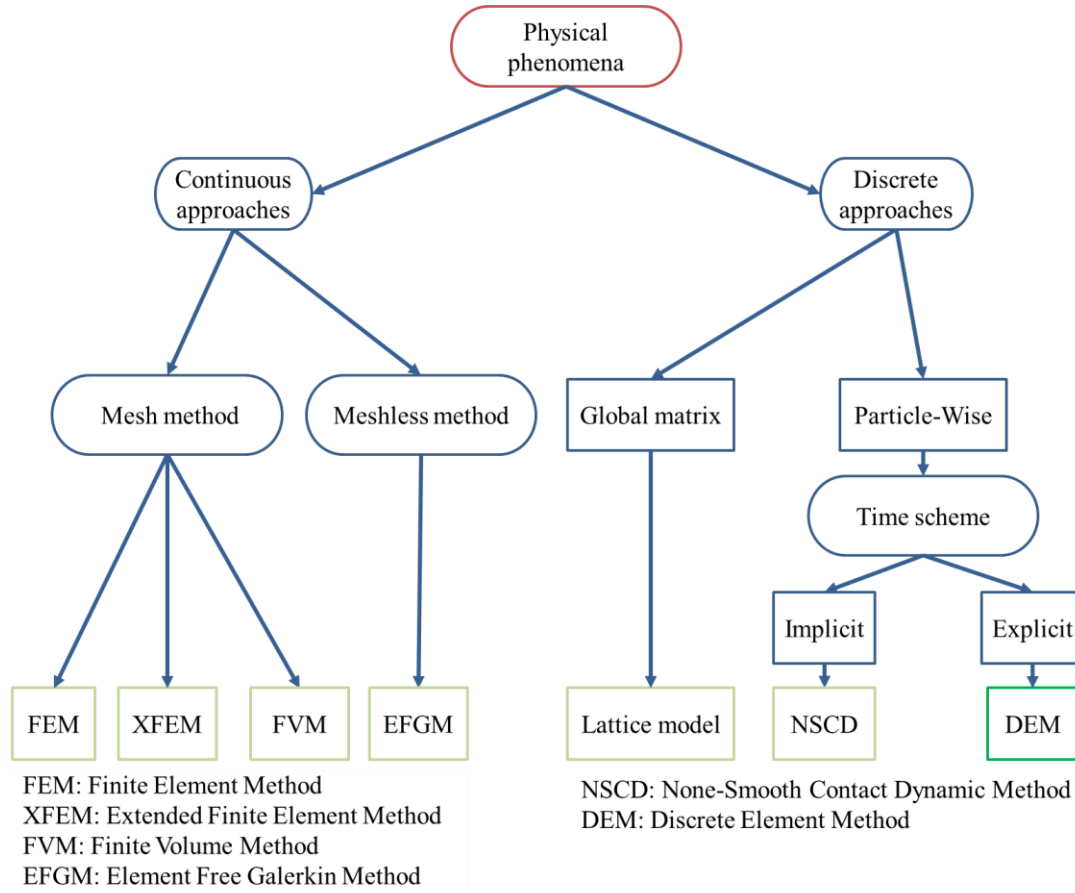
Fig. I-14. Overall categories of numerical techniques, inspired from (Gibaud 2017).

I.3.1. Continuous approaches

The thermo-mechanical continuous approaches are based on the process of subdividing the problems geometries to standard elements, for which mathematical models have been defined to describe a given physical behaviour. Then, the whole original system can be rebuilt from these elements. In this way, it let engineers model and predict complex behaviours and geometries (Zienkiewicz *et al.* 2013). Mathematicians have developed general techniques to discretise continuous problems since 1911 (Richardson *et al.* 1911). This very first study had implemented finite difference approximations to solve a masonry problem governed by differential equations. Afterwards, different other methods have been developed, especially for continuum elastic problems in solid mechanics (Mchenry 1943, Grinter 1949). In these studies, it is assumed that the whole domain is discretised into smaller elements, and these elements are made of reference local points, called nodes. Therefore, to achieve trustworthy continuum solutions, the number of these nodes should be increased.

All these continuum methods are following a general four-step algorithm as a method of approximating and/or solving the governing equations of continuum problems (Jebahi 2013):

- the continuum problem domain is approximated by a finite number of discrete components made up of reference points (nodes);

- the original mathematical models (governing equations) are changed into a system of algebraic equations;
- the resolution of this system gives the solutions or approximations at nodes;
- for other parts of the domain, the field variables can be approximated by interpolation or averaging the solutions at nodes.

The continuum methods are the ones that are following the continuum mechanics formulations, and different continuum methods exist. Some of these are widely used methods such as:

- *Finite Element Methods* (FEM), detailed in section I.3.1.1,
- *Extended Finite Element Method* (XFEM), detailed in section I.3.1.2,
- *Finite Volume Method* (FVM), detailed in section I.3.1.3,
- *Element Free Galerkin Method* (EFGM), detailed in section I.3.1.4.

These methods are used for different engineering applications, from fracture mechanics to fluid dynamics. Each of these methods uses different approaches for solving continuum problems:

- using mesh (or grids) for FEM, XFEM and FVM methods and,
- meshless methods for EFGM, which is a more recent technic.

Meshes are sets of elementary volumes (in 3D) or surfaces (in 2D) which are named as elements, connecting the discretising nodes. The meshes are used to define the geometry of the models mostly by using an assembly of simple convex polygons. As an example, in Fig. I-15 (a), the 2D rabbit geometry is described by mesh and discretised by triangular surface segments connected at their common nodes. These surface segments, at the complex boundaries of the model (here, the rabbit's fingers), will be defined smaller and with a higher number of connections to cover and shape the model boundaries properly. In meshing methods, the continuum problem's solution starts with such discretising (meshing) into a finite number of elements (Zienkiewicz *et al.* 2013). In this approach, partial or differential governing equations will be applied to each mesh. Then, the algebraic equations system for the whole model can be obtained by gathering all the local algebraic equations from the meshes (Jebahi 2013).

Since the 1970s, meshless methods became more popular (Gingold *et al.* 1977). These methods have the advantage to deal with arbitrarily distributed nodes without using any mesh or connectivity between them, as shown in (Fig. I-15 (b)). On the other hand, such methods are very time-consuming, and they suffer from several numerical problems, such as accuracy degradation near the boundaries and large approximation errors compared to the meshing methods (Jebahi *et al.* 2015). In the next section, some of the most popular continuum methods are summarised.
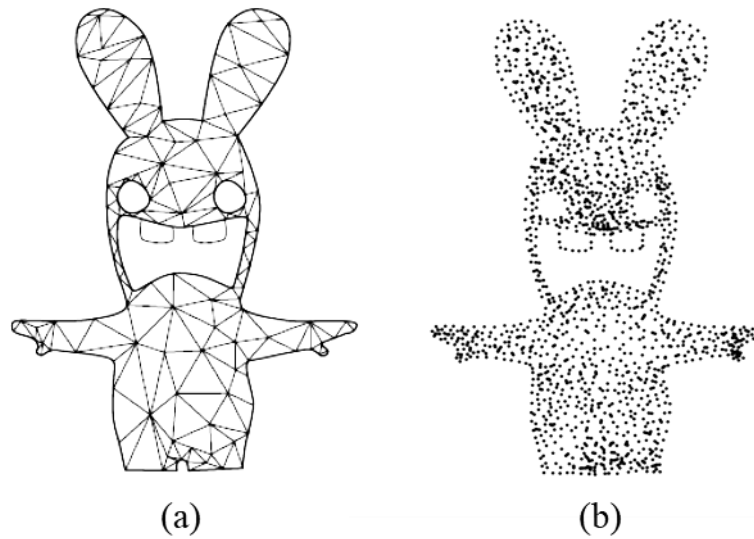
Fig. I-15. Discretisation for a rabbit geometry: (a) mesh discretisation (b) Meshfree discretisation (Jebahi 2013).

I.3.1.1. Finite Element Method (FEM)

The basis of FEM has been developed for many years, and its fundamentals have been explained in well-documented literature (Zienkiewicz *et al.* 2013). As a widespread mathematical technique for solving Partial Differential Equations (PDE), the Finite Element Method (FEM) is a well-known multidisciplinary numerical method for simulating and predicting the physical behaviours of continuum media driven by PDE. In such a way, engineering problems involving mechanical and thermomechanical phenomena are mainly solved by FEM.

For solving mechanical problems, FEM uses constitutive laws between stress and strain fields. The FEM formulation reduces the problem to the solution of a system of algebraic equations in terms of the nodal variables, where the displacements are the unknown of the problem. The main advantage of the FEM is its ability to model complex geometries and complex constitutive laws (damage and fracture mechanics, plasticity approach, multi-physics such as thermomechanics and coupling with corrosion…).

FEM could be used for classical thermomechanical applications to model temperature distributions and related stress and strain fields in refractories. In this way, by using a constitutive damage model, Damhof *et al*. investigated the thermal shock damages in a multi-scale study (Damhof *et al.* 2011). Their study was focused on a steel ladle for which the refractory lining is subjected to alternated thermal cycling (ladle being filled by molten steel in the first step and emptied in the next step); the key point was to investigate damage progression within the refractory lining. Thus, a scale transition was investigated from the steel ladle (structure scale, see Fig. I-16 (a)) to a particular section of the lining (material scale, see Fig. I-16 (b)).
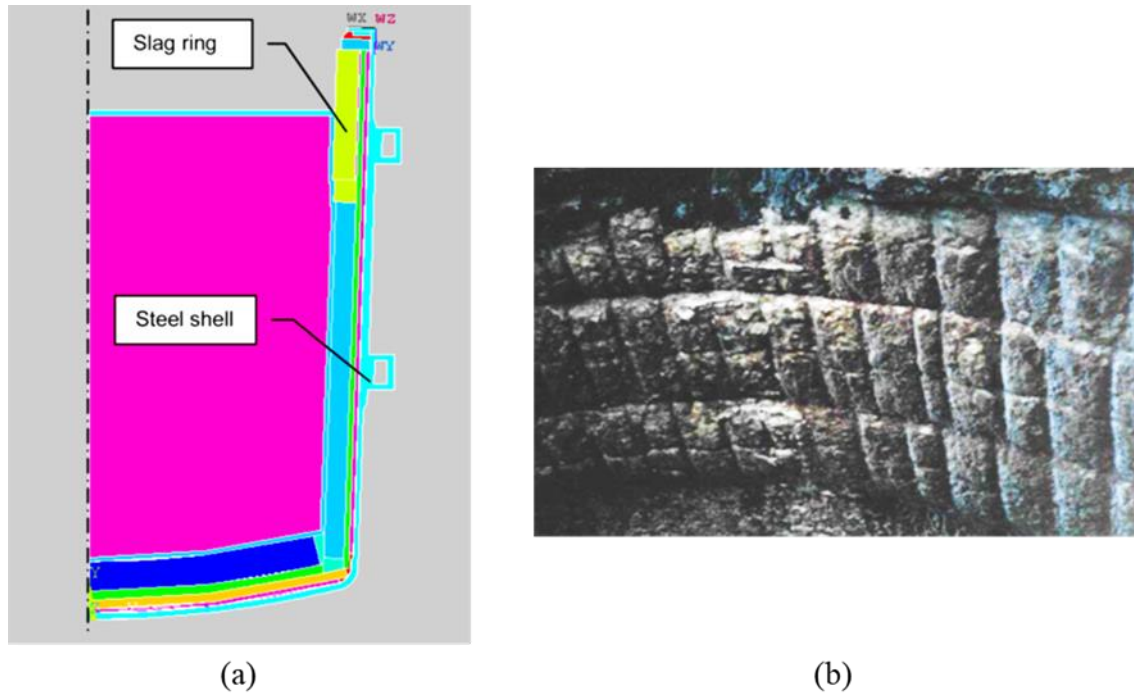
Fig. I-16. Steel ladle and the slag ring: (a) the schematic axis-symmetric cross-section view of a steel ladle (Damhof *et al.* 2011) and (b) the damaged refractory bricks in the slag ring due to the thermal cycles (Andreev *et al.* 2001).

The first step of calculations was to obtain the temperature distribution and the relative stress fields during the different sequences of filling and emptying processes at the structure scale and then at the material scale. The temperature distribution within a section of the lining is shown in Fig. I-17 (a), for the first loading cycle and for the beginning of the emptying stage. As a key result, Fig. I-17 (b) estimates damage distribution within the refractory brick close to the hot face. As mentioned by the author, these damage results were consistent with the observed failure zones within the real refractory lining.

(a)

(b)
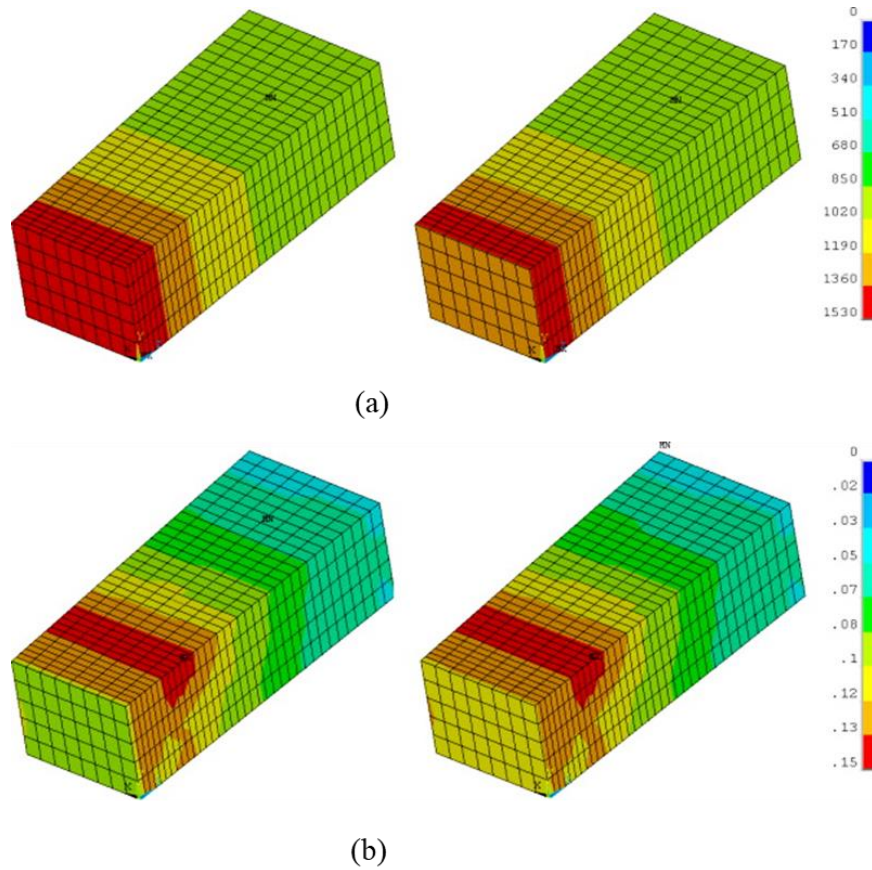
Fig. I-17. Examples of results obtained by FEM using damage model in a multi-scale approach: (a) temperature distribution (°C) in a steel ladle lining during different sequences of filling (left) and emptying (right) processes, and (b) damage estimations for the same stages (Damhof *et al.* 2011).

Despite this success, it should be noted that in case of material that could be progressively damaged during loading, it is relatively easy to account for this damage by considering a local variable (associated with the element) such as the Kachanov parameter (which can be isotropic or anisotropic) (Kachanov 1993). However, such an approach does not precisely represent the local discontinuities resulting from cracks within the microstructures.

To describe the discontinuities resulting from fracturing in FEM in much more detail, one of the most common approaches is to use the cohesive elements within the model. The cohesive finite element method provides a practical approach for quantitative analysis of fracture behaviour through explicit simulation of the fracture processes (Chen *et al.* 2009). This approach is based on the cohesive zone concept proposed by Dugdale (Dugdale 1960) and Barenblatt (Barenblatt 1962). The cohesive zone approach characterizes the fracture process by a traction-separation law at the crack tip instead of assuming an elastic stiffness reduction in LEFM (as explained in section I.2.1). In this way, this approach prevents the stress singularity at the crack tip, which in classical fracture mechanics was considered to be infinite and causing certain numerical errors. By implementation of cohesive elements into the FEM model, Jin *et al.*, investigated the fracture energy (see section I.1.3) and tensile strength of refractories in a WST (see section I.2.3) by inverse estimation (Jin *et al.* 2014). In the mentioned study, a

two-dimensional and symmetrical model was built based on the WST test configurations, as shown in Fig. I-18(a). Then, a strain-softening behaviour was assigned to the cohesive elements within the ligament area, where the fracturing process is supposed to be occurred (No.3 in Fig. I-18(a)). By running cycles of simulations, Young's modulus and fracture parameters of the material were inversely fitted to the experimental results through an adaptive non-linear least-squares algorithm. As shown in Fig. I-18(b), the proposed model successfully reproduced the three experimental WST load-displacement curves by using cohesive elements in FEM.
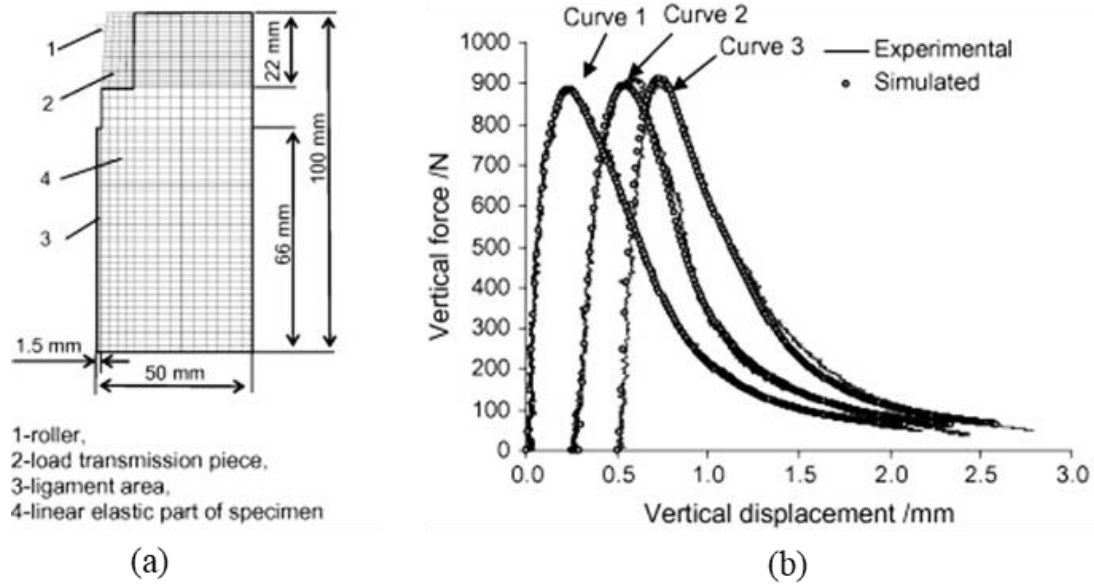
Fig. I-18. Using cohesive elements in FEM for WST simulation:
(a) prepared geometry of the model and (b) experimental and simulated force-displacement curves for three WST on the same material (Jin *et al.* 2014).

It should be highlighted that in the previous example of WST, the crack location was very well-defined in advance and thus, dedicated, cohesive elements were uniquely placed in the ligament area. However, when it is needed to strictly mimic crack initiation and propagation within a real microstructure of material for which the crack path cannot be predicted, the obtained results using the standard FEM approach becomes usually extremely dependent on the mesh. This point means a considerable dependency of the obtained results to the mesh size and to its distribution around the crack tip (Lopes *et al.* 2020). Hence, it could require dynamic re-meshing processes during the crack propagation and high mesh refinement toward the singularity, which are highly time-consuming. As an example, in Fig. I-19, the number of finite elements in the simulation of a tensile test drastically grows due to the presence of two cracks that are propagating (A. R. Khoei *et al.* 2008). Overall, these points make FEM inadequate for problems with a high number of discontinuities.
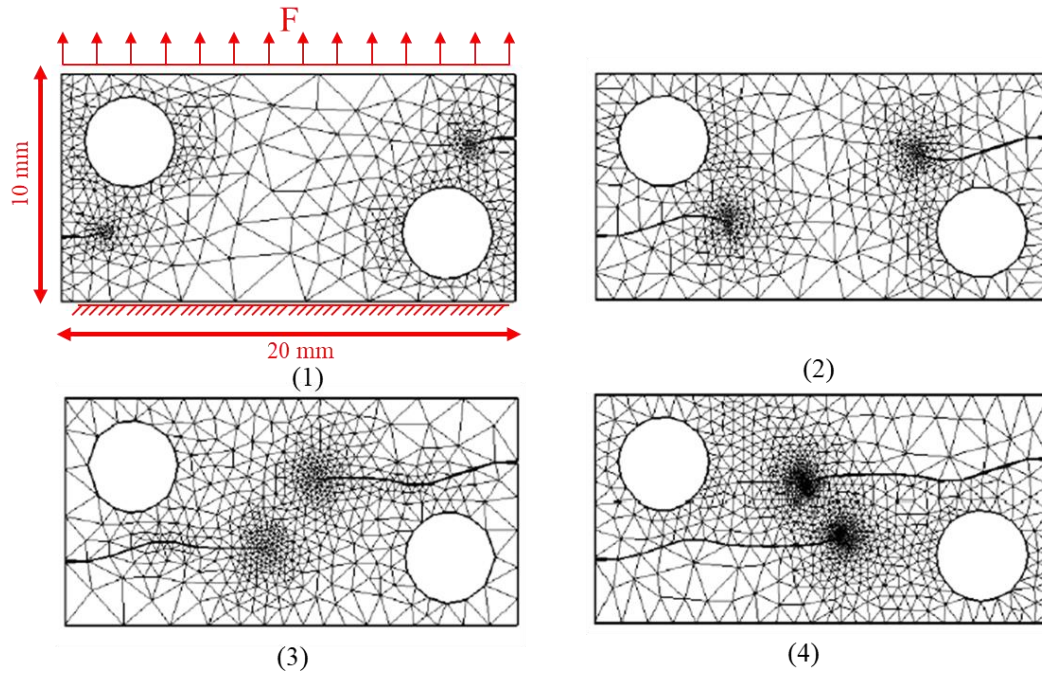
Fig. I-19. Crack propagation in direct tension modelled by FEM: mesh refinement and re-meshing are required around crack tips, increasing the number of elements from 807 to 1762 elements, by Khoie *et al.* (A. R. Khoei *et al.* 2008)

I.3.1.2. Extended Finite Element Method (XFEM)

For solving the mentioned problems of FEM to manage the initiation and growth of random cracks within a regular mesh, the Extended Finite Element Method (XFEM) was introduced by Belytschko *et al.* and Moës *et al.* in 1999 (Belytschko and Black 1999, Belytschko *et al.* 2001, Moës, Dolbow, and Belytschko 1999).

In this method, finite element discretisation is enriched with additional nodal degrees of freedom. This enrichment is managed by enrichment of each node (*enriched nodes*) where, in such case, discontinuities are supposed to occur within the *enriched element*. In other words, in comparison to the standard elements, the XFEM elements are enriched by equations of general displacement field that allows to account for local discontinuity describing crack tip and crack opening. This means that cracks can be described accurately in a single element, therefore, removing the need for iterative re-meshing to simulate crack propagation (Fig. I-20). Since the crack's final position is not known in advance, with this approach, XFEM elements should be defined in the potential cracking area, and those *enriched elements* will be activated in the case of crack occurrence.
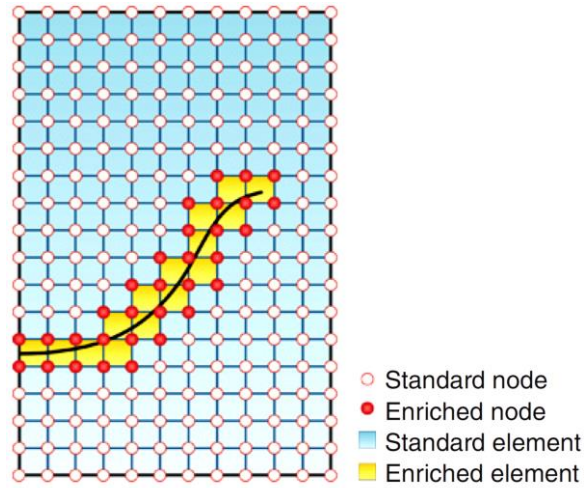
Fig. I-20. Overview of different nodes and elements within the XFEM model containing a crack (Amir R. Khoei 2015).

As an application of using XFEM for crack propagation, Farukh *et al.* have used this method to simulate crack growth within the microstructure of a polycrystalline material under cyclic mechanical loading (Farukh *et al.* 2016). The first step was to reproduce the mechanical behaviour of the polycrystalline material accurately. To do so, a Representative Volume Element (RVE) (see section III.3.1), consisting of a limited number of grains (and by considering their properties), was used to reproduce the apparent mechanical behaviour of the material. In this way, the model's microstructure was built from the real microstructure of the polycrystalline material, as shown in Fig. I-21 (a) and (b). The predicted crack propagation path within the XFEM model microstructure is shown in Fig. I-21 (c). As it can be seen, the model has successfully simulated the intergranular fracture propagation. As the authors reported, by using such an XFEM model, it was possible to observe the variation of crack growth speed, resulting from materials real microstructure and different grains properties.
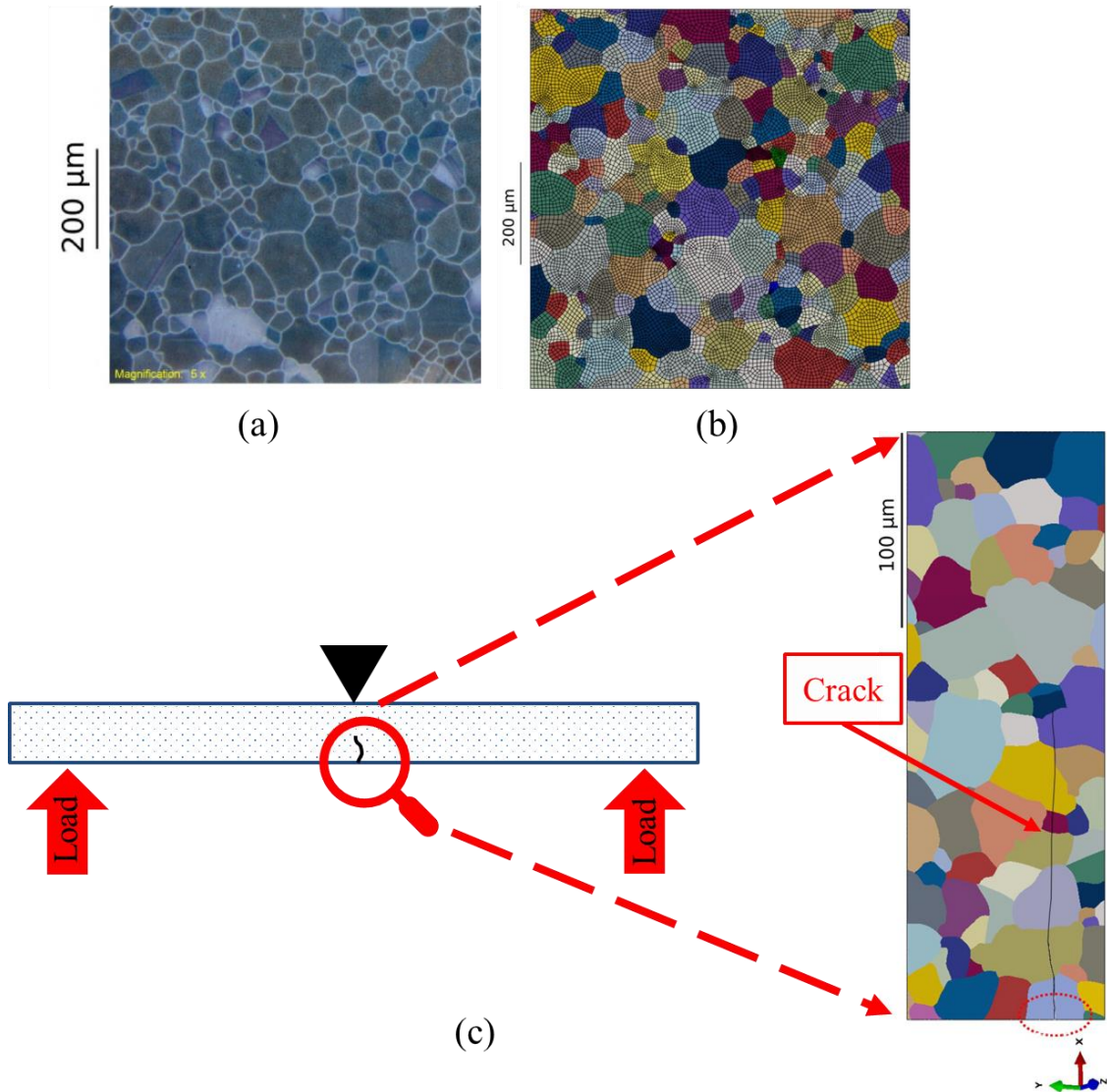
Fig. I-21. Polycrystalline microstructure: (a) the real polycrystalline alloy, (b) XFEM meshing of the real polycrystalline alloy, and (c) prediction of XFEM model for the crack path within the microstructure (grains were assigned different colours in order to show the microstructure) (Farukh *et al.* 2016).

As mentioned in section I.3.1.1, the cohesive zone approach can be introduced in the finite element models, including XFEM, by implementing cohesive elements in the model. By using cohesive elements within XFEM models, the highlighted limitation of the XFEM for the necessity of pre-defining the potential cracking zone will be improved. In this way, Mubashar *et al.* introduced an XFEM model coupled with cohesive elements to simulate an unknown crack path in a lap joint's fillet area. As a benchmark, the joint was loaded in a direct tension configuration to observe the crack path in the adhesive joint's fillet region, as shown in Fig. I-22 (a). The cohesive elements are placed in the interface layer between the aluminium bodies and the adhesive. The result of the defined model is shown in Fig. I-22 (b). Unlike the simple cohesive finite element models, the

crack was grown without needing to align the element edges to the crack path, as the XFEM method enables cracking within *enriched elements*.

On the other hand, the crack initiation was managed thanks to the implementation of the cohesive elements in the contact layer between the aluminium bodies and the adhesive efficiently. Comparing these results to other literature, the authors reported good accordance with experimental results. However, it was also observed that the combination of XFEM with cohesive elements could potentially lead to an unrealistic discontinuity in the crack path when it moves from the cohesive elements to the XFEM domain.
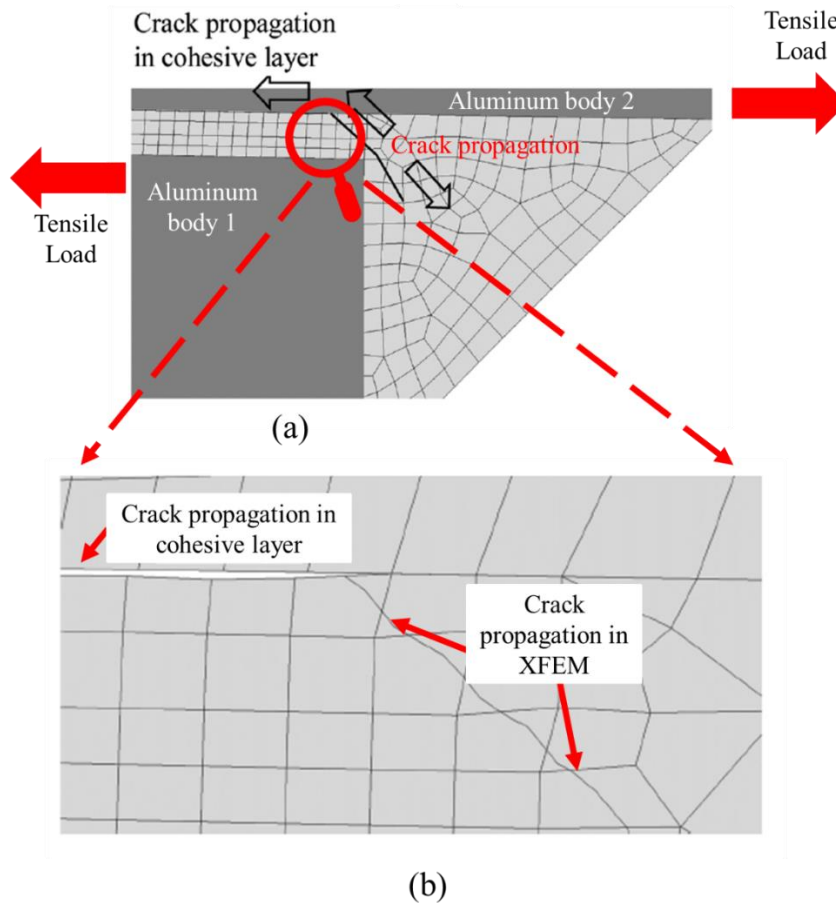
Fig. I-22. Crack propagation in a fillet area between two aluminium bodies: (a) initiation of the crack in the cohesive layer, and (b) propagation of crack from the cohesive layer to the XFEM domain (Mubashar *et al.* 2014).

The point is that, in such studies, only one crack is propagating within the continuum media. On the other hand, dealing with refractories at a micro-scale requires simulating a large number of microcracks. To sum up, XFEM could be an option for simulating a limited number of discontinuities, but it is still not capable of easily managing multiple crack initiations and propagations simultaneously (Jebahi *et al.* 2015).

I.3.1.3. Finite Volume Method (FVM)

The Finite Volume Method (FVM) is a discretisation method that has been extensively used in several engineering fields, specifically in fluid mechanics, heat and mass transfer. This method has been introduced in the early 1960s by Tichonov and Samarskii (Tikhonov *et al.* 1963). FVM basis has been well documented in recent years (Eymard *et al.* 2000). FVM is a method to solve PDEs (elliptic, parabolic, hyperbolic, multidimensional non-linear hyperbolic and…) in the form of algebraic equations. It is locally conservative because it is based on a balance approach, which means a local balance is written on each discretisation cell (zone), called a control volume. Then, by the divergence formula, an integral formulation of the fluxes over the control volume boundaries is obtained (Eymard *et al.* 2000).

The fracturing simulations in FVM is mostly limited to the applications for which the fracturing process is caused by hydraulic fluid pressure, as this method is well-suited for fluid mechanic problems. In this way, Bryant *et al.* used FVM to simulate hydraulic fracture propagating in heterogeneous geological formations (Bryant *et al.* 2015). Hydraulic fracturing is the process of initiating and opening cracks, mostly within the rock formations, by injecting fluids at high pressure. In the mentioned study, the FVM showed the capability to simulate realistic fracture networks, taking into account the influence of fracture toughness (see section I.2.1) and fracture energy (see section I.2.3). In Fig. I-23, a starter notch was introduced in the model, and then the pressure is simulated by high normal stresses within the notch to propagate the fracture. This simulation was done in anisotropic media and by varying fracturing parameters (toughness and fracturing criteria).
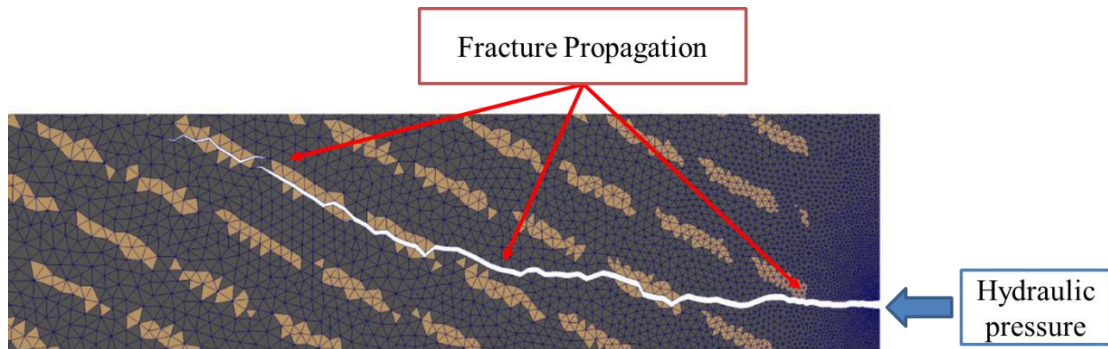
Fig. I-23. Fracture propagation using the FVM model (Bryant *et al.* 2015).

The used FVM model was capable of simulating the propagation of single and multiple cracks in 3D in non-planar configurations within heterogeneous porous materials.

To sum up, the FVM is known as a fast, robust method for industrial problems, thanks to its short and reliable computational process for simulating complicated systems. FVM and FEM (see section I.3.1.1) have similarities as both use generic variational formulations to solve PDEs. However, FVM has some shortages compared to FEM for simulation of complex geometries within the model due to the necessity of volumetric

discretisation with the FVM. Hence, in some cases, it is challenging to design schemes and geometries, which give enough precision in the calculations (Eymard *et al.* 2000).

I.3.1.4. Element Free Galerkin Method (EFGM)

The Element Free Galerkin Method (EFGM) is a meshless method mostly used for fracture mechanics problems. This method has been introduced by Belytschko *et al.* in 1994 (Belytschko *et al.* 1994). The key idea of these meshless methods is to provide a numerical model with a set of randomly distributed nodes. In the EFGM, the partial differential equation system is solved in a variational weak form. In this variational weak form, the test and trial functions are the shape functions of moving least-squares approximation. The EFGM can be used on complex geometries because it requires only nodal data and does not use any volumetric elements (Dehghan *et al.* 2016). Due to its meshless nature, in case of the occurrence of a crack in EFGM, it is not required to pass the re-meshing process (such as the one that has been explained for FEM, see section I.3.1.1). Hence, this method suits fracture propagation modelling, especially for the linear elastic fracture mechanics (LEFM) assumptions (Ventura *et al.* 2002). Later, this method was developed for the non-linear materials and cohesive cracks as well (Rabczuk *et al.* 2007). In this way, in a study by Shao *et al.*, this method was used for 3D crack propagation, based on the phase-field model. In this case, the phase-field is a continuous spatial scalar function for describing the transition from an intact un-cracked material to a fully broken state (Shao *et al.* 2020). To verify the accuracy of such EFGM simulations, different benchmark tests such as the notched tensile test, the notched shear test, and the three-point bending test were investigated. In the three-point bending test case, the notched was introduced with a horizontal inclination of 45° to observe and verify the experimental observation of the crack twisting with EFGM. The EFGM nodes, the relative phase-field measure and crack paths are shown in Fig. I-24.
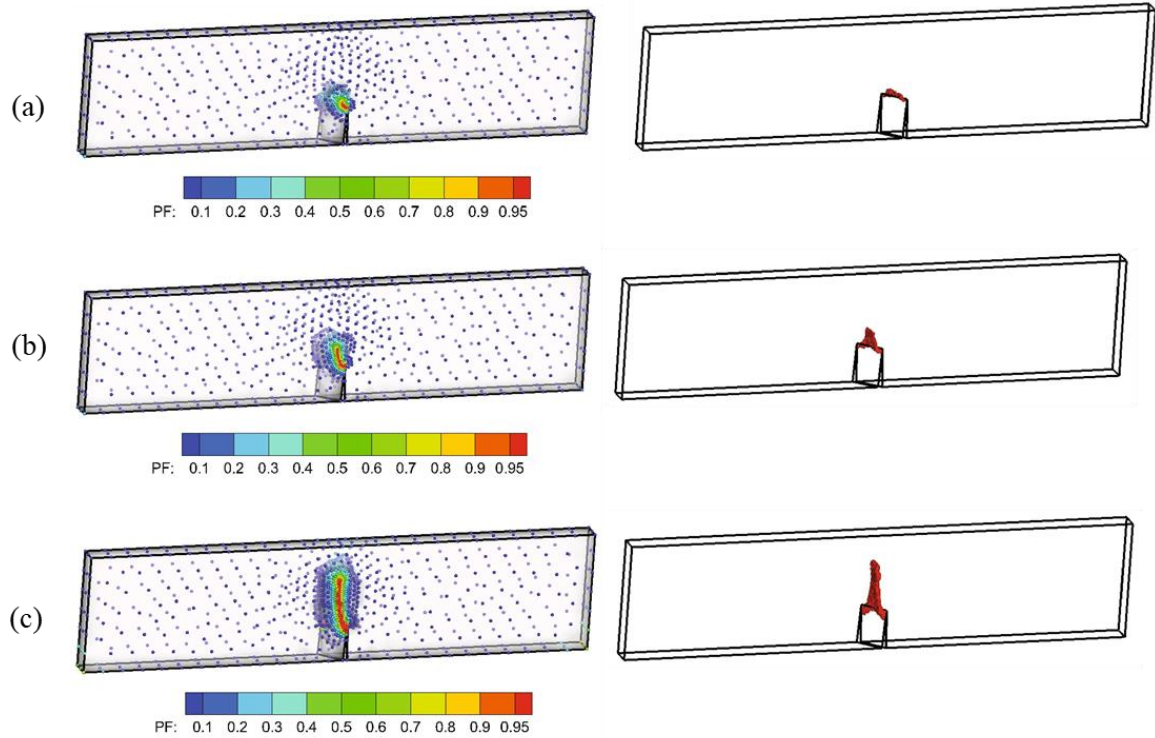
Fig. I-24. Inclined notch three-point bending test. In the right EFGM and phase-field model, and in the left, the crack propagation path. (a), (b) and (c) advancement steps of the simulations. From (Shao *et al.* 2020)

As it can be seen in the Fig. I-24, the EFGM model was able to simulate the crack path and crack twisting phenomenon, which is in line with reality.

EFGM simulation is very time-consuming and suffers from boundary inaccuracy and difficulties to impose Dirichlet boundary conditions due to meshless configuration. For example, considering Fig. I-15, it is not accurate to introduce the sharp edges of complex geometry (fingers of the rabbit) only by nodes cloud. Also, EFGM produces results with errors larger than those obtained using grid-based methods (Jebahi 2013).

I.3.2. Discrete Methods

The discrete methods involve assemblies of rigid elements or nodes that interact with each other through interaction laws. The basis of this approach is coming from the molecular dynamics models in the 1950s (Alder *et al.* 1959). The discrete methods are divided into two general groups, the global matrix model (lattice model) and the particle wise models. The principal difference between these two approaches is that the lattice model uses material points as elements (see section I.3.2.1), while in particle wise models, materials are modelled by discrete elements (see section I.3.2.3) (André *et al.* 2019). The other difference is that the material points have no geometries while the discrete elements have well-defined geometries; therefore, it is necessary to detect the interactions between these discrete elements during simulations.

In comparison with continuum-based methods, the discrete approaches are capable of modelling micro-mechanical behaviour of materials where the continuity assumption is

no longer valid because of the presence of microcracks. Hence, these discrete approaches enable the modelling of systems with a high number of evolving discontinuities, including crack initiation and propagation (Scholtès *et al.* 2012). Therefore, many fracture initiation and propagation problems have been modelled by these approaches (Scholtès *et al.* 2013) (Lemesle *et al.* 2020). However, it should be mention that there are some challenges for modelling continuum media with discrete methods:

a) there are no continuity assumptions in these methods because of the discrete nature of these models. The constitutive equations coming from continuum thermo-mechanics, such as Hook's law or Fourier's equation, cannot directly be applied;

b) in such case, choosing cohesive links and calibrating their properties to reproduce a desirable macroscopic behaviour are challenging;

c) construction of initial model domains considering the structural properties of the material such as homogeneity and isotropy is challenging too (Jebahi 2013);

d) and finally, dependencies of the results to the scale and the discretisation fineness of the domain could be observed and should be taken into account while analysing and post-treating results.

Each of these drawbacks has been addressed dedicatedly for different discrete interaction models. For example, to address the calibration problem for the cohesive beams model, a direct calibration method has been proposed (T.-T. Nguyen *et al.* 2019), or for the flat joint model, a systematic algorithm has been proposed too (Vallejos Javier Andres *et al.* 2017 and Zhou *et al.* 2018).

I.3.2.1. Lattice models

Lattice models were developed by Herrmann *et al.* (Herrmann *et al.* 1989). In this approach, the solid body is modelled by a set of nodes connected with bonding elements. Generally, these nodes have neither masses nor volumes. Fig. I-25 is showing a simplified scheme of this method (Schlangen *et al.* 1992) where the nodes are connected with 2D Euler-Bernoulli bonding beams. Solving a mechanical problem with the lattice method is based on assembling a global stiffness matrix from the local bonds. In fact, lattice models often implement a lattice structure of Euler-Bernoulli beam finite elements, just like the FEM method.
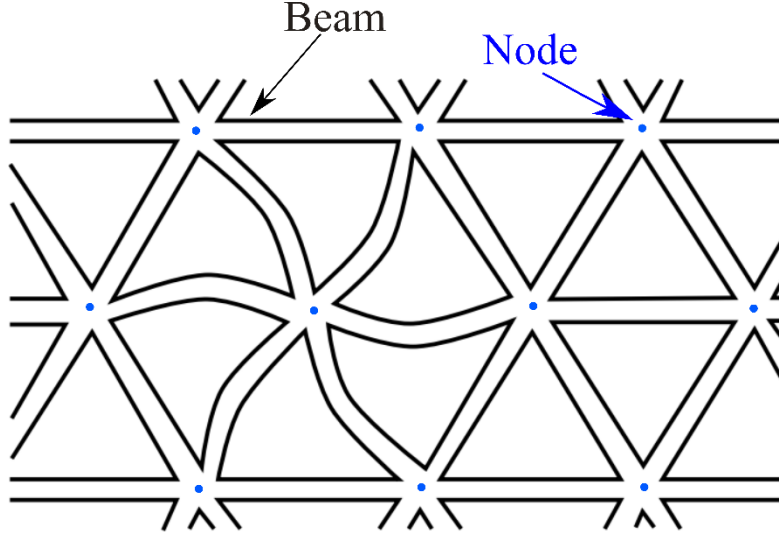
Fig. I-25. A regular triangular lattice of beams (Schlangen *et al.* 1992).

In this case, by knowing the global stiffness matrix ([K]) and displacements and rotation vectors of the nodes and, loading vector (*F*), which contains forces and torques in the beams, the problem can be written:

$$\boldsymbol{F} = [K]\ \boldsymbol{X}$$

<div align="right">Eq. I-19</div>

where *X* is an unknown vector that includes both displacements and rotations of the nodes (Jebahi *et al.* 2015).

Lattice models can model discontinuities and fractures within a continuous material. For example, as shown in Fig. I-26, Leblond simulated a brittle fracture propagation in concrete by using a dedicated lattice model (beam particle model) in different loading modes (tension, shear and rotation) (Oliver-Leblond 2019). As one of the benchmarks, the mentioned study was done for a single notched specimen, which was undergoing complex shear-rotational forces, as shown in Fig. I-26 (a). In the mentioned study, digital image correlation was used to obtain the experimental vertical displacement field (in Fig. I-26 (b)), which was compared to simulation (in Fig. I-26 (c)).
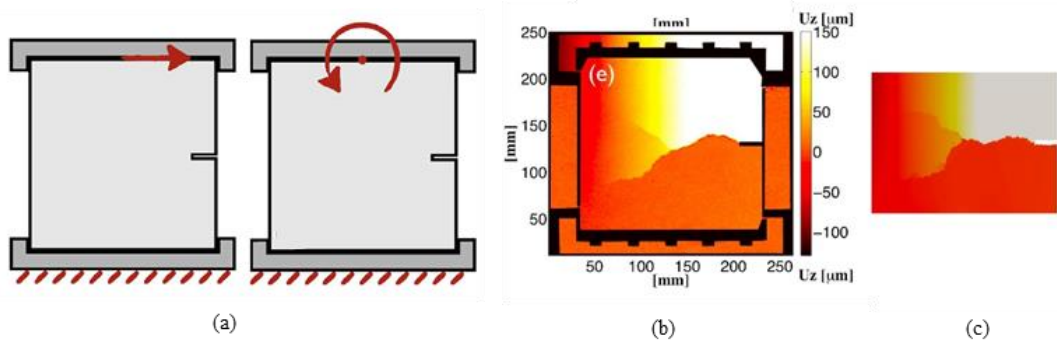
Fig. I-26. Vertical displacement field and crack propagation for a single notch sample subjected to shear and rotation test: (a) experimental device used to load the sample in shear and rotation at the same time, (b) experimental result from digital image correlation, (c) simulation output (Oliver-Leblond 2019).

As it can be seen in Fig. I-26, lattice model is capable of simulating such a complex cracking pattern which exhibits crack branching and crack bifurcation. It shows the high potential of lattice models for fracture-related problems.

As previously pointed out, in this method, the nodes do not have mass and volumes, which causes difficulty to model fracture closure phenomena. To overcome this problem, Ibrahimbegovic *et al.* proposed assigning to each node a relative equivalent volume based on the spatial Voronoi tessellation (Ibrahimbegovic *et al.* 2003). However, this solution is potentially time-consuming for 3D problems (T. T. Nguyen 2019).

I.3.2.2. Non-Smooth Contact Dynamic method (NSCD)

This method has been introduced and developed by Jean and Moreau during the 1980s and 1990s (Moreau 1988, Jean 1999). NSCD is an implicit method that uses a formulation of non-smooth dynamics through unilateral contact and dry friction between the elements. In this method, no elastic contact law is considered between the elements and the elements are assumed to be perfectly impenetrable. The contacting laws are non-differentiable laws. These laws are managed by an implicit method using a non-linear Gauss-Seidel algorithm at each calculation step. These laws manage contacts and friction, which are relevant in multi-bodies assemblies. (Dubois *et al.* 2018)

Based on a study by Dubois *et al.* (Dubois *et al.* 2018), the NSCD method is well suited for the numerical treatment of frictional contact problems (such as cohesive or viscoelastic laws). Due to the implicit approach, NSCD is able to use large time steps. However, one single time-step requires a time-consuming calculation to solve the non-linear system of equations.

I.3.2.3. Discrete Element Method (DEM)

The fundamentals of this approach are based on the molecular dynamics models, which was introduced in the 1950s (Alder *et al.* 1959). DEM numerical method was initially designed to reproduce intact rocks regarding their microstructure by Cundall in the 1970s (Cundall 1971, Cundall and Strack 1979), and later the contact representation, detection and interactions of discrete elements have been described (Cundall 1988b).

In this explicit method, mass and geometry have been assigned to each discrete element. Newton's second law is used to determine the translational and rotational movements of discrete elements taking into account their interactions coming from the overlapping contact forces. These force-displacement contact laws are used to update the forces coming from the relative motion at each contact. These force-interpenetration formulas are called "*smooth contact*", which in the simplest case, use linear interaction laws (spring model), as shown in Fig. I-27.

Spring (smooth contact)

Contacting discrete elements
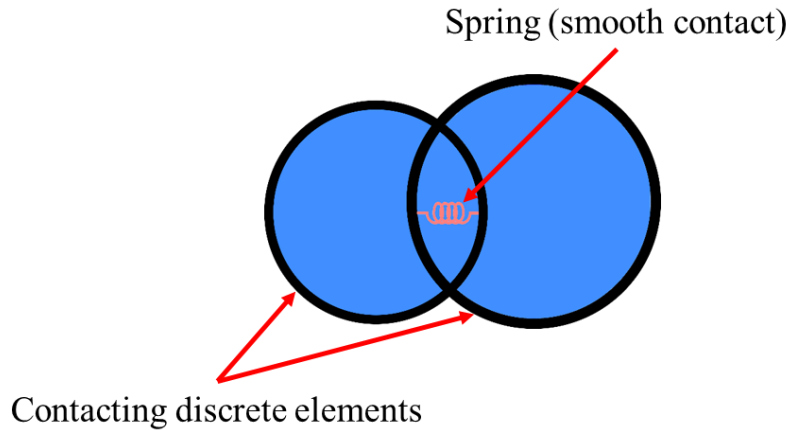
Fig. I-27. The scheme of a smooth contact model

The main difference between this method and NSCD (see section I.3.2.2) is that the DEM allows a finite penetration between the discrete elements through a penalty algorithm (Cundall 1971), which is not the case for the NSCD. In such a case, DEM is suitable for highly dynamic phenomena (short-time) whereas, NSCD is mostly used for long-time and quasi-static phenomena.

To simulate a continuum media by DEM, the media could be built up from bonded discrete elements. Here, *bonded* refers to permanent contacts which will not be vanished if the discrete elements are not penetrating. This method's main advantage is that it naturally considers the media as an assembly of individual discrete elements. Due to the discrete nature of this model, it could deal with discontinuous phenomena which are discrete by nature. Hence, there is no need for complicated transitional procedures from a continuum description of media to discontinuities, such as mentioned for the XFEM method (see section I.3.1.2). In this method, cracks could initiate and propagate through the numerical domain by breaking bonds. There are different approaches in bonding the particles in DEM: parallel bond model (Potyondy *et al.* 2004), flat joint model (Potyondy 2012), and cohesive beams model (Schlangen *et al.* 1996) are among the most cited ones.

A simple demonstration of the formation of de-bonding cracks induced by compression is shown in Fig. I-28. Here, a vertical load *F* is applied to different configurations of assemblies of discrete elements. Taking into account the different geometries of these assemblies, this imposed vertical loading leads to a separation of bodies in the horizontal direction. If these relative displacements reach a given pre-defined threshold, the horizontal bond will be broken in order to simulate a microcrack in the discrete element assembly. As shown in Fig. I-28 (c), this mechanism could occur even with discrete circular/spherical elements (Potyondy *et al.* 2004). This point explains why this simple geometry is often used to increase the efficiency of DEM calculations.
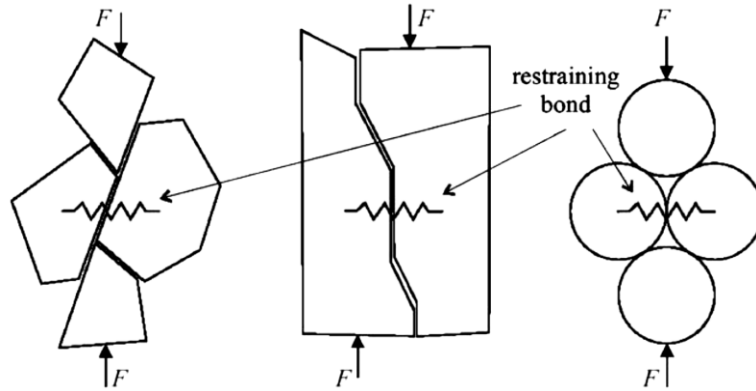
Fig. I-28. Horizontal tensile cracking induced by vertical compression: two simplified experimental cases and idealisation as a bonded assemblies of spherical discrete elements (Potyondy *et al.* 2004).

It is noteworthy to mention that, due to the lack of a robust theoretical basis, using DEM to simulate a continuum media has been limited until recent years (Jebahi *et al.* 2015). Nowadays, this method is intensively under development to simulate continuum media, and as pointed out, especially for fracture-related problems (fracture initiation and propagations). For example, as shown in Fig. I-29, André *et al.* have modelled fracture propagation in the indentation tests for a continuum media by using the cohesive beam model. As it can be seen in this picture, a 2D Hertzian brittle cone fracture was reproduced for the indentation test on a silica glass with a blunt indenter loading. In 3D, these crack paths were qualitatively and quantitatively compatible with experimental observations (André *et al.* 2013). In this way, in another recent study with the cohesive beam model by Ammar *et al.*, debonding and cracking process in 3D short glass fibre composite materials has been successfully simulated (Ammar *et al.* 2021).
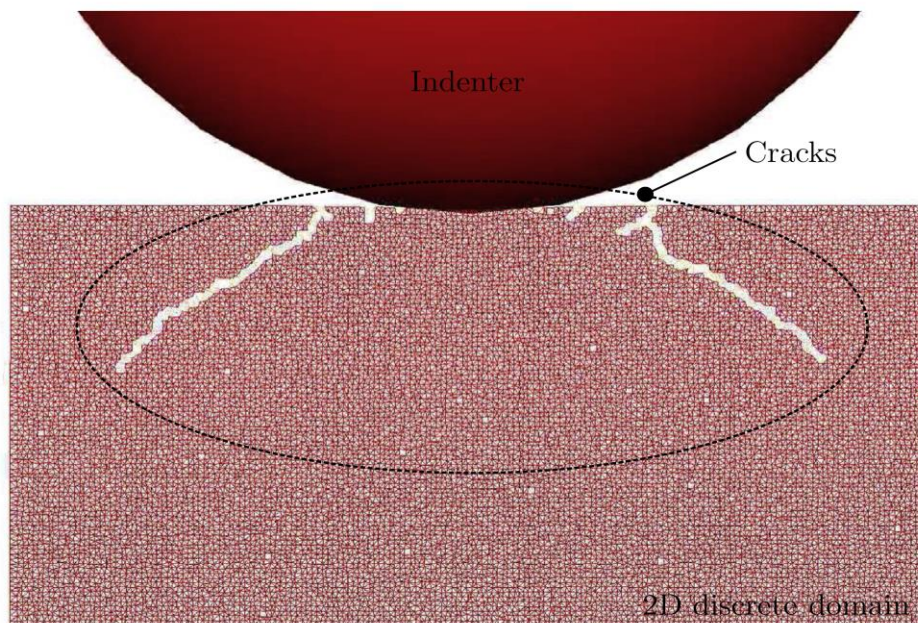
Fig. I-29. Crack propagation in the indentation tests for a continuum media by using Cohesive Beam Model (André *et al.* 2013).

As discussed, the DEM method is showing high potential in the simulation of fracturing processes. However, a relative drawback of the discrete methods is that they mostly require a high-performance calculation system since they are time-consuming. The other inconvenience of DEM for continuum problems is that a calibration step is required to reproduce the macroscopic material mechanical behaviour quantitatively. The last difficulty is that DEM uses a force-displacement approach instead of classical mechanics stress-strain description.

I.3.3. Choosing an adequate numerical simulation method to model damaged materials and fracture propagation

In the previous sections, different numerical models have been introduced for simulating physical phenomena. Each of them was using either the continuum approach or the discrete approach. On the other hand, as explained in section I.1, the present work aims to numerically investigate thermally induced damage and microcracking processes which could influence the apparent mechanical behaviour of refractory materials. Evidently, this investigation requires a numerical model that could deal with a high amount of microcracks, their initiations and propagations. Therefore, to narrow down the choices for applicable numerical methods, a comparative table has been proposed. For each method, the ability to model discontinuities, computational efficiency and suitability to model complex geometries has been summarised in Table I-3. This Table is based on each model's mentioned features, as explained in section I.3 and (Jebahi 2013).

Table I-3. A comparison between the simulation methods to model damaged materials and fracture propagation inspired from (Jebahi 2013).

Methods	Continuous methods				Discrete methods		
	FEM	XFEM	FVM	EFGM	Lattice	NSCD	DEM
Modelling discontinuities	+	++	+	++	+++	++	+++
Large deformation	+	+	+	+++	+	+++	+++
Complex geometries	+++	+++	+	++	++	+	+
Computational efficiency	+++	+++	++	+	+	+	+

+: weak ++: Good +++:Excellent

As shown in Table 3, two relatively advantageous methods for modelling the discontinuities are XFEM and DEM, which are commonly used in fracture mechanics. To focus more on these two mentioned adequate methods, the performance of these methods in fracture-related problems has been compared in more detail in Table I-4.

Table I-4. A comparison of the performance of XFEM and DEM in fracturing problems

	XFEM	DEM	Comment
Crack initiation	+++	+++	Both methods can initiate cracks (Wang *et al.* 2017)
Single crack propagation	+++	+	XFEM has a robust, proven ability to simulate discrete cracks (Spencer *et al.* 2015)
Multiple cracks interaction	+	+++	DEM can produce secondary cracks, better agreement with the experimental results (Sharafisafa *et al.* 2014)
Crack coalescence	++	+++	DEM has a better agreement with the experimental results (Sharafisafa *et al.* 2014)

Considering the comparison between XFEM and DEM, regardless of their common strengths in simulating cracks, it should be highlighted that these two methods have a completely different numerical basis. XFEM, as mentioned, is a continuum method based on the initial FEM approach, following the continuity assumptions of mechanics. In this way, it is possible to use the fracture mechanics formulations that were developed for the continuum media, such as fracture toughness (see section I.2), directly in the model. However, the interaction of discontinuities, managing a high number of cracks and predicting complex cracking patterns is challenging in XFEM (Spencer *et al.* 2015). On the other side, because of the discontinuous nature of DEM, the initiation and propagation of a high number of cracks are not problematic for the model. For example, in a study by Alhajj *et al.*, multiple crack initiation and propagation, induced by CTE mismatch, has been successfully modelled in the case of multi-inclusion composite (Alhajj Hassan *et al.* 2020). In the case of the present PhD, the focus is more on modelling damageable materials with a high number of microcracks (see section I.1). Therefore, it has been preferred to use DEM, which is a simulation technique with the ability to handle such an interacting large number of discontinuities.

In addition to the mentioned points, based on a study by Sharafisafa *et al.*, for simulation of crack propagation in the brittle materials, it was shown that DEM could realistically simulate secondary cracks branching. In contrast, secondary cracks can not be observed in XFEM models. Furthermore, DEM could simulate the entire process of crack initiation, propagation and, more importantly, the fracture's coalescence, which is not the case for XFEM (Sharafisafa *et al.* 2014). In another study, Wang *et al*. compared the fracturing process in glass, caused by a projectile impact by different numerical approaches, including DEM and XFEM. Based on this study, DEM results have shown satisfactory crack patterns and fragmentation process, while XFEM could not simulate such typical crack patterns, as shown in Fig. I-30 (Wang *et al.* 2017).
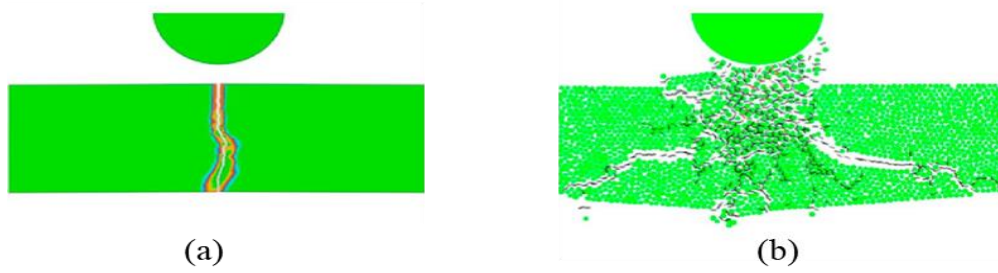
Fig. I-30. Simulations of crack propagation in a projectile impact on a brittle media:
(a) by XFEM, and (b) by DEM (Wang *et al.* 2017).

In the end, considering the above-mentioned points, the DEM approach will be used in this PhD for modelling the discontinuities and microcracking process within refractory materials. In the next chapter, the chosen DEM Flat Joint Model (FJM) and its platform, Particle Flow Code (PFC), will be introduced.

Chapter II: Discrete element method numerical framework, algorithm, and model

II.1. Introduction

In the early steps of this PhD, GranOO[6] (a free DEM workbench) was used as the simulation tool. This was due to the fact that, in IRCER (Institut de Recherche sur les Céramiques, Limoges, France), the thermomechanical research group already had some experience in developing GranOO. However, by reviewing other potential DEM contact models, the recently developed Flat Joint Model (FJM) (Potyondy 2012) showed potential advantages for the goals of this PhD (studying the multi-scale microcracking process in brittle materials). Initially, the FJM was introduced to mimic the microstructure of angular, interlocked grains, similar to marble, in the context of geomechanics. This concept of mimicking such interlocked granular materials was, in fact, very close to the general microstructure of refractories, constituted of large interlocked aggregates within a finer matrix. This FJM is implemented within a software called Particle Flow Code (PFC)[7] from ITASCA company. In fact, this PFC software is a well-known DEM framework in the civil engineering domain, mostly for geomechanical applications. Therefore, considering my personal background in geomechanical engineering and my competencies thanks to previous works with such type of codes, it was finally decided to choose the PFC software as the main numerical framework for the present thesis. In this way, this PhD was granted by an educational and research partnership with ITASCA company (Minneapolis, US and Lyon, France) to investigate the FJM potentials and applicability in the field of refractory ceramics. With such a partnership, it would be thus possible to evaluate and provide feedback about the potential of PFC and FJM within this new industrial domain for ITASCA.

In this chapter, the PFC framework and FJM will be introduced. Firstly, the general PFC numerical scheme, including its modelling bodies and contacts, will be presented. Then, the computational steps of this framework will be summarised. Afterwards, the Flat Joint Model (FJM) and its input parameters will be introduced. Moreover, the influence of the FJM local fracture parameters and of the sample geometry will be investigated, and at the end, a rationalised trial and error calibration process for FJM local parameters will be proposed.

II.2. Particle Flow Code (PFC) numerical scheme

Particle Flow Code (PFC) is a general-purpose DEM framework developed by ITASCA company in Minneapolis, US. PFC supports its own programming language, called FISH, which is the common language for ITASCA codes. It enables a high level of interaction with the core of PFC, which is an interesting feature for scientific research.

PFC allows large displacements and rotations of the discrete elements. PFC uses Newton's second law and force-displacement laws at the contact points to calculate force

---

[6] https://www.granoo.org/
[7] https://www.itascacg.com/software/PFC

and predict motions of discrete elements. At first, PFC was designed for interacting rigid granular assemblies without bonding (Cundall *et al.* 1979). Later, bonded particle models were introduced to this framework (Potyondy *et al.* 2004) in order to simulate continuum media, such as intact rocks or ceramics, like the present study. The detailed formulation and mathematical basis of this framework are explained in the PFC's documentation (Itasca Consulting Group Inc. 2020); therefore, an overview of these bases will be presented here.

II.2.1. PFC modelling bodies

As mentioned, the PFC DEM code simulates the interaction of discrete rigid bodies called modelling objects. Basically, there are different types of model objects in PFC (Fig. II-1), as described below (Itasca Consulting Group Inc. 2020):

a) *balls* are simple spherical objects, which are geometrically defined only by their radii. Balls could have translational and rotational movements. Balls are the classical model objects in PFC for simulating granular assemblies and the most used objects for building up a continuum media. Balls are often used in DEM because the computational performance for collision detection is high thanks to such a simple geometry.

b) *clumps* are rigid objects composed of assemblies of spherical *pebbles*. Clumps are used to mimic complex geometries as a set of highly interpenetrated spheres. Clumps are not able to deform and act as single rigid bodies with translational and rotational movements. An example of an ellipsoid geometry built up as a clump is given in Fig. II-1 (b).

c) *rigid blocks* have been recently introduced to PFC code in order to enable the DEM models to simulate convex shapes and manifolds by using complex polyhedra. The interest of using rigid blocks is to introduce a single discrete element with a complex shape within DEM simulations. Again, as an example, the ellipsoid is reproduced as a single rigid block, shaped directly as a single discrete element (Fig. II-1 (c)).

d) *walls* are manifold surfaces made from triangular *facets,* which are defined by meshes (see section I.3.1). Walls could have translational and rotational movements. However, wall motions are not governed by the equation of motions as it is used only as boundaries with user-defined displacements.

(a) (b) (c) (d)
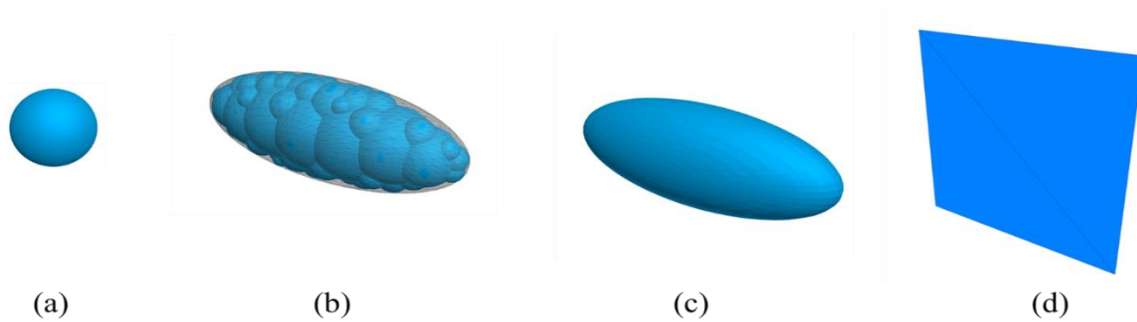
Fig. II-1. Different model objects in PFC: (a) a spherical ball, (b) an ellipsoid clump with its constituent pebbles and (c) an ellipsoid rigid block and (d) a planar wall consisting of two triangular facets

II.2.2. Modelling interactions between bodies

In PFC, the model objects (balls, clumps, rigid blocks and walls) interact with each other through their contact overlaps. The mechanical response of these interactions is defined by different mechanical contact laws. These contacts are considered soft contacts, as previously introduced in Fig. I-27 (see section I.3.2.3). It means that the apparent deformation of the whole granular assembly is rendered due to the penetrations of discrete elements, which occur at the contact points. In fact, the mechanical response of modelled granular or continuum media is coming from these mechanical contacts. These mechanical contacts follow pre-defined force-displacement laws called contact models. Generally, most of the contact models implement normal stiffness, shear stiffness, rotational stiffness, cohesion and friction into their mathematical equations.

In the same way, in order to simulate a continuum media by DEM, the media could be built up from *bonded* discrete elements. Here, *bonded* refers to a permanent mechanical link between two nearby discrete elements inducing compression when they overlap and tension when they are not touching anymore, as shown in Fig. II-2. As mentioned in section I.3.2.3, different contact models can be proposed for different applications. In PFC, the three main contact models are the *linear contact bond model*, the *parallel bond model* and the *flat joint model*.
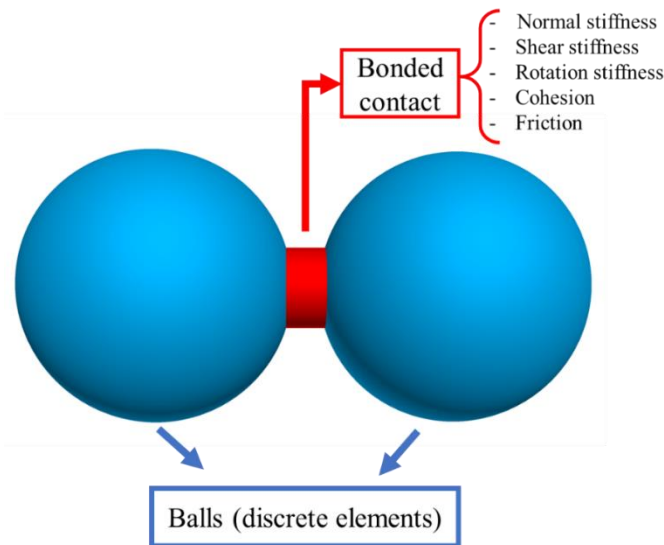
Fig. II-2. A bonded contact between two discrete elements in PFC

II.3. Overview of the computational steps

PFC uses an explicit dynamic numerical scheme to solve Newton's laws of motions. The solution will be achieved for small increments (dt) of in-simulation time (t) in order to update the model state step by step. A simplified scheme of such a cycle is shown in Fig. II-3.
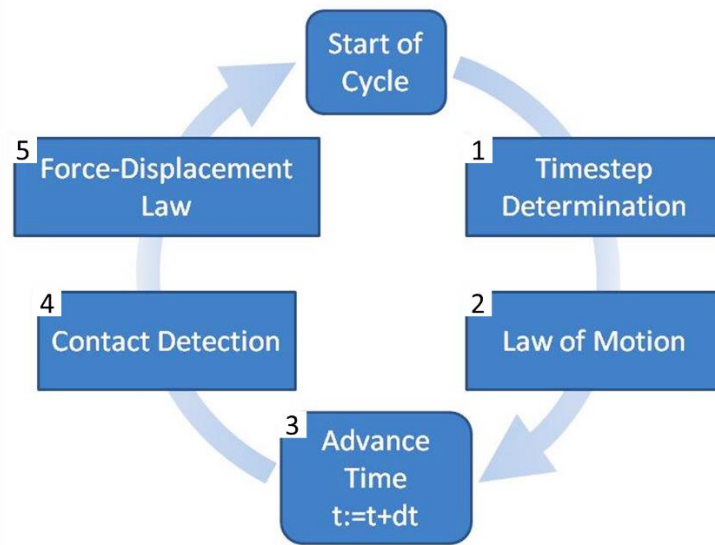
Fig. II-3. Overview of a computational cycle in PFC (Itasca Consulting Group Inc. 2020).

As shown in Fig. II-3, one calculation step corresponds to one single complete cycle, including several sub-steps. Each of these sub-steps is summarised below (Itasca Consulting Group Inc. 2020).

1. *Time-step (dt) determination*: it is a well-known fact that large time-steps lead to instability of the numerical scheme. On the other hand, too small time-steps cause an unnecessary increase in calculation time (Potyondy *et al.* 2004). That is why an automatic determination of the time-step is used in PFC. At the beginning of each cycle, the time-step will be determined based on the stiffness of the contacts and on the kinematic constraint of the discrete elements. This kinematic constraint is imposed to ensure that contacts are created between objects before the step that forces/moments are calculated (step 4).

2. *Law of motion*: this step is divided into two parts. The first step is applying Newton's second law to obtain translational and angular accelerations from the forces and torques. The second part is numerical integration, which updates linear and angular velocities as well as positions of each discrete elements. This update can be managed from current accelerations and previous velocities as well as positions (computed at the previous cycle).

3. *Advance time (dt)*: the in-simulation time advances by adding the current time-step to the previous in-simulation time.

4. *Contact detection*: the contact detection process is automatically done for each cycle. An axis-aligned bounding box is associated with the whole computational domain. In this way, this axis-aligned bounding box is divided into several equidimensional sub-boxes called "spatial cells". Each of these cells has a list of overlapping or approaching objects. By using such an approach, the computational time dedicated to contact detection could significantly decrease, as the contacts will be searched only for the objects in its cell and in neighbouring cells and not in the whole system. By the end of this step, new contacts will be formed, and inactive contacts will be deleted based on the updated positions.

5. *Force-displacement law*: at this point, the obtained contact list from the previous sub-step is used. By using the contact model (force-displacement laws), the forces and the moments at the contacts will be computed and updated from the relative angular and linear positions of the contacting objects. As mentioned before, the apparent mechanical response of the model comes from these force-displacement laws. Hence, choosing adequate laws are highly important in DEM.

Such an algorithm is based on an infinite loop, and the calculation should be stopped thanks to different criteria, depending on the nature of the simulation. For example, the simulation can be stopped after a certain number of iterations or after a pre-defined in-simulation time. Besides, it is also possible to define more complicated customised criteria such as dropping to 15% of the peak after failure in a uniaxial tensile test simulation or reaching a certain level of pressure in a triaxial compressive simulation.

The present PhD being focused on bulk materials, as mentioned in Chapter I:, the targeted simulation media thus requires a bonded particle contact model. In 2004, the bonded particle model (BPM) approach was introduced to the PFC framework (Potyondy *et al.* 2004). In 2007, the two first bonded particle models of PFC were investigated by Cho *et al.* (Cho *et al.* 2007): the linear contact bond model and the parallel bond model. This study has clearly shown that these two models had noticeable limitations, in particular, for reproducing a realistic ratio between tensile and compressive strengths. In 2012, Flat Joint contact Model (FJM) was introduced as another BPM in PFC (Potyondy 2012) to tackle the previously mentioned limitation. This contact model will thus be explained more in detail in the next section.

II.4. Flat Joint contact Model (FJM)

The Flat Joint Model (FJM) was introduced to PFC in order to represent the apparent behaviour of bonded frictional contacts, which can contain partial damages (Potyondy 2012). Therefore, FJM solved the common problem of other BPMs for predicting a realistic compressive to tensile strength ratio of materials (Potyondy 2018). Briefly, it can simulate the microstructure of angular and interlocked grains within a material thanks to flat contact interfaces, which allows the model to exhibit translational and rotational frictions between discrete elements. These features will be explained in detail in the following sections. Firstly, the general description and the input parameters of FJM will be introduced. Afterwards, the influences of the introduced parameters and the geometry of the numerical sample will be investigated. Finally, a customized rationalised calibration process will be proposed for FJM.

II.4.1. General description and key parameters of FJM

As mentioned, FJM can simulate the microstructure of interlocked grains within a material thanks to the flat contact interfaces. This feature allows the model to exhibit translational and rotational frictions between discrete elements. This key point made this contact model suitable for the present study, targeting multi-scale simulation of partially damaged grain-based materials (see section I.1) as shown in Fig. II-4. The detailed

formulation of FJM has been explained in the PFC code documentation (Itasca Consulting Group Inc. 2020); therefore, the main points of this model will be presented here.
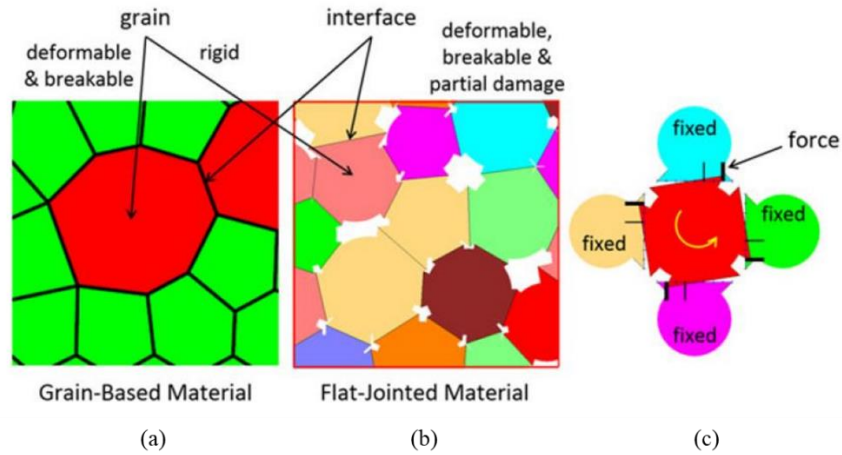
Fig. II-4. Grain-based materials: (a) simplified microstructure, (b) related model using flat joint, (c) focus on a single grain and its neighbours (Potyondy 2015).

Commonly flat-jointed bonded numerical material is built up from a compacted granular assembly of spherical discrete elements as introduced in section II.2.2. Before assigning FJM between nearby discrete elements within this assembly, an initial small distance gap (g_0) is set up to define which discrete elements should be bonded. An FJM bonded contact is thus created if the distance between two discrete elements is smaller than this assigned initial gap (g_0) as shown in Fig. II-5 (b). This g_0 value has a large influence on the connectivity of the discrete elements of the assembly and thus, could significantly influence the relation between local and apparent property. As an illustration, if g_0 is initially set to zero, only the touching (or slightly overlapping) elements will be bonded. Therefore, it is preferable to assign a non-zero value as a bonding gap, usually set to a given ratio of the average of discrete elements size. This point will be detailed in the calibration section (see section II.4.4).

Considering Fig. II-5, the full FJM contact geometry is a line in 2D and a disk in 3D. These geometries are different from most DEM contact models, which represent the contact as a point in both 2D and 3D. Besides, an FJM contact is built up from a certain number of contacting sub-surfaces (referred as "*elements*" in PFC technical documentation, which use thus superscript "*e*" in later formulations) which could carry forces and moments that obey the force-displacement law. For example, in Fig. II-5 (a), the FJM contact could be considered partially damaged as some of the sub-surfaces are "*unglued*". In the unglued configuration, the concerned sub-surface is not able to transmit attractive tensile forces, while it can still transmit repulsive compressive forces. Thanks to this planar contact geometry associated with sub-surfaces, it is possible to model resisting against rotations in order to mimic a grain-based interlocked assembly.
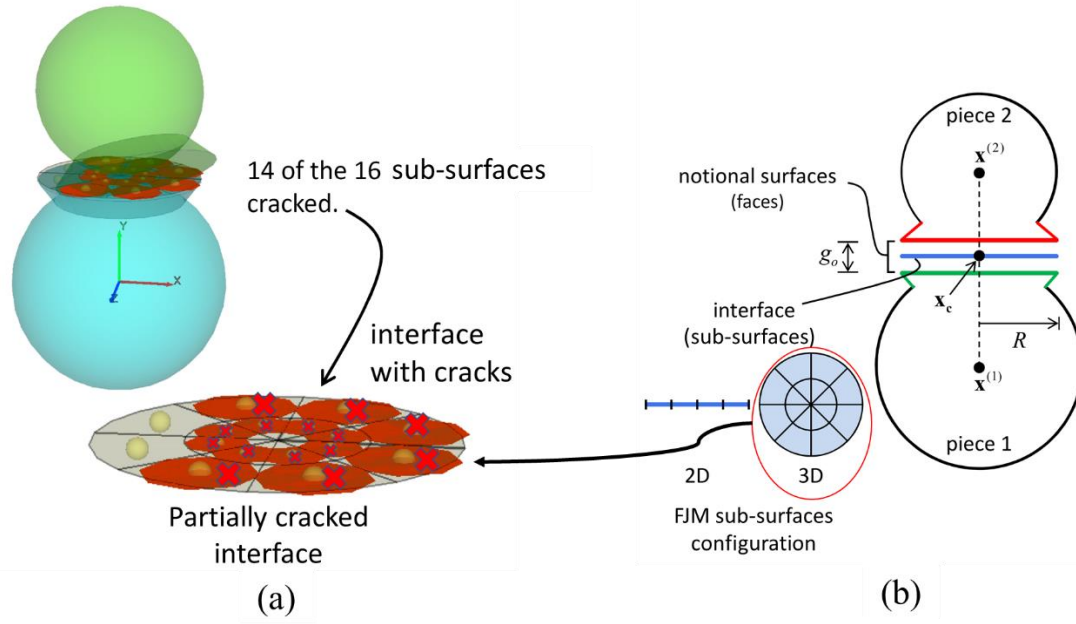
Fig. II-5. The FJM contact: (a) focus on a partially damaged flat joint, and (b) the schematic basis of the FJM, adapted from (Itasca Consulting Group Inc. 2020).

As it was shown in Fig. II-5 (a), a full FJM bonded contact in 3D is built up from 16 sub-surfaces. The fracturing criterion of a single sub-surface in FJM is shown in Fig. II-6. This criterion is inspired from the classical truncated Mohr-Coulomb theory, which is represented in the shear stress ($\tau^{(e)}$) vs compression stress ($-\sigma^{(e)}$) plane and adapted to rock mechanics, for which compression is considered positive (tension being thus negative). The parameters t^{loc}, c^{loc} and ϕ^{loc} correspond to the tensile strength, the cohesion and the friction angle used locally as rupture criteria for each single sub-surface.

Before rupture, each single sub-surface exhibits a linear elastic mechanical behaviour (based on K_n^{loc} corresponding to the normal stiffness and K_s^{loc} to the shear stiffness) until its equivalent stress in the Mohr-Coulomb stress space reaches the limit. Then, the sub-surface is considered unglued and detached. A detached FJM sub-surface can no longer carry tensile stresses. However, as mentioned previously, the detached sub-surface still can be active in compression with associated friction.
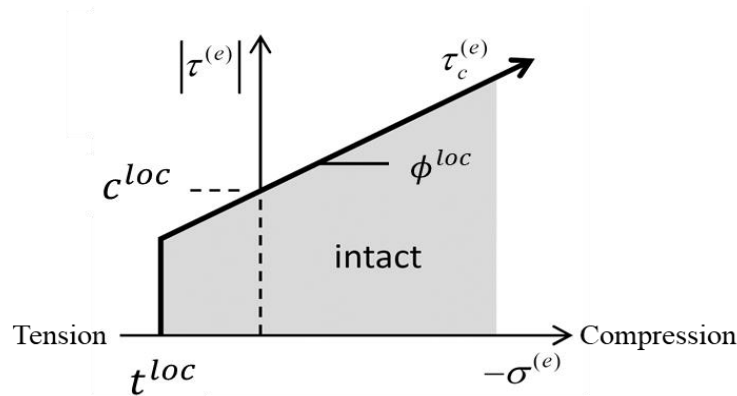
Fig. II-6. Typical Mohr-Coulomb graph and associated different fracturing criteria used for a single FJM sub-surface

The global rheological model of each FJM sub-surface is summarised in Fig. II-7. For a given FJM bond, all of its 16 sub-surfaces follow the same rheological model and share the same parameter values of K_n^{loc}, K_s^{loc}, t^{loc}, c^{loc} and ϕ^{loc}. These local input parameters are marked by superscript "*loc*", in contrast with apparent macroscopic properties, marked by superscript "*ap*".
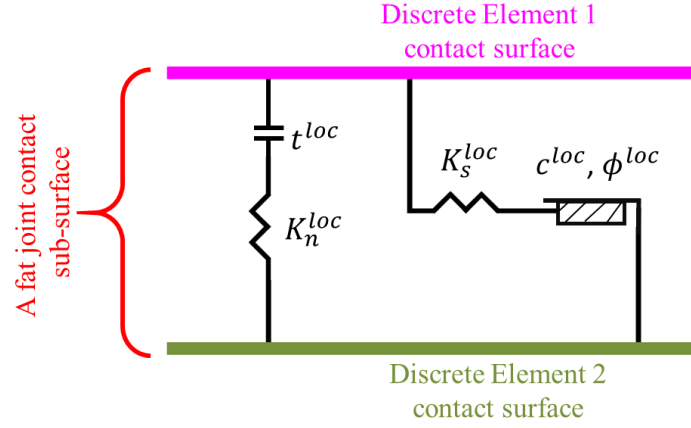
Fig. II-7. Bonded flat joint contact: the rheological model and the associated parameters, adapted from (Itasca Consulting Group Inc. 2020)

Table II-1, is showing the list of FJM bonded contact parameters that were used in this study. An introduction to each parameter will be made afterwards.

Table II-1. The input parameters in Flat Joint contact model

Parameter description	Symbol	Elastic / fracture	Unit
Initial gap	g_i^{loc}	-	m
Normal stiffness of bond	K_n^{loc}	Elastic	N/m
Shear stiffness of bond	K_s^{loc}	Elastic	N/m
Local Young's modulus of bond	*E^{*loc}*	*Elastic*	*GPa*
Local stiffness ratio (K_n^{loc}/K_s^{loc}) of bond	*K^{*loc}*	*Elastic*	*-*
Local tensile strength of bond	t^{loc}	Fracture	MPa
Local cohesion of bond	c^{loc}	Fracture	MPa
Local friction angle	ϕ^{loc}	Fracture	Degrees

Initial gap (g_i^{loc}): as previously mentioned, this parameter defines the maximum distance between two discrete elements for having a bonded contact configuration.

Normal stiffness of bond (K_n^{loc}) and *shear stiffness of bond* (K_s^{loc}): these two parameters define the stiffness of the two perpendicular springs (normal and tangential directions) in a smooth DEM contact. With such local parameters, the apparent macroscopic elastic properties are scale-size dependent, and this direct relation is not easy to handle. To solve this classical problem in DEM, PFC uses another intermediary parameter taking into account the size of the discrete elements. These intermediary parameters are the local Young's modulus (E^{*loc}) and the local stiffness ratio (K^{*loc}).

Local Young's modulus of bond (E^{*loc}): this elastic parameter is defined as the effective elastic modulus at the contact, as it is defined in Eq. II-1.

$$E^{*loc} = K_n^{loc} L^{loc}$$
<div align="right">Eq. II-1</div>

In Eq. II-1, L^{loc} is the local bond length (in the case of balls, the sum of the radii). By assigning E^{*loc} and knowing the local bond length L^{loc} for the concerned contact, the K_n^{loc} can be calculated automatically. In this way, E^{*loc} remain the same value for all contacts, but the K_n^{loc} is locally adjusted to the size of the concerned discrete elements. This E^{*loc} parameter is thus one of the main controlling parameters of the apparent elastic modulus (E^{ap}) of the assembly.

Local stiffness ratio of bond (K^{*loc}): this elastic parameter is defined as the ratio between the normal and the shear local stiffnesses and is given in Eq. II-2.

$$K^{*loc} = \frac{K_n^{loc}}{K_s^{loc}}$$
<div align="right">Eq. II-2</div>

By assigning K^{*loc} and knowing the K_n^{loc}, which was determined previously, the K_s^{loc} of the concerned contact can be calculated automatically. This K^{*loc} parameter has, in fact, a strong influence on the apparent macroscopic Poisson's ratio (v^{ap}) of the assembly.

Local tensile strength of bond (t^{loc}): this fracture parameter is the local fracture criteria of the bond in pure tension, as shown in Fig. II-6 and Fig. II-7. The t^{loc} value defines a local tensile stress threshold. If the applied tensile stress of the bond exceeds this value, the related sub-surface will be detached and will later act only in compression. This t^{loc} parameter is directly linked to the apparent tensile strength (t^{ap}) of the assembly.

local cohesion of bond (c^{loc}): this fracture parameter is related to the local cohesion of the bond in pure shear, as shown in Fig. II-6 and Fig. II-7. This c^{loc} parameter is directly linked to the apparent shear strength of the assembly. As expected, and after verification, the c^{loc} has a negligible influence for apparent macroscopic fracturing in mode I, governed by tension.

Local friction angle (ϕ^{loc}): this fracture parameter defines the friction angle at the bonds, which is related to a solicitation combining compression and shear. This ϕ^{loc} parameter is directly linked to the apparent friction angle of the assembly. As expected, and after verification, the ϕ^{loc} has a negligible influence for apparent macroscopic fracturing in mode I, governed by tension.

As mentioned, generally, DEM continuum models are assemblies of discrete elements that interact through contacts, and the response of the model at the macro-scale emerges from the interactions at the contact (local-)scale, which is the case for FJM too. This makes DEM simulations different from Finite Element Method (FEM) simulations, which generally comply with stress-strain constitutive laws at the macro-scale. Like the other DEM models, a drawback of the FJM is that it requires transitional steps and assumptions to obtain overall stress-strain behaviour for the apparent continuum media. To be more explicit, the introduced elastic input parameters in Table II-1 are different from the apparent elastic modulus (E^{ap}) and the apparent Poisson's ratio (v^{ap}) of the assembly. The influence of the local elastic parameters E^{*loc} and K^{*loc} is well established in the literature (Zhou *et al.* 2018) and will be discussed more in section II.4.4.

Similarly, the local fracture input parameters in Table II-1 will be different from the apparent strength of the assembly. The influence of these local fracture criteria will be reviewed in section II.4.2. In addition to the local input parameter, and even if it is not well documented in the literature, it should be noticed here that the geometry of the numerical sample could also have a noticeable influence on the apparent material properties. This point will also be reviewed in section II.4.3. Considering these influential points, the calibration process is an inevitable step of FJM. Hence, a rationalised trial and error calibration process will be proposed in section II.4.4.

II.4.2. The influence of the local fracture parameters

In this section, the influence of the local fracture parameters on the apparent strength in Uniaxial Tensile (UT) and Uniaxial Compression (UC) tests simulations will be investigated. This first sensitivity study will help to understand the local to apparent relationships, which will later lead to define a pertinent calibration process, as proposed in section II.4.4.

For this investigation, a unique cubic numerical sample ($10 \times 10 \times 10$ cm^3 containing 13.7k of discrete elements) with the initial local input parameters of Table II-2 was considered. Then, for each local fracture parameter ($t^{loc}, c^{loc}, \phi^{loc}$), a set of simulations were done by varying one parameter at a time while keeping the other parameters constant.

Table II-2. FJM local values used to study the influence on apparent fracture behaviour

Description	Local Young's modulus	Local stiffness ratio	Local tensile strength	Local cohesion	Local friction angle
Abbreviation	E^{*loc}	K^{*loc}	t^{loc}	c^{loc}	ϕ^{loc}
Type	*Elastic*	*Elastic*	*Fracture*	*Fracture*	*Fracture*
Initial value	20 GPa	2	10 MPa	40 MPa	30°
Variation range	-	-	5-40 MPa	10-80 MPa	0°-60°

Sensitivity study of the local tensile strength (t^{loc}) between 5 and 40 MPa: the influence of this parameter on the apparent tensile strength of the material has been firstly investigated by running uniaxial tensile test simulations. As expected this t^{loc} Value has no influence on the elastic behaviour in tension (slopes of the stress-strain curves, in Fig. II-8 (a)). In contrast, as shown in Fig. II-8 (a) and (b), t^{loc} has logically a direct effect on the apparent tensile strength, which can be considered as linear. In the present configuration, the ratio between local and apparent tensile strength is about 80%. However, this ratio may differ, depending on the other local parameters and on the considered numerical sample geometry. These considerations will be taken into account for the calibration procedure detailed in section II.4.4.
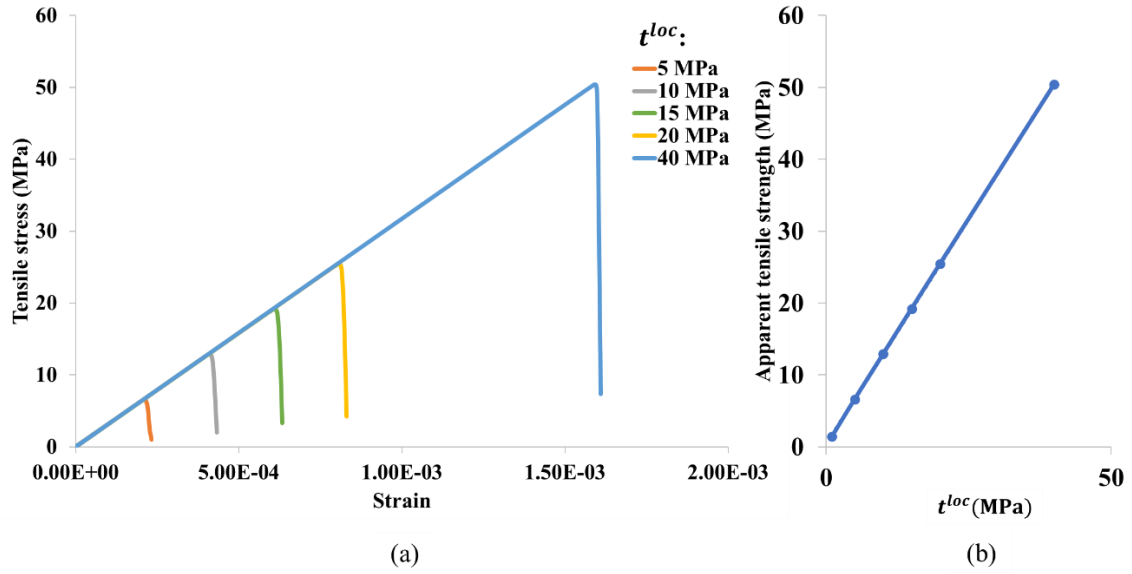
Fig. II-8. Results of uniaxial tensile test for different t^{loc} values: (a) stress-strain curves, and (b) apparent tensile strength vs t^{loc}.

Afterwards, the influence of t^{loc} on the apparent compressive strength of the material has been investigated by running uniaxial compression test simulations. Surprisingly, this t^{loc} value, seems to have an influence on the global shape of the pre-peak behaviour in compression (first part of the stress-strain curves in Fig. II-9 (a)). As shown in Fig. II-9 (a), t^{loc} has also logically an effect on the apparent compressive strength. Similarly to tension, the relation between t^{loc} and the apparent compressive strength seems to be linear, Fig. II-9 (b), but with an important intercept (more than 400 MPa). This can be explained by the dominancy of shear fracturing mode during compressive tests, which is in fact mostly controlled by c^{loc} value (which will be investigated later).

Coming back to the loading part of the curves (Fig. II-9 (a)), and looking very carefully at the beginning of these curves, the slopes at the origin (initial elastic modulus) does not vary with changing t^{loc}. During loading, it appears that the stress-strain curves deviate from the initial slope for a given stress threshold which is dependent of t^{loc} value. Thus, t^{loc} seems to have a direct influence on the microcracking process, in tension perpendicular to the applied uniaxial compressive load. This leads to a progressive decrease of the apparent Young's modulus (E^{ap}). These considerations will be taken into account for the calibration procedure detailed in section II.4.4.

Fig. II-9. Results of uniaxial compression test for different t^{loc} values: (a) stress-strain curves, and (b) apparent compressive strength vs t^{loc}.

Sensitivity study of local cohesion (c^{loc}) between 10 and 80 MPa: As expected, the influence of this parameter on apparent tensile strength, given by the uniaxial tensile test (additional results not presented here), is negligible. Therefore, the influence of this parameter in a uniaxial compression test was investigated. By considering the results of simulations in Fig. II-10 (a) and Fig. II-10 (b), it confirms that c^{loc} is highly influential on uniaxial compressive strength value. As shown in Fig. II-10 (b), c^{loc} has a direct effect on the apparent uniaxial compressive strength, which can be considered as linear with a non-zero intercept (100 MPa). In the present configuration, the ratio between local and apparent uniaxial compressive strength is about 11%. This ratio may differ, depending on the other local parameters and on the considered numerical sample geometry. On the other hand, c^{loc} has no impact on apparent pre-peak mechanical behaviour. However, it should be highlighted that there is a subtle change in the stress-strain slopes (around 300 MPa in the present case), resulting from the initiation of the tensile microcracking process. This initiation point is the same for all the curves, as the assigned t^{loc} value was kept constant in these simulations.
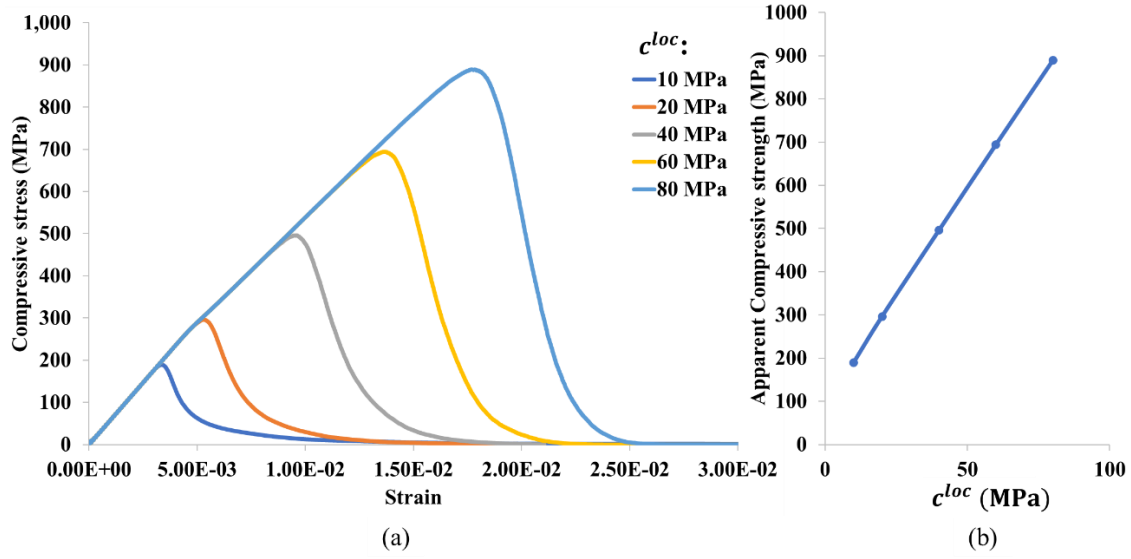
Fig. II-10. Results of uniaxial compressive test for different c^{loc} values: (a) stress-strain curves, and (b) apparent compressive strength vs c^{loc}.

Sensitivity study of local friction angle (ϕ^{loc}) between 0 to 60 degrees: As expected, the influence of this parameter on apparent tensile strength, given by the uniaxial tensile test (additional results not presented here), is negligible. Therefore, the influence of this parameter in a uniaxial compression test was investigated. By considering the results of simulations in Fig. II-11 (a), ϕ^{loc} is mainly influential on the uniaxial compressive strength, as shown in Fig. II-11 (b). Besides, it is worth highlighting that ϕ^{loc} has also an influence on the post-peak mechanical behaviour. It seems that increasing the ϕ^{loc} value could lead to an increase of fracture energy in the post-peak area. On the other hand, ϕ^{loc} has no impact on apparent pre-peak mechanical behaviour.
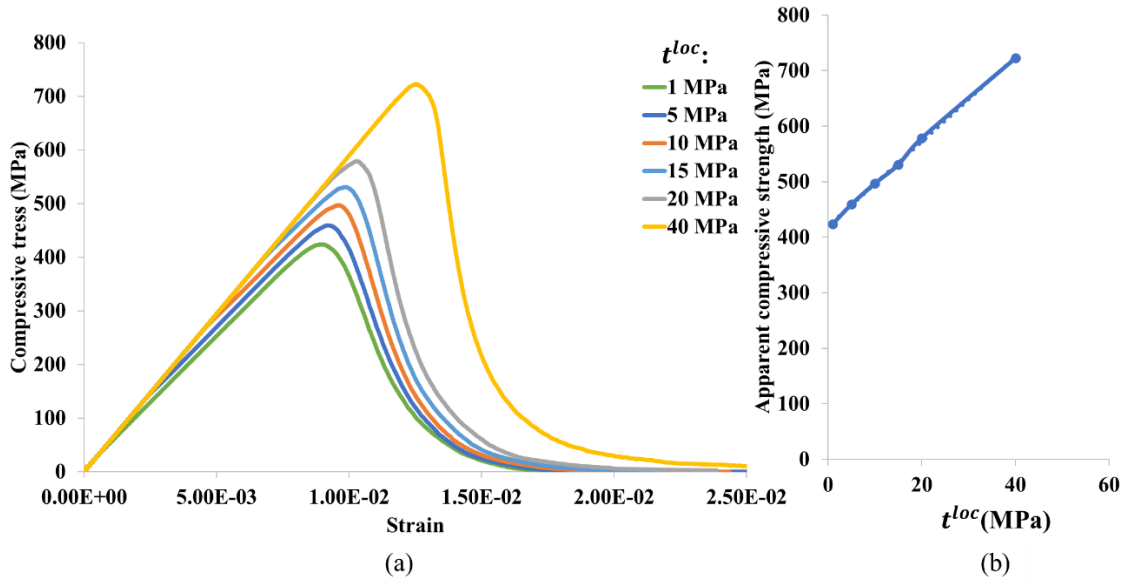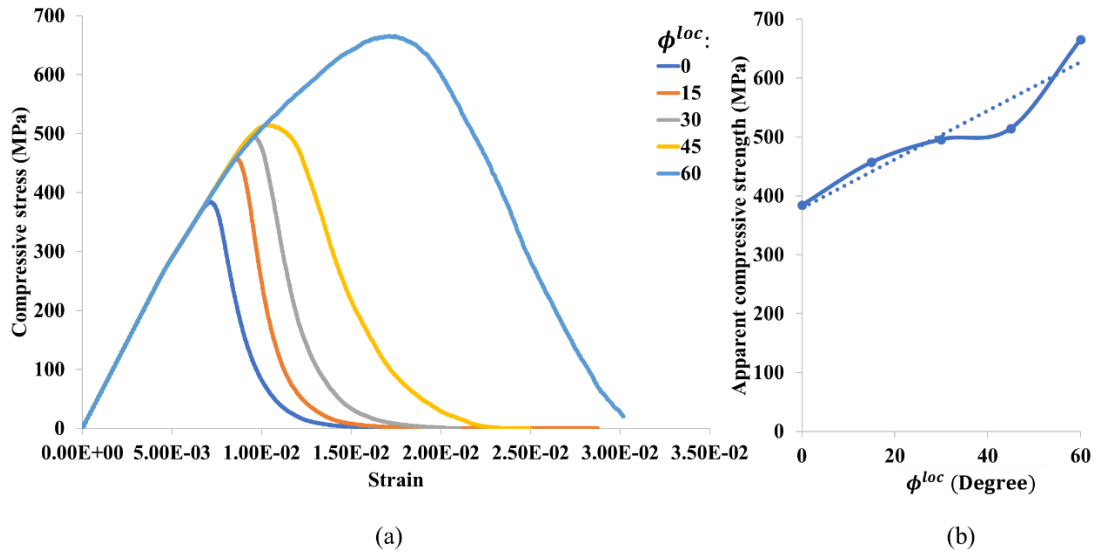

Fig. II-11. Results of uniaxial compressive test for different ϕ^{loc} values: (a) stress-strain curves, and (b) apparent compressive strengths vs ϕ^{loc}.

As mentioned in section II.4.1, the tensile load in a single FJM sub-surface is carried only for a glued configuration. In contrast, a compressive load is carried only if the contact gap is negative, either the sub-surface is glued or not. For uniaxial tensile tests, where the tensile loads on the FJM sub-surfaces are dominant, the t^{loc} is directly controlling the apparent tensile strength. On the other hand, when the numerical sample is subjected to a compressive load, the dominant fracturing mode will be locally in the mixed mode, which is driven by t^{loc}, c^{loc} and ϕ^{loc} parameters of the Mohr-Coulomb criteria (Fig. II-6). Hence, the apparent compressive strength will be controlled by all these parameters.

II.4.3. Influences of the numerical sample geometry

Generally, in DEM, the numerical sample geometry, size, and discrete elements fineness (related to the level of discretisation) could affect the apparent properties of the material. It means that even by using the same input parameters, the apparent properties of the numerical sample could vary by changing its geometry, length and discrete elements sizes. Hence, to investigate the influence of these points, different configurations were considered. In this regard, by using the same set of local input parameter values, as shown in Table II-3, the main apparent mechanical properties (Young's modulus, Poisson's ratio, tensile strength) were compared for different sample geometries, length and fineness. These simulations were done only for the uniaxial tensile test case.

Table II-3. The FJM input local parameters for studying the influence of geometry in the uniaxial tensile test case

Description	Local Young's modulus (E^{*loc})	Local stiffness ratio (K^{*loc})	Local tensile strength (t^{loc})	Ball (discrete elements) radius
Type	*Elastic*	*Elastic*	*Fracture*	-
Value	20 GPa	2	10 MPa	2-3mm

The influence of the shape and dimension of the numerical sample on the apparent mechanical behaviour was first investigated. As shown in Fig. II-12, different geometries with various fineness and sizes were investigated. The sample which is shown in Fig. II-12 (a), is a 10×10×10 cm^3 cube containing 13.7k of discrete elements, is taken as the reference.

This reference was compared to the cylindrical sample shown in Fig. II-12 (e). The length and the fineness of this cylindrical sample are comparable to the reference one. Therefore, for such a case, only the apparent shapes are considered to be different. As indicated in column (e) of Table II-4, the apparent Poisson's ratio (v^{ap}) exhibits similar values, while the apparent Young's modulus E^{ap} and apparent tensile strength t^{ap} are noticeably different (-3% for E^{ap} and +7% for t^{ap}).

Afterwards, this reference was also compared to a sample with a similar shape and fineness but with a different length in one direction, as shown in Fig. II-12 (d). Therefore, the influence of the shape length was studied. As indicated in column (d) of Table II-4, the apparent Poisson's ratio (v^{ap}) exhibit similar values. On the other hand, the other mechanical parameters, E^{ap} and t^{ap} are noticeably different (-3% for E^{ap} and +7% for t^{ap}).

Similar differences were observed for the cylindrical shapes (see Fig. II-12 (e), Fig. II-12 (f) and Table II-4).

The influence of the sample size was also investigated for similar values of fineness. As can be seen, by comparing the reference cube with a larger one, shown in Fig. II-12 (c), all the apparent parameters have acceptable accordance except for E^{ap}, which is having a relative difference of -8%.

Finally, the influence of the fineness was investigated for similar cubic shapes and lengths, as shown in Fig. II-12 (b). As indicated in column (b) of Table II-4, by decreasing the ball distribution range from 2-3 mm to 1.2-1.8 mm, the number of elements increases from 13.7k to 61.7k. Here again, the apparent Poisson's ratio (ν^{ap}) exhibit similar values. However, E^{ap} and t^{ap} are noticeably different (-3% for E^{ap} and +4% for t^{ap}).
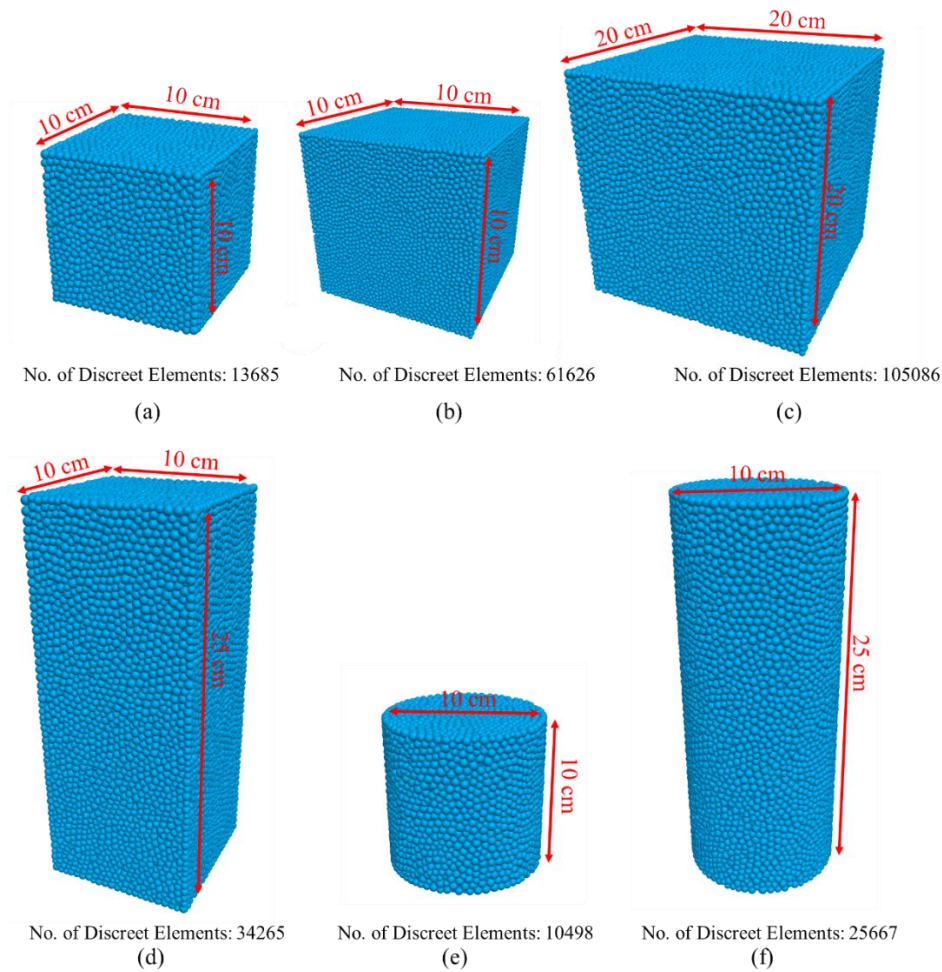
Fig. II-12. Different tested geometries, size and fitness of the numerical sample.

Table II-4. Apparent brittle elastic properties for different geometries, size, and fineness

Shape/size	Cube	Cube	2×Cube	Parallelepiped	Cylinder	Tall cylinder
Fig. II-12 reference	(a) (Ref)	(b)	(c)	(d)	(e)	(f)
Fineness level	standard	elevated	standard	standard	standard	standard
Number of discrete elements	13.7k	61.7k	105.0k	34.2k	10.5k	25.7k
Apparent Young's modulus (E^{ap}) (GPa)	26.6	25.7	24.6	25.9	25.8	24.2
Apparent Poisson's ratio (v^{ap})	0.159	0.159	0.158	0.157	0.159	0.155
Apparent tensile strength (t^{ap}) (MPa)	10.1	10.5	10.0	10.9	10.9	10.0

To conclude, it seems that numerical sample size and fineness variations mostly impact the apparent Young's modulus (E^{ap}) while the apparent Poisson's ratio (v^{ap}) remains constant. This means that the shear modulus (not directly measured here) is probably changing proportionally to the apparent Young's modulus. However, in the cases of length variation, in addition to the apparent Young's modulus (E^{ap}), the apparent tensile strength (t^{ap}) is impacted as well. In all cases, the apparent Poisson's ratio (v^{ap}) is quite constant.

These variations are well-known in the FJM, even if there is no well-documented study about them. In fact, as these variations are not so high (max 8%), the usual solution (discussing with other FJM users) is to fix the numerical sample prior to the calibration steps (see section II.4.4). In this way, the calibration process is involved dedicatedly for a given targeted numerical sample. If the targeted sample has a complex shape (such as WST, section I.2.3), then the calibration process should be done for a simple geometry close to the targeted one, as shown in Fig. II-13. However, the mentioned limitations could be fixed in the case of periodic boundary conditions, which will be explained in detail in section III.3.1.
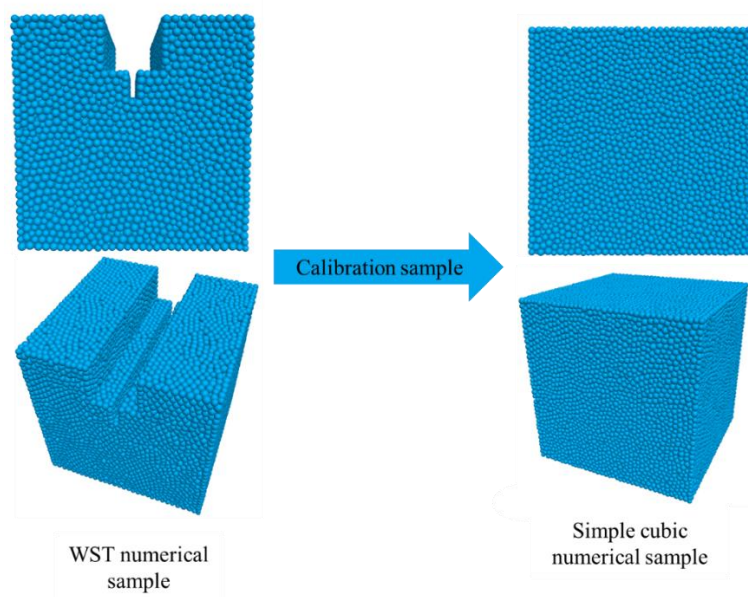
Fig. II-13. WST numerical sample and its related calibration numerical sample.

II.4.4. Rationalised trial and error calibration process
of FJM local parameters

As mentioned, the main disadvantage of such a DEM approach is the lack of well-defined relationships between the contact properties (the local parameters of the bonds between discrete elements) and the apparent brittle elastic properties, which are related to the simulated material. Hence, the FJM requires a calibration process to assign the correct values for the contact properties to reproduce the desired apparent brittle elastic properties. Generally, the calibration process can be done either by a rationalised trial and error (Zhou *et al.* 2018, Vallejos Javier Andres *et al.* 2017) or a direct calibration process (T.-T. Nguyen *et al.* 2019). Due to the high number of local input parameters of the FJM and of the complex interdependencies of these parameters on the apparent behaviour, no direct calibration process has been proposed for FJM yet. Nevertheless, an indirect calibration algorithm has been recently proposed by (Vallejos Javier Andres *et al.* 2017). From this work, an improved indirect calibration algorithm is proposed here in order to adjust the local input parameters to apparent targeted properties. The proposed algorithm (shown in Fig. II-14) considers the different calibrations steps for the most influential local parameters (see section II.4.2) involved in the targeted simulations of this PhD.

As mentioned in section II.4.3, the very preliminary step for the calibration is to fix the numerical sample geometry. Then, the modelled sample should be mechanically loaded in order to obtain the apparent mechanical behaviour targeted for the material. It should be mentioned that the calibration process proposed in Fig. II-14 is exclusively focused here on tensile behaviour. In fact, the present PhD is dedicated to refractory materials, which are well-known to be more sensitive in tension (mode I). Thus, the local input parameters which have an influence on the apparent compressive strength (c^{loc} and ϕ^{loc}) have been intentionally excluded from the proposed calibration process.

The proposed calibration of FJM contact model parameters follows a systematic step by step approach where each step is detailed below.

1. *Initial gap* (g_i^{loc}): assigning a small value for the bonding gap will result in an asymmetric rigidity between compression and tension, which is unwanted for the purpose of this study. Thus, this initial gap value should be set at a level high enough to prevent such asymmetry. This level has been, in fact, numerically quantified as a fraction of the average discrete element diameter (ball) by testing different values of this fraction. By this approach, the minimum value which satisfies the mentioned condition is about 40% of the average discrete element's diameters.

2. *Local stiffness ratio* (K^{*loc}): in the second step, the local stiffness ratio (K^{*loc}) is calibrated. As mentioned earlier, this parameter greatly influences the apparent Poisson's ratio (v^{ap}). Hence, the local stiffness ratio (K^{*loc}) should be set to a value that produces the targeted apparent Poisson's ratio (v^{ap}). It should be mentioned that this step must be done before calibrating the local Young's

modulus (E^{*loc}) as the apparent Young's modulus also depends on the K^{*loc} parameter (Zhou *et al.* 2018).

3. *Local Young's modulus* (E^{*loc}): after calibrating and fixing the local stiffness ratio (K^{*loc}), the local Young's modulus (E^{*loc}) should be set to a value that produces the targeted apparent Young's modulus (E^{ap}).

4. *Local tensile strength* (t^{loc}): finally, after calibrating the elastic properties, the targeted apparent tensile strength (t^{ap}) is calibrated by changing the local tensile strength (t^{loc}). The starting guess for t^{loc} can be the t^{ap} value itself. As highlighted in Fig. II-8, generally, the apparent tensile strength of the material is not so far from the local tensile strength.
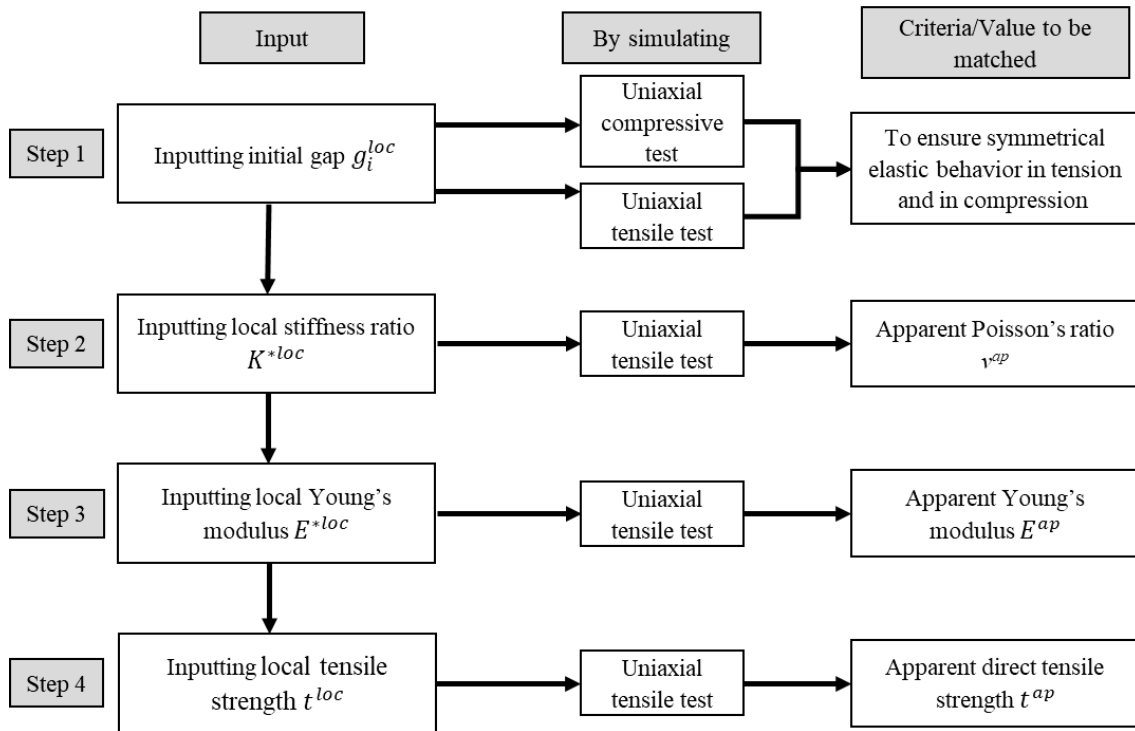
Fig. II-14. The modified algorithm to calibrate apparent brittle elastic parameters of the numerical sample inspired from (Vallejos Javier Andres *et al.* 2017).

II.5. Conclusions

As detailed in this section, the Flat Joint Model (FJM) shows a high potential for simulating fracturing processes in quasi-brittle materials. This type of DEM simulations mainly involves continuum mechanics, while my previous experience in geomechanics was primarily concerned with the rigid granular media, such as rockfalls simulations. Therefore, during these three years, I developed my expertise in fracture mechanics, continuum mechanics and materials science, as well as my competence in working with the PFC framework.

Here, to summarise the overall assessment of the PFC framework, it is noteworthy to mention that PFC provides a sufficient variety of modelling objects, resulting in a high capability of this DEM framework to model complex geometries and configurations (see section II.2). PFC provides the FJM contact model, which is adequate to simulate interlocked, angular grains microstructures (similar to large grain refractories), thanks to the bonded frictional contacts (see section II.4). On the other hand, PFC lacks an automated, direct calibration process for local FJM parameters, whereas such a fastidious calibration process is already developed in other frameworks, namely in GranOO.

Finally, the introduced PFC framework and FJM contact model will be firstly used for the multiscale homogenisation modelling of elastic properties (Chapter III:). Then, the influence of microcracking on the apparent behaviour of refractory materials will be deeply investigated (Chapter IV: and Chapter V:) since it was, in fact, the main target of this PhD. The discussed points of this chapter were the foundations of the PFC framework and FJM contact model and were used to build up and calibrate considered models in the following chapters.

Chapter III:Modelling the elastic properties of bi-phase and porous materials by using periodic homogenisation approach (in DEM)

III.1. Introduction

As discussed in detail in section I.1, the heterogeneous microstructure design of refractories significantly influences their ability to sustain thermal shocks in their application. As explained in section I.1.2, the thermal expansion mismatch between constituents (large aggregates within a matrix) leads to microcracking around the aggregates and allows to improve the thermal shock resistance. Therefore, to define the most suitable microstructure design, a rational experimental procedure of optimisation has been considered working with model materials containing only a limited number of constituents called "model material" (see section III.2.2). In fact, despite the simplified microstructure of model material, they could exhibit a thermomechanical behaviour that can mimic some aspects of industrial refractories behaviour. Hence, it is crucial to understand better the strong relationships between such microstructures and the macroscopic thermomechanical behaviour of these model materials. Beyond this experimental procedure of optimisation, evidently, numerical modelling, like DEM, can help to have a better view of such complex phenomena.

In fact, the homogenisation aspect in DEM is still today not as robust as in FEM. In this way, one of the first goals of this PhD was to carefully investigate the elastic properties (Young's modulus, Poisson's ratio, and potential anisotropy) from the micro-scale (related to local inclusions or pores) to the macro-scale (related to the volume fraction of inclusions or pores). Hence, to achieve such local to apparent (micro to macro) multi-scale simulations in DEM, a dedicated numerical approach will be proposed in this chapter. This proposed numerical approach aims to simulate the elastic properties of bi-phase and porous materials by using periodic homogenisation technique (see section III.3.1), not taking into account any discontinuity at this stage.

The implementation of the periodic homogenisation approach in DEM allows working on a pseudo-infinite domain with a limited number of discrete elements by replicating a representative volume cell (see section III.3.2). Thus, this approach enables such cross-scale transition from the unit cell to the infinite domain. Here, the elastic properties of bi-phase and porous materials will be investigated as a first study in order to validate such an original approach with DEM (not so well-documented at the moment). In fact, validating such an approach will be an opening to introduce later the thermal damages resulting from thermal expansion mismatch between constituents in order to study the effect on thermal shock resistance. This possible damage progression, which makes simulations much more complicated, could be thus introduced in the DEM model to mimic the real case of thermal damage. In such a perspective, the Flat Joint DEM contact model was chosen as it is capable of reproducing realistic crack initiation and propagation at micro-scale. This model was introduced in detail in section II.4.

To compare the accuracy and the efficiency of this proposed homogenisation approach in DEM, the given apparent elastic properties will be compared to experimental results measured on real model materials: bi-phase and porous materials (see section III.2.2). In addition, the obtained numerical results will be compared to an analytical model and to FEM simulations. Finally, the apparent stiffnesses tensors for a given arrangement (Face-Centred Cubic) within the Representative Volume Element (RVE)

will be compared to the ones provided by analytical model and FEM simulations (see section III.4.4).

III.2. Background of periodic homogenisation and description of the reference material

In this section, a brief review on periodic homogenisation with DEM to describe the macroscopic behaviour of heterogenous materials will be discussed. Later, the reference bi-phase model material will be introduced.

III.2.1. A brief review on periodic homogenisation with DEM

The homogenisation technique was developed in 1978 by Papanicolau and Bensoussan (Papanicolau *et al.* 1978). This mathematical technique, coupled with numerical methods, is used for the scale transition of material properties from a local scale (micro) to a global scale (macro). For instance, in a particle-based simulation, even to upscale the behaviour of a clay matrix from the nanoscale, a self-consistent homogenisation approach could be used (Brochard *et al.* 2017). Homogenisation had been used for a long time in the FEM models. However, it is relatively less popular in the DEM approach applied to continuum media. During the 1980s, periodic conditions were introduced for molecular dynamics, which is quite close to DEM, to remove the boundaries limitations by (Parrinello *et al.* 1981) and (Allen *et al.* 1987). Later, it was proposed in DEM simulation to apply strains on specimens without imposing boundary effects (Cundall 1988a).

In fact, today, there is a lack of studies about homogenisation technique in DEM for predicting the apparent elastic behaviour of materials, especially in 3D. Therefore, the primary motivation of this chapter was to implement a periodic homogenisation technique in the DEM model for predicting the apparent elastic properties of a simplified microstructure, such as bi-phase and porous materials. This study should be considered as the very first stage to validate such a homogenisation technique before introducing cracks propagation within the model.

III.2.2. Description of reference (uncracked) bi-phase and porous model materials

The microstructures of refractory materials are having complex couplings (for example, physicochemistry couplings) between aggregates and matrix, which affect different macroscopic properties of the material. Thus, to study the elastic properties of bi-phase materials, it was necessary to design and produce a simplified material called "model material". In such simplified materials, only the thermomechanical interactions of two solid phases are expected. This simplification was required in order to clearly observe the effect of increasing the inclusions fraction (or porosity) on the elastic macroscopic response of the materials.

To study elastic behaviour of the bi-phase material regarding the inclusions fraction and porosity, Tessier-Doyen *et al.* (N. Tessier-Doyen *et al.* 2007) have designed and built two bi-phase "model materials":

- *Bi-phase material with solid inclusions:* Glass matrix with Alumina inclusions (G/A). This model material is made from the composition of a dense aluminosilicate glass matrix containing randomly distributed single-sized spherical alumina beads (with a mean diameter of 500 μm). The elastic properties of each phase are shown in Table III-1. These two solid-phase materials can reproduce a simple isotropic microstructure. The Coefficient of Thermal Expansions (CTE) of both phases are quite close to each other (6.5×10^{-6} K^{-1} for glass and 7.6×10^{-6} K^{-1} for alumina beads). This close CTE values prevent microcracking or debonding between matrix and inclusions during the cooling down process after the sintering of this bi-phase material (Nicolas Tessier-Doyen 2003) (as shown in section I.1.2, Fig. I-2). Different samples of this material have been produced by varying inclusion fractions in order to observe the effect on the apparent elastic behaviour of the material. The microstructure of this model material has been shown in Fig. III-1 (a) for 28% of the inclusion volume fraction.

- *Porous bi-phase material:* Glass matrix with Pores (G/P). This material is a dense aluminosilicate glass matrix (the same as for G/A material) containing randomly distributed isolated spherical pores (Nicolas Tessier-Doyen 2003). These pores were introduced by using pore-forming agents without inducing any microcracks. Different samples of this material have been produced by varying the porosity in order to observe the effect on the apparent elastic behaviour of the material. Nonetheless, due to experimental limitations, the maximum porosity was about 42%. In fact, higher values were inducing interconnected pores. The microstructure of this model material has been shown in Fig. III-1 (b) for the porosity of 18%.

(a)   (b)
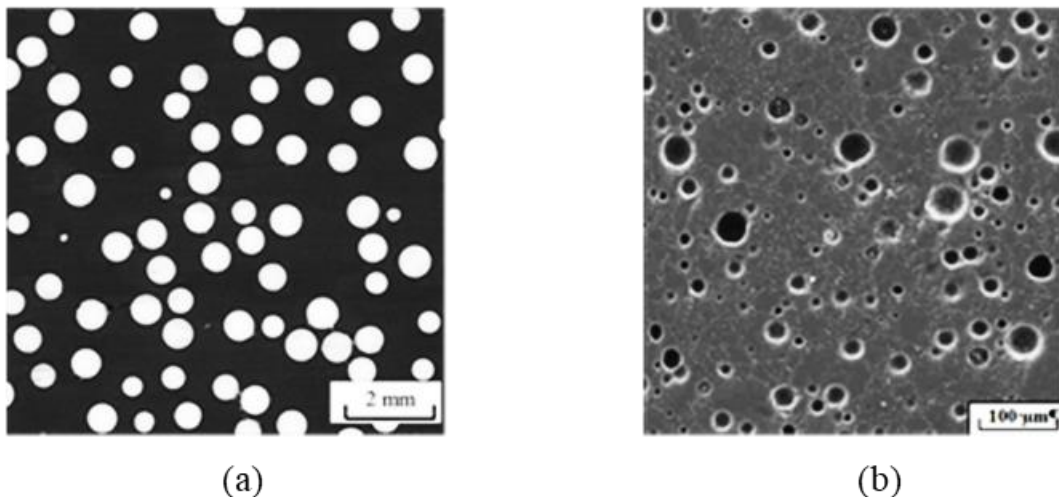
Fig. III-1. Model bi-phase materials: (a) glass matrix with spherical alumina inclusions and (b) glass matrix with isolated spherical pores (Nicolas Tessier-Doyen 2003).

Table III-1. Measured properties of constituents of model bi-phase materials
(Nicolas Tessier-Doyen 2003).

	Property	Measured model material property
Matrix (Glass)	Young's modulus	78 GPa
	Poisson's ratio	0.206
Inclusions (Alumina)	Young's modulus	340 GPa
	Poisson's ratio	0.240

III.3. Numerical foundations for homogenisation applied to DEM

In this section, the numerical methods and techniques which are required to apply the homogenisation to DEM models are explained. At first, the periodic boundary conditions (PBC) will be explained (section III.3.1), then a Representative Volume Elements (RVE) will be chosen and built to be used with the Periodic Boundary Conditions (PBC) (section III.3.2). In order to obtain apparent properties of RVE, it was necessary to load the sample mechanically. Therefore, the required techniques to load the numerical sample in PBC and to measure the apparent properties will be discussed (sections III.3.3, III.3.4 and III.3.5). Afterwards, the calibration process with PBC will be explained (section III.3.6). At the end of this section, the computational method to calculate RVE's apparent stiffness tensor will be introduced (section III.3.7).

III.3.1. Periodic Boundary Conditions (PBC) in DEM

In numerical models, periodic boundaries are often used to remove free boundary effects (Cundall 1988a). Theoretically, in a PBC applied to a DEM model, if a discrete element centroid goes outside the periodic boundary box, it translates back to the opposite face of the box. In order to ensure contacts between element located at opposite faces (or corners) of the boundary, "ghost" elements are introduced (Itasca Consulting Group Inc. 2020). The ghost elements are shown in red in Fig. III-2 for a perfect 2D square RVE. The blue square at the centre of the picture is called a unit cell.
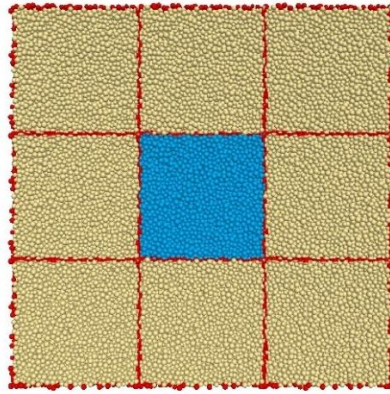
Fig. III-2. A square specimen in PBC (in 2D). Ghost elements and PBC borders are shown in red. The main RVE is in blue (only eight copies are shown here in 2D; However, 26 copies should be considered in 3D).

III.3.2. Representative Volume Elements (RVEs)

For building the unit cell in the periodic 3D space for homogenisation technique, it was necessary to choose a periodic microstructure arrangement that induces a low degree of anisotropy in order to reproduce a statistically isotropic behaviour of the bi-phase material (see section III.2.2). Based on the previous studies, a Face-Centered Cubic (FCC) arrangement had shown a low degree of anisotropy for periodic homogenisation (R. Grasset-Bourdel *et al.* 2011). Therefore, the FCC arrangement has been chosen for the present study to represent a bi-phase material (matrix-inclusion system) RVE. In Fig. III-3, the matrix is shown in blue, and the inclusions are in grey.

For creating a bi-phase RVE with two different constituents, it was necessary to assign different contact (local) properties for the matrix and inclusions regions. As will be mentioned in the calibration part (see section III.3.6), local values were obtained independently by going through the calibration process in PBC for each constituent separately. The interface properties (the contacts between inclusion elements and matrix elements) could be assigned as the matrix, the inclusions, or other desired properties. In this study, for these interface contacts, the matrix properties have been assigned. In other words, no particular property was given to the interface. In fact, in the present case for which no particular properties have been targeted for the interface during the processing of the model material, and thus promoting a very well bond of the glass matrix (by sintering) on the surface of the Alumina beads, properties of the interface could assume similar to the matrix. The contact network is shown in Fig. III-3 (c), where the interface contacts are specifically shown in red.
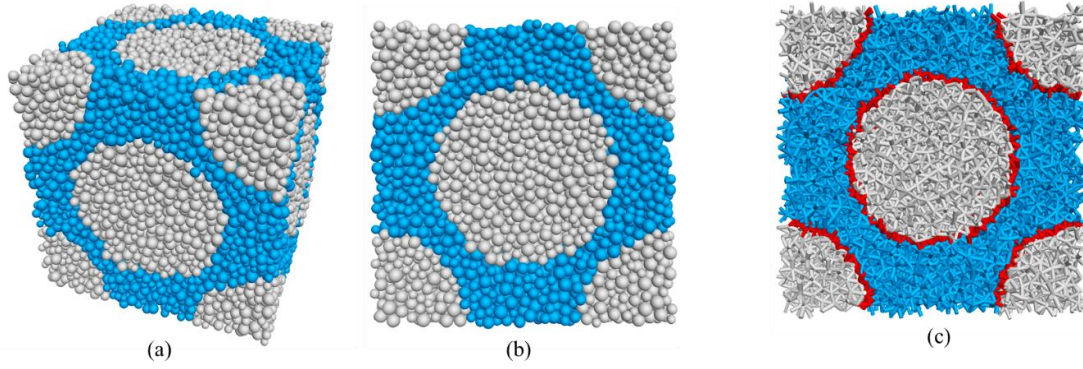
Fig. III-3. FCC arrangement: (a) and (b) numerical sample produced by around 20k discrete elements, and (c) the contacts among the discrete elements.

It is noteworthy to mention that the total number of 20k discrete elements was enough for this RVE, considering the computation time efficiency and accuracy of results. Further detail about the procedure to choose the number of elements is discussed in section III.4.2.2.

The proposed study aims to compare the influence of the inclusion volume fraction on the apparent elastic properties of the model with an analytical model and experimental observations. In such a perspective, several inclusion radii were considered inside the RVEs (Fig. III-4). It should be mentioned that all these RVEs are built from the same spatial arrangement of discrete elements in order to avoid any influence of this spatial arrangement on the apparent properties coming from the calibration process (as discussed in section II.4.3).
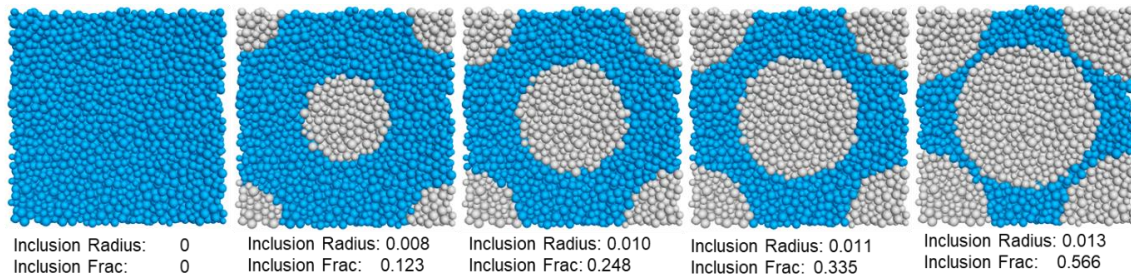
Fig. III-4. Illustrations of some numerical samples with different inclusion fractions, increasing from 0% to 57% in an FCC arrangement.

In the same way, to study the porosity effect, another set of RVEs was built using the same FCC arrangement and replacing the inclusions with voids (Fig. III-5).
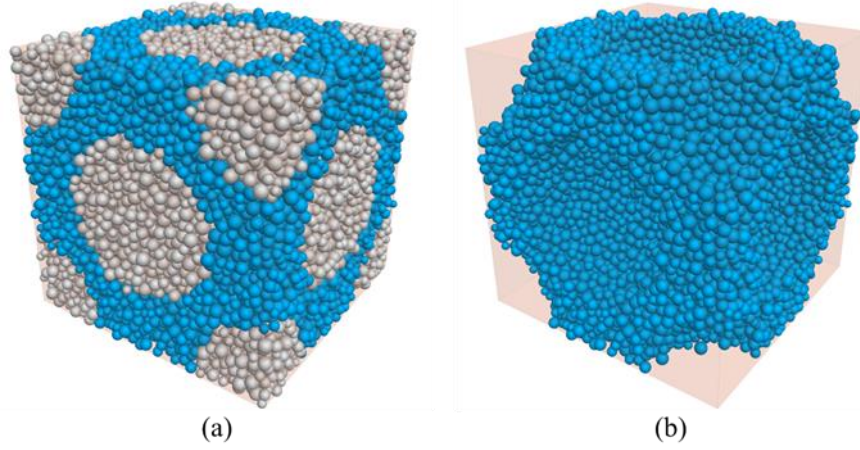
Fig. III-5. Side-by-side comparison of simulated FCC-arranged RVEs in periodic space: (a) bi-phase material (b) porous material.

III.3.3. Distortion technique of PBC for applying strain to RVE

In order to measure numerically apparent elastic properties of RVE, it was necessary to load the sample mechanically. In the case of periodic boundaries, this loading should be applied with particular conditions named "distortion technique". Initially, the concept of distortion of boundary conditions was introduced by Parrinello and Rahaman for molecular dynamics in 1981 (Parrinello *et al.* 1981). Later, this technique was adapted to DEM simulation to apply strains on specimens without imposing boundary effects (Cundall 1988a).

In this study, this method was used to load the RVEs by distorting the PBC in the loading direction while keeping the PBC shape parallelepipedic. The PBC is also distorted in the other directions to ensure pure loading modes (pure tension and pure/simple shear). In such a case, the deformation of the PBC is modelled by imposing a uniform velocity field over the discrete elements, which is coming from the equation of the motions. This point has been explained more in detail in section III.3.5.

Theoretical description of the distortion of PBC in PFC was described by S. Emam as follows (Emam 2009). The coordinate vector $\{x^b\}$ gives the centroid position of an element "*b*":

$$\{x^b\} = (x_i^b)_{1 \le i \le 3}$$

Eq. III-1

The lower and the upper corner of the PBC is P_0 and P_1, respectively. PBC can be distorted by assigning a diagonal strain-rate tensor $[\dot{\varepsilon}]$. For defining the PBC extents, the [L] matrix is introduced:

$$[L] = L_{ij} = \begin{bmatrix} l_x & 0 & 0 \\ 0 & l_y & 0 \\ 0 & 0 & l_z \end{bmatrix}$$

Eq. III-2

where l_j is the extent of the PBC in the j direction. By introducing [L] to Eq. III-1, the position of the element can be written as:

$${x^b} = {x^{P_0}} + [L]{s^b}$$

Eq. III-3

where ${x^{P_0}}$ is the position of the lower corner of PBC, and ${s^b} = (s_i^b)_{1 \leq i \leq 3}$ (reduced coordinate vector) is the reduced position of the vector of the element b centroid:

$$s_i^b = \frac{x_i^b - x_i^{P_0}}{l_i}$$

Eq. III-4

To illustrate these formulas, a transition from reduced coordinate to global coordinate in 2D is shown in Fig. III-6.
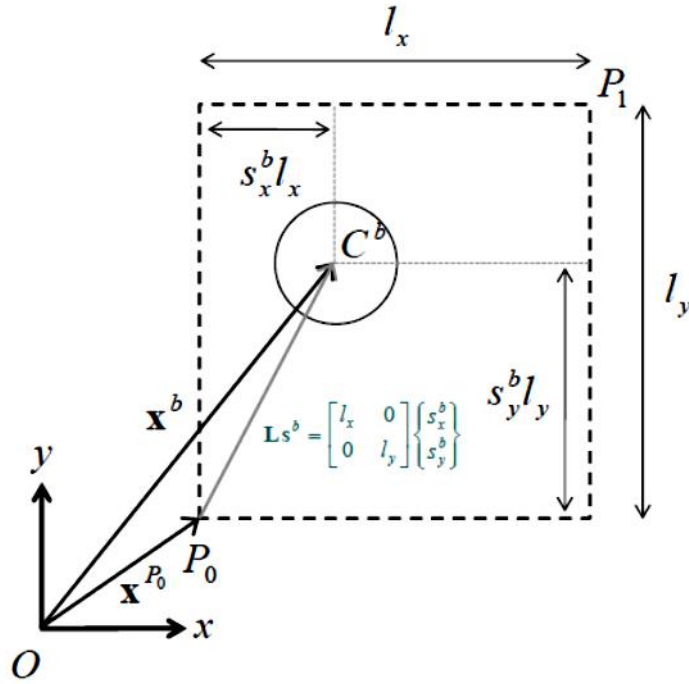
Fig. III-6. Illustration of the transition from reduced coordinate to the global coordinate in 2D, from S. Emam (Emam 2009)

Commonly in DEM, for loading a sample, a velocity may be applied. With PBC, a strain-rate is applied in order to impose a velocity on discrete elements. To apply the assigned strain-rate, the time derivative of tensor $[L]$ is introduced as $[\dot{L}]$. In Eq. III-5, tensors $[L], [\dot{L}]$ and reduced coordinate vector $\{\dot{x}^b\}$ are known. Also, $\{\dot{s}^b\}$ can be calculated from the integration of the acceleration of the elements, which is given by Newton's second law. Therefore, the element velocity $\{\dot{x}^b\}$ can be determined as:

$$\{\dot{x}^b\} = \{\dot{x}^{P_0}\} + [\dot{L}]\{s^b\} + [L]\{\dot{s}^b\}$$

Eq. III-5

and can be simplified as:

$$\{A\} = \{\dot{x}^{P_0}\} + [\dot{L}]\{s^b\}$$

<div align="right">Eq. III-6</div>

$$\{B\} = [L]\{\dot{s}^b\}$$

<div align="right">Eq. III-7</div>

where the vector $\{A\}$ is the velocity of the spatial point $\{x^b\}$ during the distortion of the periodic domain and the vector $\{B\}$ is the velocity of the element b centroid, with respect to PBC. Hence, to apply the distortion to PBC, the tensor $[\dot{L}]$ should be calculated. As an example, in the case of a uniaxial tensile test along the Z direction, this tensor should be:

$$[\dot{L}] = \begin{bmatrix} 0 & 0 & 0 \\ 0 & 0 & 0 \\ 0 & 0 & \dot{l}_z \end{bmatrix}$$

<div align="right">Eq. III-8</div>

where $\dot{l}_z$ is the applied deformation rate in the tension direction.

III.3.4. Measurement ball technique to obtain global stress within RVE

In this study, the discrete domain is considered as a pseudo-continuum media. However, the medium is still discrete, so it is impossible to calculate stress directly, as stress is a continuum quantity. Hence, in order to measure apparent properties during a test, such as stresses or strains, the "measurement ball" technic was applied.

The measurement ball consists of a virtual sphere that measures a given quantity such as stress or strain in a specified DEM model region. It gives the average values of the assigned measurable quantities, such as stress tensor, strain rate, and porosity (Itasca Consulting Group Inc. 2020). In this study, only the stress tensors were measured by using this technique, while the strain was computed from the imposed PBC strain-rate.

To obtain the stress, an averaging procedure is used to convert local forces to a continuum apparent stress of the RVE. The average stress $\overline{\sigma_{ij}}$ in a measurement region of volume V is computed as (Christoffersen *et al.* 1981):

$$[\bar{\sigma}] = -\frac{1}{V}\sum_{N_c} F^{(c)} \otimes L^{(c)}$$

<div align="right">Eq. III-9</div>

where N_c is the number of contacts in the specified region, $F^{(c)}$ is the contact force vector, $L^{(c)}$ is the branch vector between the centroids of the two bodies in contact and $\otimes$ is the outer product.

III.3.5. Servo-control technique

In this study, virtual uniaxial tensile and simple shear tests have to be considered. In the case of uniaxial tensile tests, they should be performed by distorting the PBC with a constant small user-defined strain-rate in order to load the sample. In PBC, this strain-

controlled condition is applied by distorting the PBC in a given direction while using the servo-control mechanism to distort the two other perpendicular directions. In these perpendicular directions, the servo-control technique ensures maintaining a small constant value of confining stresses (also defined by user) during the test by distorting the PBC. These stresses, in perpendicular directions to the loading, are thus monitored continuously by using the measurement ball. Then, a strain-rate (in these perpendicular directions) is automatically adjusted (thanks to a controller gain) in order to keep constant these stresses at a level close to the user-defined value of confining stress. In this case of simple shear test, the same principle is applied. This mechanism of servo-control technique is explained in detail in documentations (Itasca Consulting Group Inc. 2020).

III.3.6. Calibration of local properties in Periodic Boundary Conditions (PBC)

As a reminder from section II.4, the FJM requires a calibration process to assign the correct values for the local properties to reproduce the desired apparent elastic properties. It should be highlighted that in this chapter, the calibration process was done for a non-damaged material in PBC. Therefore, here, as the focus is on the elastic properties of the material, the local fracture parameters (local tensile strength t^{loc} and local cohesion c^{loc}, see section II.4.2) were set to high values to ensure a fully elastic behaviour without any crack. Therefore, the proposed calibration algorithm in section II.4.4 (in Fig. II-14) can be simplified, just using the three first steps. In this chapter, the calibration process was done on a 4×4×4 cm^3 cubic sample consisting of around 20k discrete elements in PBC. The process of choosing this number of elements will be explained in section III.4.2.2.

To build up the bi-phase materials, firstly, it was necessary to go through the calibration process for each constituent separately (Glass matrix and Alumina inclusions) to reproduce their own apparent elastic properties, using the same spatial arrangement of discrete elements. In Table III-2, the input parameters and the apparent properties for each pure constituent are summarised.

Chapter *III:Modelling the elastic properties of bi-phase and porous materials by using periodic*
homogenisation approach (in DEM): Numerical foundations for homogenisation
applied to DEM

Table III-2. The input parameters and apparent properties of the bi-phase material

Targeted Experimental Material property			FJM input parameter		Simulated Apparent Material property	
Description		Value	Description	Value	Description	Value
Reproduce symmetrical elastic behaviour in tension and compression		-	Initial gap (g_i^{loc})	40% of the ball radius	Reproduce symmetrical elastic behaviour in tension and compression	Achieved
Matrix (Glass)	Young's modulus	78 GPa	local Young's modulus (E^{*loc})	88.2 GPa	Apparent Young's modulus (E^{ap})	78 GPa
	Poisson's ratio	0.206	local stiffness ratio (K^{*loc})	5.6	Apparent Poisson's ratio (v^{ap})	0.2060
Inclusions (Alumina)	Young's modulus	340 GPa	local Young's modulus (E^{*loc})	438.8 GPa	Apparent Young's modulus (E^{ap})	340 GPa
	Poisson's ratio	0.24	local stiffness ratio (K^{*loc})	12.1	Apparent Poisson's ratio (v^{ap})	0.2400

It should be mentioned that with free boundary conditions (without considering the periodic homogenisation), the geometry of the specimen influences the calibration process (as discussed in section II.4.3) (Potyondy 2019). After investigation of some other geometries rather than a cube (parallelepiped two times larger in one direction), it should be noted that using periodic homogenisation strongly limits the influence of the shape of the sample in the calibration process.

III.3.7. Computational method of RVEs apparent stiffness tensor

As mentioned in section III.3.2, for using the periodic homogenisation technique, it was necessary to build an RVE with a low degree of anisotropy to match the behaviour of the model materials. Therefore, the FCC arrangement was chosen for building the RVEs. On the other hand, the DEM is a model with a random spatial positioning of discrete elements which could not respect a perfect symmetry. In such a case, the random spatial positioning of discrete elements could lead to a certain level of mechanical anisotropy coming from this spatial asymmetry.

To investigate this influence, the effective stiffness tensor of RVEs was calculated by two different approaches for the DEM model RVE: assuming a perfect geometrical planar symmetry in 3D of the sample or not. For the first case, the effective stiffness tensor of the FCC arrangement could be calculated as a cubic symmetry stiffness tensor (Hearmon 1964). For the second case, to investigate the impact of asymmetry, it was essential to measure the apparent elastic properties of RVEs in each main direction of RVE, which are shown in Fig. III-7. Hence, the cubic symmetry assumption of the previous approach was not retained, and the orthotropic symmetry assumption was considered. The technical steps to calculate each of these approaches for the DEM models are explained in the following sections.
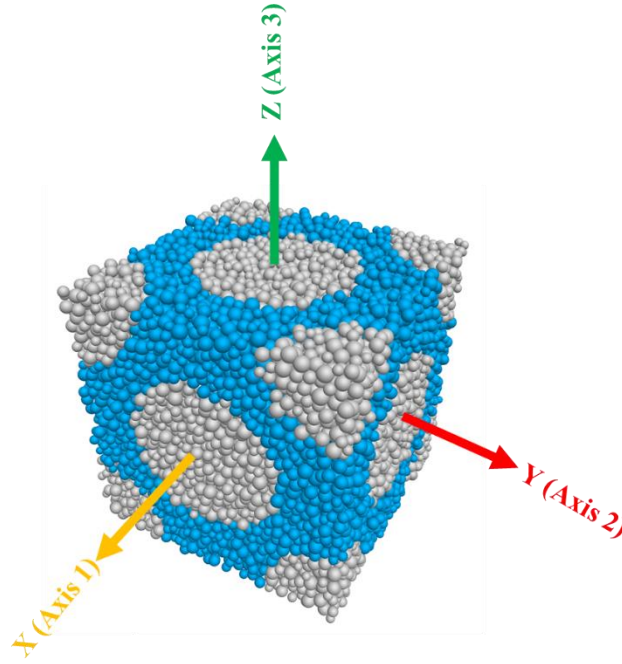
Fig. III-7. The main directions of the modelled FCC arranged RVE

III.3.7.1. Cubic symmetry assumption

By assuming a perfect geometrical planar symmetry in 3D, it was possible to calculate the effective stiffness tensor with three independent elastic elements, as shown in Eq. III-10.

$$C_{ij} = \begin{pmatrix} C_{11} & C_{12} & C_{12} & 0 & 0 & 0 \\ & C_{11} & C_{12} & 0 & 0 & 0 \\ & & C_{11} & 0 & 0 & 0 \\ & Sym & & C_{44} & 0 & 0 \\ & & & 0 & C_{44} & 0 \\ & & & 0 & 0 & C_{44} \end{pmatrix} \quad (a)$$

$$C_{ij} = \begin{pmatrix} E^{ap}(1-v)/(1-v-2v^2) & E^{ap}v/(1-v-2v^2) & E^{ap}v/(1-v-2v^2) & 0 & 0 & 0 \\ & E^{ap}(1-v)/(1-v-2v^2) & E^{ap}v/(1-v-2v^2) & 0 & 0 & 0 \\ & & E^{ap}(1-v)/(1-v-2v^2) & 0 & 0 & 0 \\ & Sym & & G^{ap} & 0 & 0 \\ & & & 0 & G^{ap} & 0 \\ & & & 0 & 0 & G^{ap} \end{pmatrix} \quad (b)$$

Eq. III-10

For calculating the first two elastic elements in the cubic symmetric stiffness tensor (C_{11} and C_{12}), it was required to measure the apparent properties, E^{ap} and v^{ap}. To measure apparent Young's modulus (E^{ap}) a direct uniaxial tensile test was performed by distorting the PBC with a constant small strain-rate (Fig. III-8 (a)). By using the distortion of PBC technique (section III.3.3) and measurement ball (section III.3.4), the principal stress within the RVE was measured. Then by having the total applied strain, the apparent Young's modulus (E^{ap}) was calculated. The apparent Poisson's ratio (v^{ap}) could be obtained by measuring the perpendicular strains and by having the applied strain in the T direction, as shown in Fig. III-8 (a), which are coming from the distortion of the PBC.

For calculating the last elastic element in the cubic symmetric stiffness tensor (C_{44}), the apparent shear modulus (G^{ap}) had to be measured. To do so, a simple shear test was performed by distorting the PBC with a constant small shear strain-rate, only in the S direction, as shown in Fig. III-8 (b).

At a given applied shear strain, the shear stress was calculated within the RVE (with respect to the loading direction) using the measurement ball technique. By having the shear stress and the applied shear strain, the apparent shear modulus (G^{ap}) was calculated.
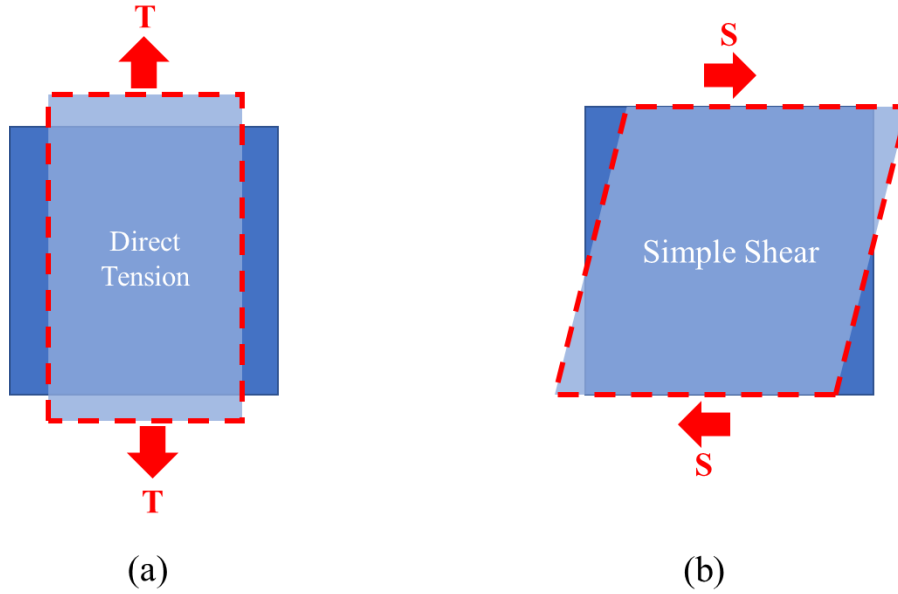
Fig. III-8. The schematic of mechanical tests simulation: (a) a uniaxial tensile test simulation in T direction on the numerical sample, and (b) a simple shear test in S direction on the numerical sample.

Finally, after obtaining the apparent Young's modulus (E^{ap}), Poisson's ratio (v^{ap}) and shear modulus (G^{ap}), it was possible to use the constitutive law for cubic symmetry as noted in Eq. III-10 to calculate C_{11}, C_{12}, and C_{44} elements and build the stiffness tensor of RVE (Bower 2009). The calculation time for each simulation took about 5 to 8 minutes for 20k discrete elements on a system with Intel Core Xeon E2186M 4.0 GHz, SSD, 16 GB RAM, 12 parallel threads.

III.3.7.2. Orthotropic symmetry assumption

This time, it was assumed that there is no perfect geometrical planar symmetry in 3D due to the spatial randomness of the discrete elements positioning. Considering this asymmetry, the cubic symmetry assumption was not considered, and the same RVEs were considered orthotropic, with nine independent elastic coefficients and three mutually perpendicular symmetry planes (as noted in Eq. III-11 for the theoretical orthotropic assumption).

$$C_{ij} = \begin{pmatrix} C_{11} & C_{12} & C_{13} & 0 & 0 & 0 \\ & C_{22} & C_{23} & 0 & 0 & 0 \\ & & C_{33} & 0 & 0 & 0 \\ & Sym & & C_{44} & 0 & 0 \\ & & & 0 & C_{55} & 0 \\ & & & 0 & 0 & C_{66} \end{pmatrix}$$

$$C_{ij} = \begin{pmatrix} E_{11}^{ap}(1-v_{23}v_{32})Y & E_{11}^{ap}(v_{21}+v_{31}v_{23})Y & E_{11}^{ap}(v_{31}+v_{21}v_{32})Y & 0 & 0 & 0 \\ & E_{22}^{ap}(1-v_{13}v_{31})Y & E_{22}^{ap}(v_{32}+v_{12}v_{31})Y & 0 & 0 & 0 \\ & & E_{33}^{ap}(1-v_{12}v_{21})Y & 0 & 0 & 0 \\ & Sym & & G_{23}^{ap} & 0 & 0 \\ & & & 0 & G_{13}^{ap} & 0 \\ & & & 0 & 0 & G_{12}^{ap} \end{pmatrix}$$

$$Y = \frac{1}{1-v_{12}v_{21}-v_{23}v_{32}-v_{31}v_{13}-2v_{21}v_{32}v_{13}}$$

Eq. III-11

For calculating the first three elastic elements of the main diagonal (C_{11}, C_{22}, and C_{33}), and three off-diagonal symmetric elements (C_{12}, C_{13}, and C_{23}), it is required to perform three uniaxial tensile tests on each main axes (Fig. III-7). Each of these uniaxial tensile tests gave one of the mentioned main diagonals and one of the off-diagonal elements independently. These uniaxial tensile tests were performed, as explained earlier in the previous section. However, as mentioned in Eq. III-11 for orthotropic assumption, in the case of the geometrical cubic sample, the Poisson's ratio (v^{ap}) should be measured in two perpendicular directions, independently. To satisfy this point, in each simulation for obtaining the elements of the orthotropic matrix, the Poisson's ratio (v^{ap}) was measured in the two perpendicular directions.

Finally, for calculating the last three independent elements of the main diagonal of orthotropic stiffness tensor (C_{44}, C_{55}, and C_{66}), the apparent shear modulus (G^{ap}) had to be measured along the three main axes. The procedure of measuring the apparent shear modulus (G^{ap}) was explained earlier in the previous section.

After obtaining the apparent Young's modulus (E^{ap}), Poisson's ratio (v^{ap}) and shear modulus (G^{ap}), it was possible to use the constitutive law for orthotropic materials as shown in Eq. III-11 to calculate the nine elements (C_{11}, C_{22}, C_{33}, C_{44}, C_{55}, C_{66}, C_{12}, C_{13}, and C_{23}) and build the stiffness tensor of RVE. (Bower 2009)

Note that the first three diagonal components (C_{11}, C_{22}, C_{33}) are related to the tension-compression stiffness of the material in the main three directions. The last three diagonal components (C_{44}, C_{55}, C_{66}) are related to the shear stiffness of the material. Also, the three off-diagonal components (C_{12}, C_{13}, C_{23}) are related to the extension-extension coupling. These relations are the same for the cubic assumption as well.

The results of these different approaches were compared in section III.4.4 to check the difference between the two assumptions and evaluate the influence of spatial randomness of the discrete elements positioning on the anisotropy degree of the RVEs. Also, in other predictive methods, such as most FEM models, the first approach was used; hence, it was essential to make a comparison between these two approaches, FEM (R. Grasset-Bourdel *et al.* 2011) and analytical (Hashin *et al.* 1963) models, to check the validity of this model.

III.4. Modelling apparent elastic properties of bi-phase and porous materials

Based on the numerical techniques of the previous sections, the applications and results of the DEM simulations in predicting the elastic properties of bi-phase and porous materials by using the periodic homogenisation approach are presented and discussed in the following parts.

Firstly, the reference values coming from experimental, analytical, and numerical (FEM) results are introduced. Later, a series of numerical investigations are carried out to refine the DEM periodic models. In the end, to validate the accuracy of the DEM models, Young's modulus and Poisson's ratio obtained by DEM using PBC are confronted with reference values.

III.4.1. Reference values coming from experimental data, analytical approach and numerical FEM model

To verify the proposed periodic homogenisation in the DEM model for bi-phase and porous materials, it was essential to confront the obtained results to experimental data and/or other predictive methods such as FEM. Firstly, a comparison is made with experimental results. Secondly, the results are compared to other existing methods, such as an analytical method (by using Hashin and Shtrikman relationships) and a numerical approach (Finite Element Method simulations).

III.4.1.1. Experimental technique for measuring elastic properties of model materials (EXP)

As mentioned in section III.2.2, two kinds of model materials were studied: a Glass matrix with randomly distributed Alumina inclusions (G/A) and a Glass matrix with randomly distributed spherical Pores (G/P). For the material G/A, different samples were prepared in the study by Tessier-Doyen (N. Tessier-Doyen *et al.* 2007), with different inclusion fractions, as shown in Fig. III-9. Similarly, for material G/P, various porosity values were considered.
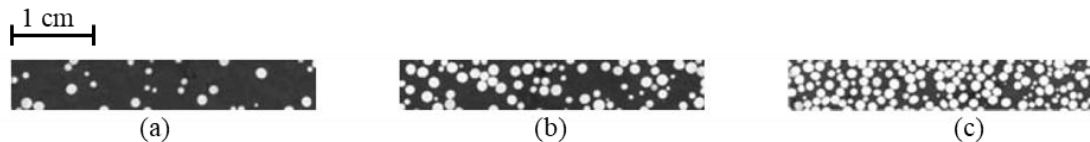
Fig. III-9. Optical images of bi-phase model material with different inclusion volume fractions: (a) 7 %, (b) 28 % and (c) 48 % (N. Tessier-Doyen *et al.* 2007).

For measuring elastic properties, these model materials were considered isotropic materials at the macroscopic scale. Their elastic properties, Young's modulus and Poisson's ratio, were measured by ultrasonic wave propagation technique with contact

transducers. Besides, to limit the attenuation of the waves causing by inclusions or pores, the measurements were done in transmission at low frequency (1 MHz). The same technique was used for G/P materials (Nicolas Tessier-Doyen 2003) (N. Tessier-Doyen *et al.* 2007).

III.4.1.2. Hashin and Shtrikman (HS) bounds for model bi-phase and porous materials

To predict analytically elastic properties of the bi-phase or porous model materials, Hashin and Shtrikman (HS) model was chosen for this study (Hashin *et al.* 1963). This analytical predictive approach defines two bounds for bi-phase materials: Hashin and Shtrikman upper bound (HS+) and Hashin and Shtrikman lower bound (HS-).

For the G/A case, as it was mentioned in section III.2.2, the inclusions are nearly four times stiffer than the matrix: 78 GPa for matrix and 340 GPa for the inclusions. In such a case, as mentioned in previous studies, Young's modulus and Poisson's ratio should follow the lower HS bond (HS-) while increasing the inclusion volume fraction (Brisard *et al.* 2010) (N. Tessier-Doyen *et al.* 2007) (Tucker *et al.* 1999) (Lakes 1998).

For G/P material, which is a porous material, it is assumed that void's bulk modulus (K) and shear modulus (G) is zero; therefore, the bulk modulus (K) and shear modulus (G) of the matrix is considered as very high in comparison to the voids. In such a case, the reference given by HS bounds is inversed. This means the HS upper bound (HS+) will be the analytical reference for the porous material, whereas HS lower bound (HS-) is zero (Pabst *et al.* 2004) (Joliff *et al.* 2007) (Živcová *et al.* 2009).

In the HS model, the apparent Young's modulus (E^{ap}) and Poisson's ratio (v^{ap}) can be predicted by knowing the volume fraction of inclusions (or porosity) as well as bulk and shear modulus of each constituent. The analytical relationships of the Hashin and Shtrikman (HS) model are shown in Table III-3. These relationships are used to plot upper and lower Hashin and Shtrikman bounds (HS+ and HS-).

Table III-3. The main HS analytical relationships for the elastic properties of a bi-phase material

Property	Lower Hashin and Shtrikman bound (HS-)	Upper Hashin and Shtrikman bound (HS+)
Bulk modulus	$K^{HS-} = K_m + \dfrac{f_i}{\dfrac{1}{K_i - K_m} + \dfrac{3(1 - f_i)}{3K_m + 4G_m}}$	$K^{HS+} = K_i + \dfrac{1 - f_i}{\dfrac{1}{K_m - K_i} + \dfrac{3f_i}{3K_i + 4G_i}}$
Shear modulus	$G^{HS-} = G_m + \dfrac{f_i}{\dfrac{1}{G_i - G_m} + \dfrac{6(K_m + 2G_m)(1 - f_i)}{5G_m(3K_m + 4G_m)}}$	$G^{HS+} = G_i + \dfrac{1 - f_i}{\dfrac{1}{G_m - G_i} + \dfrac{6(K_i + 2G_i)f_i}{5G_i(3K_i + 4G_i)}}$
Young's modulus	$E^{HS-} = \dfrac{9K^{HS-} \cdot G^{HS-}}{3K^{HS-} + G^{HS-}}$	$E^{HS+} = \dfrac{9K^{HS+} \cdot G^{HS+}}{3K^{HS+} + G^{HS+}}$

Table III-3 summarises the analytical formula given by HS where f_i is the volume fraction of inclusions, K_m and K_i are bulk moduli of matrix and inclusions, G_m and G_i are shear moduli of matrix and inclusions.

III.4.1.3. Periodic Homogenisation by Finite Element Method (FEM)

Another reference results come from the study of Grasset-Bourdel *et al.* (R. Grasset-Bourdel *et al.* 2011). The mentioned bi-phase model materials (G/A and G/P) were modelled by finite element periodic homogenisation. Here, the FCC arrangement is considered for the RVEs (Fig. III-10) (R. Grasset-Bourdel *et al.* 2011). Therefore, both FEM and DEM models simulated the FCC arrangement that made a direct comparison between the FEM and DEM models possible.
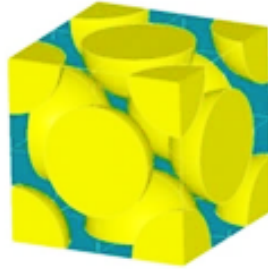
Fig. III-10. The continuum RVEs modelled with FEM in Face-Centred Cubic (FCC) arrangement (R. Grasset-Bourdel *et al.* 2011)

III.4.2. Numerical investigations for producing DEM periodic homogenisation

To build an accurate numerical DEM model, the impact of different numerical approaches and techniques has been investigated. In this regard, the influence of using periodic homogenisation technique, the impact of the number of discrete elements, and different possible numerical approaches to calculate experimental inclusion volume fraction (and porosity) are investigated. All these points are very well-documented in literature for FEM modelling, but in the specific case of DEM applied to continuous media, these concepts are, in fact, not well established yet.

III.4.2.1. Periodic homogenisation

The first comparison presented here is to ensure the efficiency and the accuracy of the homogenisation technique on the prediction of apparent elastic properties. In this aim, the results obtained by PBC is compared to the Free Boundary Condition (FBC), which is without any homogenisation. As mentioned in section III.4.1.2, the apparent elastic properties should follow:
- the lower HS- bound in the case of G/A bi-phase material;
- the upper HS+ bound in the case of G/P porous material.

Fig. III-11 (a) and (b) are showing the simulation results of the apparent Young's modulus (E^{ap}) and Poisson's ratio (ν^{ap}) for the different considered volume fractions of inclusions. The analytical Hashin and Shtrikman (HS) bounds have been calculated and plotted for comparison.

Fig. III-11. Comparison of PBC and FBC for (a) apparent Young's modulus (E^{ap}) and (b) Poisson's ratio (ν^{ap}) in the case of G/A bi-phase materials.

As shown in Fig. III-11 (a), the FBC model starts to deviate from the HS- lower bound, especially for high volume fractions of inclusion (higher than 25%). This

deviation tends to the middle range of the HS bounds, which is in line with previous studies by another DEM code, GranOO, which used randomly distributed inclusions (André *et al.* 2017). However, the model with the periodic homogenisation, which is used for this study, was in accordance with the theoretical HS- lower bound.

As it was shown in Fig. III-11 (b), the apparent Poisson's ratio (v^{ap}) simulations with the periodic homogenisation are closely following the lower bound (HS-) while the model without homogenisation is not following HS bounds. Additionally, these FBC apparent Poisson's ratio results exhibit some irregularities. To explain this inaccuracy with FBC, it should be mentioned that, for measuring the apparent Poisson's ratio (v^{ap}) in the simulations, uniform tensile displacements were applied on one of the main axes of the sample, and the strains were measured on the faces in perpendicular directions (for which some roughness could come from the spatial distribution of discrete elements). Nevertheless, a uniform strain hypothesis was used to compute the apparent Poisson's ratio. This hypothesis remains questionable and may lead to these significant discrepancies. In the case of PBC, since the boundaries remain planar, this problem does not exist.

To compare quantitatively FBC and PBC, the relative deviation of Young's modulus (E_{error}) and Poisson's ratio (v_{error}) from the HS- bound for each simulation has been calculated as follows:

$$E_{error} = \frac{|E_{simu} - E_{HS-}|}{E_{HS-}} \qquad \text{Eq. III-12}$$

$$v_{error} = \frac{|v_{simu} - v_{HS-}|}{v_{HS-}} \qquad \text{Eq. III-13}$$

Then by having relative deviation for each simulated inclusion fraction, the mean deviations for PBC and FBC were calculated. The mean deviation of Young's modulus for the PBC model was 0.3% (min 0 % and max 0.7%), while for the FBC, it was 1.4% (min 0% and max 4.9%). In addition, the mean deviation for Poisson's ratio for the PBC was 0.2% (min 0% and max 0.4%) while for the FBC, it was 1.5% (min 0% and max 3.0%).

Similar investigations were managed for the case of G/P porous material. Fig. III-12 (a) and (b) are showing the simulation results of the apparent Young's modulus (E^{ap}) and Poisson's ratio (v^{ap}) for the different considered porosities, in this case. The analytical Hashin and Shtrikman (HS) bounds have also been calculated and plotted for comparison.
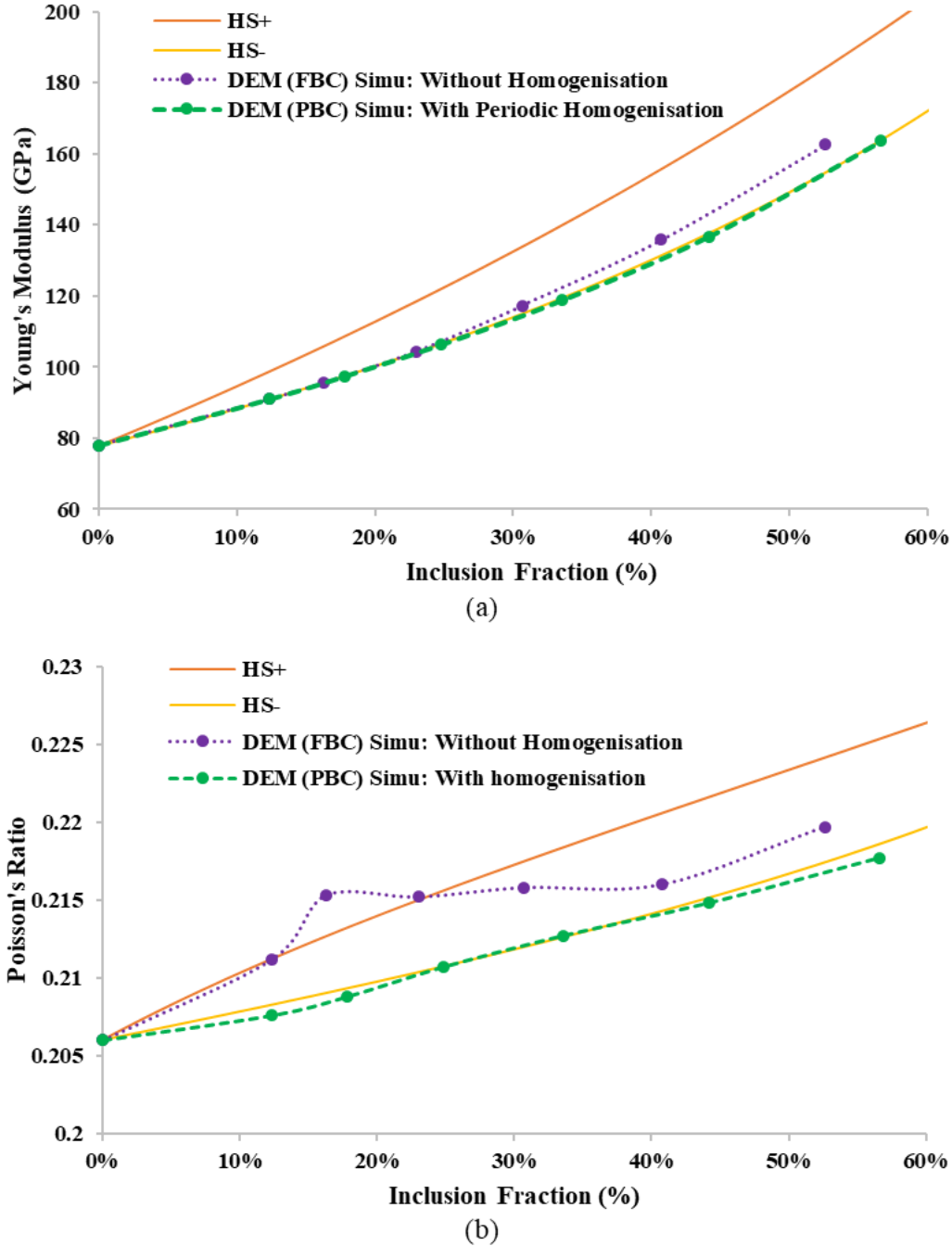
(a)

(b)
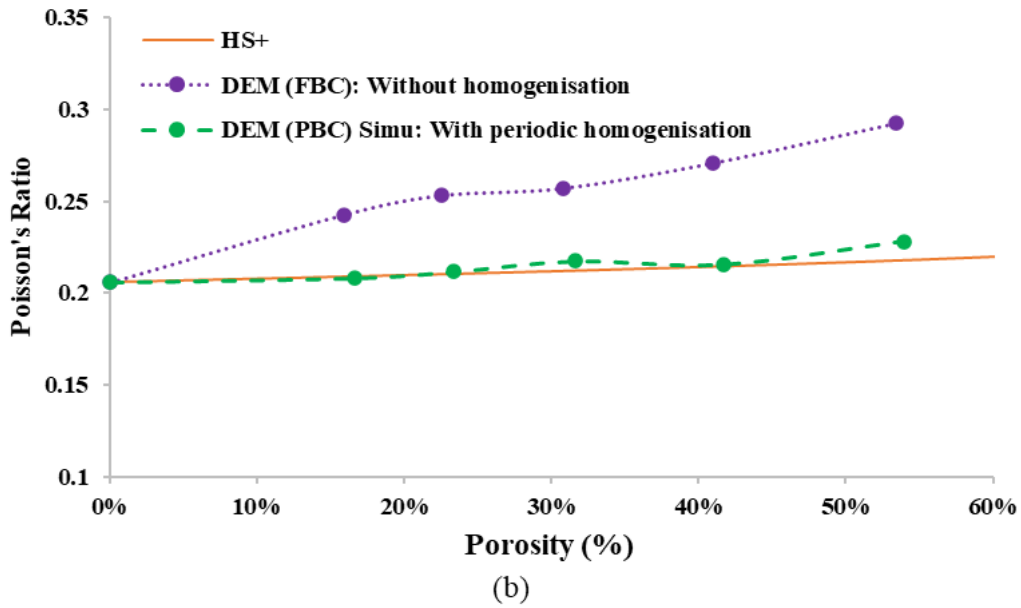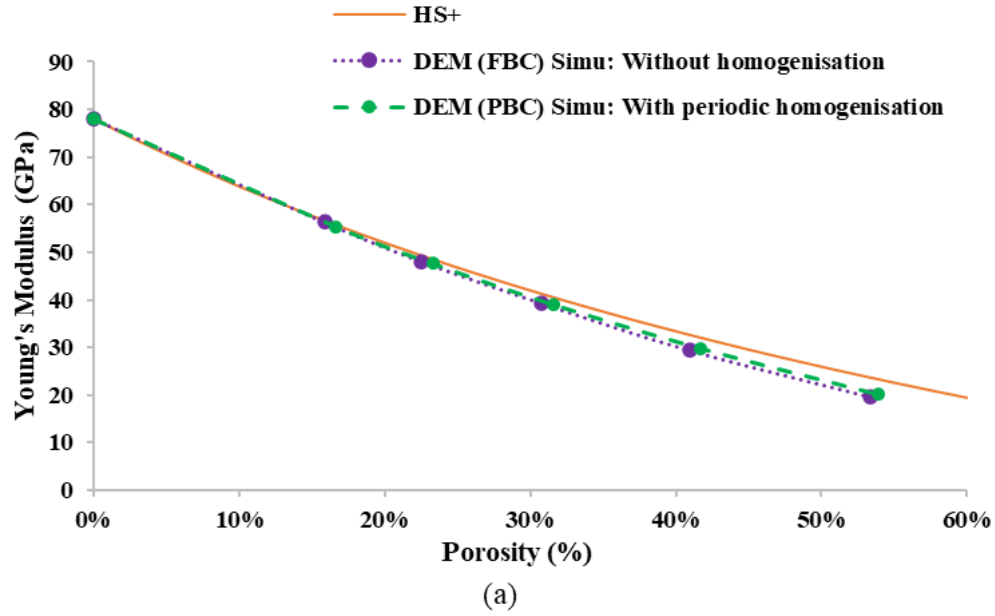
Fig. III-12. Comparison of PBC and FBC for (a) apparent Young's modulus (E^{ap}) and (b) Poisson's ratio (v^{ap}) in the case of G/P porous materials.

As it is shown in Fig. III-12 (a), for the case of porous materials G/P, the FBC model tends again to deviate from the HS+ analytical reference for Young's modulus, while the PBC model shows a better agreement, as previously.

In the same way, in Fig. III-12 (b), the FBC model is progressively deviating from the HS+ analytical reference for Poisson's ratio, while the PBC follows the upper bound (HS+) with good accordance. However, in the case of porous materials, these FBC discrepancies for Poisson's ratio are more significant, probably due to higher contrast between the elastic properties of matrix and pores.

Again, to quantitatively compare FBC and PBC, the relative deviations from the HS+ bound has been calculated in the same way.

The mean relative deviation E_{error} for the PBC model was 4.5% (min 0% and max 13.9%), while for the FBC model, it was 5.8% (min 0% and max 17.3%). The mean relative deviation v_{error} for the PBC model was 4.9% (min 0% and max 12.0%) while for the FBC model, it was 24.1% (min 0% and max 43.6%).

Overall, this study demonstrates that DEM models using periodic homogenisation exhibit much better agreement with the analytical HS bounds for both bi-phase and porous materials than using free boundary conditions. This study highlights the interest in using PBC for predicting apparent elastic properties of multiphase material within the DEM frameworks.

III.4.2.2. Number of discrete elements

In this section, the number of discrete elements to build an RVE is discussed. The primary motivation of using the presented homogenisation technique is to scale up the behaviour of the materials from micro to macro scale. This means that the apparent properties of a heterogeneous material could be reproduced by only simulating a small fraction of the whole specimen. Compared to FEM, this advantage is even more tangible due to the high calculation cost of DEM simulations. In DEM, an infinite heterogeneous media could be reproduced by a relatively small number of discrete elements in RVEs combined with PBC. However, even in building an RVE, the number of discrete elements could be influential. To study this influence, FCC-arranged RVEs have been produced with approximately 20k discrete elements, as shown in Fig. III-13 (a) and compared to 68k discrete elements as shown in Fig. III-13 (b). It is worth mentioning that the input parameters of 20k and 68k samples were calibrated separately. However, the calibrated input values were relatively close (see section III.3.6 for 20k).

For 20k discrete elements, the calculation time for each simulation took about 8 to 10 minutes. For 68k discrete elements, the calculation time for each simulation took an average of 6 to 7 times longer than 20k (both on a system with Intel Core Xeon E2186M 4.0 GHz, SSD, 16 GB RAM, 12 parallel threads). The results of simulations for different numbers of DEs (20k and 68k) are plotted in Fig. III-14.

(a)

(b)
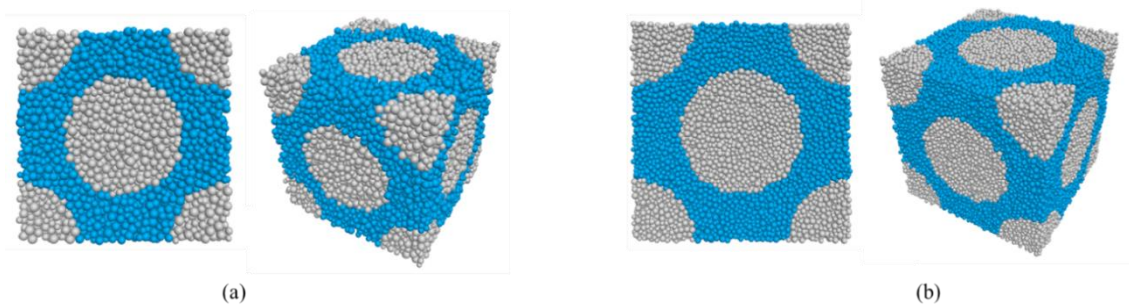
Fig. III-13. RVEs with a different number of DEs and fineness:
(a) 20k discrete elements and (b) 68k discrete elements

(a)

(b)
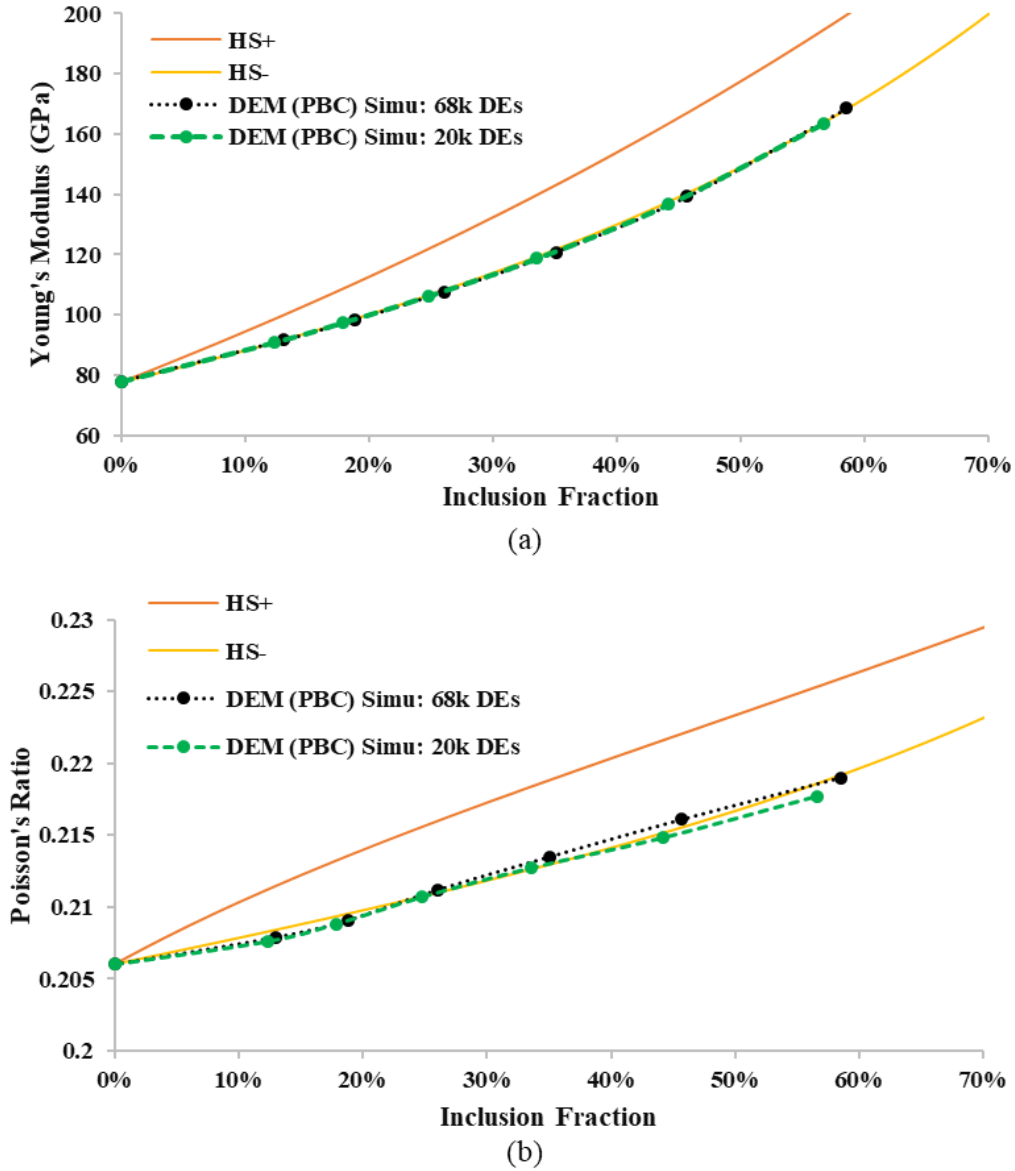
Fig. III-14. Comparison of 20k and 68k RVEs with PBC for G/A bi-phase material: (a) apparent Young's modulus (E^{ap}) and (b) apparent Poisson's ratio (v^{ap}).

As shown in Fig. III-14 (a), the relative deviation from Young's modulus HS- lower bound is less than 1.0% for both 20k and 68k RVEs. Also, as shown in Fig. III-14 (b), the relative deviation from Poisson's ratio HS- lower bound is less than 0.4% for both RVEs. By considering these deviations, both models exhibit a very similar high accuracy in representing the apparent elastic behaviour of bi-phase materials. This means, by having the same relative accuracy, the model with 20k DEs is more efficient in terms of calculation performance. It emphasises that, even with a relatively low number of DEs (20k DEs), the model is giving a valid response for the apparent elastic behaviour. These results demonstrate the importance of using periodic homogenisation for decreasing the computation time and cost by decreasing the number of DEs and the fineness of the models. It is a critical point in DEM models, where calculation efficiency is much more

demanding in comparison to the other numerical methods. For this reason, the RVEs with 20k DEs considering PBC was mainly used in the present study.

III.4.2.3. Inclusion fraction calculation

As mentioned in section III.4.1.2, for positioning and comparing the simulated results of the apparent elastic properties of bi-phase or porous materials on the HS bounds diagrams, one of the influential parameters is the inclusion fraction. For precisely calculating the inclusion fractions of the simulated FCC arrangements of RVEs, two approaches were investigated. Firstly, it was calculated based on the volume of the DEs in each part (matrix and inclusion) as follows:

$$f_i^V = \frac{\sum V_{inclu}^{DE}}{\sum V_{inclu}^{DE} + \sum V_{matrix}^{DE}}$$
Eq. III-14

where f_i^V is the inclusion fraction calculated by volume fraction, $\sum V_{inclu}^{DE}$ is the total volume of DEs within the inclusions, and $\sum V_{matrix}^{DE}$ is the total volume of DEs within the matrix. With this formulation, the porosity between the DEs is supposed to be the same in the inclusions and in the matrix, allowing to simplify the porosity term from each.

The second approach calculates the inclusion fraction by the relative number of the contacts in each part of the material, and this means the total number of contacts within the inclusions over the total number of existing contacts (Eq. III-15). Note that as mentioned in section III.3.2, the matrix-inclusion interface contacts were considered as a matrix-matrix contact. Therefore, the proposed inclusion fraction calculation is:

$$f_i^C = \frac{N_{inclu}^C}{N_{inclu}^C + N_{matrix}^C}$$
Eq. III-15

where f_i^C is the inclusion fraction calculated by the number of contacts, N_{inclu}^C is the total number of contacts within the inclusions, and N_{matrix}^C is the total number of contacts within the matrix (including the interface contacts).

In Fig. III-15, the comparison and the accuracy of these two methods have been compared regarding the HS bounds.

(a)

(b)
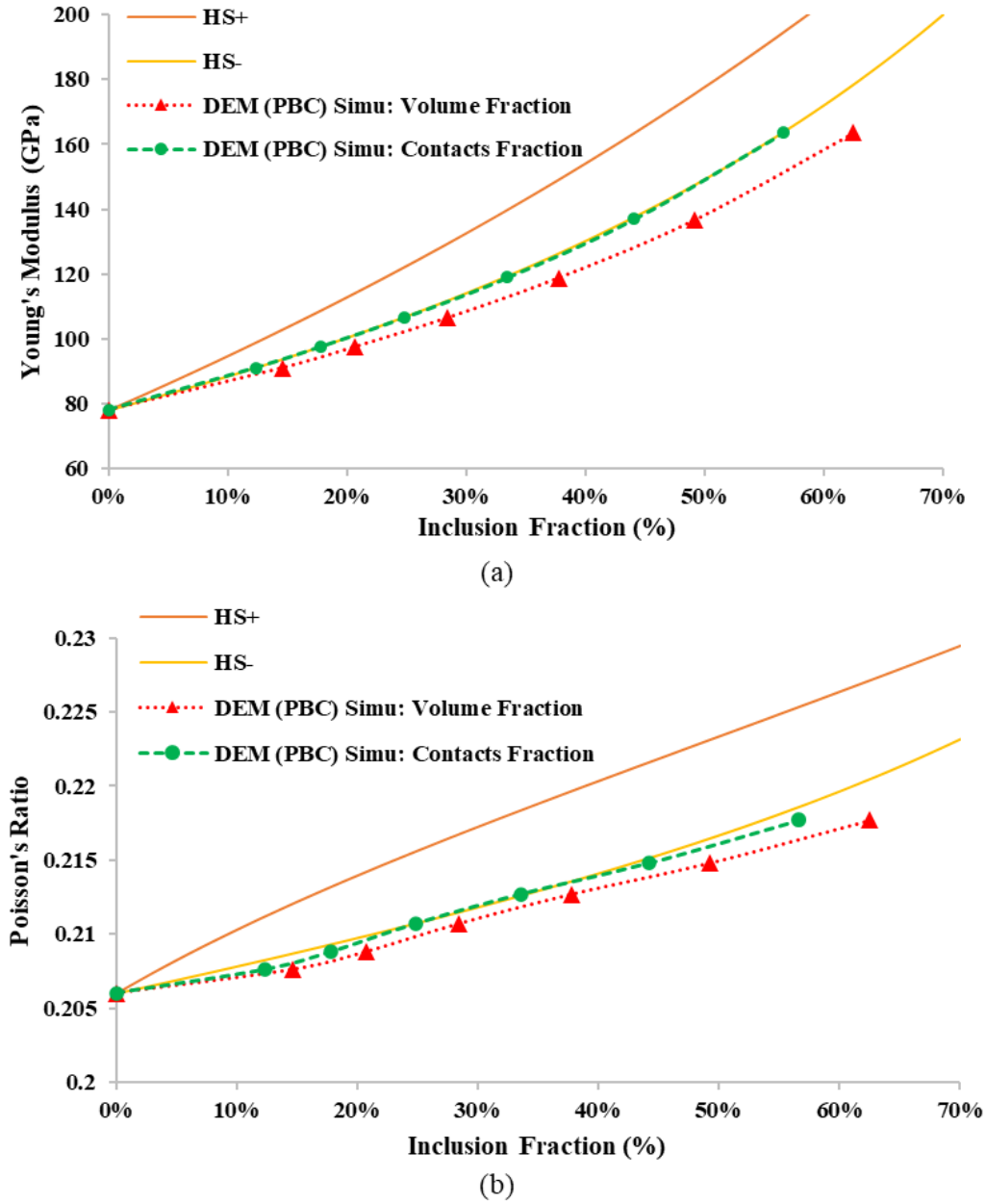
Fig. III-15. Comparison of DEs volume fraction and
contact fraction approaches for calculating inclusion fractions:
(a) apparent Young's modulus (E^{ap}) and (b) apparent Poisson's ratio (v^{ap}).

As shown in Fig. III-15, the calculation of the inclusion fraction by contacts is much more closer to the HS- reference bound. The average deviation from HS- bound for the positioning of the apparent Young's modulus (E^{ap}) by using contacts number is 0.3% (min 0% and max 0.7%) while this deviation reaches up to 4.7 (min 0% and max 8.4%) for the volume fraction approach. In the same way, for the apparent Poisson's ratio (v^{ap}), this deviation for contacts number approach is 0.2% (min 0% and max 0.4%) while this deviation reaches up to for 2.6% (min 0% and max 4.2%) for the volume fraction approach.

At first sight, this better accuracy of the contacts number approach could appear surprising. However, it should be highlighted that in DEM, the apparent properties of materials are coming from the responses of the contacts and not from the discrete elements themselves since they are considered as rigid bodies. Hence, it is logical that in DEM, the most pertinent parameter to account for the experimental inclusion volume fraction is the contacts number (and not the volume of the elements).

By considering the mentioned results in Fig. III-15, the contacts number approach was chosen later to calculate the inclusions fraction in the periodic homogenisation of DEM models. Regarding the porosity percentage calculation in the DEM models, this approach was used by simply replacing the total number of the inclusion contacts (N^C_{inclu}) with the total number of the deleted contacts during the building procedure of porous material RVEs.

III.4.3. Young's modulus and Poisson's ratio obtained by DEM using PBC confronted with reference values

To quantitatively ensure the validity of the proposed DEM model, the obtained results using the periodic homogenisation have been confronted with the other reference values coming from experimental measurements, analytical approaches and FEM calculations.

III.4.3.1. Stiffer inclusions case: G/A materials

In this section, the results of the simulation of the model material with stiffer inclusions (glass matrix with alumina spherical inclusions G/A) have been investigated. As mentioned before, theoretically, by increasing the inclusion fraction in the RVEs, the results should follow the lower HS bound (HS-) (Brisard *et al.* 2010) (Lakes 1998) (Tucker *et al.* 1999). Therefore, the inclusion fraction in the DEM model RVEs increased as well as in the FEM model and then compared to the experimental reference values. Besides, both DEM and FEM models used RVEs in the FCC arrangement with periodic homogenisation.
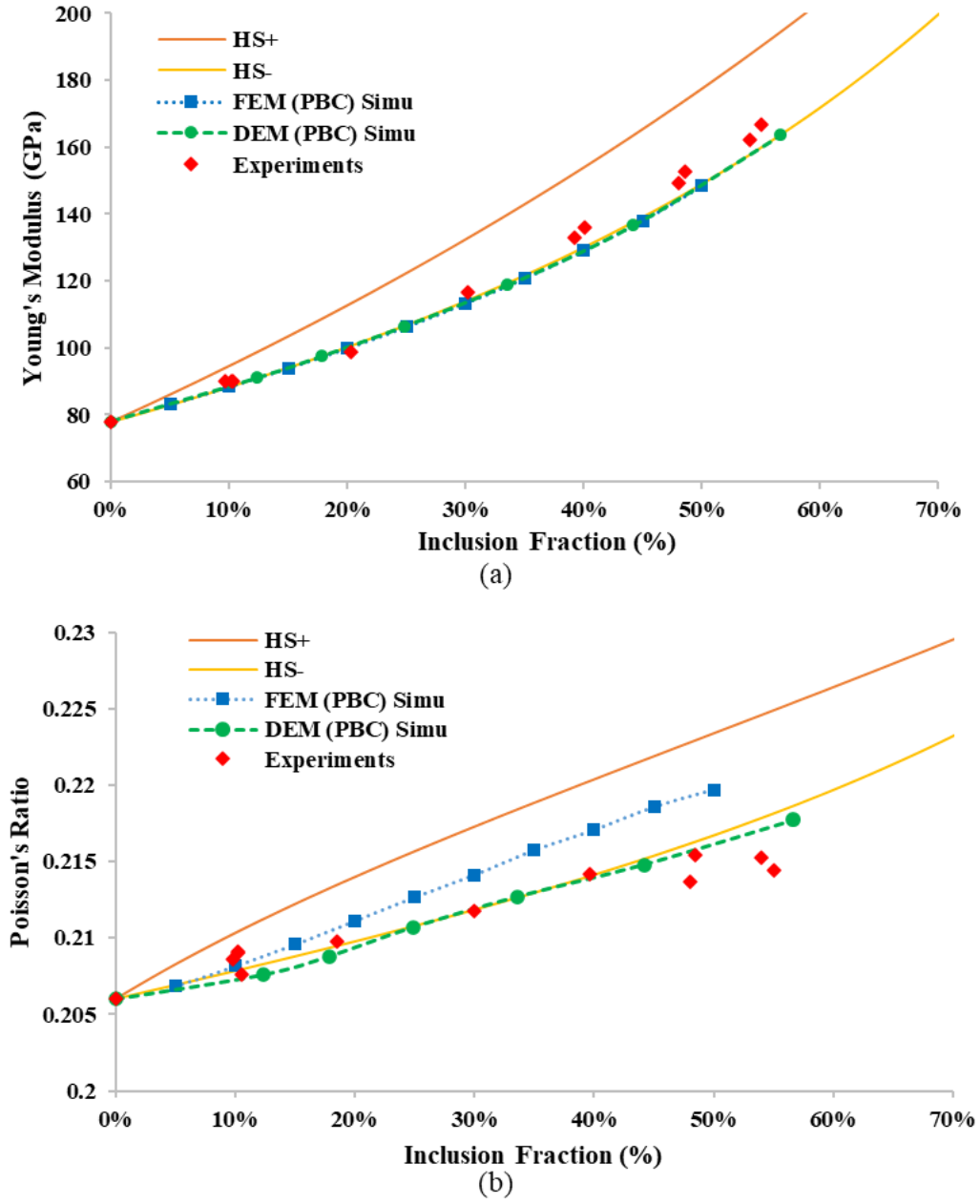
Fig. III-16. DEM periodic homogenisation results
confronted to HS bounds, FEM models and real experimental data:
(a) apparent Young's modulus (E^{ap}) and (b) apparent Poisson's ratio (ν^{ap}).

As it can be seen in Fig. III-16 (a), the DEM simulation using PBC and FEM periodic homogenisation are in perfect accordance with HS lower bound (HS-). Also, the experimental points are following the HS lower bound too, but with a slight tendency to the middle range of HS bounds for the higher inclusion fractions.

Regarding Fig. III-16 (b), although the HS bounds width was small (values between 0.2 and 0.23), the DEM model exhibits better accordance with reference HS- bound for predicting the apparent Poisson's ratio, which is more coherent with the experimental results as well.

A summary of the relative deviation of DEM using PBC, DEM using FBC, and FEM using PBC from HS- is shown in Table III-4.

Table III-4. Summary of the relative deviations from HS- reference bound
for DEM using PBC, DEM using FBC and FEM using PBC

Method	Deviation of apparent Young's modulus from HS-			Deviation of apparent Poisson's ratio from HS-		
	Minimum	Maximum	Average	Minimum	Maximum	Average
FEM PBC	0.03%	0.91%	0.55%	0.02%	1.49%	0.88%
DEM PBC	0.00%	0.73%	0.29%	0.00%	0.42%	0.17%
DEM FBC	0.00%	4.91%	1.44%	0.00%	3.01%	1.48%

Considering Table III-4 for both apparent elastic parameters, the DEM model shows a smaller deviation compared to the FEM model, either mean or maximum values, especially for modelling the apparent Poisson's ratio. These results highlight the potential of DEM for solving multiscale problems by using periodic homogenisation.

III.4.3.2. Porous case: G/P materials

In this section, the effect of porosity has been studied (glass matrix with spherical pores G/P). In this case, as mentioned in section III.4.1.2, the HS upper bound (HS+) will be the analytical reference for the porous material G/P, whereas HS lower bound (HS-) is zero (Pabst *et al.* 2004) (Joliff *et al.* 2007) (Živcová *et al.* 2009).
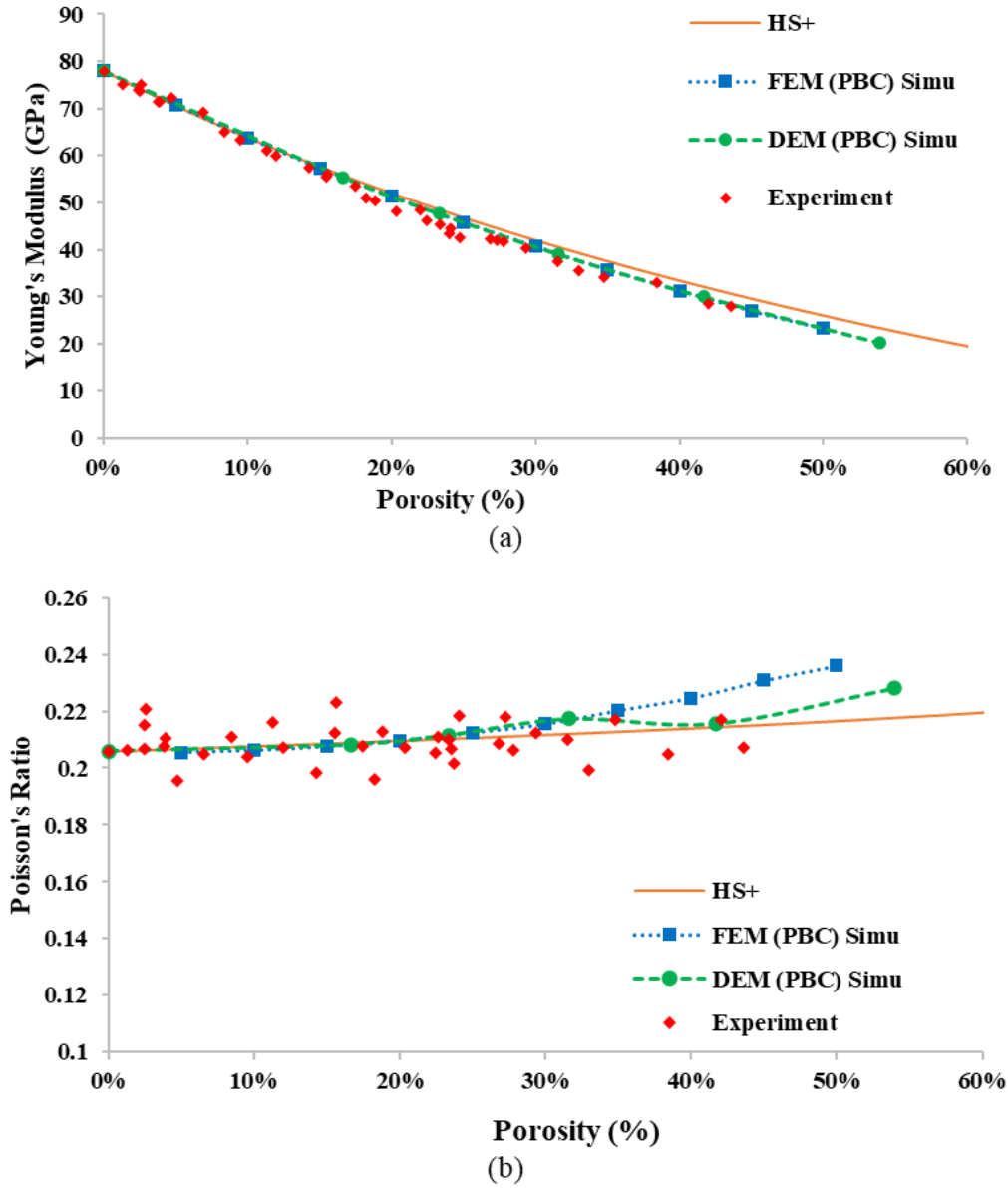
Fig. III-17. DEM periodic homogenisation results
confronted to HS bounds, FEM models and real experimental data:
(a) apparent Young's modulus (E^{ap}) and (b) apparent Poisson's ratio (v^{ap}).

As shown in Fig. III-17 (a), both DEM and FEM periodic homogenisations are in perfect accordance with the lower inclusion fraction values (up to 30%). It exhibits an increasingly small difference for higher values. On the other hand, both simulation results match with the tendency of the experimental values considering the discrepancy of measurements.

In Fig. III-17 (b), the DEM model shows better accordance with HS upper bound (HS+) globally compared to the FEM model for apparent Poisson's ratio, which confirms the results of the previous section. However, both models started to deviate from HS+ for high porosities (above 35% for FEM and above 45% for DEM). Despite the discrepancy

of the experimental measurements (fluctuating in the range of 0.19 to 0.22 around the HS+) and the slight deviation for high porosity, both FEM and DEM exhibit good accordance with experimental results. A summary of the relative deviation of DEM using PBC, DEM using FBC, and FEM using PBC from HS+ is shown in Table III-5.

Table III-5. Summary of the relative deviations from HS+ reference bound
for DEM using PBC, DEM using FBC and FEM using PBC

Method	Deviation of apparent Young's modulus from HS+			Deviation of apparent Poisson's ratio from HS+		
	Minimum	Maximum	Average	Minimum	Maximum	Average
FEM PBC	0.00%	11.23%	3.99%	0.05%	15.85%	6.06%
DEM PBC	0.00%	13.88%	4.54%	0.00%	12.05%	4.87%
DEM FBC	0.00%	17.25%	5.84%	0.00%	43.64%	24.06%

Simulation of the porous media by using DEM periodic homogenisation results shows matching values with FEM simulations and experimental results. Hence, even if FEM modelling is well-known to predict elastic properties of porous materials (Pabst *et al.* 2018), the DEM modelling with PBC can also be used to predict accurately such homogenised elastic properties. To verify further the proposed DEM approach, the stiffness tensors calculation will be discussed in the following section.

III.4.4. Stiffness tensors investigations

In this section, the apparent stiffness tensors given by DEM RVEs is investigated. As a first step, the potential anisotropy of the equivalent modelled media is discussed. To do so, the DEM model stiffness tensors were calculated by cubic and orthotropic symmetry assumptions (see section III.3.7). Then, the stiffness tensors obtained by DEM are compared to the reference values coming from the HS relationships and the FEM model. To be able to compare the values, the inclusion fraction of 50% for the RVEs was chosen as the comparison reference for all the cases.

III.4.4.1. Stiffness tensors obtained by cubic and orthotropic symmetry assumptions

As previously explained for calculating the RVEs stiffness tensor in the DEM model, two different approaches were used: calculating the RVEs stiffness tensors by cubic symmetry assumption from Eq. III-10 and orthotropic symmetry assumption from Eq. III-11. A comparison was made between these two assumptions to reveal any potential influence of the random spatial positioning of discrete elements in RVEs, which could lead to a certain level of mechanical anisotropy coming from this asymmetry. The numerical steps for calculating the stiffness tensors in DEM by using PBC and distortion

of the boundaries have been explained in section III.3.7. The resulting stiffness tensors are given below:

$$
C_{ij} = \begin{pmatrix}
168.8 & 46.6 & 46.6 & 0 & 0 & 0 \\
 & 168.8 & 46.6 & 0 & 0 & 0 \\
 & & 168.8 & 0 & 0 & 0 \\
 & Sym & & 65.5 & 0 & 0 \\
 & & & 0 & 65.5 & 0 \\
 & & & 0 & 0 & 65.5
\end{pmatrix}
\qquad
C_{ij} = \begin{pmatrix}
168.7 & 46.6 & 46.3 & 0 & 0 & 0 \\
 & 168.5 & 46.3 & 0 & 0 & 0 \\
 & & 168.4 & 0 & 0 & 0 \\
 & Sym & & 65.5 & 0 & 0 \\
 & & & 0 & 65.4 & 0 \\
 & & & 0 & 0 & 65.7
\end{pmatrix}
$$

(a)   (b)

Fig. III-18. Stiffness tensors for DEM model in the case of the G/A with 50% inclusion:
(a) cubic symmetry assumption, (b) orthotropic symmetry assumption.

In order to compare these two stiffness tensors, the HS- reference will be used. By knowing the elastic properties of the constituents, the HS- bound elastic properties can be calculated. Finally, from these properties and considering an isotropic assumption, the stiffness tensor for the reference HS- is obtained as bellow:

$$
C_{ij} = \begin{pmatrix}
169.5 & 46.9 & 46.9 & 0 & 0 & 0 \\
 & 169.5 & 46.9 & 0 & 0 & 0 \\
 & & 169.5 & 0 & 0 & 0 \\
 & Sym & & 61.3 & 0 & 0 \\
 & & & 0 & 61.3 & 0 \\
 & & & 0 & 0 & 61.3
\end{pmatrix}
$$

Fig. III-19. Stiffness tensors for the G/A model bi-phase material with 50% inclusion calculated for the reference HS-.

Afterwards, to compare to the reference HS-, the differences of C_{ij} matrices for the DEM using cubic and orthotropic assumptions with the reference tensor have been calculated:

$$
\Delta C_{ij} = \begin{pmatrix}
-0.7 & -0.3 & -0.3 & 0 & 0 & 0 \\
 & -0.7 & -0.3 & 0 & 0 & 0 \\
 & & -0.7 & 0 & 0 & 0 \\
 & Sym & & 4.2 & 0 & 0 \\
 & & & 0 & 4.2 & 0 \\
 & & & 0 & 0 & 4.2
\end{pmatrix}
\qquad
\Delta C_{ij} = \begin{pmatrix}
-0.8 & -0.3 & -0.3 & 0 & 0 & 0 \\
 & -1 & -0.3 & 0 & 0 & 0 \\
 & & -1.1 & 0 & 0 & 0 \\
 & Sym & & 4.2 & 0 & 0 \\
 & & & 0 & 4.1 & 0 \\
 & & & 0 & 0 & 4.4
\end{pmatrix}
$$

(a)   (b)

Fig. III-20. Differences matrices to HS- bound for DEM model:
(a) cubic symmetry assumption (b) orthotropic symmetry assumption.

Considering different approaches in the DEM model for calculating the stiffness tensors, as shown in Fig. III-20 (a) and (b), the obtained stiffness tensors for both assumptions are in accordance. The errors between cubic symmetry tensors and the orthotropic tensors for:

- the main diagonal elements C_{11}, C_{22}, C_{33}, was less than 0.2%,
- the main diagonal elements C_{44}, C_{55}, C_{66}, was less than 0.5% and
- the off-diagonal elements C_{12}, C_{13}, C_{23}, was less than 0.6%.

These results show that the random spatial positioning of discrete elements in RVEs had a minimal impact on the anisotropy of the RVE, even with a relatively low number

of DEs for RVEs. It showed the sufficiency of 20k DEs for RVEs in the PBC, and yet validating the efficiency of using periodic homogenisation in DEM, for saving calculation time and resources.

III.4.4.2. Stiffness tensors obtained by DEM using PBC confronted with reference values

Here, the obtained values for the stiffness tensor of the DEM model is compared to the reference values coming from the HS- bound (in Fig. III-19) and FEM numerical model. The obtained stiffness tensors results are shown below:

$$
C_{ij} = \begin{pmatrix}
168.8 & 46.6 & 46.6 & 0 & 0 & 0 \\
 & 168.8 & 46.6 & 0 & 0 & 0 \\
 & & 168.8 & 0 & 0 & 0 \\
 & Sym & & 65.5 & 0 & 0 \\
 & & & 0 & 65.5 & 0 \\
 & & & 0 & 0 & 65.5
\end{pmatrix}
\qquad
C_{ij} = \begin{pmatrix}
169.3 & 47.7 & 47.7 & 0 & 0 & 0 \\
 & 169.3 & 47.7 & 0 & 0 & 0 \\
 & & 169.3 & 0 & 0 & 0 \\
 & Sym & & 63.5 & 0 & 0 \\
 & & & 0 & 63.5 & 0 \\
 & & & 0 & 0 & 63.5
\end{pmatrix}
$$

(a)   (b)

Fig. III-21. Stiffness tensors for the G/A model bi-phase material with 50% inclusion calculated for (a) the DEM model, (b) the FEM model.
FEM results from (R. Grasset-Bourdel *et al.* 2011)

Considering the stiffness tensors obtained by DEM (Fig. III-21 (a)) and FEM (Fig. III-21 (b)) and comparing these values with HS- reference, both numerical methods are having good accordance with HS-.

For the first three diagonal components (C_{11}, C_{22}, C_{33}), DEM and FEM models had excellent accordance with HS-, by having 0.4% and 0.1% of errors, respectively. For the last three diagonal components (C_{44}, C_{55}, C_{66}), the FEM model showed a better agreement with HS- compared to the DEM model by having 3.6% error while the DEM model error was 6.8%. Finally, the three off-diagonal components (C_{12}, C_{13}, C_{23}) in the DEM model showed better accordance with HS- by having 0.6% error while the FEM model has 1.7% error.

Overall, the material stiffness tensor matrix, obtained by the DEM model and using PBC, showed excellent accordance with HS- values and the FEM model. It verifies the accuracy and efficiency of DEM models with periodic homogenisation to predict the elastic properties and stiffness coefficients of bi-phase material.

III.5. Conclusions

In this chapter, the elastic properties of a model bi-phase and a porous material were accurately simulated by using a DEM numerical approach combined with a periodic homogenisation method. In fact, the homogenisation technique is usually a key point for multiscale modelling and reducing calculation times. Well-known in FEM, this approach is much less developed in DEM for continuum media. The proposed method and the associated algorithm procedures constitute a promising route for a better understanding

of the thermomechanical behaviour of heterogeneous materials. The first results presented here, only about elastic behaviour in non-damaged materials, validate the DEM efficiency and demonstrate its accuracy for homogenisation and up-scaling problems for bi-phase and porous materials. Also, this study highlights the importance of using periodic boundaries instead of free boundary conditions.

The DEM periodic homogenisation simulation outputs, which were used to predict and to scale up the elastic behaviour of bi-phase and porous materials, were compared and were validated thanks to excellent accordance with experimental results as well as other predictive analytical and numerical methods:

I.   Experimental results: regarding the elastic behaviour of real model material with Alumina inclusions, the DEM simulations exhibit very good accordance with both Young's modulus and Poisson's ratio values versus the different percentage of inclusions. In the case of the elastic behaviour of real porous model material, the DEM simulations also exhibit very good accordance with Young's modulus values versus porosity. About Poisson's ratio, although the experimental results were a bit scattered, the DEM predictions were still in acceptable accordance with experimental values.

II.   Hashin and Shtrikman bounds: for both the DEM models, either the bi-phase material with Alumina inclusions and the porous model, Young's modulus and Poisson's ratio values exhibit excellent accordance with the HS bounds (HS- in the case of alumina inclusions and HS+ in the case of porous materials). This confirms the results of other related studies about the elastic behaviour of bi-phase materials with stiff inclusions in a soft matrix (Brisard *et al.* 2010) (Lakes 1998) (Tucker *et al.* 1999) and porous materials (Zerhouni *et al.* 2019).

III. FEM simulation: comparison between FEM and DEM for simulating the same bi-phase and porous materials demonstrates that the DEM approach leads to closer predictions for the elastic properties (considering both experimental and analytical values as reference) in comparison to the FEM simulations. It was especially the case for Poisson's ratio in bi-phase and porous materials. In fact, in this case, the DEM approach seems to exhibit better accordance with the HS lower bound.

Later, the stiffness tensor of each analytical (calculated from HS- values), FEM, and DEM methods were calculated and compared. It appears that DEM and FEM results exhibit an acceptable agreement with the stiffness tensor calculated from analytical HS- values. However, the FEM model showed a bit better accuracy in predicting the shear stiffness than the DEM model. At this stage, the reason for the better prediction of FEM in the shear stiffness requires further dedicated studies.

The main limitation of the present study was the time-consuming trial-and-error process for calibrating the DEM input parameters to reproduce the apparent properties of real materials. Nevertheless, this well-known drawback in DEM could be later overcome by an automated calibration process, for example, using a machine learning approach.

Overall, the proposed DEM approach, combined with periodic homogenisation technique, leads to valid elastic properties determination for bi-phase and porous materials. These key results open very interesting new ways to use DEM to predict the thermomechanical behaviour of heterogeneous materials containing numerous microcracks that could propagate simultaneously. In fact, the fracturing process and

microcracking simulations are among the key interests of using DEM in such a case compared to FEM. Therefore, the next chapter will be focused on the simulation of simultaneous microcracking in a continuum media that could be induced by thermal expansion mismatch between constituents.

Chapter IV: Modelling the non-linear behaviour of materials under tensile loadings by Weibull distribution of strength at the mesoscale

IV.1. Introduction

As mentioned in section I.1, refractory ceramics are regularly subjected to thermal shocks and cycles. For example, during the steelmaking process, due to the filling and emptying of melted iron in the steel ladle, refractories are facing severe thermal cycles. Therefore, these refractories should be resistant to such thermal loadings. Experimentally, it is observed that pre-existing microcracks significantly impact this thermal shock resistance of refractories (as discussed in section I.1). However, the presence of these microcracks will induce a non-linear quasi-brittle mechanical behaviour (see section I.1.5). Therefore, this chapter aims to use the Discrete Element Method (DEM) to simulate such fracture mechanisms to reproduce this quasi-brittle behaviour. In fact, fracture propagation requires a large number of discontinuities, and the Finite Element Method (FEM) is not easily capable of managing this kind of microstructural effects (as discussed in section I.3.3). As mentioned in section I.3, using DEM to model fracture mechanisms in a pseudo-continuum media, especially in the ceramics field, is a new and promising approach under active development. Here again, the Flat Joint DEM Contact Model (FJM) is used (see section II.4).

Even if PFC with FJM is well-adapted to account for multiple crack propagation within a quasi-brittle material, unfortunately, up to now, this model is not able to account for mechanical interactions and temperature variation simultaneously. This current limitation is a significant drawback to model refractory materials, which contain initial defects coming from CTE mismatch between constituents during the cooling stage after sintering. In fact, internal development within ITASCA is ongoing to account for mechanical interactions and temperature variation simultaneously and will be available soon. Considering this perspective and the fact that FJM has a high potential in simulating the fracturing process of quasi-brittle materials, it could nevertheless be a valuable approach in the near future. To overcome this temporary drawback, the present study investigated the randomisation of local fracture criteria within the virtual sample using a Weibull distribution (as explained in section I.2.4.1). The key idea is here to verify if the non-linear mechanical behaviour of a continuum media can be reproduced by initial well-distributed damages with a strength dispersion following a Weibull distribution. This approach could allow studying the effect of pre-existing microcracks on the non-linear quasi-brittle behaviour of a numerical sample under uniaxial and cyclic tensile tests. Ultimately, this introduced approach will lead to a qualitative and quantitative DEM model to simulate the non-linear quasi-brittle of refractory materials.

In this chapter, prior to focus on the numerical aspect, the reference material of this chapter, Alumina Spinel, and the technics to monitor its microcracking during the thermal cycles will be presented. Afterwards, the numerical foundation for this study will be introduced. At first, a reminder about the calibration of the FJM input parameter for perfect linear elastic brittle material will be done. This calibration process leads to a perfect brittle linear behaviour which will be compared to the real experimental uniaxial test of Alumina Spinel. Later, a randomisation process of bond strengths will be introduced following Weibull distributions. Then, the influence of this randomisation process on the apparent mechanical behaviour and microcracking will be studied. Finally,

a quantitative DEM numerical approach will be proposed to model the non-linear quasi-brittle behaviour.

IV.2. Description of the reference material and monitoring the microcracking process

The chosen reference material for this study is an Alumina Spinel brick because it promotes a strong non-linear quasi-brittle behaviour which suits the overall goal of this chapter. This particular material is commonly used in the working lining of steel ladle (a very central point of the overall ATHOR project). The purpose of this short section is to illustrate (by a couple of key experimental results) where the microcracks (which constitute the central point of the present study) come from and how these microcracks lead to non-linear quasi-brittle behaviour.

Kaczmarek *et al.* has investigated this material, and the experimental data of this material is taken from (Kaczmarek *et al.* 2019). This Alumina Spinel brick is composed of tabular Alumina grains (up to ~3 mm), Alumina Spinel matrix and 19.7 % of porosity. A typical microstructure of this Alumina Spinel is shown in Fig. IV-1.
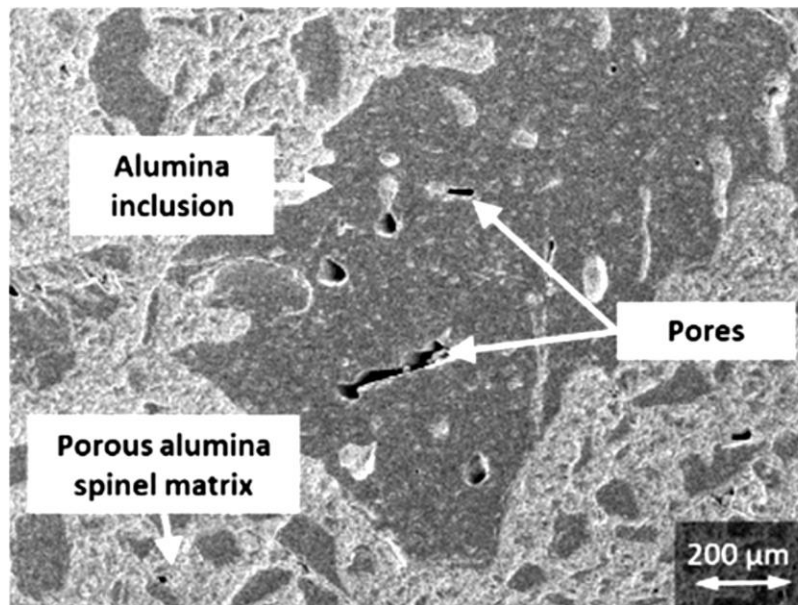
Fig. IV-1. SEM image of Alumina Spinel microstructure (Kaczmarek *et al.* 2019)

The influence of the microcracking process on the elastic properties can be examined by using the ultrasonic method and acoustic emission. The ultrasonic method was used to detected and record the evolution of Young's modulus versus temperature. This low-frequency method uses a long bar configuration to perform measurements at high temperature. This method has high precision in measuring the impact of microcrack on the macroscopic elastic properties.

The acoustic emission method records and analyses acoustic waves coming from the sample. An acoustic emission event is the result of the propagation of an elastic wave coming from a localised source within the sample. Each event is counted, which finally

lead to present the results as accumulative numbers of events versus temperature (Khlifi 2019).

Linking the ultrasonic measurements and acoustic emission events could help to have a better overview of the relationships between elastic properties and microcracking process. In this way, Young's modulus and acoustic events evolutions of the referenced Alumina Spinel is plotted in Fig. IV-2 versus temperature. Just focusing on the cooling part of this curve, Young's modulus increases from 1500°C to 700°C (rather normal evolution for most materials) and then decreases from 700°C to ambient temperature (quite abnormal behaviour). In fact, this decrease is due to microcrack initiation and propagation resulting from CTE mismatch between constituents (as discussed in section I.1.2), which lead to simultaneous acoustic emission (increase in acoustic events).
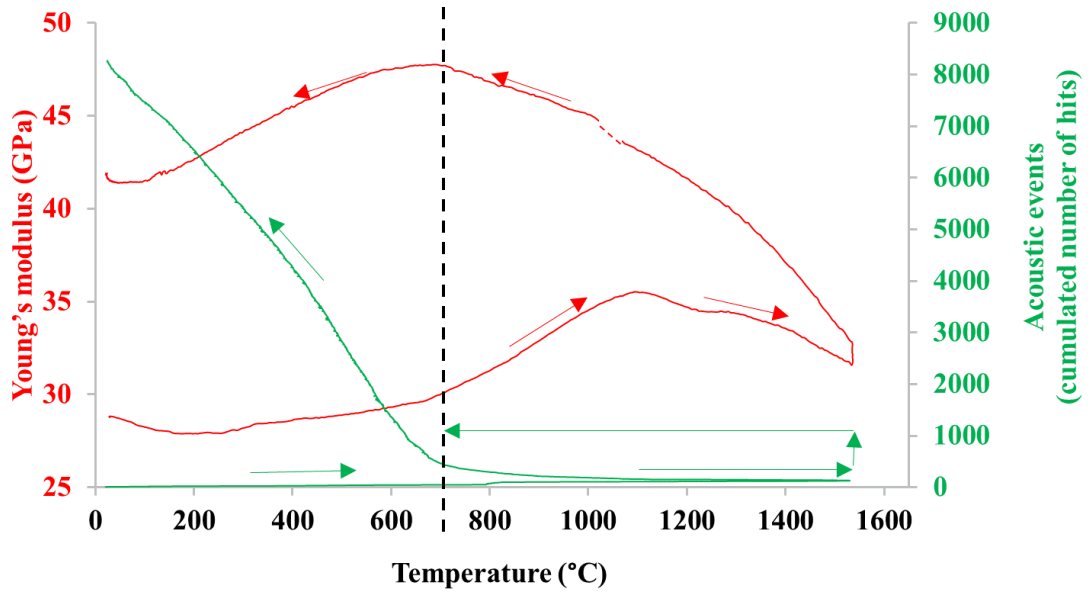
Fig. IV-2. Young's modulus and acoustic events evolutions during thermal treatment (Kaczmarek *et al.* 2019)

Now, to focus on the mechanical behaviour of Alumina Spinel, a uniaxial tensile test was performed to characterise this material at ambient temperature. Fig. IV-3 is showing Alumina Spinel brick experimental results during incremental cyclic loadings.
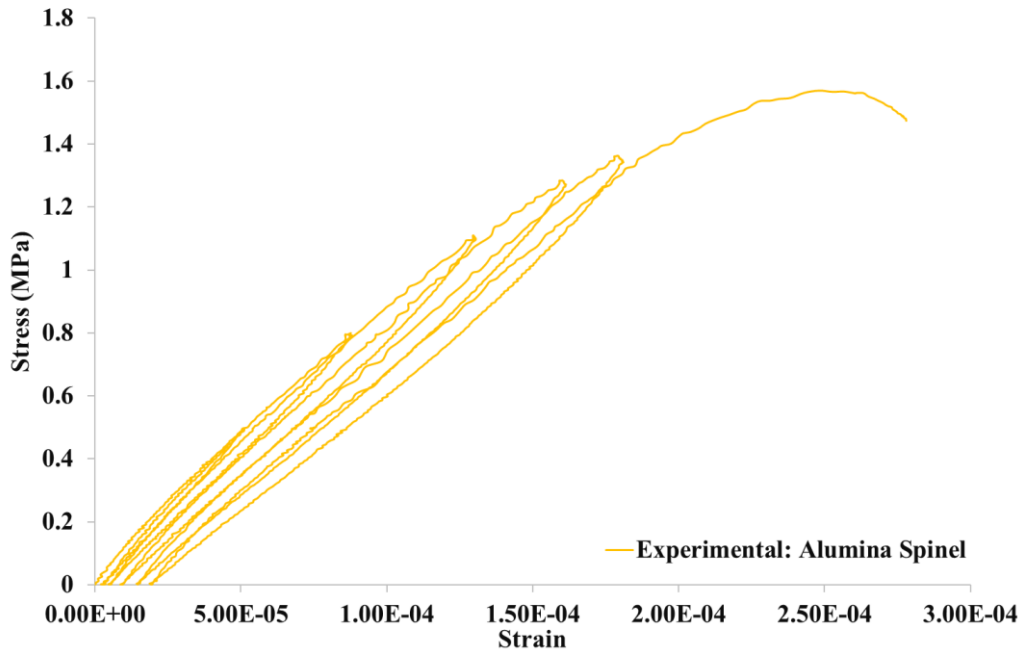
Fig. IV-3. Experimental stress-strain behaviour during incremental cyclic loadings of Alumina Spinel (Kaczmarek *et al.* 2019)

Considering Fig. IV-3, the Alumina Spinel brick is showing:

    a.   a progressive decrease of its rigidity after each cycle;
    b.   a hysteresis loop between each unloading and reloading;
    c.   a residual strain after each unloading.

In order to model this experimental behaviour accurately, a calibration process for simulating non-linear quasi-brittle behaviour should be defined. In the following section, such a quantitative calibration process will be proposed.

IV.3. Numerical approach for simulating non-linear quasi-brittle behaviour with DEM

In this section, the numerical basis required for simulating non-linear behaviour using Weibull distribution with DEM will be introduced. At first, the calibration of the FJM input parameters for a perfect linear elastic brittle material will be reminded. Then, the apparent behaviour given by this calibration process will be compared to the experimental uniaxial test of Alumina Spinel. Later, a randomisation process of bond strengths will be introduced following Weibull distributions. Then, the influence of this randomisation process on the apparent mechanical behaviour and microcracking will be studied.

IV.3.1. A reminder to the calibration process for perfect brittle linear elastic material

As a brief reminder to section II.4, the FJM requires a calibration process to assign the correct values for the local properties in order to reproduce the desired apparent perfect linear elastic properties. It should be highlighted that in this chapter, contrary to the previous chapter, the calibration process was done in a Free Boundary Conditions (FBC), without considering the periodic homogenisation. The reason is that this simulation is dealing here with mesoscale, corresponding to the scale of the real experimental sample without considering the real heterogeneous microstructure (which will be, in fact, later introduced by Weibull distribution of local bond strengths). Therefore, here, in addition to the elastic properties of the material, the apparent non-linear behaviour will be investigated as well, thanks to the implementation of Weibull statistical distribution.

In this way, the local fracture parameters (local tensile strength t^{loc} and local cohesion c^{loc}, see section II.4.2) were considered for this model. Then, the proposed calibration algorithm in section II.4.4 (in Fig. II-14) were used to calibrate the apparent parameters. Regarding t^{loc} value, it will be calibrated by trial and error process (step 4 in Fig. II-14) and c^{loc} value will be set proportionally to t^{loc}, around 5 times higher. Note that, as mentioned previously, the present PhD is dedicated to refractory materials, which are well-known to be more sensitive to tensile fracturing in mode I. Thus, this study is focusing on the behaviour of materials in tensile tests. In this way, almost all of the fracturing process will happen in mode I, governed by t^{loc} and making the influence of c^{loc} negligible.

It is important to highlight that the proposed calibration algorithm in section II.4.4 was for perfect brittle linear elastic materials. Therefore, in the case of Alumina Spinel (which is a quasi-brittle material), these calibration steps were used for the initial linear part of the tensile behaviour of the material, which is measured at the very beginning of the stress-strain curve (Fig. IV-3).

In this chapter, the calibration process was managed on a $10 \times 10 \times 10$ cm^3 cubic sample consisting of around 14k discrete elements (with the radius range of 2 mm to 3 mm) in a non-periodic boundary condition. Fig. IV-4 shows the virtual sample prepared for the calibration process in a displacement-driven uniaxial tensile test.
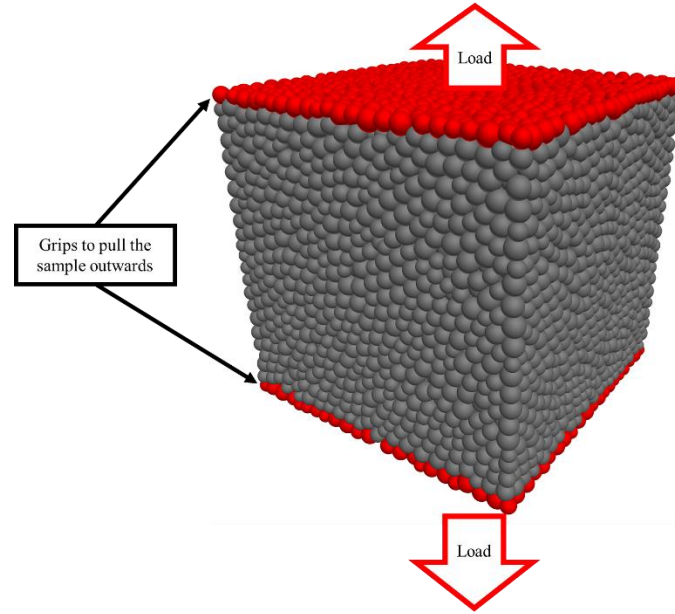
Fig. IV-4. Uniaxial tensile test configuration: the top and bottom discrete element group (in red) move in opposite vertical directions.

The FJM local parameters calibrated in order to fit the targeted Alumina Spinel initial linear properties are presented in Table IV-1. After calibrating the initial linear properties of Alumina Spinel, a uniaxial tensile test simulation was done and discussed in the next section.

Table IV-1. Summary of Alumina Spinel initial linear properties, FJM input parameters coming from calibration and simulated apparent properties

Targeted experimental material property		FJM input parameter		Simulated apparent material property	
Description	Value	Description	Value	Description	Value
Young's modulus	10.37 GPa	local Young's modulus (E^{*loc})	7.7 GPa	Apparent Young's modulus (E^{ap})	10.34 GPa
Poisson's ratio	0.17	local stiffness ratio (K^{*loc})	4	Apparent Poisson's ratio (v^{ap})	0.16
Uniaxial tensile strength	1.57 MPa	local bond tensile strength (t^{loc})	1.33 MPa	Apparent tensile strength (t^{ap})	1.58 MPa
Reproduce symmetrical elastic behaviour in tension and compression	-	Initial gap (g_i^{loc})	40% of the ball radius	Reproduce symmetrical elastic behaviour in tension and compression	Achieved

IV.3.2. Uniaxial tensile test simulation with non-randomised (uniform) strength of bonds

As described in the previous section, the calibration algorithm for a perfect brittle linear elastic material was used in order to achieve apparent Young's modulus (E^{ap}), apparent Poisson's ratio (v^{ap}) and apparent direct tensile strength (t^{ap}) of the material. It should be emphasised that at this stage, the t^{loc} has a uniform value of 1.33 MPa for all FJM bonds. Then, by using these FJM input parameters, a uniaxial tensile test was simulated and compared to the experimental Alumina Spinel results in Fig. IV-5.
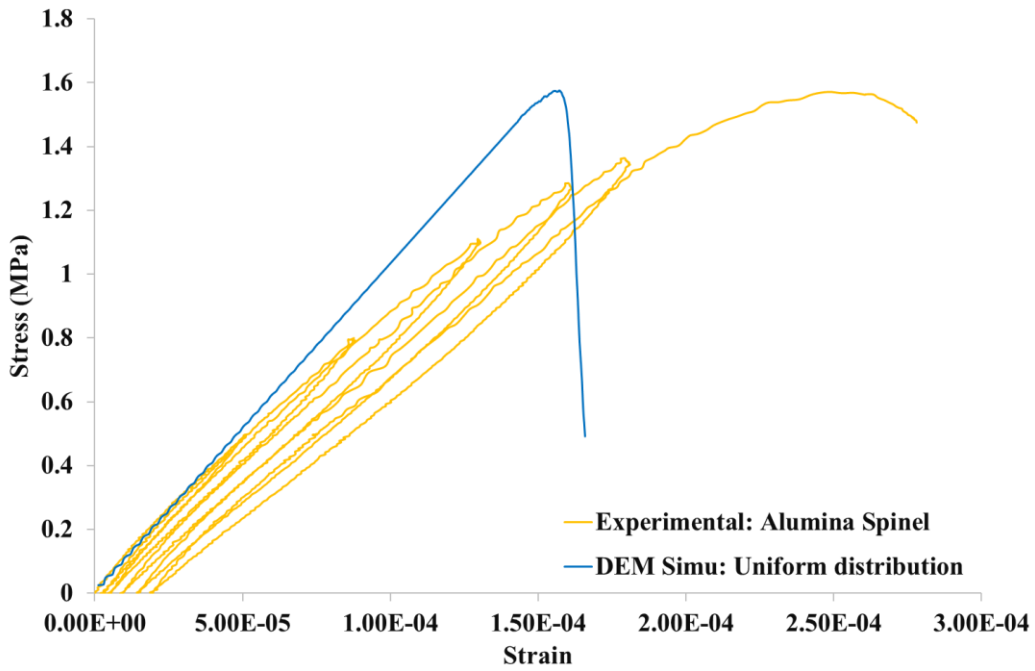
Fig. IV-5. Uniaxial tensile tests: preliminary perfect brittle linear elastic calibration result vs experimental results on Alumina Spinel brick.

As shown in Fig. IV-5, this preliminary calibration step leads to a perfectly brittle elastic behaviour that successfully targets the right value of the macroscopic failure strength (1.58 MPa). At the very beginning of the stress-strain curve, the simulated curve tangent the experimental one, which means that the initial Young's modulus value was successfully calibrated. On the other hand, the simulation is not showing any quasi-brittle behaviour, as expected, since no parameter was introduced into the model for that purpose. At this stage, the simulation simply exhibits an abrupt failure that is not in line with the real material behaviour. Therefore, it is necessary to introduce the Weibull distribution in order to model such non-linear behaviour quantitatively. In the following parts, a dedicated quantitative calibration procedure will be proposed and explained step by step.

IV.3.3. Introduction of a Weibull distribution within bond strengths

As a reminder of section I.2.4, by using Weibull distribution, the probability of failure for a solid material under a tensile load $P_f(\sigma)$ is given as (Weibull 1951):

$$P_f(\sigma) = 1 - e^{-\left(\frac{\sigma}{\sigma_0}\right)^m} \qquad \text{Eq. IV-1}$$

where σ, m and σ_0 are the tensile stress (MPa), the Weibull modulus, and the scaling parameter, respectively.

The Weibull statistical distribution is commonly used as a macroscopic concept to describe the occurrence of random defects within a 3D solid sample, which could cause a variation in the macroscopic tensile strength of different specimens for a given material. As a material parameter, the Weibull modulus (m) could be experimentally obtained from different mechanical tests (such as uniaxial tensile test or 3-point bending test) conducted on the same sample geometries.

In the present study, this concept is used in the context of refractory ceramics under tension by varying the local bond tensile strength (t^{loc}) of the Flat Joint contact Model (as described in section II.4). Hence, it is proposed to reproduce the microscopic defects (coming from CTE mismatch during cooling after sintering) within the DEM numerical sample by randomisation of the local bond tensile strength (t^{loc}) values. In such perspective, the Weibull distribution law is chosen here to randomly set t^{loc} values, following Eq. IV-1, where σ corresponds thus to local bond tensile strength values (t^{loc}). Moreover, the scaling parameter σ_0 for these local tensile strengths is set, at this stage, to the t^{loc} value previously determined without any Weibull distribution (corresponding in fact to $m = \infty$ and thus will be noted later as $\sigma^0_{m=\infty} = t^{loc}_{m=\infty}$). In this way, the impact of this local randomisation will be investigated on the macroscopic non-linear behaviour of the Alumina Spinel refractory under tensile loadings. In reality, this non-linear effect comes from defects originated by thermal expansion mismatch between constituents within the microstructure.

IV.3.4. Influence of Weibull distribution on the mechanical behaviour and microcracking process during loading

The impact of applying randomisation on the local bond tensile strength (t^{loc}) is studied on Alumina Spinel brick as the reference material. As mentioned, Alumina Spinel exhibits a quasi-brittle behaviour with an apparent tensile strength of 1.57 MPa, which corresponds to the $t^{loc}_{m=\infty}$ value of 1.33 MPa in the case of a uniform value. It is worth mentioning that this case (a uniform value) corresponds to an *infinite* Weibull modulus ($m = \infty$). This value of 1.33 MPa is used as the scaling parameter ($\sigma^0_{m=\infty}$), in the Weibull equation (Eq. IV-1). It should be noted that, contrary to the normal distribution, the Weibull distribution is not a symmetrical statistical distribution. Hence, the scaling parameter (classically named σ_0) of Weibull distribution does not correspond to the mean value. Indeed, this point is one of the interests of choosing Weibull distribution for this study. Because, by using Weibull distribution, it is possible to distribute much smaller values asymmetrically to the scaling parameter by only decreasing the Weibull modulus.

This point will facilitate establishing a relationship between *m* and the non-linear behaviour in order to calibrate the quasi-brittleness of the referenced Alumina Spinel refractory (see section IV.4.2).

To highlight the impact of Weibull modulus *m* on the behaviour, three different values of *m* were tested: *1.75*, *5* and *infinite*. The Weibull distribution and its relative parameters were introduced to the initial numerical sample using the NumPy[8] Python library. By keeping the scaling parameter constant ($t^{loc}_{m=\infty} = 1.33$ MPa), the t^{loc} distributions for the different considered Weibull modulus (*m = 1.75*, *5* and *infinite*) are shown in the upper part of Fig. IV-6. In addition, the 3D distribution of t^{loc} value within the numerical sample is shown in the lower part of Fig. IV-6.
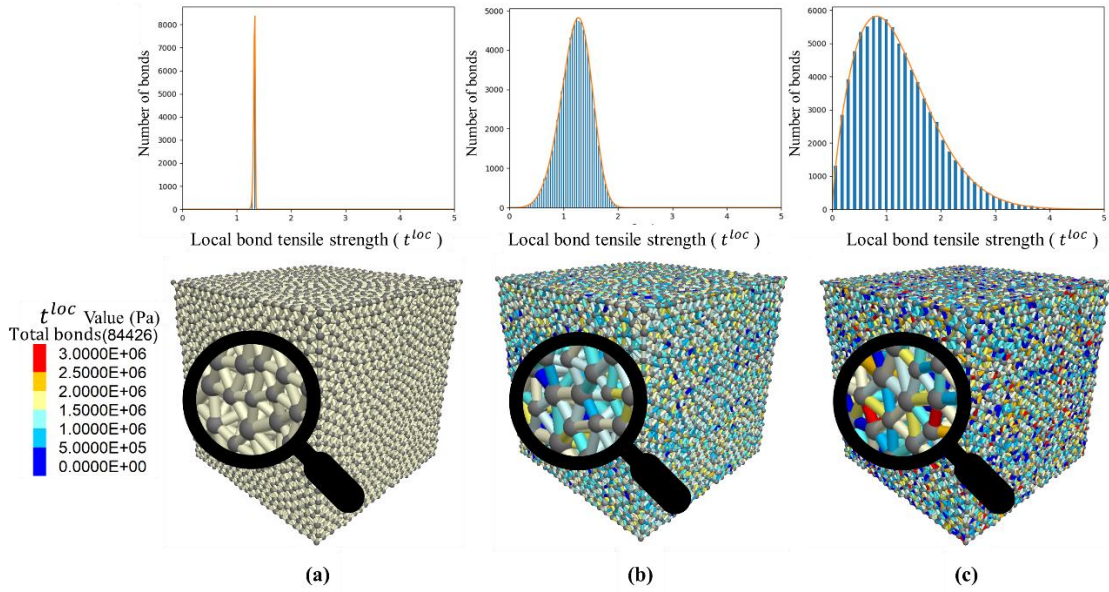
Fig. IV-6. Weibull distribution curves and related 3D distributions
of t^{loc} value within the numerical specimens:
(a) *m = ∞*, (b) *m = 5* and (c) *m = 1.75*.

In order to verify the t^{loc} distribution implemented in the model, they are represented as histograms on the top part of Fig. IV-6. It worth mentioning that these histogram bars are fitting well to the theoretical curve of Weibull distributions which are plotted by solid orange lines.

The bottom part of Fig. IV-6 is showing the distributions of t^{loc} in the 3D samples. The bonds in the sample with a uniform value of 1.33 MPa for the t^{loc} (*m = ∞*) are shown in cream white (a), while the bonds in the sample with low Weibull modulus (*m = 1.75*) are in scaled colours, based on their differences from 1.33 MPa value (c). Case (b) simply corresponds to an intermediate case where *m = 5*.

These samples were submitted to a uniaxial tensile test in order to study the influence of Weibull modulus on the stress-strain curve. The results, which include more cases for Weibull modulus, are shown in Fig. IV-7 (a). This figure shows that using Weibull distribution to randomise t^{loc} had a strong influence on the mechanical behaviour of the

---

[8] https://numpy.org/

numerical samples. Low values of Weibull modulus (m) promotes non-linearity in the behaviour of the sample during tension. During the progressive loading of the samples, the weakened bonds created by the randomisation process breaks earlier than the stronger ones, as expected. These weaker bonds can be considered as micro defects. While decreasing Weibull modulus (m), it increases the number of these micro defects that induces a progressive decrease in the apparent rigidity during loading (non-linear mechanical response). In addition to the stress-strain curves (Fig. IV-7 (a)), the number of detached FJM elements (see section II.4), which is related to microcracks, is shown in Fig. IV-7 (b) for different m values. It highlights that by decreasing m:

   (a)   the microcracking process starts for lower strains;
   (b)   the complete failure is achieved with a higher number of microcracks.

(a)

(b)

Fig. IV-7. Influence of different Weibull modulus values on uniaxial tensile tests:
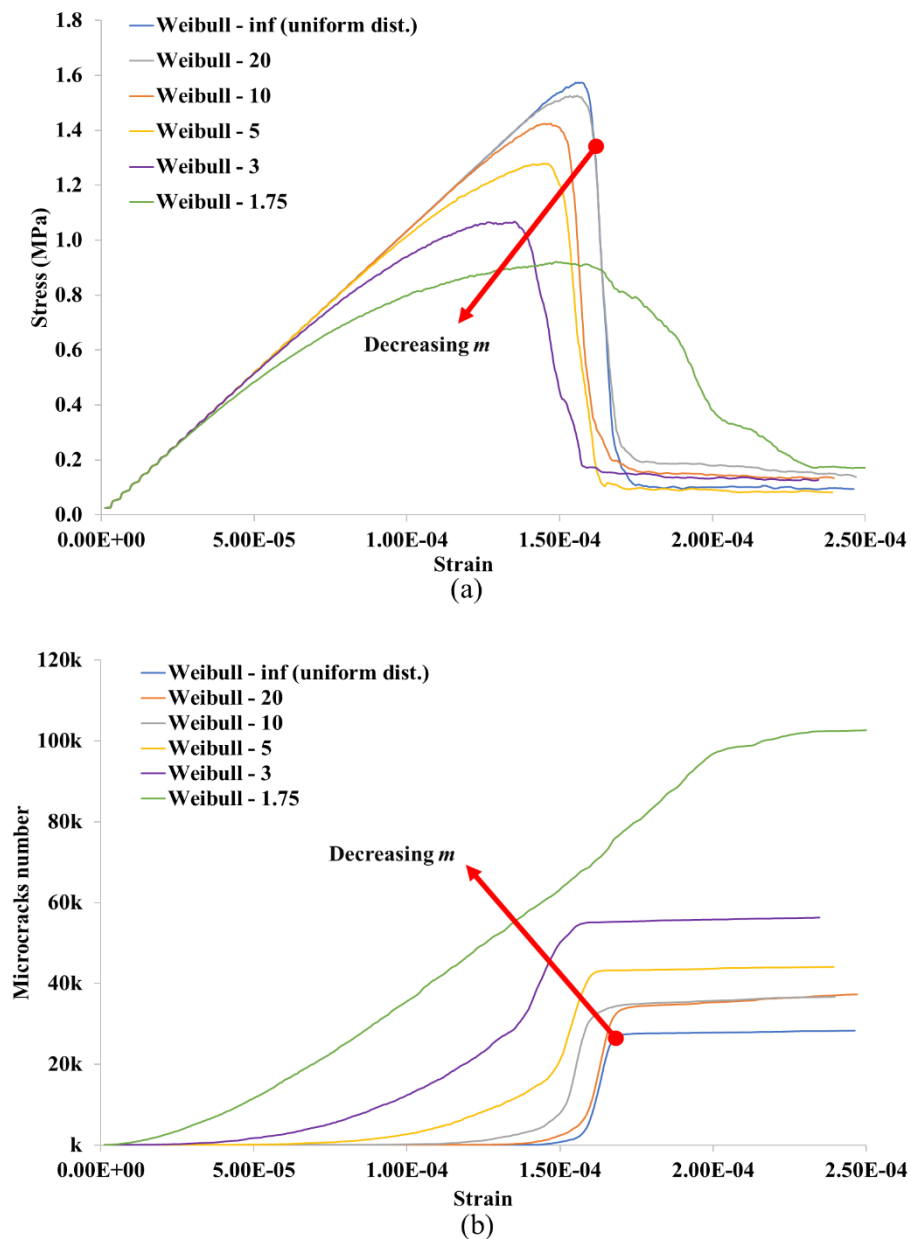(a) stress-strain curves and (b) microcracks number.

It could be noticed that a significant change in the apparent mechanical response and in the progression of microcracking can be observed for the lowest m value ($m = 1.75$). Even if no explanation can be given at this stage of the study, it probably indicates that it could be interesting to investigate further this range of low values of Weibull modulus ($m = [0.5, 2]$). This point could be particularly important because the fracture energy (surface below the green curve of $m = 1.75$ in Fig. IV-7 (a)) seems to become larger.

Fig. IV-8 shows the position of microcracks within the numerical sample during these direct tensile tests for three different Weibull moduli ($m = \infty$, 5 and 1.75) at the same loading state corresponding to 40% of maximal stress after each peak (post-peak region). Note that for plotting these figures, the complete detachment of an FJM contact is considered as one microcrack (shown in yellow). It means that all the 16 FJM sub-surface elements have been broken (as explained in section II.4). On these figures, the red dashed areas show the macroscopic failures which come from the localisation of diffuse microcracks. The sample with a uniform value of 1.33 MPa for the t^{loc} distribution (where $m = \infty$, (a)) is showing a single fracture, which leads to an abrupt failure of the sample. While, the sample with low Weibull modulus ($m = 1.75$, (c)) is showing diffuse microcracking, which result in a quasi-brittle behaviour. Hence, lowering the Weibull modulus (m) promotes non-linear mechanical behaviour by increasing the occurrence of diffuse microcracks.

(a)   **(b)**   **(c)**
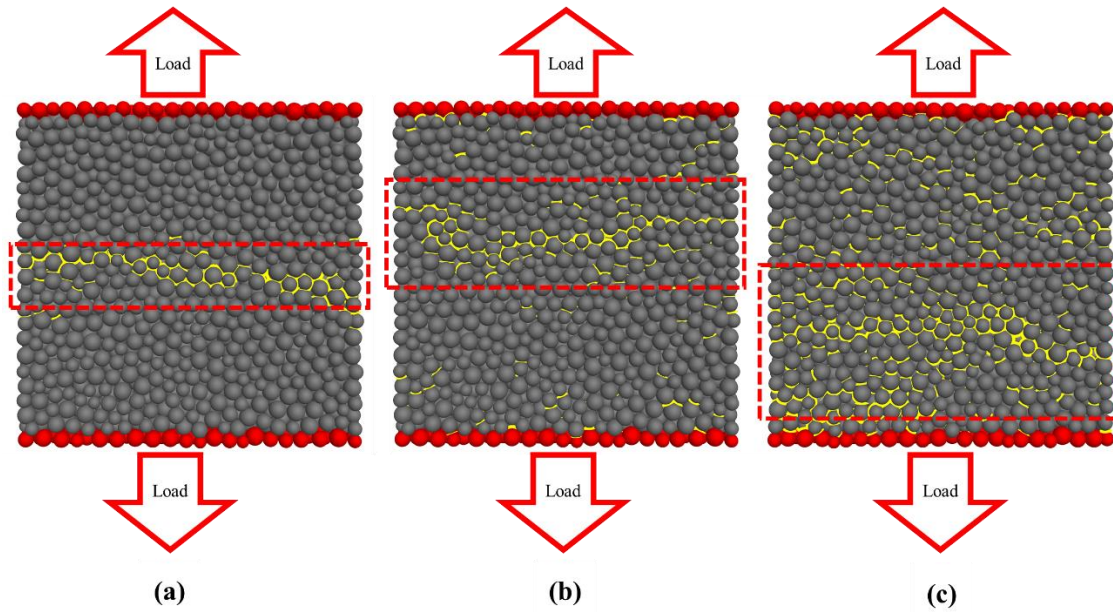
Fig. IV-8. FJM cracks in uniaxial tensile tests for different Weibull modulus:
(a) $m = \infty$ (uniform value), (b) $m = 5$ and (c) $m = 1.75$.

This fracturing process is quite similar to the phenomena that explain the quasi-brittle behaviour of certain refractory materials (Khlifi 2019). In addition to the influence on non-linear mechanical behaviour, the Weibull modulus also has a strong influence on the ultimate apparent tensile strength (as shown in Fig. IV-7 (a)). By decreasing m, the ultimate apparent tensile strength decreases. Considering these points, in order to achieve quantitative simulations of the non-linear behaviour of such real material, a robust calibration method is proposed in the next section.

IV.4. Quantitative modelling of non-linear quasi- brittle behaviour

As discussed in the previous section, the proposed numerical technique has shown the ability to qualitatively introduce non-linear behaviour to DEM by using Weibull distribution over the t^{loc} values. Although in literature, the Weibull distribution has been used to model damaged materials (Zhou *et al.* 2020) (Liu *et al.* 2015) (Li *et al.* 2012), there is no well-defined calibration procedure for tensile configuration. In order to achieve quantitative results, a new calibration process for reproducing the non-linear behaviour of refractories is proposed in the following sections.

IV.4.1. Quantifying experimental non-linear behaviour

The first step to calibrate the Alumina Spinel reference material is to quantify its non-linear behaviour. In this regard, the secant modulus (E_s^{ap}) at the peak have been used, which corresponds to the slope between the origin and the stress-strain curve for maximum stress, described as follows:

$$E_s^{ap} = \frac{\sigma_{Peak}}{\varepsilon_{Peak}}$$

Eq. IV-2

where, σ_{Peak} and ε_{Peak} are the stress and strain at the peak of the curve, respectively.

In fact, using the secant modulus for non-linear materials, such as soils, especially under cyclic tests, is common in the field of civil engineering for characterising and predicting the behaviour of such materials (Briaud 2001).

By calculating this secant modulus (E_s^{ap}) and having the initial Young's modulus (E_i^{ap}), which has been measured at the early stages of loading, it is possible to quantify Young's modulus decreasing rate. These two parameters were calculated for Alumina Spinel reference material, as shown in Fig. IV-9.
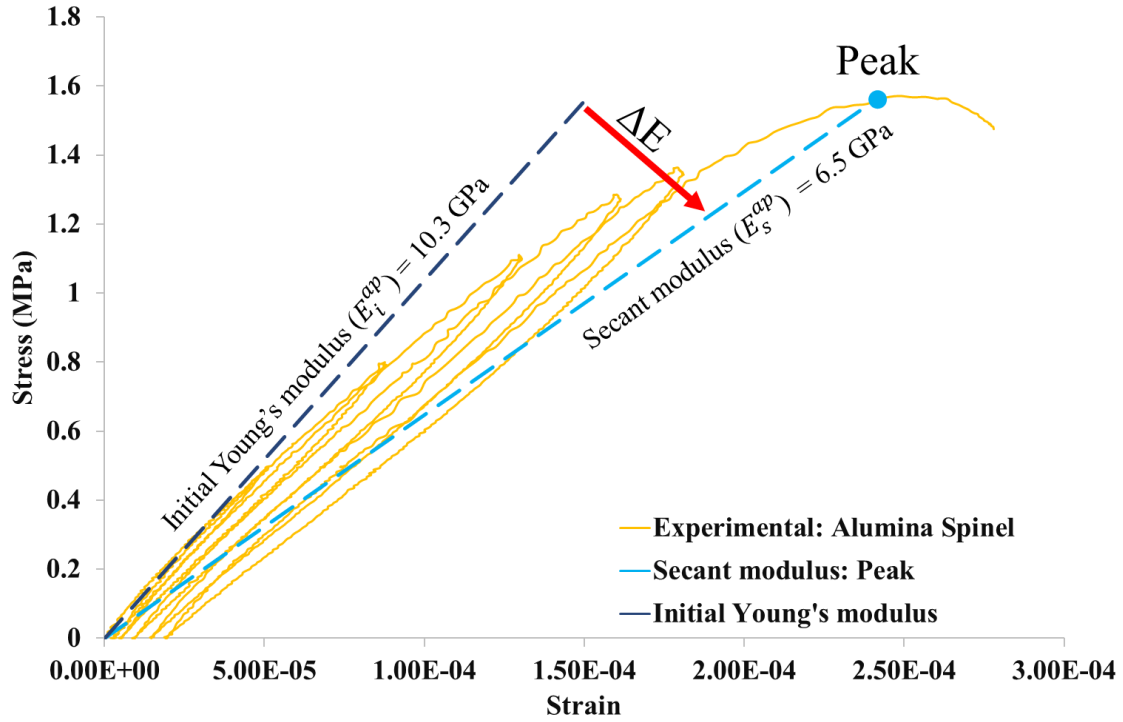
Fig. IV-9. Quantification of Alumina Spinel non-linear behaviour through initial Young's modulus E_i^{ap} and secant modulus E_s^{ap}.

As shown in Fig. IV-9, the initial Young's modulus E_i^{ap} is 10.37 GPa. After subjecting to six cycles of tensile loadings, the secant modulus E_s^{ap} of the peak was measured equal to 6.47 GPa. Instead of using absolute values, normalised values of the decreasing Young's modulus rate are used to be more general and case-independent. Hence, this Young's modulus normalised decreasing rate E_r^{ap} is defined as:

$$E_r^{ap} \;=\; \frac{E_s^{ap}}{E_i^{ap}}$$

Eq. IV-3

In the case of Alumina Spinel brick, this normalised decreasing rate E_r^{ap} was 62.4%. From this experimental rate, the way to mimic this decrease quantitatively in DEM will be explained in the next section.

IV.4.2. Mimicking the apparent non-linear behaviour

As already presented in Fig. IV-7 (a), the Weibull modulus (m) has a strong influence on the non-linear behaviour in tension. In order to go a step further, it could be valuable to find a reliable relationship between m and this non-linear behaviour through the secant modulus, as defined in the previous section. In this regard, eight uniaxial tensile test simulations on a cubic sample (as explained in section IV.3.1) with different values of Weibull modulus (m = 1, 2, 3, 5, 7, 10, 20, 30) have been performed. Therefore, all initial elastic parameters (Young's modulus and Poisson's ratio) for these series of simulations

were kept constant. Again, to remain independent from initial elastic values, the results were normalised and plotted in Fig. IV-10.
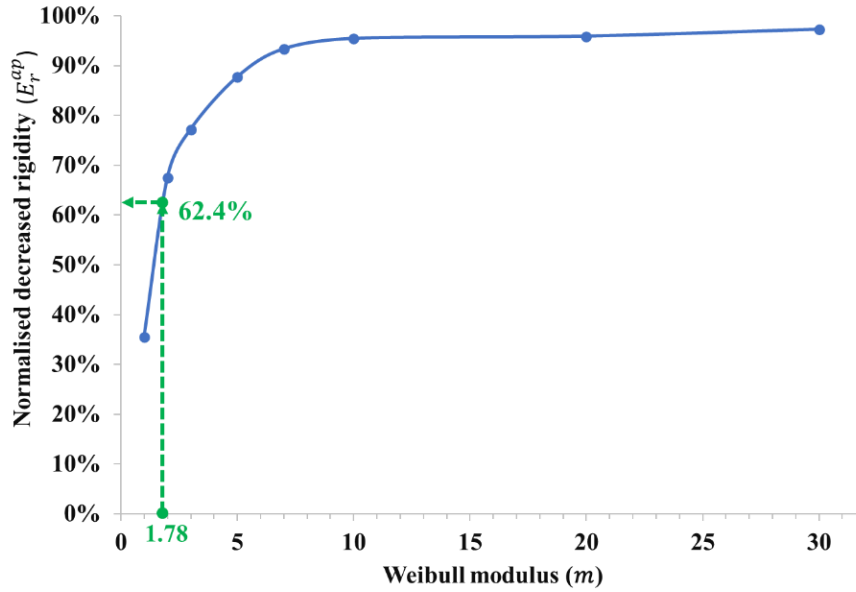
Fig. IV-10. Evolution of Young's modulus normalised decreasing rate (E_r^{ap}) vs Weibull modulus (m).

For a better understanding of this curve (Fig. IV-10), E_r^{ap} value close to 100% means that the numerical sample exhibits very limited damage before its complete rupture. On the opposite, E_r^{ap} value very far from 100% (e.g. 35%) indicates that a large quantity of damage occurs within the numerical sample before its complete rupture (in the pre-peak region).

Thus, for the infinite value of *m*, very limited damage is observed, and the final rupture takes place in a brittle way. This brittle behaviour remains rather similar by lowering *m* down to *m* = 8. For further decrease of *m*, a larger quantity of damage can be observed before the final rupture, which becomes, in these cases, quasi-brittle. From this curve, which can be used as a calibration chart, it becomes very easy to set the *m* value ($m \cong 1.78$) in accordance with the targeted value of E_r^{ap} (E_r^{ap} = 62.4%) in the case of Alumina Spinel reference material. In such a way, as shown in Fig. IV-11, the result of the simulation for this value of *m* (*m* = 1.78) perfectly fit the experimental results for both initial Young's modulus E_i^{ap} and peak secant modulus E_s^{ap}. Of course, at this stage, the ultimate tensile strength still needs to be adjusted. Therefore, the model should go through another step of calibration to reproduce the same ultimate apparent tensile strength of the Alumina Spinel reference material.
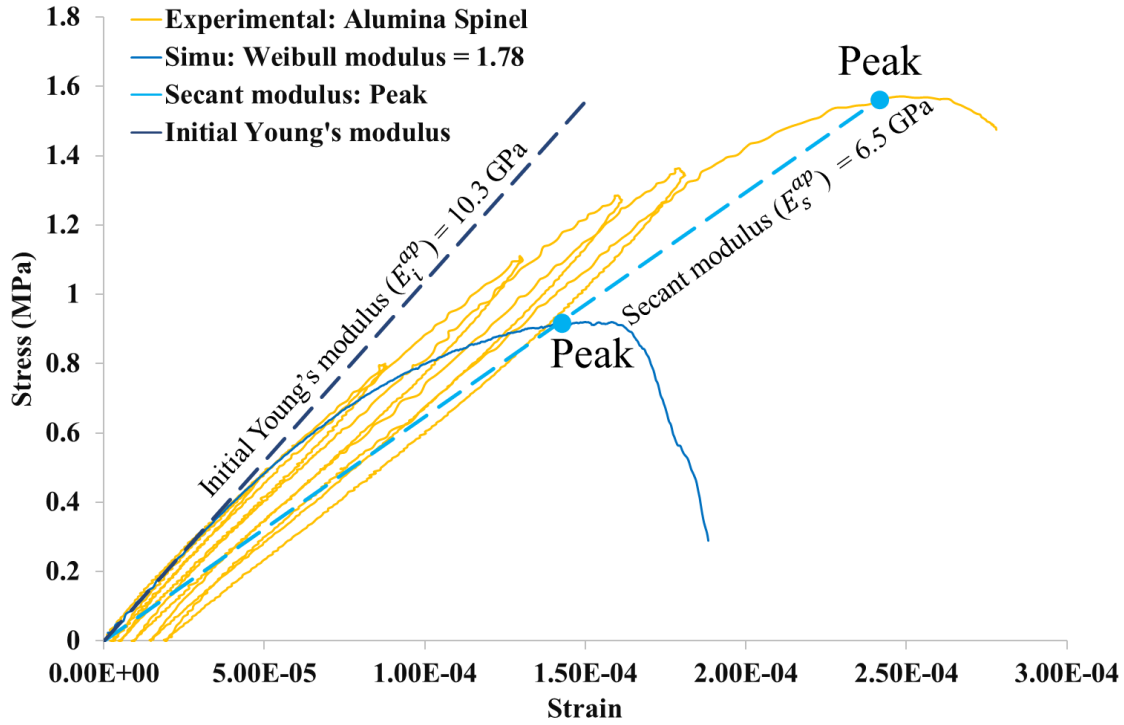
Fig. IV-11. Uniaxial tensile test simulation for *m* = 1.78 compared to
Alumina Spinel reference material.

IV.4.3. Calibrating ultimate apparent tensile strength

In Fig. IV-11, it was shown that despite the accordance of the non-linear behaviour, the ultimate apparent tensile strength of the simulation was not equal to the experimental result. The reason is that considering Fig. IV-7 (a), decreasing the Weibull modulus *m* will decrease, at the same time, the ultimate apparent tensile strength (t^{ap}) of the numerical model. To quantify the impact of *m* on t^{ap}, eight uniaxial tensile test simulations on a cubic sample, with different values of Weibull modulus (*m* = 1, 2, 3, 5, 7, 10, 20, 30), have been performed and plotted in Fig. IV-12 (a). Instead of using absolute values of t^{ap}, the normalised ultimate strength values (t_r^{ap}) have been again preferred, which is defined as follows:

$$t_r^{ap} \ = \ \frac{t^{ap}}{t_{m=\infty}^{ap}}$$

Eq. IV-4

where t^{ap} correspond to the apparent tensile strength for a given value of *m* and $t_{m=\infty}^{ap}$ correspond to the apparent tensile strength in the case of *m* = ∞.

(a) (b)
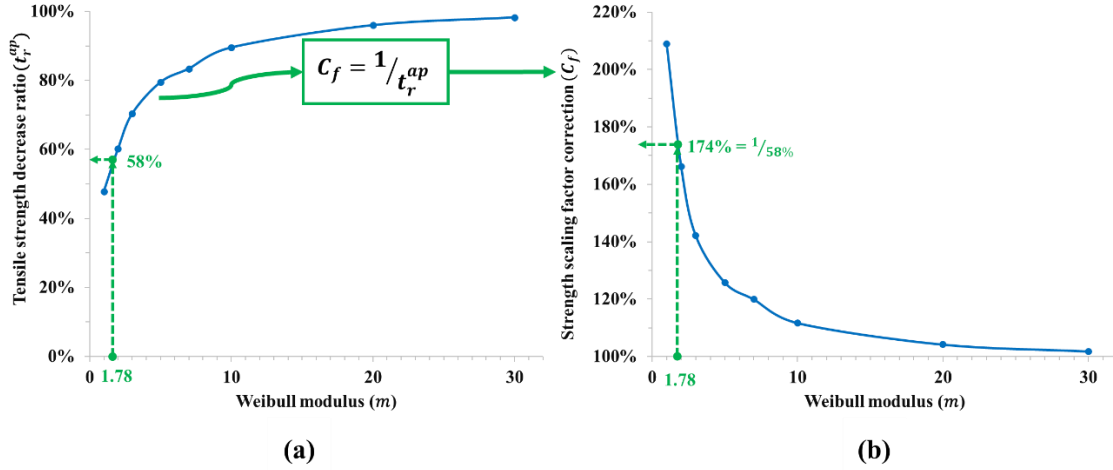
Fig. IV-12. Procedure to calibrate the apparent tensile strength: (a) decrease in ultimate apparent tensile strength t_r^{ap} coming from the decrease in Weibull modulus m value and (b) correction factor C_f to be thus applied to the scaling parameter initially set to $\sigma_{m=\infty}^0 = t_{m=\infty}^{loc}$ in order to keep finally the same apparent tensile strength $t_{m=\infty}^{ap}$.

From Fig. IV-12 (a), it is obvious that large values of m (higher than 25) do not influence the apparent tensile strength significantly. On the other hand, for low values of m (lower than 5), a strong decrease in apparent tensile strength can be observed (more than 50% for $m = 1$).

Therefore, globally, a decrease in m allows in one hand to generate a non-linear behaviour in the stress-strain curve (main initial target developed in the previous section), but on the other hand, it also leads to a strong decrease in the apparent tensile strength value (not the desired target). Thus, this decrease in apparent tensile strength should be compensated by an increase in the scaling parameter of the Weibull formulation. In this way, the inverse of t_r^{ap} has been plotted in Fig. IV-12 (b) in order to obtain a pertinent correction factor C_f that need to be applied to the scaling parameter of the Weibull formulation initially set to $\sigma_{m=\infty}^0 = t_{m=\infty}^{loc}$. The objective here is to recover the same apparent tensile strength as $t_{m=\infty}^{ap}$ by applying the following scaling parameter:

$$\sigma_m^0 = C_f \times t_{m=\infty}^{loc}$$

Eq. IV-5

In the present case of Alumina Spinel reference material, for which $m = 1.78$, Fig. IV-12 (b) allows to estimate this correction factor to 174% leading to a scaling parameter (σ_m^0) of 2.3 MPa. In order to validate the proposed approach, the numerical results obtained by the calibrated parameters have been compared to the real experimental results for Alumina Spinel brick in Fig. IV-13.
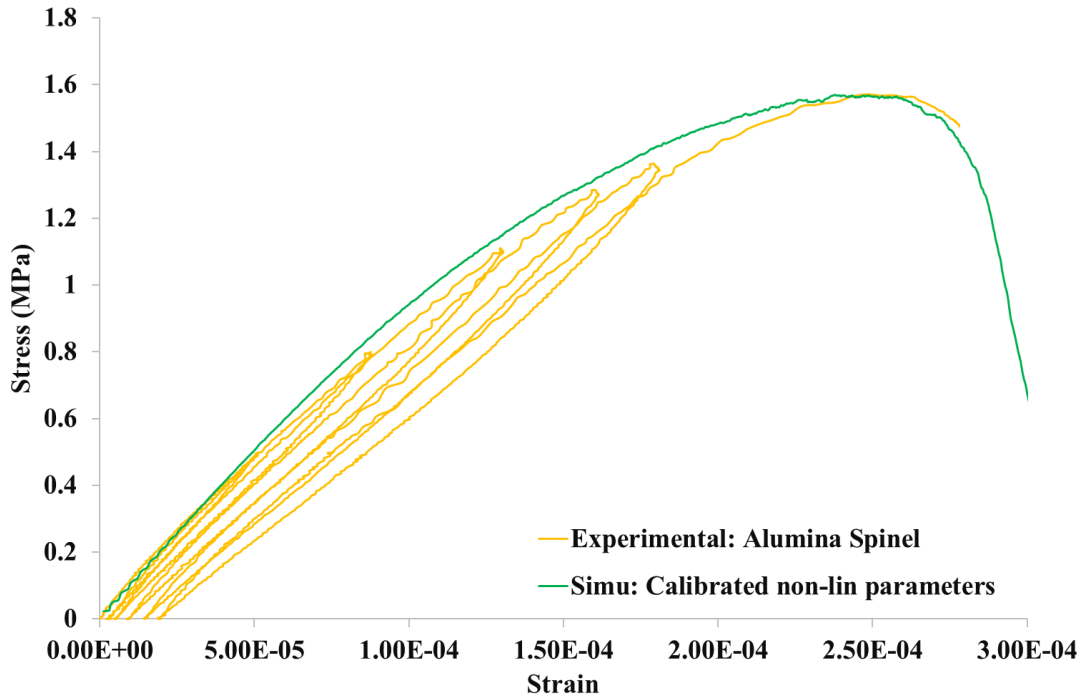
Fig. IV-13. Comparison of DEM simulation using proposed non-linear calibrated parameters to Alumina Spinel brick experimental result.

Concerning Fig. IV-13, after calibrating the non-linear behaviour, the simulation shows a really good qualitative and quantitative accordance with the pushovers of the experimental results of Alumina Spinel brick. The stress-strain curve of the simulation starts with the same initial Young's modulus. Afterwards, it promotes non-linear behaviour, following the pushovers of the cyclic loadings of the experimental curves. Then, it fails at the same ultimate tensile strength as the real material, and in the end, it potentially predicts a reasonable post-peak failure behaviour of the material.

Overall, it can be said that the proposed procedure for calibrating the DEM model to reproduce the non-linear behaviour of the quasi-brittle materials is validated by comparing it to the real experimental results. This procedure has been summarised in the next section.

IV.4.4. Proposed meta-algorithm for non-linear behaviour calibration

The summary of the proposed calibration process for non-linear behaviour is shown in the following meta-algorithm (Fig. IV-14). In this meta-algorithm, additional steps are added to the initial calibration process for linear brittle behaviour (see section II.4.4) in order to achieve non-linear quasi-brittle behaviour. These additional steps can be summarised as:

    (a) implementing the Weibull distribution law in the DEM model;

    (b) producing Young's modulus normalised decreasing rate (E_r^{ap}) vs Weibull modulus (m) chart;

    (c) producing the normalised ultimate strength decreasing rate (t_r^{ap}) vs Weibull modulus (m) chart.
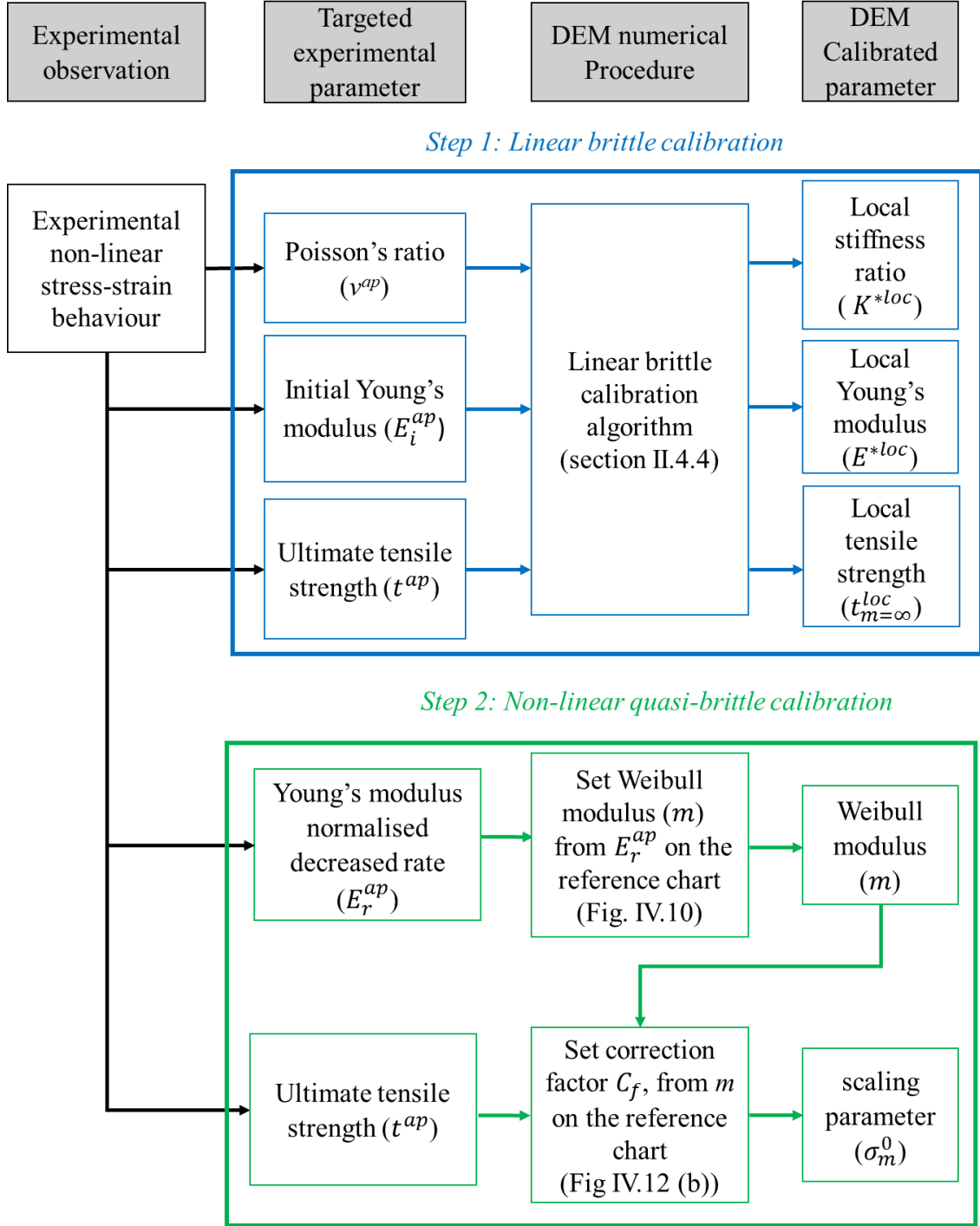
Fig. IV-14. Proposed meta-algorithm for calibration of non-linear behaviour in DEM models

The proposed calibration process is here independent of initial elastic brittle properties (Young's modulus, Poisson's ratio and apparent tensile strength) thanks to the normalisation of these parameters. Hence, if a similar DEM model is used (FJM model with Weibull distribution), the proposed charts (Fig. IV-10 and Fig. IV-12) can be used as references to calibrate both m and σ_m^0 parameters which define the Weibull distribution

law. In the case of other DEM models, these charts must be re-computed, and the same meta-algorithm can be applied to simulate quantitatively non-linear quasi-brittle behaviour with DEM. Thus, this meta-algorithm could be potentially applied to other DEM bond models with other distribution laws of bond strength.

IV.5. Influence of cyclic loadings on non-linearity

In this section, the simulation of cyclic loadings will be reviewed. Firstly, the non-linear stress-strain curve during cyclic loading will be presented. Then the microcracking and elastic properties evolution during cyclic loading will be investigated. At the end of this section, the cyclic and monotonic uniaxial tensile test simulations will be compared.

IV.5.1. Modelling non-linear stress-strain curve during cyclic loading

For verification of the proposed DEM model accuracy, cyclic tensile loading tests are simulated with the same conditions, as explained in section IV.3.1. To fit the experimental curve (Fig. IV-3), five uniaxial tensile cycles were simulated, which target the experimental cyclic peaks at 0.8 MPa, 1.1 MPa, 1.3 MPa, 1.4 MPa and 1.6 MPa (where material failed at 1.57 MPa). In this regard, a series of stress-controlled cyclic tests were done by targeting these five experimental stress peaks. In this simulation, the vertical stresses were gradually applied until it reaches each targeted peak thanks to displacement-driven conditions. After reaching the targeted peak, the displacement directions were inversed to decrease the stress down to the relaxing state equivalent to zero stress. These steps were repeated for each loading cycles up to the failure point. The result of this simulation is quantitatively compared to the experimental test in Fig. IV-15.

Fig. IV-15. Comparison of stress-strain curve for cyclic tensile loading:
DEM simulation vs experimental Alumina Spinel results

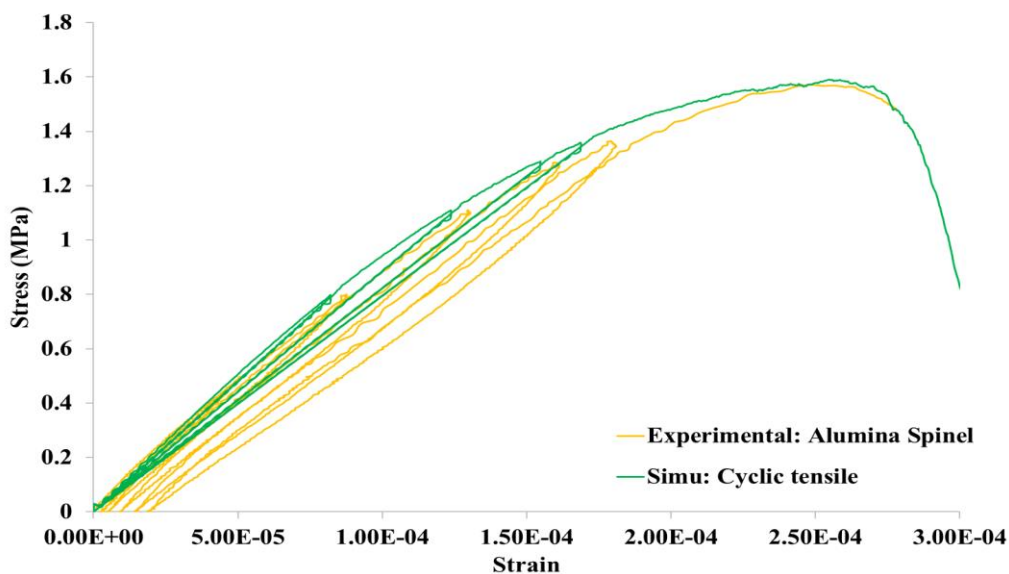By comparing the simulation results and the experimental curve in Fig. IV-15, it can be observed that the simulation is able to model the progressive decrease of rigidity after each cycle. The overall mechanical behaviour of simulated material and peak of each cycle are quantitatively close to the real material behaviour. This approach could also precisely model the failure peak (+ 0.9% error) of the material after undergoing five cycles. The post-failure behaviour of the material is also modelled reasonably.

On the other hand, the residual strain after each unloading cannot be modelled by this approach. In reality, for Alumina Spinel material, these residual strains are due to internal stress relaxations, which happen during microcrack extensions. These internal stresses are coming from the cooling phase (after sintering the material), and they are due to the CTE mismatch between the different constituents of the material (see section I.1.2). At this stage, the proposed DEM model is not able to simulate these internal stresses coming from CTE mismatch and, consequently, the related apparent residual strains. This limitation is because, up to now, the FJM is not capable of modelling mechanical interactions and temperature variation simultaneously (as mentioned in section IV.1). Considering the ongoing development of FJM, this limitation could be solved soon.

The other reason for not mimicking such residual strains could be the perfect fracture closure in the numerical model. This means that after creating a fracture surface during the loading stage, the fracture will close perfectly during unloading without exhibiting any surface mismatch. To simulate a certain level of surface mismatch, an additional artificial gap could potentially be introduced. However, this potential solution was not investigated as a part of this PhD.

IV.5.2. Microcracking and elastic properties evolution during cyclic loading

To investigate further this cyclic simulation, the stress, the microcracks number and the elastic properties evolutions are plotted versus the simulation time in Fig. IV-16. To analyse a given cycle, all four plots and the corresponded pictures that show the positioning of cracks should be considered.

Each given cycle starts with a progressive increase of the uniaxial tensile stress up to the targeted peak stress. This progressive increase can be described in two stages:
- (I) from starting point up to the previous cycle stress peak value corresponding to points a, b, c, and d.
- (II) from previous cycle stress peak value to the targeted peak corresponding to points 2, 3, 4 and 5.

It is worth mentioning that during stage (I), the number of cracks, apparent Young's modulus and Poisson's ratio are constant. While during stage (II), new microcracks are formed, which lead to a non-reversible linear decrease of the apparent Young's modulus. Besides, the slopes of microcrack number (versus time) during the (II) stages are quite similar. It means that the microcracking forming rate is relatively constant. This point is due to the constant displacement rate, which is applied for loading the sample.

After reaching the targeted stress peak, the loading direction is inverted, and the stress decreases to the relaxation state (zero stress). Despite a numerical artefact in elastic properties measurements (which is due to very low values of strain at this point of the

curve), the number of microcracks, apparent Young's modulus and Poisson's ratio are quite constant during this stage (I).

For the last cycle, the targeted stress peak was 1.6 MPa, but the sample failed at 1.58 MPa (point 5 to 6) with a sudden drop in the stress. During the failure, the number of microcracks suddenly increases with a slope higher than the observed ones during the previous stages (II). The rising of microcracks number in a short time results in a sharper decrease in apparent Young's modulus.

Finally, in the post-failure part (point 6 to the end of the simulation), the stress tends to zero. During this stage, the microcrack forming rate decreases, and the number of microcracks tends to be constant because the complete failure happens. In this part, the apparent Young's modulus and the apparent Poisson's ratio turns to zero.

To get a qualitative visualisation of the microcracking process, pictures of the sample with highlighted cracks are shown for each cycle peak on the top of the figure. These pictures highlight the progression of microcracks for each cycle due to the imposed increasing stress after each cycle. In the last cycle, these microcracks merge into a macroscopic fracture (shown in the red dashed area), leading to the complete failure of the sample. This numerical result is in perfect accordance with the localisation phenomenon, which typically is observed experimentally. As expected, this increase of microcracks leads to a progressive decrease in apparent Young's modulus. Also, a noticeable decrease in Poisson's ratio is observed (from 0.16 to 0.13). In fact, this observation is also in accordance with experimental measurements, which in many cases indicate a low value of Poisson's ratio for highly damaged materials. Overall, these different points highlight the pertinence of the proposed model compared to physical phenomena observed experimentally in quasi-brittle materials.
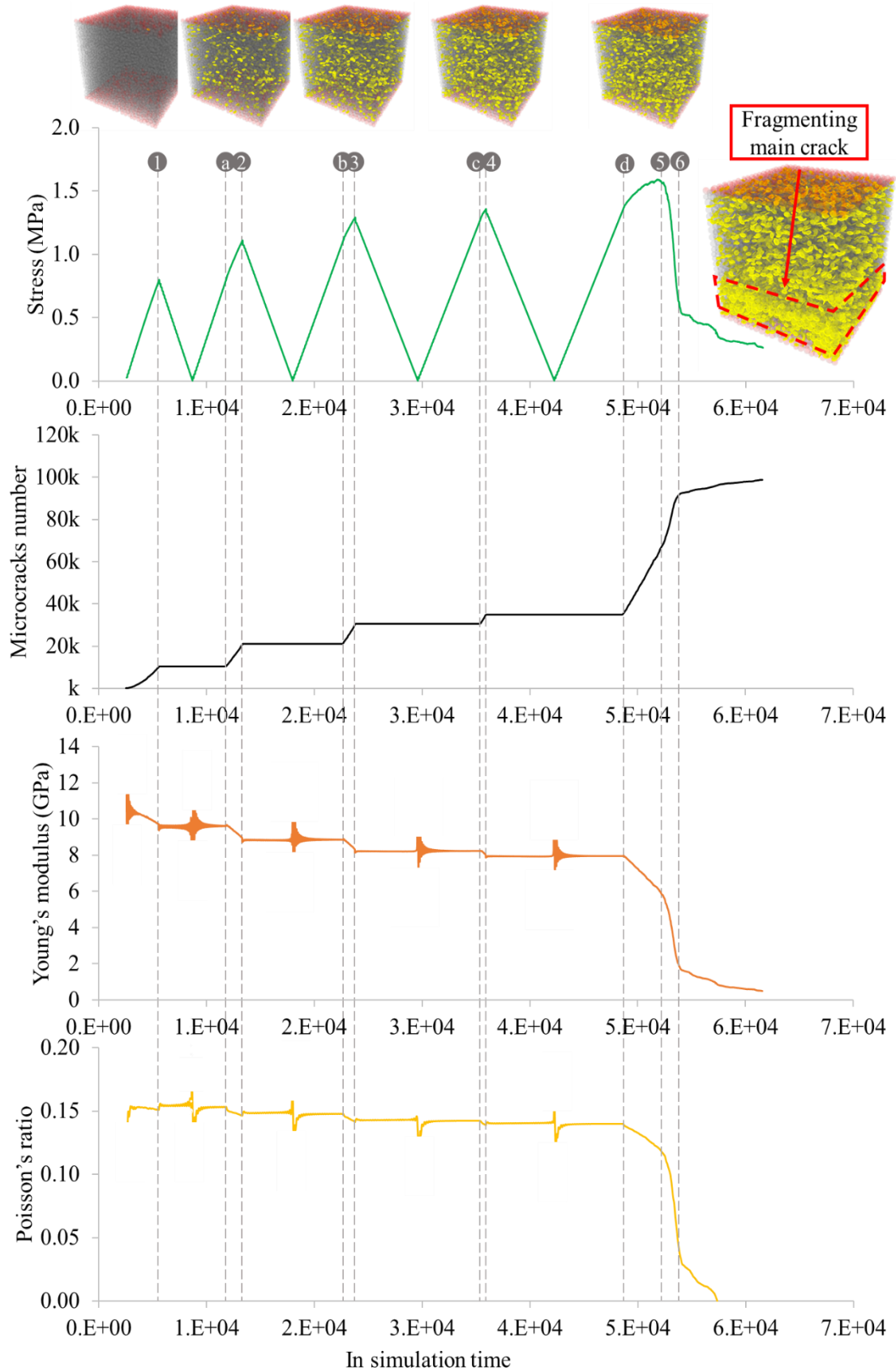
Fig. IV-16. Evolution of stress, microcracks number, apparent Young's modulus and Poisson's ratio during the cyclic uniaxial test DEM simulation.

As introduced in section IV.2, the number of microcracks in simulation could qualitatively be associated with acoustic emission events. To verify this point, the presented simulation is qualitatively compared to experimental observations from (Yuan *et al.* 2018) of a cyclic tensile test on a quasi-brittle material (marble rock) in Fig. IV-17.
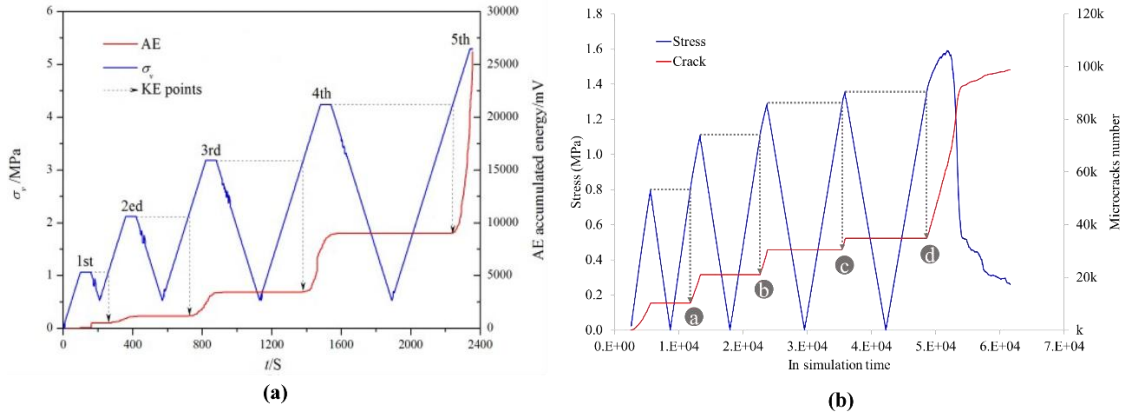
Fig. IV-17. Cyclic tensile loadings: (a) experimental observation of
stress and acoustic emissions on marble (Yuan *et al.* 2018) and
(b) simulation of stress and microcracks number on Alumina Spinel brick.

In experimental results, Fig. IV-17 (a), the drawn KE points refer to Kaiser Effect acoustic emission points. The Kaiser effect is defined as the absence of detectable acoustic emissions until the previous stress peak in a cyclic mechanical test was reached (Kaiser 1950). In fact, the Kaiser acoustic effect in tensile cyclic loading indicates damage accumulation in material under tensile stress (Yuan *et al.* 2018) and can be used as another verification parameter for the proposed numerical approach.

It can be observed that the evolution of the number of microcracks in this simulation qualitatively resembles the experimental acoustic emission events of a similar experimental test. Moreover, the experimental Kaiser Effect (KE) points (in Fig. IV-17 (a)) are qualitatively reproduced in the simulation during the forming microcrack stages (as introduced as stage (II)), which is corresponding to the points a, b, c and d in Fig. IV-17 (b).

IV.5.3. Comparison of cyclic and monotonic uniaxial tensile tests

In order to verify the absence of energy loss in the simulation, potentially due to friction during unloading, the cyclic and monotonic uniaxial tensile tests are compared in Fig. IV-18. It should be mention that these simulations have been done on the same numerical sample with the same input parameters. As can be seen here, the stress-strain curve of the monotonic test is following the cyclic simulation. The potential reason for this match is the absence of stress relaxation and energy loss in the system. In this way, the cycles will not dissipate more energy in comparison to a monotonic test. This point is confirmed by having the same way of increase in microcracks number.
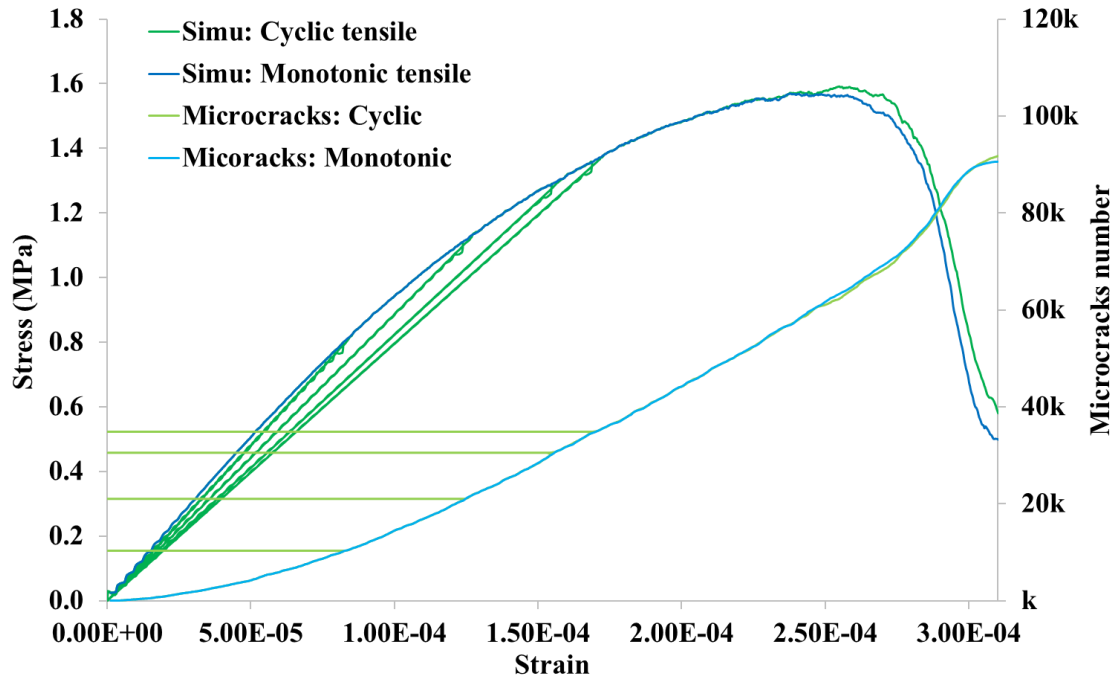
Fig. IV-18. Cyclic and monotonic uniaxial tensile stress-strain curve and the associated evolution of microcracks number.

The previous comparison demonstrates the high potential of DEM numerical models in simulating the acoustic emission events and their evolution. This point could strongly facilitate the interpretation of experimental acoustic emissions results and even, in the future, help to identify the type of defect associated with a given type of event recorded during mechanical tests.

IV.6. Conclusions

In this chapter, a qualitative and quantitative DEM approach was proposed to model the non-linear quasi-brittle behaviour of a continuum media by introducing in the bond strength distribution a randomisation process that follows a Weibull distribution. This proposed approach is able to take into account simultaneous microcrack initiations and propagations. Modelling these multi fracturing processes is of a high degree of interest for simulating refractories because such materials involve a high amount of microcracks which are induced by thermal expansion mismatches between constituents. This fracturing process and microcracking simulations are among the key interests of using DEM in such a case compared to FEM.

In this study, the experimental reference material was Alumina Spinel brick which promotes a typical quasi-brittle behaviour highlighted by a strong non-linear response. To achieve this typical non-linear response, the proposed DEM approach involves a customised calibration process in two steps:

1. a preliminary calibration step capable of reproducing a linear elastic brittle behaviour without considering any randomisation of bond strength and,
2. a complementary calibration step capable to quantitatively reproduce a non-linear quasi-brittle behaviour by introducing bond strength randomisation, which follows an adjusted Weibull distribution.

For the linear part, the calibration of the FJM input parameter was done for a perfect linear elastic brittle material (section IV.3.1). This calibration process led to a perfect brittle linear behaviour, reproducing the initial elastic behaviour of the real material. For the non-linear part, a randomisation process of bond strengths was introduced following a Weibull distribution. Depending on the assigned Weibull modulus (m), this randomisation process influenced the apparent mechanical behaviour resulting from the microcracking process within the simulated material. As investigated in section IV.3.3, by decreasing Weibull modulus (m), the microcracking process would increase, and consequently, it induced higher mechanical non-linearities and a lower apparent tensile strength. To achieve quantitative simulations, the secant modulus at the peak was introduced as the parameter able to quantify the experimental non-linear behaviour. Thanks to this parameter, it was possible to find a relationship between quasi-brittle behaviour and the Weibull modulus (m). In addition, a relationship between apparent tensile strength and the Weibull modulus (m) was defined. By having these two relationships, it was possible to propose a quantitative calibration process to model a targeted non-linear behaviour. To make this non-linear calibration method more general and applicable for other DEM contact models, a meta-algorithm was proposed in section IV.4.4.

In the last part, a cyclic tensile test was investigated on the reference Alumina Spinel material. In this way, a numerical sample was calibrated by the proposed approach. Results of simulation applied on this numerical sample was compared to experimental observations. The related simulation was designed to reproduce the cyclic loading of the experimental one. The obtained result matched quantitatively to the experimental Alumina Spinel curve, as shown in section IV.5. Afterwards, to investigate further the obtained numerical results, the microcrack and elastic properties were monitored. A qualitative comparison with acoustic emissions measurements shown that the simulation was able to reproduce the experimental Kaiser effect.

Overall, the proposed procedure for calibrating the DEM model to reproduce the non-linear behaviour of the quasi-brittle materials is validated by comparing it to real experimental data. The proposed numerical algorithm could be potentially applied to other DEM bond models and other bond strength distribution laws. Also, this approach can potentially be used to tune the brittleness of material by promoting crack branching processes and diffused damage creation. Therefore, in the next chapter, this approach is applied to the Wedge Splitting Test, which is commonly used to quantify the brittleness of refractories, to verify this last point.

Chapter V: Towards mimicking microstructural aspects that enhance fracture toughness of refractory material - Application to Wedge Splitting Test (WST)

V.1. Introduction

The key interest of DEM application in the refractory field is its ability to improve, in future, the microstructure design of heterogeneous materials for higher thermal shock resistance (linked to fracture toughness). In this way, as mentioned in section I.2.3, the widely used mechanical test used for mechanical fracture studies is the Wedge Splitting Test (WST). The principle of this test is to open a notch by a wedge in a displacement-driven condition able to produce a stable fracture propagation. This test gives more information about fracture energy and brittleness number of the material. Hence, WST results could be an index for characterising the quasi-brittle behaviour of refractories. In fact, this quasi-brittle behaviour is closely linked to the presence of pre-existing microcracks and their ability to promote crack branching.

This chapter aims to verify the ability of the proposed numerical approach (introduced in Chapter IV:) to reproduce key phenomena such as crack branching and diffused damage creation during WST. In this way, two model materials will be used as a reference: a highly brittle refractory and a quasi-brittle refractory with a strong mechanical non-linearity.

In addition, dedicated Digital Image Correlation (DIC) measurements, able to highlight macroscopic cracks, will be used as references in order to compare the crack paths given by DEM simulations. Also, the impact of implementing the proposed numerical model (using Weibull modulus to randomise local tensile strengths) will be investigated. In the end, a discrete-continuous hybrid model will be proposed to optimise the WST simulations in order to save computational time and calculations resources. Hence, a coupled model of discrete DEM with a continuous Finite Volume Model (FVM, introduced in section I.3.1.3) will be proposed.

V.2. Description of the reference materials

The purpose of this chapter is to study two typical fracture behaviour through two reference materials:

- a pure Magnesia (MgO) material which exhibits a highly brittle behaviour;
- a Magnesia Hercynite with 15% of large Hercynite aggregates (MH15), which exhibits a strong non-linear quasi-brittle behaviour.

V.2.1. Microstructures description

The two investigated materials have been chosen because they exhibit simplified microstructures that focus on fracturing behaviour. In this way, the experimental fracture behaviour of pure MgO and MH15 has been studied by Khlifi *et al.* (Khlifi 2019). The typical microstructures of these materials are shown in Fig. V-1.

(a)   (b)
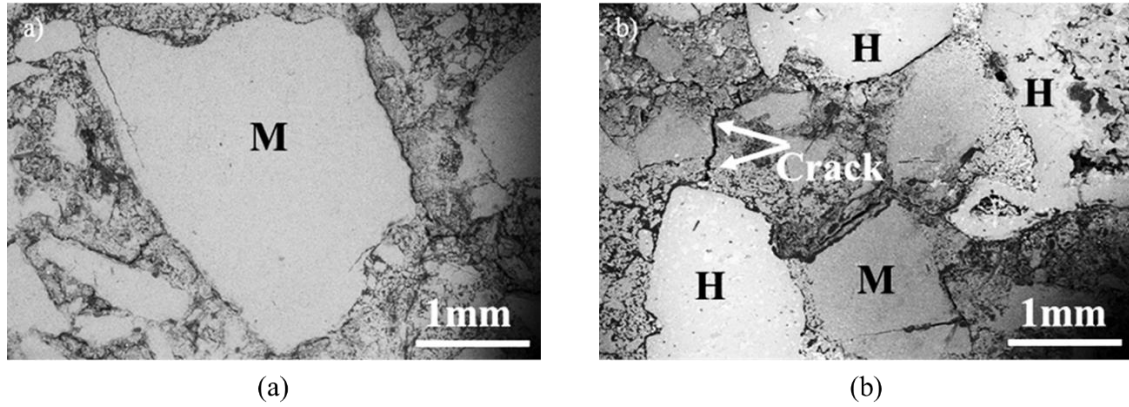
Fig. V-1. SEM images of (a) pure MgO and (b) MH15 composite (Khlifi *et al.* 2019).

Fig. V-1 (a) shows the microstructure of a pure MgO material, where large aggregates are Magnesia grains (M in the figure) are embedded in a pure MgO matrix (finer MgO grains). Fig. V-1 (b) shows the microstructure of MH15 material, where some large MgO aggregates are substituted by large Hercynite grains (H in the figure) within the same pure MgO matrix. Besides, as highlighted in the figure, after sintering and passing the cooling stage, the resulting microstructure of MH15 exhibits microcracks. These microcracks are formed due to thermal stresses coming from the CTE mismatch between the MgO matrix ($\alpha_{MgO~(400-200~°C)} = 13.2 \times 10^{-6}~K^{-1}$) and Hercynite aggregates ($\alpha_{FeAl2O4~(400-200~°C)} = 6.96 \times 10^{-6}~K^{-1}$) (Khlifi *et al.* 2019). This phenomenon has been explained in detail in section I.1.2. On the other hand, compared to MH15, pure MgO has no microcrack due to its monophase microstructure. As shown in Fig. V-2, this point is confirmed by the acoustic emissions recorded during the cooling stage of a thermal cycle (up to 1400 °C). In fact, this figure clearly shows that MH15 exhibit huge cumulated hits (up to 45000) during cooling in comparison with pure MgO (no acoustic emission). As an intermediate case, MH5 (with 5% of Hercynite aggregates) is simply between the two mentioned cases. It highlights the impact of the amount of Hercynite content on the microcracking process.
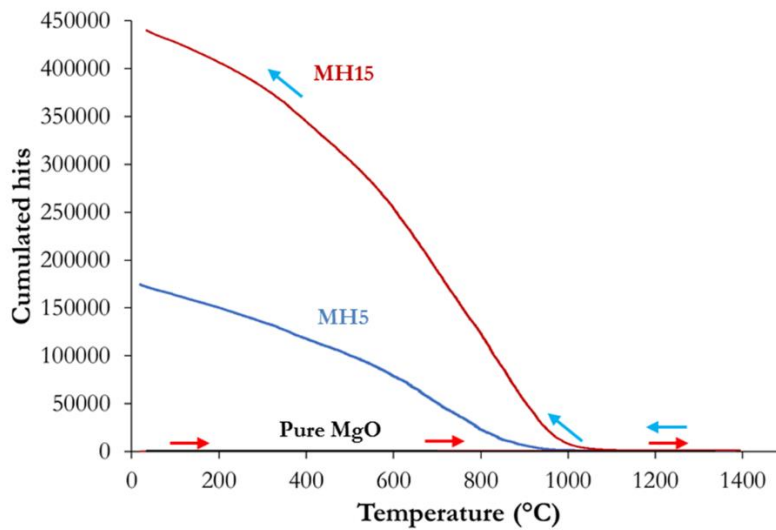
Fig. V-2. Acoustic emission evolution vs temperature for pure MgO, MH5 and MH15 (Khlifi *et al.* 2019).

Considering the high amount of acoustic emissions event for MH15 during the cooling stage, it is expected that this material promotes a quasi-brittle mechanical behaviour with a strong mechanical non-linearity (this point has been discussed in section I.1). On the other side, pure MgO does not promote any acoustic emission activity. Consequently, a quasi-perfect brittle mechanical behaviour is expected.

V.2.2. Force-displacement curves for Wedge Splitting Tests (WST)

The fracturing behaviour of these two materials was investigated through Wedge Splitting Test (WST). As introduced in section I.2.3, the WST is used to measure fracture parameters such as the specific fracture energy (G'_f) and brittleness number (B), introduced in Eq. I-15 and Eq. I-17, respectively. The force-displacement curves of WST for four materials, including pure MgO and MH15, is plotted in Fig. V-3. In addition to pure MgO and MH15, MH5 and MH25 are also plotted to highlight the evolution of brittleness. It worth mentioning that, even if MH15 is not the most 'quasi-brittle' one, this material was chosen as the reference because more experimental data were available.
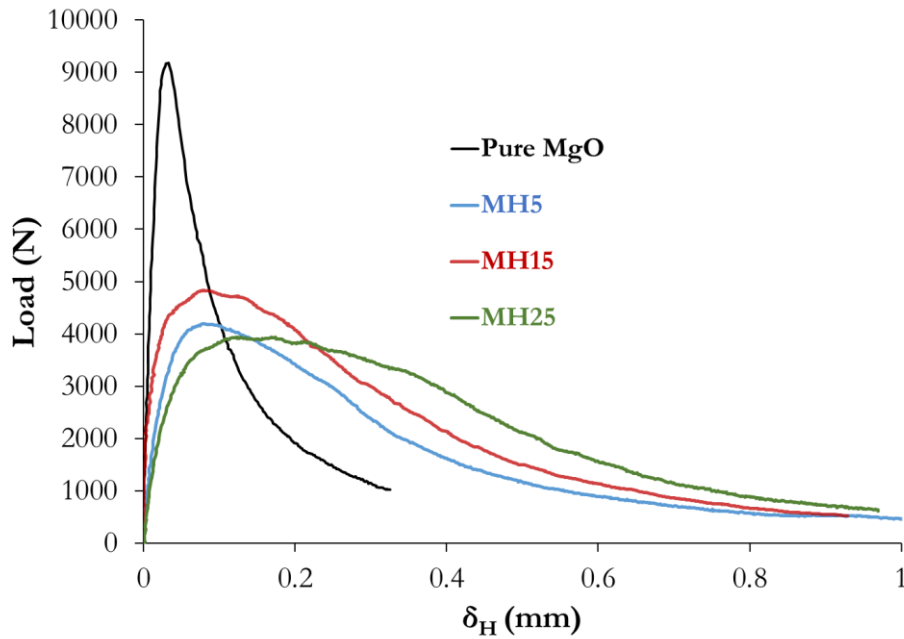
Fig. V-3. Force-displacement curves for Wedge Splitting Tests (WST) of pure MgO, MH5, MH15 and MH25 (Khlifi *et al.* 2019).

As shown in Fig. V-3, the specific fracture energy (the area under the force-displacement curve) of pure MgO is lower than MH15 and MH25. To quantify these results, the specific fracture energies and the brittleness numbers for these two experimental reference materials samples are discussed in the next chapter.

V.2.3. Fracture energy and brittleness number

As highlighted in the previous chapter, qualitatively, the specific fracture energy of pure MgO is lower than MH15. To characterise the fracture behaviour of these two materials, the specific fracture energies and the brittleness numbers for these two experimental reference materials samples are shown in Table V-1.

Table V-1. Experimental fracture parameters for two reference samples (Khlifi 2019)

Reference material	Specific fracture energy (J/m^2)	Brittleness number (-)
pure MgO	130	0.77
MH15	266	0.44

These results highlight the difference in the brittle behaviour for these two model materials, from a highly brittle one to a quasi-brittle one. In addition to the force-displacement curves, the fracture propagation evolution has been monitored with Digital Image Correlation (DIC). It allows to observe some interesting phenomena such as crack branching or crack bifurcation, which can be associated with force-displacement curves, which will be discussed in the next section.

V.2.4. Crack paths monitoring during Wedge Splitting Test (WST) with Digital Image Correlation (DIC)

Digital Image Correlation (DIC) allows the evaluation of the displacement fields all over the specimen surface. Additional post treating techniques could be managed to track fracture propagation. In this regard, the Two Parts-DIC (2P-DIC) method (Dupré *et al.* 2017) was used to detect and visualise the crack propagations during WST. Before presenting the experimental results, which are taken from (Khlifi 2019), the crack length notion should be introduced. According to Khlifi *et al.* (Khlifi 2019), thanks to the calculated strain field by 2P-DIC, the crack length can be evaluated in two ways, as shown in Fig. V-4:

- *equivalent crack length*, which is defined as a straight line going from the notch of the sample down to the lowest detectable position of crack;
- *cumulated damage length*, which is defined as the sum of all detectable crack lengths during WST.
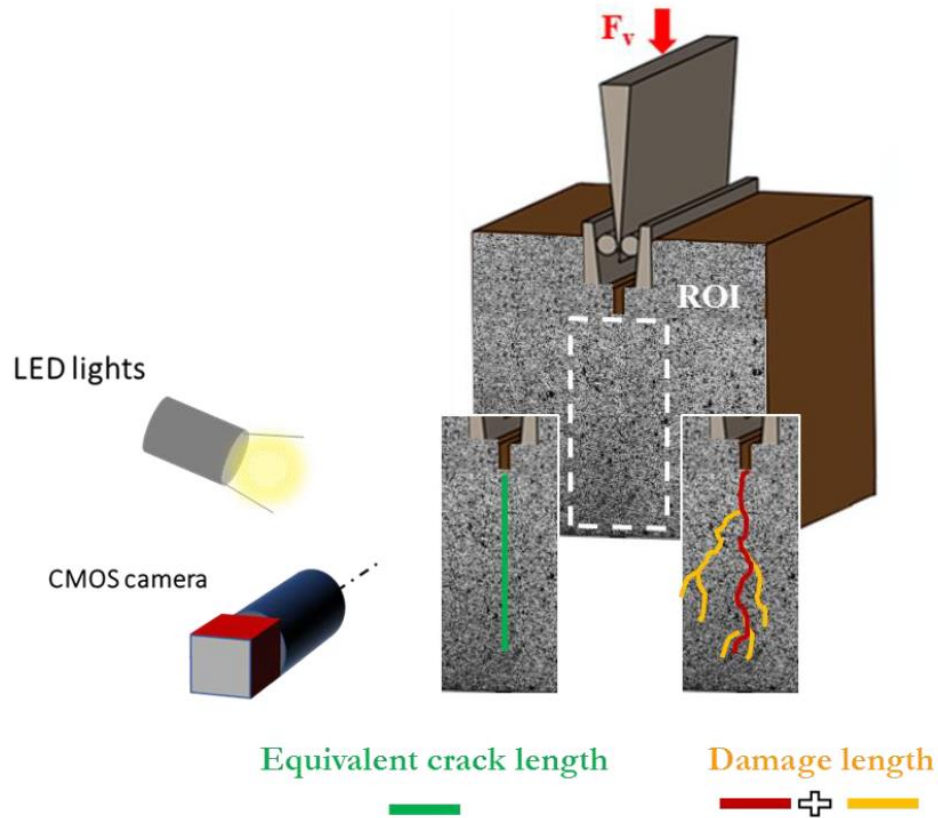
Fig. V-4. Two different crack length types measured by 2P-DIC: equivalent crack length and cumulated damage length (Khlifi 2019).

After introducing these two crack length quantification methods, the fracture behaviour of the two referenced materials during WST was characterised to compare two typical fracturing process from quasi-perfect brittle pure MgO to quasi-brittle MH15. In this way, force and fracture energy evolutions versus displacement were plotted in Fig. V-5 (a) and Fig. V-6 (a). Besides, at each loading stage, crack propagations are visualised, thanks to 2P-DIC, as shown in Fig. V-5 (c) and Fig. V-6 (c). From these visualisations, the difference between the equivalent crack length and the cumulated damage length can be considered as a damage evolution in these two materials, as shown in Fig. V-5 (b) and Fig. V-6 (b). As can be seen, this difference in MH15 is much higher than pure MgO, showing the ability of MH15 to develop far more fracture surfaces, which induce more fracture energy, as shown in Fig. V-6 (a). This fact is confirmed by the observation of numerous crack branching in MH15 (as highlighted in Fig. V-6 (c)) compared to pure MgO.

(a)

(b)

(c)
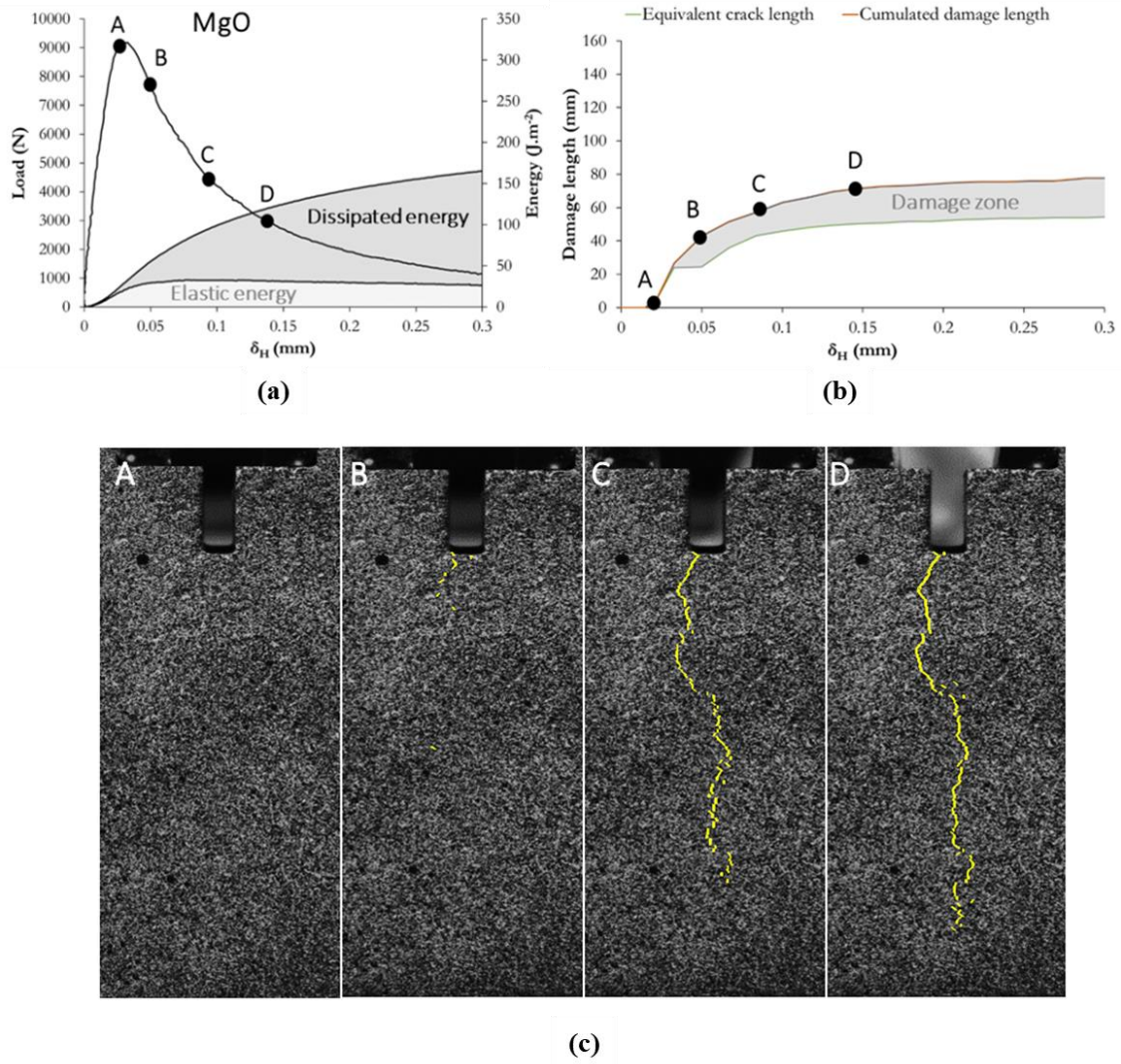
Fig. V-5. Fracture characterisation of pure MgO: (a) force-displacement curve and evolution of fracture energy, (b) evolution of damage and (c) 2P-DIC images of crack propagation during a WST (Khlifi 2019).

(a)

(b)

(c)
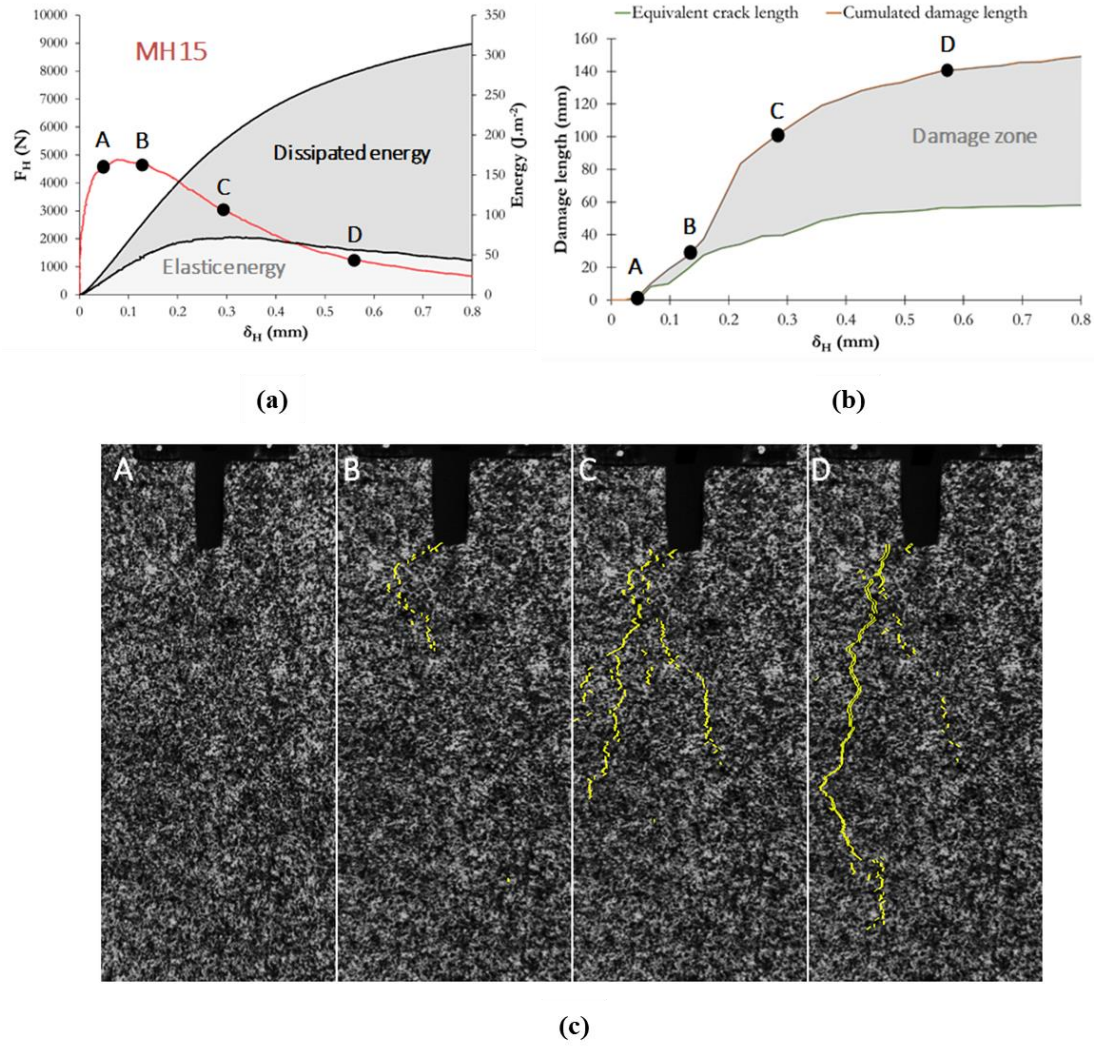
Fig. V-6. Fracture characterisation of MH15: (a) force-displacement curve and evolution of fracture energy, (b) evolution of damage and (c) 2P-DIC images of crack propagation during a WST (Khlifi 2019).

As reported in (Khlifi 2019), the other practical extraction of data from these results is to confront the fracture energy at each loading state of the WST to the corresponding equivalent crack length (here, as an example, the visual results for MH5 is shown in Fig. V-7). It aims to use this approach to evaluate the evolution of the crack propagation resistance of a material. Therefore, in Fig. V-7, the evolution of fracture energy as a function of equivalent crack length during WST is plotted.

For better understanding, it should be noted that horizontal parts in the curves correspond to straight crack propagation, going down from the notch during WST, which is relatively the case for a pure MgO curve. On the other hand, in a quasi-brittle material, such as MH5, there is an increase in the fracture energy, which is linked to a certain crack branching process, as highlighted in Fig. V-7. In fact, such experimental data could later open an interesting way to validate the current qualitative simulations of crack branching in WST.
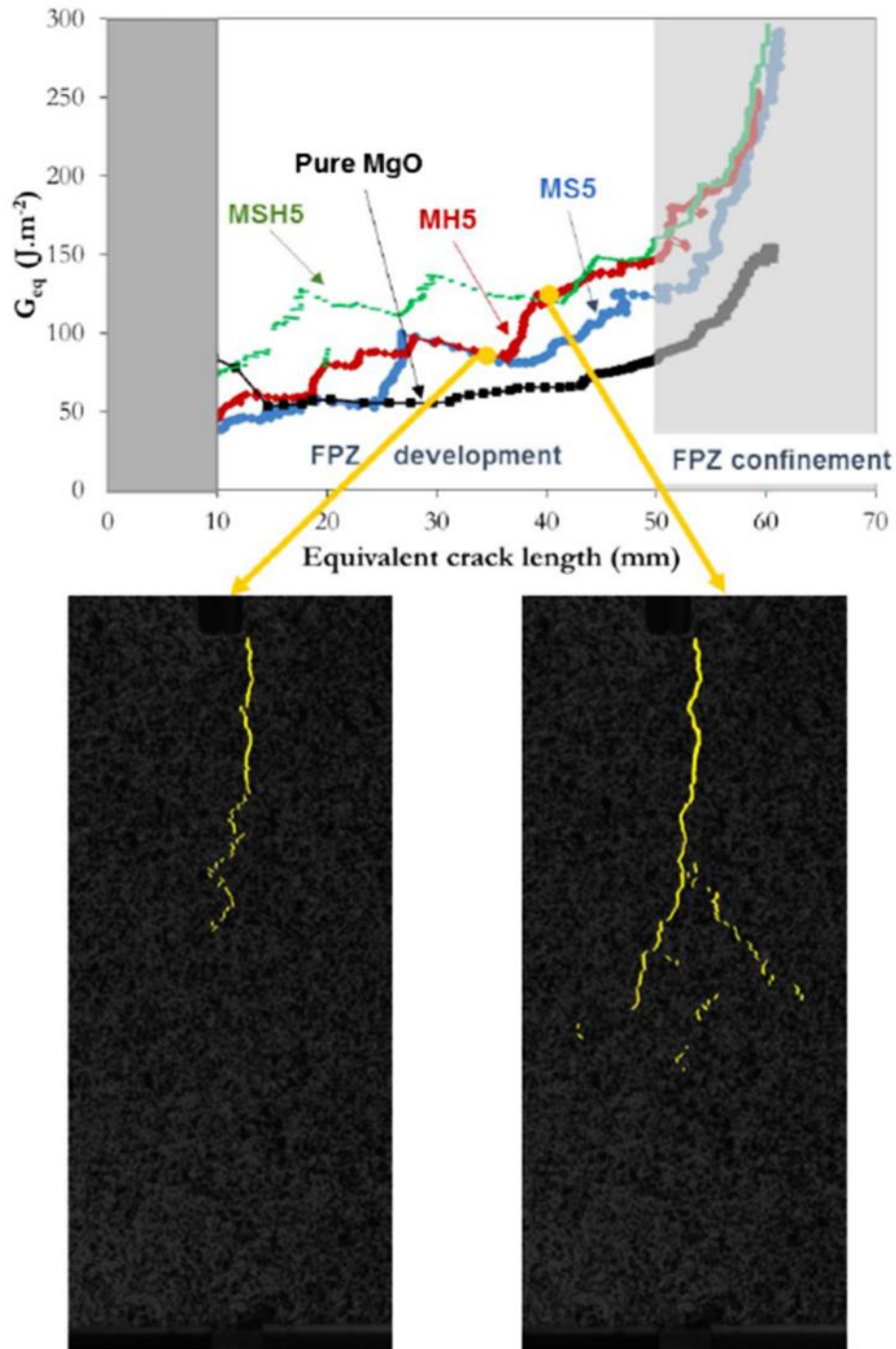
Fig. V-7. Evolution of equivalent fracture energy (G_{eq}) vs equivalent crack length for MgO, MS5, MH5 and MSH5 with the 2P-DIC illustration of crack branching in MH5 (Khlifi 2019).

V.3. DEM simulation of Wedge Splitting Test (WST)

In the present section, the numerical modelling has been managed in order to mimic WST experiments qualitatively. In this way, firstly, the numerical techniques to represent

the apparent non-linear behaviour of these two materials will be discussed. Then, the impact of this proposed model on the fracture energy and brittleness of the modelled numerical samples will be studied. At the end of this section, the DEM crack branching simulation results for these two materials will be compared to the experimental DIC observations.

V.3.1. Setting local parameters to mimic microstructure aspects

To qualitatively simulate the crack propagations for the two reference materials (MgO and MH15), the same numerical sample was used with two different local parameter sets:

- a uniform value of 10 MPa for the local tensile strength ($m = \infty$) to exhibit the pure MgO brittle behaviour;
- a Weibull distribution ($m = 3$ and $\sigma_0 = 10$ MPa) of the local tensile strength to exhibit the MH15 quasi-brittle behaviour.

It should be mentioned that, in order to only focus on the impact of using Weibull distribution to randomise local tensile strength, all elastic and fracture input parameters were the same, as shown in Table V-2. The following section will describe the implementation of these local parameters in the WST simulation.

Table V-2. FJM input parameters for WST

Description	Local Young's modulus	Local stiffness ratio	Local tensile strength	Local tensile strength		Local cohesion	Local friction angle
Material	both	both	MgO	MH15		both	both
Type	*Elastic*	*Elastic*	*Fracture*	*Fracture*		*Fracture*	*Fracture*
Abbreviation	E^{*loc}	K^{*loc}	t^{loc}	m	σ_0	c^{loc}	ϕ^{loc}
Initial value	20	4	10	3	10	25	0
Unit	GPa	-	MPa	-	MPa	MPa	Degrees

V.3.2. Force-displacement curves for Wedge Splitting Test (WST)

After assigning the local parameters, the preliminary cubic sample is shaped as the experimental WST geometry (see Fig. I-8) by removing discrete elements which are located in the notch region. Besides, to mimic the WST loading wedge, two rigid walls were added and put in contact with discrete elements in the loading region, as shown in Fig. V-8. Opposite displacements with a constant rate were applied to these rigid walls in order to open the sample in mode I. To obtain the force-displacement curve, the resulting force on walls, which are coming from the mechanical response of the sample, is monitored.
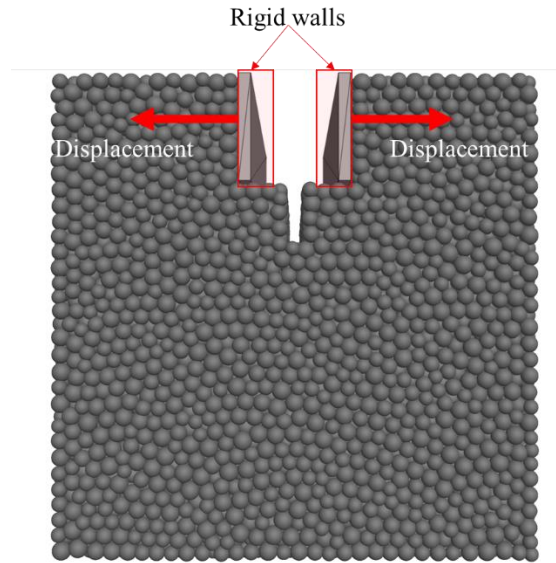
Fig. V-8. Prepared DEM numerical sample for WST.

By using this numerical procedure, the force-displacement curves can be plotted as shown in Fig. V-9. In agreement with the real experimental procedure, these curves are voluntary stopped when the force decrease down to 15% of the force peak value (to calculate the specific fracture energy numerically in a similar way to the experimental procedure). Surprisingly, it seems that decreasing the Weibull modulus (m) does not significantly change the apparent pre-peak behaviour and the maximum value of the force-displacement curve. On the other hand, the low Weibull modulus (m) seems to enlarge the post-peak part and reaches 15% of the curve for a higher displacement.

Concerning the evolution of the number of cracks, the model with Weibull distribution ($m = 3$) shows that:

- the cracking process starts for a lower displacement;
- the total number of cracks at 15% of the peak is much higher.

These points show that for the model with Weibull distribution ($m = 3$, representing MH15), more energy should be consumed to produce and propagate a higher number of microcracks. In fact, in the model using Weibull distributions, the enlarged post-peak area in the force-displacement curve is correlated to higher fracture energy (as mentioned in section I.2.3).

It should be highlighted that the goal of this section was to verify the impact of decreasing the Weibull modulus (m) on increasing the fracture energy. Hence, as explained, by only changing m, it is not possible to calibrate the overall behaviour of these materials for WST simulation. It will need an additional step to calibrate the decreased peak failure, which is not investigated here.
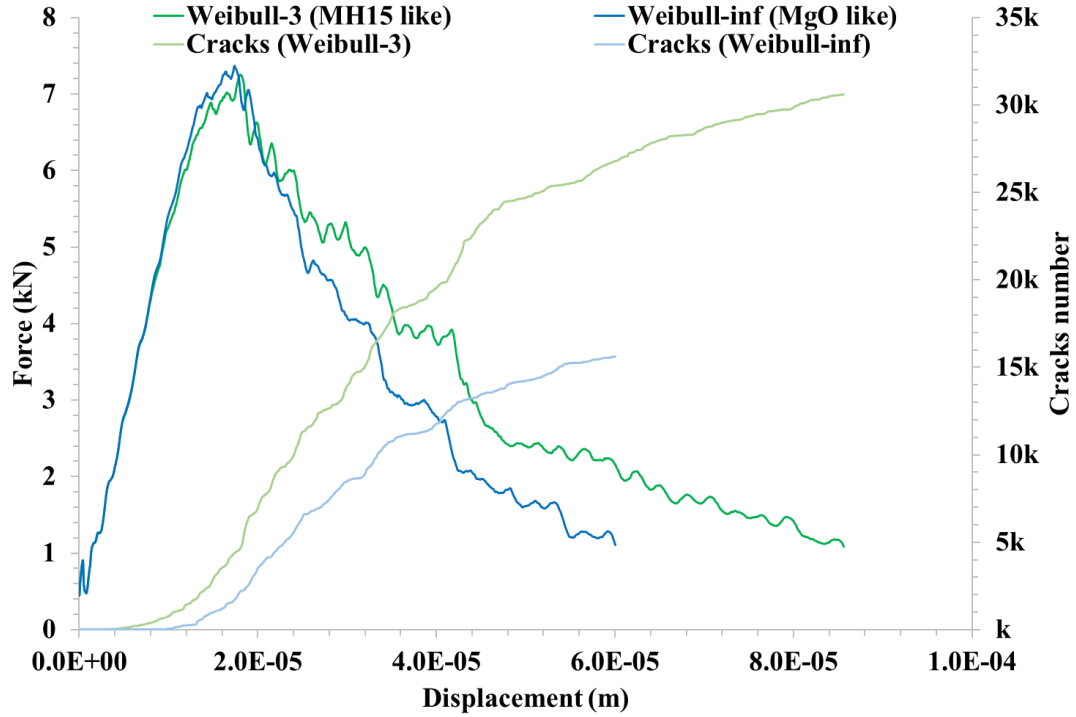
Fig. V-9. Comparison of the force-displacement curves and cracks evolutions during numerical DEM simulation of WST for two different Weibull moduli (m =3 and ∞).

Overall, the impact of decreasing *m* in increasing post-peak area is evident. It is showing that in WST, contrary to the uniaxial tensile test, most of the crack branching phenomenon occurs after the force-displacement peak. This increase in the post-peak area of WST, which corresponds to the total fracture energy, will be quantified in the next section.

V.3.3. Fracture energy and brittleness number

Based on the curves obtained for the WST simulation, a quantitative verification for fracture behaviours was considered. For this purpose, firstly, the area under the force-displacement curve up to 15% of the peak was calculated, as described in Eq. I-15. The calculated total energy is then separated into two parts: the stored elastic energy and the actual fracture energy, which relates to the energy consumption for crack propagation as described in Fig. V-10. Hence, the fracture energy is obtained from the difference between the total energy and the elastic energy. In this way, the elastic and fracture energies evolution for the two numerical results were plotted in Fig. V-11. As can be seen, the fracture energy for the sample using Weibull distribution ($m = 3$, representing MH15) is significantly higher compared to the sample with uniform local tensile strength value ($m = \infty$, representing MgO).
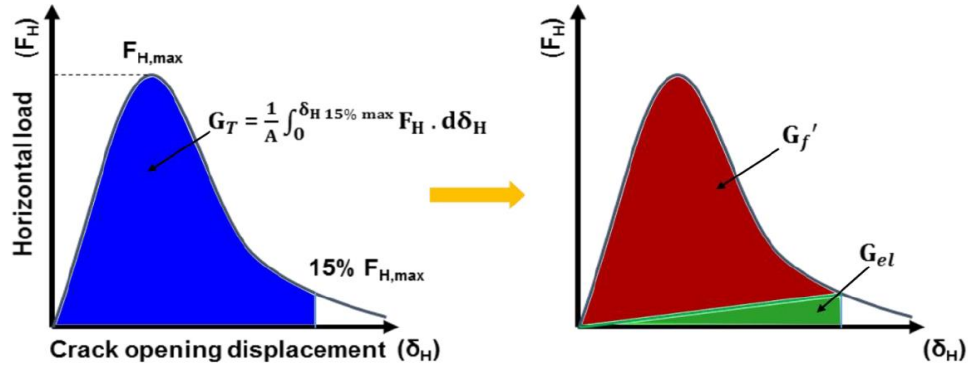
Fig. V-10. Typical WST force-displacement curve and area under the curve corresponding to: (a) total energy and (b) dividing total energy into fracture (red) and stored elastic (green) energies (Khlifi 2019).
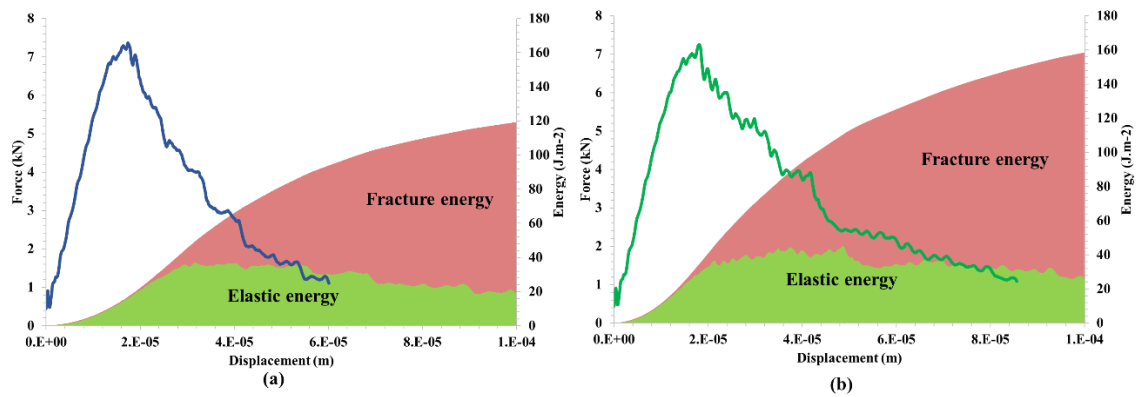
Fig. V-11. Force-displacement curves combined with elastic and fracture energies evolution during numerical DEM simulation of WST for two different Weibull moduli: (a) representing MgO ($m = \infty$) and (b) representing MH15 ($m = 3$).

It should be noted that absolutely no work has been managed to mimic the energy consumption during WST quantitatively. Nevertheless, the numerical fracture energy (120 J/m^2, as reported in Table V-3) resulting from uniform local tensile strength value ($m = \infty$, representing MgO) is in rather good accordance with the experimental result on pure MgO (130 J/m^2, as reported in Table V-1). Moreover, in the case of the sample with Weibull distribution of $m = 3$ (representing MH15), the numerical fracture energy (158 J/m^2, as reported in Table V-3) is higher than the MgO-like sample which is in line with experimental observation. However, this value compared to the experimental result on pure MH15 (266 J/m^2, as reported in Table V-1) is not high enough. By the way, if the quantitative calibration is aimed, it is possible to achieve higher fracturing by reducing further the Weibull modulus, as shown in Chapter IV:.

Table V-3. Calculated fracture parameters for two numerical samples ($m = 3$ and ∞)

Representative experimental material	Weibull modulus (m)	Specific fracture energy (J/m^2)	Brittleness number (-)
pure MgO	∞	120	0.56
MH15	3	158	0.38

Afterwards, the brittleness number was used as an indicator for the brittleness of refractories (Harmuth *et al.* 1997b). The obtained force-displacement diagrams (Fig. V-9) were used to calculate the brittleness number in this numerical study.

As a reminder, the brittleness number (*B*) is a shape-independent and size-independent index in order to characterise fracturing behaviour (Bazant *et al.* 1988) (Harmuth *et al.* 1997a). In this context, the Brittleness number (*B*) is proportional to energy stored elastically at crack initiation over total fracture energy:

$$B \propto \frac{energy\ stored\ elastically\ at\ crack\ initiation}{fracture\ energy\ for\ total\ fracture} = \frac{W_{Elastic}}{W_{Fracture}}$$

Using this concept in combination with previously introduce Eq. I-17 will allow computing the brittleness number of numerical samples. The calculated specific fracture energies and the brittleness numbers for these two numerical samples was shown in Table V-3. These results confirm that using Weibull distributions for local tensile strength decreases the brittleness of the sample.

Overall, random local strength distributions in DEM models, such as Weibull distributions, which were used in the present study, could be used to calibrate the amount of fracture energy and its related brittleness number. It should be emphasised that, at this stage, this section aimed only to verify the impact of using Weibull modulus for randomisation of the local tensile strength on the brittleness number of the material qualitatively. Therefore, this comparison has been made only between two numerical samples, one of them using Weibull modulus (*m* = 3) determined previously from the pre-peak shape of the experimental stress-strain curve in tension. Nevertheless, the work of fracture is more related to the post-peak shape of the experimental load-displacement curve in WST. Therefore, it could be better in future to refine the Weibull modulus from this experimental WST curve. This would most probably lead to assigning a lower value of *m*.

V.3.4. Crack branching simulation confronted to DIC results

In this section, the crack propagation simulations during the WST for the two investigated numerical samples is qualitatively compared to the pure MgO and MH15 DIC experimental outputs in Fig. V-12. Note that for plotting these figures, the complete detachment of an FJM contact is considered as one crack (shown in yellow) on the surface of the sample. It means that all the 16 FJM sub-surface elements have been broken (as explained in section II.4). Thus, other bonds with partial detachments of these 16 FJM sub-surfaces are not plotted here.
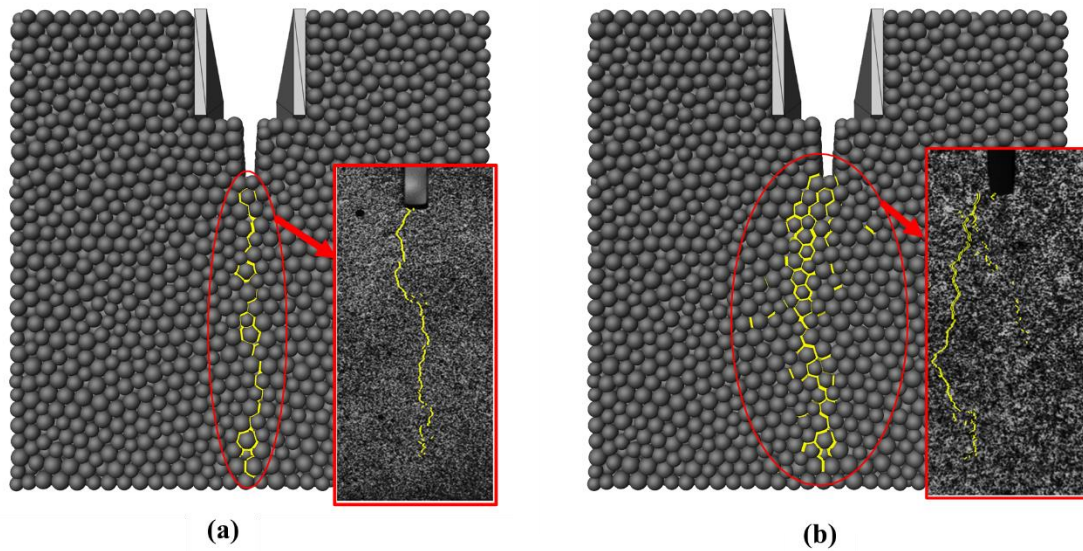
Fig. V-12. Comparison of the crack paths from DEM simulation vs DIC outputs (in the red frame, zoom of D cases from Fig. V-5 and Fig. V-6):
(a) case of pure MgO with a relatively straight crack path, and (b) case of MH15 with a deviated crack path. DIC results from Khlifi *et al.* (Khlifi *et al.* 2019)

Regarding Fig. V-12 (a), at first glance, it shows that in the simulation of the pure MgO, the sample was broken with a relatively straight fracture path, without any crack branching, which is in line with a highly brittle material. On the other hand, regarding Fig. V-12 (b), in the simulation of the MH15, the sample exhibits a rather deviated crack path and crack branching, which is in line with a quasi-brittle behaviour.

Overall, these results are showing acceptable qualitative fracture behaviour in comparison to the real model materials, which confirms the ability of the proposed DEM numerical approach in reproducing the crack branching phenomenon during WST. These very first results on that matter should be seen as a first attempt to describe the micromechanical behaviour of pre-cracked materials with a DEM approach using local strength randomisation based on Weibull modulus. Of course, further steps should try to consider the thermal history of the material (generation of microcracks by CTE mismatch between constituents) and integrate local physical mechanisms responsible for energy consumption during cracking (involved surface energy during cracking and friction between unbonded elements).

V.4. DEM/FVM coupling for Wedge Splitting Test simulation

For sure, DEM modelling is a promising approach that is currently under development by different research groups in order to provide a better description of micromechanical behaviour emerging from heterogeneous microstructure, which contains pre-existent microcracks. However, this type of modelling requires a large amount of calculations resources due to its discrete nature. For example, here, the presented WST numerical models of the previous section require 55 minutes on a rather powerful work station (Intel Core Xeon E2186M 4.0 GHz, SSD, 16 GB RAM, 12 parallel threads) even with a rather

limited number of elements (36k). Therefore, in order to go a step further in the future (more complex local numerical treatments and larger concentration of discrete elements), the general strategy will be to concentrate the discrete elements to the zone of interest where potential fractures could occur and apply another more efficient numerical scheme (FEM, FVM…) for the zones where no cracks are expected.

Since the 1980s, such different discrete/continuous coupling approaches were developed for different scales: from the molecular scales (Clementi *et al.* 1988) to the metric scales such as rock slopes simulations (Munjiza 2004). In recent years, these coupling approaches were intensively developed to be able to simulate complex phenomena such as fracturing (Zhang *et al.* 2017) (Leclerc *et al.* 2019). The main goal of this section is to investigate the application of a hybrid model by coupling a discrete DEM model with a continuous model for enhancing the simulation of WST. As mentioned, in fracture mechanics simulations, the main interest of discrete-continuous coupling is thus, to increase the performance of the model by replacing the potential non-damaging zones with a continuous model. Here, in the case of WST, the potential fracturing zone has a relatively small volume compared to the whole sample. Therefore, to make the simulations more efficient, it is proposed to replace the non-damaged zones with a continuous model, as shown in Fig. V-13. It should be noted that for this first attempt, the fracturing region thickness has been arbitrary set (for the sake of geometrical simplicity) to the thickness of the larger notch (24 mm, on top of the sample). This thickness will be enough for the demonstration of feasibility but probably should be enlarged later for the less brittle materials.

In the PFC framework, the proposed continuous approach for coupling with DEM is the Finite Volume Method (FVM), as introduced in section I.3.1.3, provided by FLAC3D[9] (Fast Lagrangian Analysis of Continua). In this way, the sample will be divided into three zones:

- one central DEM region where it is possible to initiate and propagate numerous cracks;
- two lateral FVM zones, which are considered purely elastic (without any cracks), where the boundary conditions are applied.

The advantage of such an approach is to potentially increase the resolution of the DEM region, leading to a more precise fracturing simulation. Besides, thanks to this optimisation, it will be possible to introduce other types of discrete elements, such as rigid blocks, to simulate the microstructures closer to reality, as will be described in section V.4.6.

---

[9] https://www.itascacg.com/software/FLAC3D
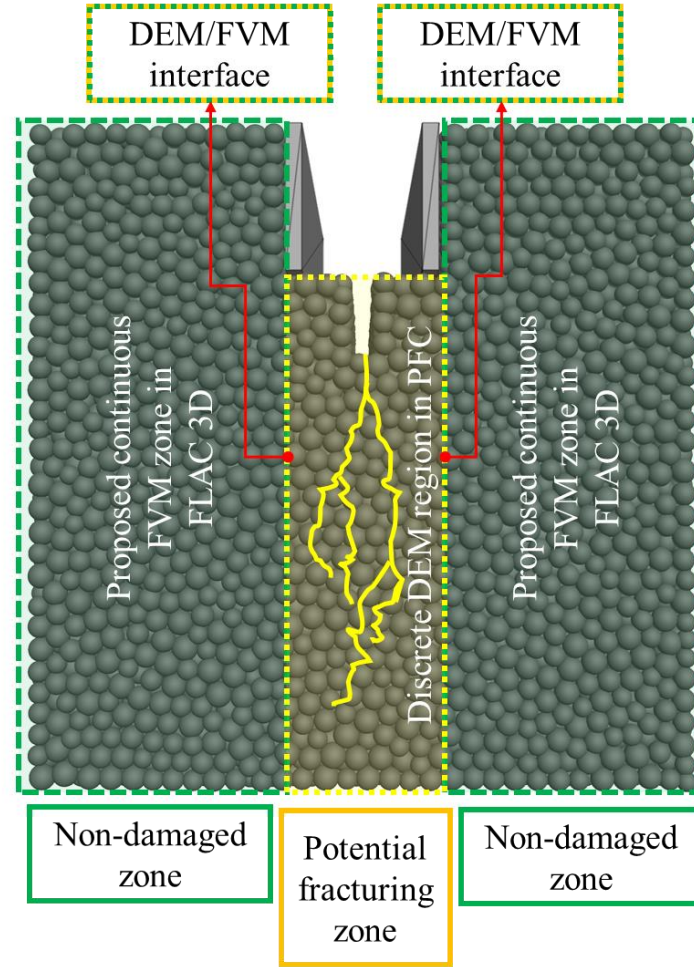
Fig. V-13. Description of the proposed hybrid DEM/FVM model for simulating WST.

V.4.1. A brief reminder for DEM input parameters

In this study, the same input DEM parameters were considered ($m = \infty$ and 3), used as in section V.3. As a reminder, an overview of these DEM input parameters is given in Table V-4.

Table V-4. DEM region input parameters in the hybrid model for WST

Description	Density	Local Young's modulus	Local stiffness ratio	Local tensile strength	Local tensile strength		Local cohesion	Local friction angle
Material	both	both	both	MgO	MH15		both	both
Abbreviation	(ρ)	E^{*loc}	K^{*loc}	t^{loc}	m	σ_0	c^{loc}	ϕ^{loc}
Initial value	2600	20	4	10	3	10	25	0
Unit	Kg/cm^3	GPa	-	MPa	-	MPa	MPa	Degrees

It should be mentioned that, at this stage, the size of the elements has been voluntarily kept at the same value in order to conserve the same local parameters (calibration being dependant on the size of elements as pointed out in section II.4.3) and thus be able to compare the final results to previously presented full DEM model (section V.3). Of

course, for further studies, it could be more interesting to enlarge the number of elements by decreasing their size in the zone of interest (as mentioned previously).

V.4.2. An overview of DEM/FVM coupling strategy

In order to manage DEM/FVM coupling, DEM walls (section II.2.1) are introduced at the interfaces between DEM and FVM domains (see *DEM walls wrapped FVM zones* in Fig. V-14). This wrapping process, which is able to create DEM walls from FVM surface meshes, is possible thanks to the *wall-zone* interaction command in PFC3D. In this way, the surface FVM elements at the interfaces that come from FLAC3D will act as DEM walls with translational and rotational movement abilities (Itasca Consulting Group Inc. 2020) that follows the FVM surface meshes. In this way, it should be noted that each surface FVM elements, which are wrapped with DEM walls, consist of two triangular facets (as explained in II.2.1), and thus, the global DEM wall is flexible enough to strictly follow the strain of each FVM element. The contacting discrete elements at these interface walls were *glued*. These *glued* contacts are shown in red in Fig. V-14. Here, again, the FJM contact model is used for these *glued* contacts. The elastic parameters of these *glued* contacts were set equal to the values of the rest of the discrete domain (see Table V-4). However, to avoid any cracks at the interface, the fracture parameters of these *glued* FJM bonds were set to infinite values ($t^{loc} = 1 \times 10^{100}$ MPa, $c^{loc} = 1 \times 10^{100}$ MPa).
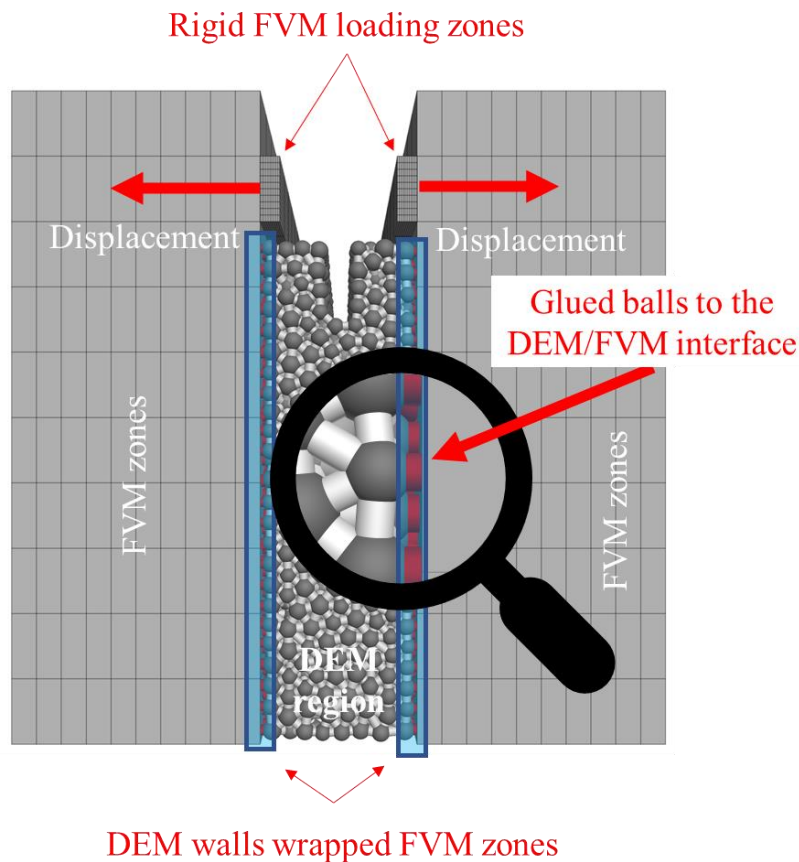

Fig. V-14. Proposed DEM/FVM hybrid model for WST.

In order to ensure continuity of stress and strain between DEM and FVM domains, special attention should be paid to the definition of material properties:

- *elastic parameters* - both media should have the same elastic behaviour (Heider *et al.* 2012). In this way, both Young's modulus and Poisson's ratio of the FVM domains should be set to the DEM apparent elastic properties (E^{ap} = 26 GPa and ν^{ap} = 0.15);

- *density* - to guarantee the continuity of the dynamic behaviour, the same density should be applied to both domains (Lempriere 2003). Special attention must be made in the case of the DEM domain by considering its apparent density, which does not correspond to the density of each element. In fact, the apparent density should be obtained by considering the local density of the discrete elements and the associated porosity. Therefore, the density of the elements should be voluntarily higher (ρ = 2600 Kg/cm^3) in order to obtain the targeted apparent density (ρ = 2120 Kg/cm^3) of the DEM domain (including porosity);

- *time step* - to ensure a synchronized exchange of data in each time increment between the two domains, the same calculation time step values should be imposed for both discrete and continuous models. In this way, the information needed for the coupling between the two domains (the displacements of the discrete elements for DEM and the node displacements for and FVM zones) is transmitted at each time step from one code to another (Breugnot *et al.* 2016).

V.4.3. Force-displacement curves for Wedge Splitting Test (WST)

Similar to full DEM models (as explained in section V.3.2), these DEM/FVM hybrid simulations were done in displacements-driven loading at a constant rate. These displacements are applied to the *rigid FVM loading zones* (as shown in Fig. V-14) in opposite directions in order to open the sample in mode I. To obtain the force-displacement curves (see Fig. V-15), the resulting forces coming from the sample response on these loading zones are monitored. These force-displacement curves and the crack numbers evolution have been again compared for the two previously investigated Weibull moduli: $m = 3$ and $m = \infty$. As previously observed in full DEM simulations, the present DEM/FVM simulations are showing that:

- low Weibull modulus (m) enlarges the post-peak part;
- low Weibull modulus (m) does not significantly change the apparent pre-peak behaviour and the peak values (force and displacement);
- the cracking process starts at lower displacements and leads to a higher number of cracks for low Weibull modulus (m).

As expected, these points show that the proposed hybrid model is able to simulate higher fracture energy for the lower Weibull modulus ($m = 3$, representing MH15) compared to the numerical sample with high Weibull modulus ($m = \infty$, representing MgO).

To validate this approach, the obtained force-displacement curves for the hybrid model are also compared to the full DEM simulations (see grey dashed curves in Fig. V-15). This comparison shows very similar behaviour between hybrid and full DEM

models. This observation highlights the interest in using the hybrid model to significantly decrease the calculation time while obtaining quite similar results.
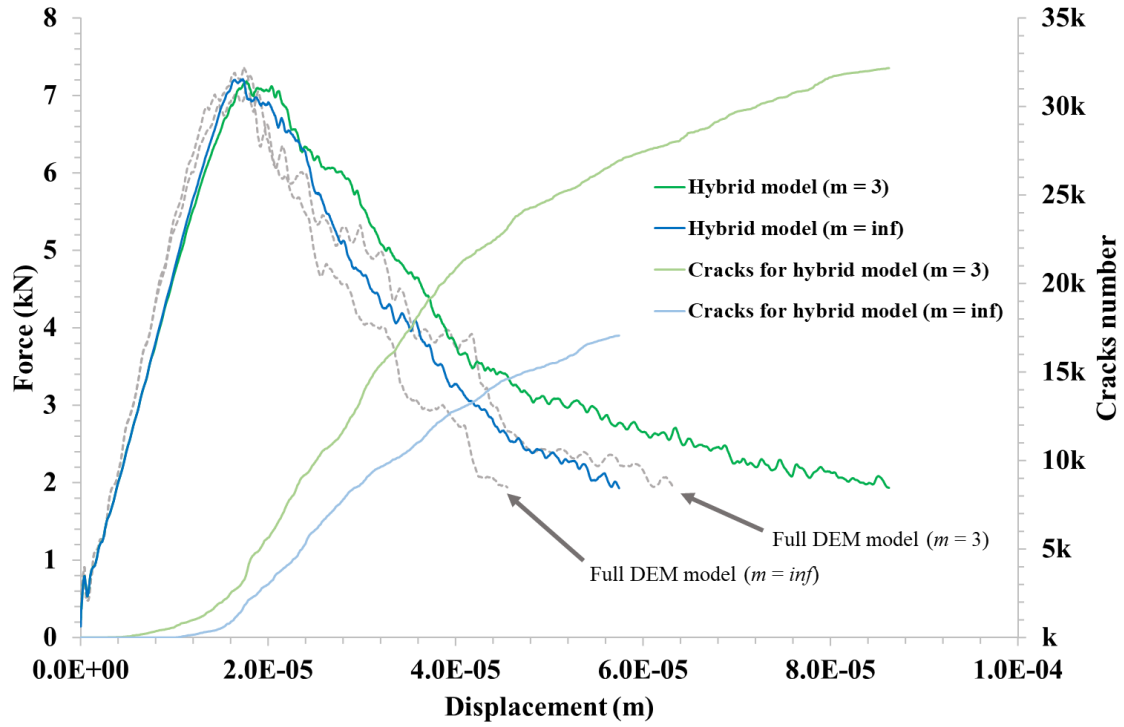
Fig. V-15. Comparison of the force-displacement curves of WST for hybrid DEM/FVM and full DEM simulations with the two different Weibull moduli ($m = 3$ and ∞).

The main advantage of using such a hybrid model is, in the future, to decrease the computational time that could be required for more complex microstructure design in the zone of interest. In the present case, which should be seen as the simple demonstrator, the calculations time was decreased from 55 minutes for the full DEM model down to 8 minutes in the hybrid model. Even if, in the present case, the number of discrete elements in the central part of the sample is not huge (8k discrete elements in all samples), the force-displacement and the crack number evolutions are rather similar to the full DEM model. A higher level of similarity would probably be obtained for a larger number of elements in the central part.

V.4.4. Fracture energy and brittleness number

Again here, the brittleness number notion was used as an indicator for the brittleness of these models. The obtained force-displacement diagrams of the DEM/FVM hybrid model (Fig. V-15) is used to calculate the brittleness number. The calculated specific fracture energies and the brittleness numbers are shown in Table V-5. These results show that using a Weibull distribution significantly influences brittleness number and the specific fracture energy. This is in line with the previous observations for full DEM models. Table V-5 allows to quantitatively compare the two proposed approaches (hybrid and full DEM). The brittleness numbers and the specific fracture energies are relatively in accordance with the full DEM model.

Table V-5. Calculated fracture parameters for hybrid and full DEM models with the two considered Weibull moduli (m = 3 and ∞).

Representative experimental material	Weibull modulus (m)	Specific fracture energy (J/m^2)		Brittleness number (-)	
		Full DEM	Hybrid	Full DEM	Hybrid
pure MgO	∞	120	128	0.56	0.44
MH15	3	158	178	0.38	0.29

V.4.5. Crack branching simulation

As mentioned in section V.2, there is a strong link between microcracking process and fracture energy consumption, as highlighted by DIC observations (see Fig. V-5 (c) and Fig. V-6 (c)). In this way, the crack propagations for the two different Weibull moduli of the hybrid model are compared (see Fig. V-16). As expected:

- the sample with $m = ∞$ (pure MgO like) exhibits a relatively straight brittle fracture path without any crack branching;
- the sample with $m = 3$ (MH15 like) exhibits a deviated crack path with diffused damages and crack branching;

which are in accordance with the full DEM model.

Overall, these results show acceptable qualitative accordance between the hybrid model and the experimental observations shown in section V.3.4. It confirms the ability of the proposed DEM/FVM hybrid model to reproduce the crack branching phenomenon during WST. At this stage, the crack branching mechanisms are evidently limited to the central part (here defined to a width of 24 mm) managed by the DEM approach in the present work. In comparison to the real size of the process zone (30 to 40 mm, Grasset-Bourdel, 2011) that could be experimentally observed by DIC (Khlifi 2019) on quasi-brittle materials, the current size of crack branching in the presented numerical model is, in fact, rather limited. For sure, this area of crack branching development could be enlarged by a further decrease of Weibull modulus and by assigning a larger thickness to the central area to be treated by DEM.
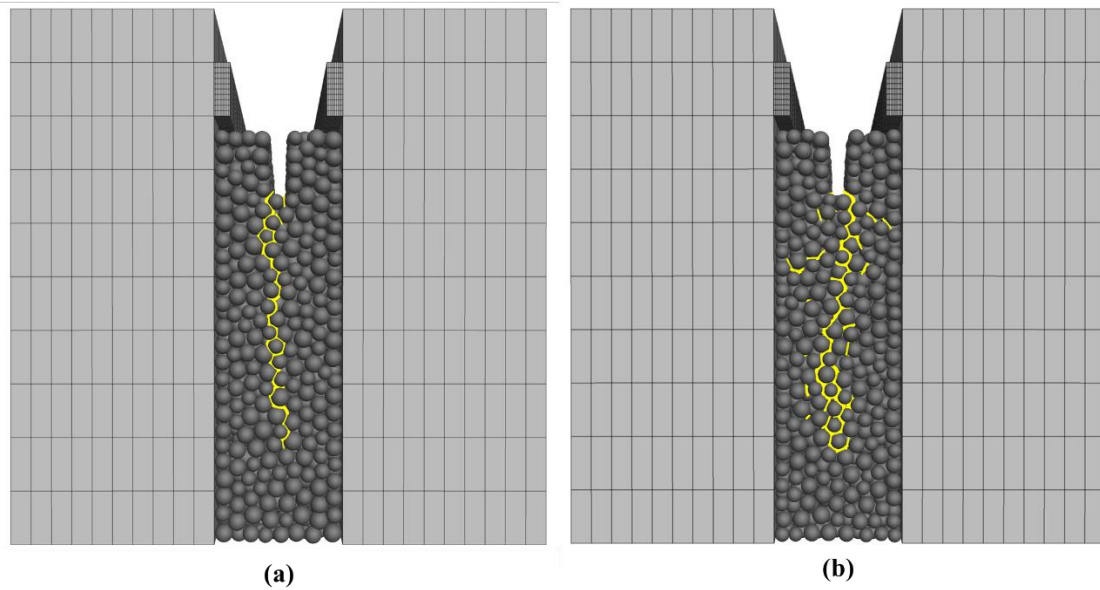
Fig. V-16. Comparison of the simulated crack paths between the two considered Weibull moduli: (a) $m = \infty$ and (b) $m = 3$.
These figures were taken at 40% of the peak in the post-peak phase.

V.4.6. DEM/FVM WST simulation by using rigid blocks

This section aims to investigate the potential feasibility of using Rigid Blocks (RB, as introduced in section II.2.1) to simulate accurately diffused damages and crack branching phenomena by considering the effect of the large aggregates which constitute the skeleton of the microstructure. It should be noted that aggregates in refractories are usually much stiffer than the matrix. In this way, as a reminder, RBs are a rigid single discrete element with complex (convex) geometries. By considering such complex geometries, these RBs could be advantageously used to mimic these large aggregates within the microstructure. In the case of MH15-like material, RBs could mimic the large rigid aggregates of both MgO and Hercynite, while the smaller discrete elements could mimic the brittle MgO matrix. As a first trial, random aggregates shapes (inspired from the real MgO and Hercynite aggregates) were distributed up to nearly 36% of the total volume. To do so:

a) a sample only containing matrix discrete elements has been first prepared;
b) the RBs were introduced randomly within the matrix until it reaches 36% of the total volume;
c) the matrix discrete elements inside RBs were removed;
d) finally, contacts between RBs and matrix were assigned with FJM bonds.

This process is shown in Fig. V-17 for a single RB aggregate within the discrete element matrix.

Fig. V-17. Illustration of the four steps procedure for RB grain insertion:
(a) Initial sample only containing discrete elements, (b) introduction of RB,
(c) removing local discrete elements and (d) assigning the FJM bonds at the interface.
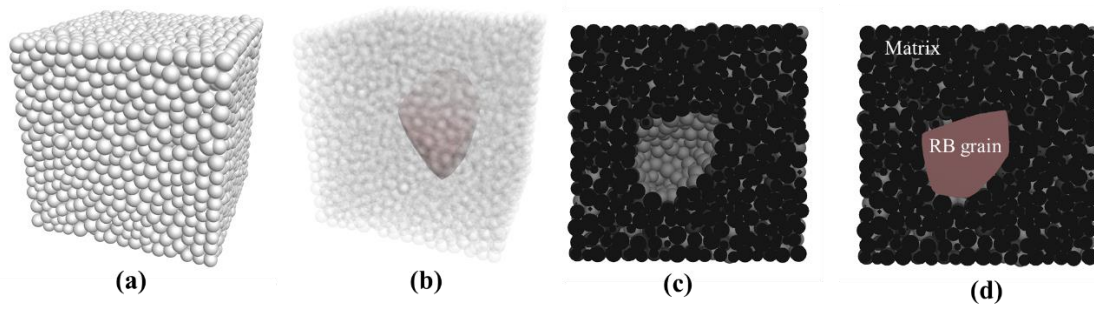
In the same way as the previous section, two models (same positioning of discrete elements and RBs within the sample) were prepared with different Weibull moduli ($m = \infty$ and 3). All the other input parameters were set equal to values already mentioned in Table V-4. For aggregates/matrix contacts in this first attempt, FJM bonds have been used with the same properties as matrix/matrix, even if different local properties could be attributed later.

Firstly, to only investigate the impact of introducing aggregates, the force-displacement curve of the sample with $m = \infty$ (see Fig. V-18 (a)) is compared to the case $m = \infty$ without aggregates. As can be seen, by introducing aggregates to the model:

- the apparent pre-peak rigidity decreases. This result is, in fact, quite surprising since RBs exhibit an infinite Young's modulus and would need further investigations to understand the effect of the bond properties at the interface with discrete elements;
- the force peak remains relatively the same;
- the post-peak region is for sure much larger. This important result is completely in line with experimental results, for which it is clear that the aggregate skeleton of a refractory material also plays a key role in fracture energy.

In the same way, the force-displacement curve of the sample with $m = 3$ (see Fig. V-18 (b)) is compared to the case $m = 3$ without aggregates. Similarly to $m = \infty$ previously commented, the aggregates strongly increase the fracture energy. From these results, it appears that decreasing m to 3 does not significantly change the shape of the force-displacement curve (comparison between Fig. V-18 (a) and Fig. V-18 (b)). Nevertheless, it could be interesting in the future to consider lower values of Weibull modulus.

Concerning the accumulated number of cracks which are plotted in both cases (Fig. V-18 (a) and Fig. V-18 (b)), it appears:

- for the same Weibull modulus, the accumulated number of cracks is a little bit smaller when aggregates are introduced. This result is, in fact, quite surprising regarding the fracture energy (area below the force-displacement curve) but may result from the fact that rather flat surfaces of the aggregates lead to a decrease in the average density of contacts;
- decreasing the Weibull modulus (with aggregates) again leads to a significant increase in the accumulated number of cracks (16k for $m = \infty$ and 24k for $m = 3$ at the same displacement level of ≈ 0.1 mm)

<div align="center">(a)   (b)</div>
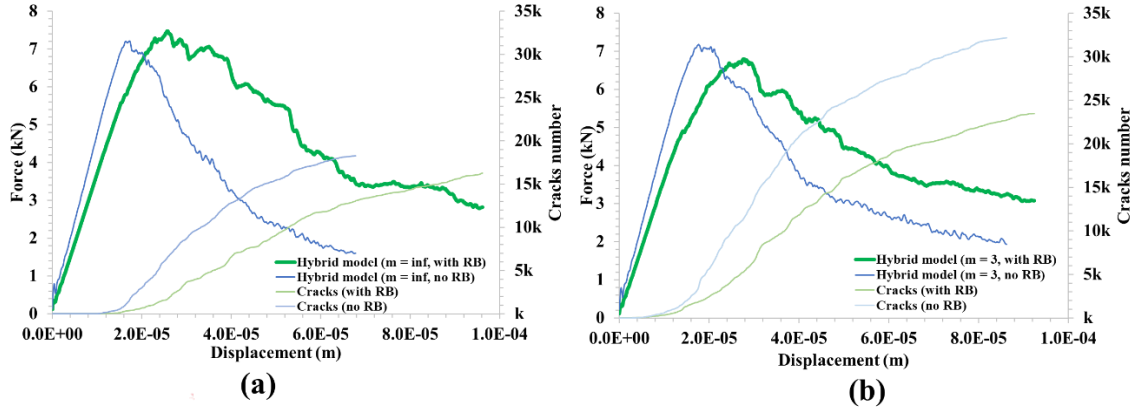
Fig. V-18. Comparison of the force-displacement curves of WST for the hybrid DEM/FVM model containing RBs with the two different Weibull moduli: (a) $m = \infty$ and (b) $m = 3$.

In the end, the simulations of the crack propagation during the WST in the hybrid model containing RBs for different Weibull moduli ($m = \infty$ and 3) are shown in Fig. V-19 (a) and (b). Note that for the sake of display of RBs, the same cross-section inside the material is shown. As expected:

- the sample (a) with $m = \infty$ (pure MgO like) exhibits a relatively straight brittle fracture path that goes around the aggregates;
- the sample (b) with $m = 3$ (MH15 like) exhibits a deviated crack path with some diffused damages and crack branching going around the aggregates.

<div align="center">(a)   (b)</div>
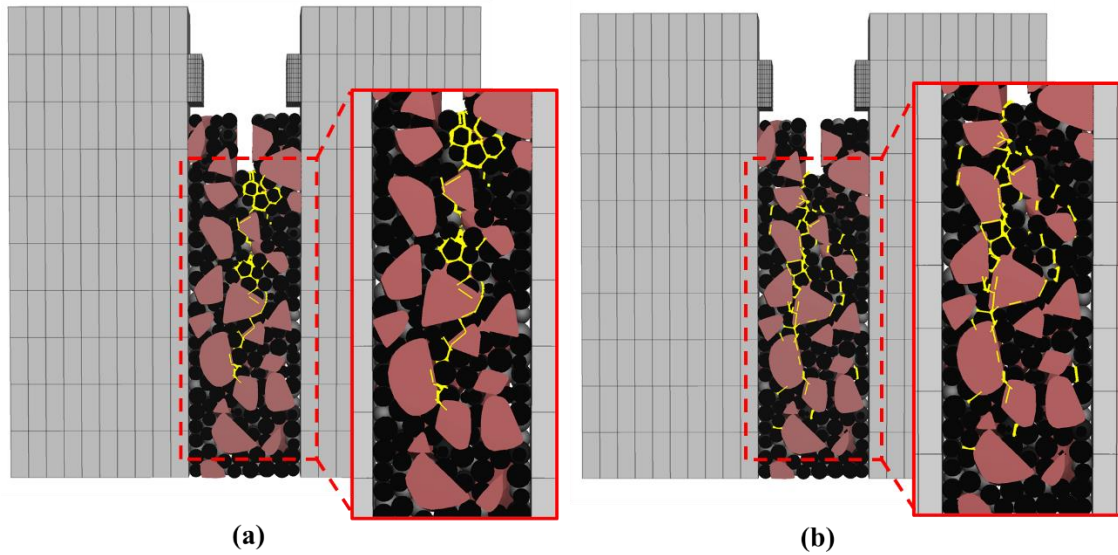
Fig. V-19. Comparison of the simulated crack paths produced by DEM/FVM hybrid model containing rigid blocks between the two considered Weibull moduli: (a) $m = \infty$ and (b) $m = 3$.
These figures were taken at 40% of the peak in the post-peak phase.

Overall, this part of the work should be seen as the first attempt of combining DEM using RBs, coupled with FVM continuous zones. This approach would allow to concentrate computing resources in the central part of the sample, trying to mimic as close

as possible microstructure effect on the macroscopic thermomechanical property. For sure, there still many points to be studied in that area in the future. At this stage, only very qualitative results were presented. More quantitative investigations should be managed to mimic:

- the granular distribution of these aggregates within the microstructure of real refractory materials;
- the different shape of these grains that could influence the fracture behaviour;
- the pre-cracks which could be introduced within the microstructures by CTE mismatch;
- the thermal history of the material that could affect the microstructure.

V.5. Conclusions

The main idea of the DEM approach proposed in Chapter IV was to use a statistical distribution of local strength. This approach aims to mimic the impact of the pre-existing microcracks, which strongly influence the macroscopic mechanical behaviour. This chapter aimed to investigate further the applicability of this proposed approach to reproduce key phenomena such as diffused damages and crack branching. In such a way, the Wedge Splitting Test (WST), commonly used in the refractory field to characterise the fracturing behaviour, was considered in this chapter as the reference test. Here, two typical refractories were considered: pure MgO, which is highly brittle and MH15 which exhibits strong mechanical non-linearities. The experimental data from WST coupled with Digital Image Correlation (DIC) measurements of these two materials were used as reference results.

Firstly, two numerical samples with two different statistical distributions of local strengths were simulated in a WST configuration:

- a sample with a single uniform value for local strength to represent pure MgO;
- a sample with a Weibull distribution ($m = 3$) for local strength to represent MH15.

The proposed DEM model showed good qualitative accordance to force-displacement curves, pre-peak and post-peak behaviours, specific fracture energies and brittleness numbers. Also, the fracture paths exhibited qualitatively good agreements in comparison with experimental DIC observations.

However, such DEM calculations require huge computational resources and time. Hence, some solutions to improve the computational performance were investigated in this chapter. The first approach was to couple the DEM model with the Finite Volume Method (FVM). In this way, the DEM domain was localised only in the fracturing zone of the WST sample. It allows reducing the number of discrete elements significantly. The continuous FVM zones are placed in the regions where the damages are not expected. This technique allows to reduce up to 85% of the calculation time. To go further, an additional optimisation technique was considered using rigid blocks for mimicking large aggregates within the microstructure. A comparison with full DEM model simulations showed that these optimisation techniques did not significantly affect the results.

Despite the good qualitative accordance, further works are needed to achieve more quantitative results. However, the significant gain in terms of calculation times

encourages further investigations in order to provide quantitative simulations of non-linear behaviour of refractories in WST configuration in a more reasonable time.

General conclusions and perspectives

In different industrial fields, refractories are continually exposed to extreme conditions such as high temperature, mechanical loads, corrosion, and, more importantly, thermal shocks. Especially in the steel making industries, due to the filling and emptying of melted iron in the steel ladle, refractories face severe thermal cycles. These thermal cycles induce stresses, which could weaken the in-service refractories and potentially leads to complete failure. Such failures could be very costly and result in a significant loss of production, polluting the environment and, more importantly, threatening the personals' safety. Therefore, focusing on designing and improving the thermal shock resistance of the refractories has gained increasing interest. In this way, the ATHOR project (Advanced THermomechanical multiscale mOdelling of Refractory linings, supported by the European Commission) was defined and focused on the thermomechanical investigation and behaviour prediction of refractory linings: from the grain scale to the whole steel ladle structure.

In fact, the thermal shock resistance of refractories is closely related to the material ability to resist against crack propagation through significant energy dissipation by creating new surfaces and friction mechanisms. More specifically, as mentioned in the literature, voluntarily introducing a large number of microcracks within the microstructure of refractories could improve their thermal shock resistance through a high non-linear behaviour in tension. However, due to the complexity of the thermal shock phenomenon, it is difficult to predict it precisely. As a part of the ATHOR project, this PhD aimed to take advantage of advanced numerical tools to study further this thermal shock phenomenon and its impact on the mechanical behaviour of the materials. For this purpose, a suitable numerical method was required to be able to simulate such an extended microcracking process. In this way, a comparison between different numerical methods was done to choose the one that could initiate and propagate numerous discontinuities. Even if certain continuum methods had shown an accurate approach for fracturing modelling, the interaction of discontinuities, managing a high number of cracks and predicting complex cracking patterns is still a challenging point. On the other side, because of the discontinuous nature of DEM, initiation and propagation of a high number of cracks are not problematic for such a discrete model. Hence, the DEM approach was assigned as the main modelling approach in this PhD.

In order to simulate microcracks in a continuous media by DEM, different models were investigated. In this way, the Flat Joint Model (FJM) was chosen because of its ability to mimic the microstructure of angular and interlocked grains. Based on the literature, this model had shown a high potential for simulating fracturing processes in quasi-brittle materials. Due to the necessity of calibration of the input parameters in the discrete models, a parametrical local to apparent study was managed in Chapter II:, which led to a rationalised calibration algorithm for FJM. This model is implemented in a DEM framework, called Particle Flow Code (PFC), from ITASCA company (partner of this PhD).

By choosing the modelling method and the framework, it was aimed to numerically investigate the heterogeneous microstructure of refractories, as their pre-defined microstructure significantly influence their ability to sustain thermal shocks. Therefore, it was crucial to model better the strong relationships between such heterogeneous microstructures and the macroscopic thermomechanical behaviour. For this multi-scale purpose, in Chapter III:, a DEM periodic homogenisation approach by using the notion of the Representing Volume Element (RVE) was proposed to model a pseudo-infinite media. It should be noted that up to now, the periodic homogenisation for a continuum media in DEM is not as robust as in FEM. The implementation of such periodic homogenisation approach in DEM is, in fact, advantageous as this approach allows working on a pseudo-infinite small domain, thus with a limited number of discrete elements. This proposed DEM periodic homogenisation approach was validated for bi-phase and porous materials by comparing the simulated apparent elastic properties to the referenced experimental results. In addition, the obtained numerical results were successfully compared to Hashin and Shtrikman analytical model and FEM simulations.

By validating this approach, it is possible to accurately investigate the elastic properties (Young's modulus, Poisson's ratio, and potential anisotropy) from the micro-scale (related to local inclusions or pores) to the macro-scale. As a potential further application, this validated approach could be used to predict the thermomechanical behaviour of heterogeneous materials containing numerous microcracks. In fact, as mentioned, the fracturing process and microcracking simulations are among the main interests of using DEM compared to FEM. Therefore, the simulation of the mesoscale microcracking process in a continuum media was investigated for the next step.

In reality, the numerous microcracks within the microstructure of refractories are induced by the Coefficient of Thermal Expansion (CTE) mismatch between constituents. The presence of these microcracks usually induces a non-linear quasi-brittle mechanical behaviour. To numerically reproduce this phenomenon, in Chapter IV:, a DEM model was proposed based on the randomisation of local fracture criteria, following a Weibull distribution. This proposed approach was aimed to reproduce the non-linear quasi-brittle mechanical behaviour under tensile monotonic and cyclic loads by varying the Weibull modulus. This approach was quantitatively validated by comparing simulated stress-strain curves to the reference Alumina Spinel experimental data. A meta-algorithm was proposed to calibrate potentially any DEM model qualitatively and quantitatively for simulating such non-linear quasi-brittle behaviour. In fact, this approach can tune the brittleness of the material by promoting diffused damages and crack branching into the microstructure. To verify this last point, the proposed approach was applied to mimic the Wedge Splitting Test (WST), which is commonly used to quantify the brittleness of refractories.

WST could be, in fact, an index for characterising the quasi-brittle behaviour of refractories. Again, this behaviour is closely linked to the presence of pre-existing microcracks and their ability to promote crack branching. Therefore, Chapter V: was aimed to verify the ability of the proposed statistical numerical approach to reproduce this key phenomenon. In such a way, two model materials were used as references to highlight different fracturing behaviour: a highly brittle pure Magnesia and a quasi-brittle Magnesia Hercynite. Afterwards, by using different Weibull modulus, the proposed DEM approach

for local strength randomisation simulated a wide range of fracture behaviour. Higher fracture energy can be achieved by lowering the Weibull modulus. These results were qualitatively compared to the fracture behaviour of the two reference materials. Besides, the crack branching obtained from these simulations were qualitatively compared to the experimental Digital Image Correlation (DIC) observations. In the end, a discrete/continuous hybrid model was proposed to optimise the WST simulations in order to save computational time. To go further in the optimisation way, rigid discrete blocks elements were introduced to act as large aggregates within the microstructures.

Considering the fact that the development of DEM to better understand the microstructure effects on thermomechanical behaviour of refractory materials started just a couple of years ago at IRCER (recruitment of Dr. Damien André in 2014, a first PhD on this subject between 2016 and 2019, the present PhD started in 2018), there is still for sure many improvements to manage in the future. A lot of perspectives can be thus imagined at this stage. As top priority level for coming years, further developments should target:

- **to combine complex behaviour during mechanical loadings and temperature variations.** Taking into account that the thermal history of materials is extremely important in the non-linear thermomechanical behaviour of heterogeneous refractories, the DEM tools should be able to couple this previous thermal history with the later mechanical response during loading. This is, in fact, the case for GranOO, which has been used in the thesis of Dr. Troung Thi Nguyen (defended in 2019), but in fact, PFC with FJM, unfortunately, was not able (at this stage) to account for this thermal history.

- **to comfort the coupling between DEM and other continuum methods.** As explained at the end of this work, the coupling between DEM and continuous methods could be very efficient to save computing resources and allocate a larger number of discrete elements for better simulating the zone of interest. In this aim, PFC coupled with FLAC3D have shown a great performance and produced valid results compared to the full DEM model. Unfortunately, at the beginning of this PhD, such coupling was not available in GranOO, but thanks to recent developments, the potential coupling is now available with FEM.

- **to go further with periodic homogenisation.** As explained in chapter III, periodic homogenisation is very efficient to quantitatively predict apparent properties, accounting for local properties of each constituent and for the microstructure of the material. Such periodic homogenisation works very well in PFC while it was not available in GranOO during this PhD. Nevertheless, recent developments allow to manage today such an approach. It could be thus interesting to check this new possibility in GranOO. To go a step further (in comparison to present work), it could be, of course, interesting to include microcracks coming from CTE mismatch between constituents and previous thermal history within these future models.

- **to account better for microcracks coming from CTE mismatch.** In the present work, microcracks from CTE mismatch has been represented thanks to the Weibull distribution of local strength values, and microcracks coming from the loading has been represented by partial rupture of the 16 local sub-surfaces of FJM bonds. PFC with FJM bond model is perfectly adapted to describe such microcracks during

loading, but that was a pity that such a sophisticated fracturing model was not able to model microcracks that could come from temperature variations. GranOO is able to work with both microcrack and temperature variation but with a simpler fracturing model. In fact, internal development within ITASCA is ongoing to account for mechanical interactions and temperature variation simultaneously and will be available soon.

- **to account better for the role of aggregates.** The proposed DEM/FVM hybrid model clearly demonstrated the strong influence of aggregates on fracture energy recorded during WST simulations. This first very interesting numerical result seems to be in line with some experimental observations. This study should be comfort in the future with a systematic investigation of aggregates size distribution, aggregates morphology and aggregates potential orientations coming from the production process (uniaxial pressing). This first attempt has been managed here thanks to the rigid block approach, available in PFC, which has the advantage of a user-friendly implementation (management of their sizes and geometries) but also has some drawbacks (infinite rigidity, which does not correspond to the real elastic properties, way to manage the bonds at the interfaces which seems to significantly affect the elastic response). Alternative options could be the usage of clumps in PFC or the usage of the cluster in GranOO, at the cost of larger computing time and lower resolution for angular shapes.

- **to account better for the physical mechanism, which leads to dissipate energy.** Up to now, no specific attention has been paid to the way in which the energy is consumed during cracking. In fact, from the physical point of view, one part of the energy could be consumed by the creation of new free surfaces (thermodynamic surface energy) and by frictional mechanisms (when two free surfaces are sliding). In general, nothing is currently managed in DEM tools to account for thermodynamic surface energy (during surface creation). This part of the energy consumption is probably integrated with the damping factor, which is commonly used to dissipate the vibrations. Concerning the second part of energy consumption, it could be tuned by local friction factors. Such a way may also allow adjusting macroscopic fracture energy during the WST.

These improvements of DEM modelling should lead to model accurately refractories in a multi-scale approach to better understand the impact of their microstructure on the thermomechanical macroscopic behaviour. These modelling tools may be used in the future to optimise such materials microstructures and save natural resources.

References

Alder, B.J., Wainwright, T.E. 'Studies in Molecular Dynamics. I. General Method'. *The Journal of Chemical Physics*, 1959, 31 (2): 459–66. https://doi.org/10.1063/1.1730376.

Alhajj Hassan, G., Leclerc, W., Pélegris, C., Guessasma, M., Bellenger, E. 'On the Suitability of a 3D Discrete Element Method to Model the Composite Damage Induced by Thermal Expansion Mismatch'. *Computational Particle Mechanics*, 2020, 7 (4): 679–98. https://doi.org/10.1007/s40571-019-00298-1.

Allen, M.P., Tildesley, D.J. *Computer Simulation of Liquids*, 1987. Oxford University Press.

Ammar, A., Leclerc, W., Guessasma, M., Haddar, N. 'Discrete Element Approach to Simulate Debonding Process in 3D Short Glass Fibre Composite Materials: Application to PA6/GF30'. *Composite Structures*, 2021, 270: 114035. https://doi.org/10.1016/j.compstruct.2021.114035.

Anderson, T.L. *Fracture Mechanics : Fundamentals and Applications, Fourth Edition*, 2017. CRC Press. https://doi.org/10.1201/9781315370293.

André, D., Girardot, J., Hubert, C. 'A Novel DEM Approach for Modeling Brittle Elastic Media Based on Distinct Lattice Spring Model'. *Computer Methods in Applied Mechanics and Engineering*, 2019, 350: 100–122. https://doi.org/10.1016/j.cma.2019.03.013.

André, D., Jebahi, M., Iordanoff, I., Charles, J., Néauport, J. 'Using the Discrete Element Method to Simulate Brittle Fracture in the Indentation of a Silica Glass with a Blunt Indenter'. *Computer Methods in Applied Mechanics and Engineering*, 2013, 265: 136–47. https://doi.org/10.1016/j.cma.2013.06.008.

André, D., Levraut, B., Tessier-Doyen, N., Huger, M. 'A Discrete Element Thermo-Mechanical Modelling of Diffuse Damage Induced by Thermal Expansion Mismatch of Two-Phase Materials'. *Computer Methods in Applied Mechanics and Engineering*, 2017, 318: 898–916. https://doi.org/10.1016/j.cma.2017.01.029.

Andreev, K., Harmuth, H. 'Numerische Simulation Des Mechanischen Und Thermomechanischen Verhaltens Der Feuerfestzustellungen von Stahlpfannen'. *Proc. of Gesteinshüttenkolloquium*, 2001.

Ashby, M.F. 'Chapter 4 - Material Property Charts'. In *Materials Selection in Mechanical Design (2nd Edition)*, edited by Michael F. Ashby, 57–96, 1999. Oxford, Butterworth-Heinemann. https://doi.org/10.1016/B978-1-85617-663-7.00004-7.

Askeland, D.R., Haddleton, F., Green, P., Robertson, H. *The Science and Engineering of Materials*, 2016. Springer US. https://doi.org/10.1007/978-1-4899-2895-5.

ASTM. *Refractories, Activated Carbon; Advanced Ceramics*, 2020, Vol. Volume 15.01. American Society for Testing and Materials, ASTM international.

Barenblatt, G.I. 'The Mathematical Theory of Equilibrium Cracks in Brittle Fracture'. In *Advances in Applied Mechanics*, edited by H. L. Dryden, Th. von Kármán, G. Kuerti, F. H. van den Dungen, and L. Howarth, 7:55–129, 1962. Elsevier. https://doi.org/10.1016/S0065-2156(08)70121-2.

Bazant, Z.P., Kazemi, M.T. 'Brittleness and Size Effect in Concrete Structures', 1988, 5: 8.

Belrhiti, Y. 'Etude de Matériaux Réfractaires à Comportement Mécanique Non Linéaire Par Mesure de Champs de Déformations', 2015. Doctoral dissertation, Limoges, France, University of Limoges. https://www.theses.fr/2015LIMO0128.

References

Belytschko, T., Black, T. 'Elastic Crack Growth in Finite Elements with Minimal Remeshing'. *International Journal for Numerical Methods in Engineering*, 1999, 45 (5): 601–20. https://doi.org/10.1002/(SICI)1097-0207(19990620).

Belytschko, T., Lu, Y.Y., Gu, L. 'Element-Free Galerkin Methods'. *International Journal for Numerical Methods in Engineering*, 1994, 37 (2): 229–56. https://doi.org/10.1002/nme.1620370205.

Belytschko, T., Moës, N., Usui, S., Parimi, C. 'Arbitrary Discontinuities in Finite Elements'. *International Journal for Numerical Methods in Engineering*, 2001, 50 (4): 993–1013. https://doi.org/10.1002/1097-0207(20010210).

Bower, A.F. *Applied Mechanics of Solids*, 2009. CRC Press.

Breugnot, A., Lambert, S., Villard, P., Gotteland, P. 'A Discrete/Continuous Coupled Approach for Modeling Impacts on Cellular Geostructures'. *Rock Mechanics and Rock Engineering*, 2016, 49 (5): 1831–48. https://doi.org/10.1007/s00603-015-0886-8.

Briaud, J.-L. 'Introduction to Soil Moduli'. *BiTech Publishers Ltd*, 2001, 8.

Brisard, S., Dormieux, L., Kondo, D. 'Hashin–Shtrikman Bounds on the Bulk Modulus of a Nanocomposite with Spherical Inclusions and Interface Effects'. *Computational Materials Science*, 2010, 48 (3): 589–96. https://doi.org/10.1016/j.commatsci.2010.02.027.

Brochard, L., Honório, T., Vandamme, M., Bornert, M., Peigney, M. 'Nanoscale Origin of the Thermo-Mechanical Behavior of Clays'. *Acta Geotechnica*, 2017, 12 (6): 1261–79. https://doi.org/10.1007/s11440-017-0596-3.

Brühwiler, E., Wittmann, F.H. 'The Wedge Splitting Test, a New Method of Performing Stable Fracture Mechanics Tests'. *Engineering Fracture Mechanics*, Special Issue Fracture and Damage of Concrete and Rock, 1990, 35 (1): 117–25. https://doi.org/10.1016/0013-7944(90)90189-N.

Bryant, E.C., Hwang, J., Sharma, M.M. 'Arbitrary Fracture Propagation in Heterogeneous Poroelastic Formations Using a Finite Volume-Based Cohesive Zone Model'. 2015. Society of Petroleum Engineers. https://doi.org/10.2118/173374-MS.

Chen, Z., Bunger, A.P., Zhang, X., Jeffrey, R.G. 'Cohesive Zone Finite Element-Based Modeling of Hydraulic Fractures'. *Acta Mechanica Solida Sinica*, 2009, 22 (5): 443–52. https://doi.org/10.1016/S0894-9166(09)60295-0.

Cho, N., Martin, C.D., Sego, D.C. 'A Clumped Particle Model for Rock'. *International Journal of Rock Mechanics and Mining Sciences*, 2007, 44 (7): 997–1010. https://doi.org/10.1016/j.ijrmms.2007.02.002.

Chotard, T., Soro, J., Lemercier, H., Huger, M., Gault, C. 'High Temperature Characterisation of Cordierite–Mullite Refractory by Ultrasonic Means'. *Journal of the European Ceramic Society*, 2008, 28 (11): 2129–35. https://doi.org/10.1016/j.jeurceramsoc.2008.02.029.

Christoffersen, J., Mehrabadi, M.M., Nemat-Nasser, S. 'A Micromechanical Description of Granular Material Behavior'. *Journal of Applied Mechanics*, 1981, 48 (2): 339–44. https://doi.org/10.1115/1.3157619.

Clementi, E., Reddaway, S.F., Hoare, C.A., Elliott, R.J. 'Global Scientific and Engineering Simulations on Scalar, Vector and Parallel LCAP-Type Supercomputers'. *Philosophical Transactions of the Royal Society of London. Series A, Mathematical and Physical Sciences*, 1988, 326 (1591): 445–70. https://doi.org/10.1098/rsta.1988.0097.

Cundall, P.A. 'A Computer Model for Simulating Progressive, Large-Scale Movements in Blocky Rock Systems', 1971.

Cundall, P.A. 'Computer Simulations of Dense Sphere Assemblies'. In *Studies in Applied Mechanics*, edited by Masao Satake and James T. Jenkins, 20:113–23, 1988a. Micromechanics of Granular Materials. Elsevier. https://doi.org/10.1016/B978-0-444-70523-5.50021-7.

References

Cundall, P.A. 'Formulation of a Three-Dimensional Distinct Element Model—Part I. A Scheme to Detect and Represent Contacts in a System Composed of Many Polyhedral Blocks'. *International Journal of Rock Mechanics and Mining Sciences & Geomechanics Abstracts*, 1988b, 25 (3): 107–16. https://doi.org/10.1016/0148-9062(88)92293-0.

Cundall, P.A., Strack, O.D.L. 'A Discrete Numerical Model for Granular Assemblies'. *Géotechnique*, 1979, 29 (1): 47–65. https://doi.org/10.1680/geot.1979.29.1.47.

Dai, Y., Gruber, D., Jin, S., Harmuth, H. 'Modelling and Inverse Investigation of the Fracture Process for a Magnesia Spinel Refractory Using a Heterogeneous Continuum Model'. *Engineering Fracture Mechanics*, 2017, 182: 438–48. https://doi.org/10.1016/j.engfracmech.2017.05.005.

Damhof, F., Brekelmans, W.A.M., Geers, M.G.D. 'Predictive FEM Simulation of Thermal Shock Damage in the Refractory Lining of Steelmaking Installations'. *Journal of Materials Processing Technology*, 2011, 211 (12): 2091–2105. https://doi.org/10.1016/j.jmatprotec.2011.07.005.

Dehghan, M., Abbaszadeh, M. 'Analysis of the Element Free Galerkin (EFG) Method for Solving Fractional Cable Equation with Dirichlet Boundary Condition'. *Applied Numerical Mathematics*, 2016, 109: 208–34. https://doi.org/10.1016/j.apnum.2016.07.002.

Duan, K., Hu, X., Wittmann, F.H. 'Size Effect on Specific Fracture Energy of Concrete'. *Engineering Fracture Mechanics*, Fracture of Concrete Materials and Structures, 2007, 74 (1): 87–96. https://doi.org/10.1016/j.engfracmech.2006.01.031.

Dubois, F., Acary, V., Jean, M. 'The Contact Dynamics Method: A Nonsmooth Story'. *Comptes Rendus Mécanique*, The legacy of Jean-Jacques Moreau in mechanics / L'héritage de Jean-Jacques Moreau en mécanique, 2018, 346 (3): 247–62. https://doi.org/10.1016/j.crme.2017.12.009.

Dugdale, D.S. 'Yielding of Steel Sheets Containing Slits'. *Journal of the Mechanics and Physics of Solids*, 1960, 8 (2): 100–104. https://doi.org/10.1016/0022-5096(60)90013-2.

Dupré, J.-C., Doumalin, P., Belrhiti, Y., Khlifi, I., Pop, O., Huger, M. 'Detection of Cracks in Refractory Materials by an Enhanced Digital Image Correlation Technique'. *Journal of Materials Science*, 2017, 53. https://doi.org/10.1007/s10853-017-1550-3.

Emam, S. 'Technical Memorandum: Distortion of the Periodic Space in PFC, PFC Documentation Set', 2009. Itasca Consulting Group Inc.

Eymard, R., Gallouët, T., Herbin, R. 'Finite Volume Methods'. In *Solution of Equation in $\mathbb{R}n$ (Part 3), Techniques of Scientific Computing (Part 3)*, edited by J. L. Lions and Philippe Ciarlet, 7:713–1020, 2000. Handbook of Numerical Analysis. Elsevier. https://doi.org/10.1016/S1570-8659(00)07005-8.

Farukh, F., Zhao, L.G., Jiang, R., Reed, P., Proprentner, D., Shollock, B.A. 'Realistic Microstructure-Based Modelling of Cyclic Deformation and Crack Growth Using Crystal Plasticity'. *Computational Materials Science*, 2016, 111: 395–405. https://doi.org/10.1016/j.commatsci.2015.09.054.

Ghassemi Kakroudi, M. 'Comportement thermomécanique en traction de bétons réfractaires : influence de la nature des agrégats et de l'histoire thermique', 2007. Limoges, France, University of Limoges.

Gibaud, R. 'Application de La Méthode Des Éléments Discrets Aux Déformations Finies Inélastiques Dans Les Multi-Matériaux', 2017. Doctoral dissertation, Grenoble, France, Université Grenoble Alpes (ComUE). http://www.theses.fr/2017GREAI086.

Gingold, R.A., Monaghan, J.J. 'Smoothed Particle Hydrodynamics: Theory and Application to Non-Spherical Stars'. *Monthly Notices of the Royal Astronomical Society*, 1977, 181 (3): 375–89. https://doi.org/10.1093/mnras/181.3.375.

Gogotsi, G.A. 'Determination of Brittleness of Refractories Tested for Heat Resistance'. *Strength of Materials*, 1973, 5 (10): 1186–89. https://doi.org/10.1007/BF01129398.

Grasset-Bourdel, R., Alzina, A., Tessier-Doyen, N., Schmitt, N., Huger, M., Chotard, T., Gruber, D., Harmuth, H. 'Optimisation of 3D RVE for Anisotropy Index Reduction in Modelling Thermoelastic

Properties of Two-Phase Composites Using a Periodic Homogenisation Method'. *Computational Materials Science*, 2011, 50 (11): 3136–44. https://doi.org/10.1016/j.commatsci.2011.05.042.

Grasset-Bourdel, Renaud. 'Structure/Property Relations of Magnesia-Spinel Refractories : Experimental Determination and Simulation', 2011. Doctoral dissertation, Limoges, France, University of Limoges. http://www.theses.fr/2011LIMO4050.

Grasset-Bourdel, Renaud, Alzina, A., Huger, M., Chotard, T., Emler, R., Gruber, D., Harmuth, H. 'Tensile Behaviour of Magnesia-Spinel Refractories: Comparison of Tensile and Wedge Splitting Tests'. *Journal of the European Ceramic Society*, 2013, 33 (5): 913–23. https://doi.org/10.1016/j.jeurceramsoc.2012.10.031.

Griffith, A.A., Taylor, G.I. 'VI. The Phenomena of Rupture and Flow in Solids'. *Philosophical Transactions of the Royal Society of London. Series A, Containing Papers of a Mathematical or Physical Character*, 1921, 221 (582–593): 163–98. https://doi.org/10.1098/rsta.1921.0006.

Grinter, L.E. *Numerical Methods of Analysis in Engineering (Successive Corrections)*, 1949. New York, Macmillan Co.

Harmuth, H., Tschegg, E.K. 'A Fracture Mechanics Approach for the Development of Refractory Materials with Reduced Brittleness'. *Fatigue & Fracture of Engineering Materials & Structures*, 1997a, 20 (11): 1585–1603. https://doi.org/10.1111/j.1460-2695.1997.tb01513.x.

Harmuth, H., Tschegg, E.K. 'A Fracture Mechanics Approach for the Development of Refractory Materials with Reduced Brittleness'. *Fatigue & Fracture of Engineering Materials & Structures*, 1997b, 20 (11): 1585–1603. https://doi.org/10.1111/j.1460-2695.1997.tb01513.x.

Hashin, Z., Shtrikman, S. 'A Variational Approach to the Theory of the Elastic Behaviour of Multiphase Materials'. *Journal of the Mechanics and Physics of Solids*, 1963, 11 (2): 127–40. https://doi.org/10.1016/0022-5096(63)90060-7.

Hasselman, D.P.H. 'Elastic Energy at Fracture and Surface Energy as Design Criteria for Thermal Shock'. *Journal of the American Ceramic Society*, 1963, 46 (11): 535–40. https://doi.org/10.1111/j.1151-2916.1963.tb14605.x.

Hasselman, D.P.H. 'Unified Theory of Thermal Shock Fracture Initiation and Crack Propagation in Brittle Ceramics'. *Journal of the American Ceramic Society*, 1969, 52 (11): 600–604. https://doi.org/10.1111/j.1151-2916.1969.tb15848.x.

Hasselman, D.P.H., Youngblood, G.E. 'Enhanced Thermal Stress Resistance of Structural Ceramics with Thermal Conductivity Gradient'. *Journal of the American Ceramic Society*, 1978, 61 (1–2): 49–52. https://doi.org/10.1111/j.1151-2916.1978.tb09228.x.

Hearmon, R.F.S. 'An Introduction to Applied Anisotropic Elasticity'. *The Mathematical Gazette*, 1964, 48 (363): 129–129. https://doi.org/10.2307/3614376.

Heider, Y., Markert, B., Ehlers, W. 'Dynamic Wave Propagation in Infinite Saturated Porous Media Half Spaces'. *Computational Mechanics*, 2012, 49 (3): 319–36. https://doi.org/10.1007/s00466-011-0647-9.

Herrmann, H.J., Hansen, A., Roux, S. 'Fracture of Disordered, Elastic Lattices in Two Dimensions'. *Physical Review B*, 1989, 39 (1): 637–48. https://doi.org/10.1103/PhysRevB.39.637.

Ibrahimbegovic, A., Delaplace, A. 'Microscale and Mesoscale Discrete Models for Dynamic Fracture of Structures Built of Brittle Material'. *Computers & Structures*, 2003, 81 (12): 1255–65. https://doi.org/10.1016/S0045-7949(03)00040-3.

Irwin, George.R. 'Analysis of Stresses and Strains near the End of a Crack Traversing a Plate', 1957, E24: 351–69.

Itasca Consulting Group Inc. 'PFC2D/3D Version 6.0 Documentation', 2020. Itasca Consulting Group Inc.

References

Jean, M. 'The Non-Smooth Contact Dynamics Method'. *Computer Methods in Applied Mechanics and Engineering*, 1999, 177 (3): 235–57. https://doi.org/10.1016/S0045-7825(98)00383-1.

Jebahi, M. 'Discrete-Continuum Coupling Method for Simulation of Laser-Inducced Damage in Silica Glass', 2013. Doctoral dissertation, University of Bordeaux 1. http://www.theses.fr/2013BOR14911.

Jebahi, M., Andre, D., Terreros, I., Iordanoff, I. *Discrete Element Method to Model 3D Continuous Materials*, 2015. John Wiley & Sons.

Jin, S., Gruber, D., Harmuth, H. 'Determination of Young's Modulus, Fracture Energy and Tensile Strength of Refractories by Inverse Estimation of a Wedge Splitting Procedure'. *Engineering Fracture Mechanics*, 2014, 116: 228–36. https://doi.org/10.1016/j.engfracmech.2013.11.010.

Joliff, Y., Absi, J., Huger, M., Glandus, J.C. 'Experimental and Numerical Study of the Room Temperature Elastic Modulus of Model Materials with Partly Bonded Matrix/Particles Interfaces'. *Computational Materials Science*, 2007, 39 (2): 267–73. https://doi.org/10.1016/j.commatsci.2006.06.005.

Kachanov, M. 'Elastic Solids with Many Cracks and Related Problems'. In *Advances in Applied Mechanics*, edited by John W. Hutchinson and Theodore Y. Wu, 30:259–445, 1993. Elsevier. https://doi.org/10.1016/S0065-2156(08)70176-5.

Kaczmarek, R., Dupre, JC., Doumalin, P., Pop, O., Breder-Teixeira, L., Gillibert, J., Blond, E., Huger, M. 'Thermomechanical Behaviour of an Alumina Spinel Refractory for Steel Ladle Applications'. In *UNITECR 2019*, 2019. Yokohama, Japan. https://hal-unilim.archives-ouvertes.fr/hal-02533698.

Kaiser, J. 'An Investigation into the Occurrence of Noises in Tensile Tests or a Study of Acoustic Phenomena in Tensile Tests', 1950. Munich, Germany, Technische Hochschule München.

Khlifi, I. 'Optimisation of Optical Methods for Strain Field Measurements Dedicated to the Characterisation of the Fracture Behaviour of Refractories : Application to Magnesia Based Materials', 2019. Doctoral dissertation, Limoges, France, University of Limoges. http://www.theses.fr/2019LIMO0123.

Khlifi, I., Pop, O., Dupré, J.-C., Doumalin, P., Huger, M. 'Investigation of Microstructure-Property Relantionships of Magnesia-Hercynite Refractory Composites by a Refined Digital Image Correlation Technique'. *Journal of the European Ceramic Society*, 2019, 39 (13): 3893–3902. https://doi.org/10.1016/j.jeurceramsoc.2019.05.010.

Khoei, A. R., Azadi, H., Moslemi, H. 'Modeling of Crack Propagation via an Automatic Adaptive Mesh Refinement Based on Modified Superconvergent Patch Recovery Technique'. *Engineering Fracture Mechanics*, 2008, 75 (10): 2921–45. https://doi.org/10.1016/j.engfracmech.2008.01.006.

Khoei, Amir R. *Extended Finite Element Method: Theory and Applications*, 2015. John Wiley & Sons.

Kingery, W.D. 'Factors Affecting Thermal Stress Resistance of Ceramic Materials'. *Journal of the American Ceramic Society*, 1955, 38 (1): 3–15. https://doi.org/10.1111/j.1151-2916.1955.tb14545.x.

Lakes, R.S. *Viscoelastic Solids*, 1998. CRC Press. https://doi.org/10.1201/9781315121369.

Leclerc, W., Haddad, H., Guessasma, M. 'DEM-FEM Coupling Method to Simulate Thermally Induced Stresses and Local Damage in Composite Materials'. *International Journal of Solids and Structures*, 2019, 160: 276–92. https://doi.org/10.1016/j.ijsolstr.2018.10.030.

Lemesle, J., Hubert, C., Bigerelle, M. 'Numerical Study of the Toughness of Complex Metal Matrix Composite Topologies'. *Applied Sciences*, 2020, 10 (18): 6250. https://doi.org/10.3390/app10186250.

Lempriere, B.M. *Ultrasound and Elastic Waves: Frequently Asked Questions*, 2003. Elsevier.

References

Li, X., Cao, W.-G., Su, Y.-H. 'A Statistical Damage Constitutive Model for Softening Behavior of Rocks'. *Engineering Geology*, 2012, 143–144: 1–17. https://doi.org/10.1016/j.enggeo.2012.05.005.

Liu, H., Yuan, X. 'A Damage Constitutive Model for Rock Mass with Persistent Joints Considering Joint Shear Strength'. *Canadian Geotechnical Journal*, 2015, 52 (8): 1136–43. https://doi.org/10.1139/cgj-2014-0252.

Lopes, B., Arruda, M.R.T., Almeida-Fernandes, L., Castro, L., Silvestre, N., Correia, J.R. 'Assessment of Mesh Dependency in the Numerical Simulation of Compact Tension Tests for Orthotropic Materials'. *Composites Part C: Open Access*, 2020, 1: 100006. https://doi.org/10.1016/j.jcomc.2020.100006.

Mchenry, D. 'A Lattice Analogy for the Solution of Stress Problems.' *Journal of the Institution of Civil Engineers*, 1943, 21 (2): 59–82. https://doi.org/10.1680/ijoti.1943.13967.

Moës, N., Dolbow, J., Belytschko, T. 'A Finite Element Method for Crack Growth without Remeshing'. *International Journal for Numerical Methods in Engineering*, 1999, 46 (1): 131–50. https://doi.org/10.1002/(SICI)1097-0207(19990910).

Moreau, J.J. 'Unilateral Contact and Dry Friction in Finite Freedom Dynamics'. In *Nonsmooth Mechanics and Applications*, edited by J. J. Moreau and P. D. Panagiotopoulos, 1–82, 1988. International Centre for Mechanical Sciences. Vienna, Springer. https://doi.org/10.1007/978-3-7091-2624-0_1.

Mubashar, A., Ashcroft, I.A., Crocombe, A.D. 'Modelling Damage and Failure in Adhesive Joints Using A Combined XFEM-Cohesive Element Methodology'. *The Journal of Adhesion*, 2014, 90 (8): 682–97. https://doi.org/10.1080/00218464.2013.826580.

Munjiza, A.A. *The Combined Finite-Discrete Element Method*, 2004. John Wiley & Sons.

Nguyen, T.T. 'Numerical Modeling of Microstructure-Properties Relationships of Refractories: Micro-Mechanical Approach with the Discrete Element Method', 2019. Doctoral dissertation, Limoges, France, University of Limoges. https://www.theses.fr/2019LIMO0089.

Nguyen, T.-T., André, D., Huger, M. 'Analytic Laws for Direct Calibration of Discrete Element Modeling of Brittle Elastic Media Using Cohesive Beam Model'. *Computational Particle Mechanics*, 2019, 6 (3): 393–409. https://doi.org/10.1007/s40571-018-00221-0.

Oliver-Leblond, C. 'Discontinuous Crack Growth and Toughening Mechanisms in Concrete: A Numerical Study Based on the Beam-Particle Approach'. *Engineering Fracture Mechanics*, 2019, 207: 1–22. https://doi.org/10.1016/j.engfracmech.2018.11.050.

Pabst, W., Gregorová, E. 'Effective Elastic Properties of Alumina-Zirconia Composite Ceramics - Part 2. Micromechanical Modeling', 2004, 10.

Pabst, W., Uhlířová, T., Gregorová, E., Wiegmann, A. 'Young's Modulus and Thermal Conductivity of Model Materials with Convex or Concave Pores – from Analytical Predictions to Numerical Results'. *Journal of the European Ceramic Society*, 2018, 38 (7): 2694–2707. https://doi.org/10.1016/j.jeurceramsoc.2018.01.040.

Papanicolau, G., Bensoussan, A., Lions, J.-L. *Asymptotic Analysis for Periodic Structures*, 1978. Elsevier.

Parrinello, M., Rahman, A. 'Polymorphic Transitions in Single Crystals: A New Molecular Dynamics Method'. *Journal of Applied Physics*, 1981, 52 (12): 7182–90. https://doi.org/10.1063/1.328693.

Popov, E.P. *Engineering Mechanics of Solids 2Nd Ed.*, 1998. Prentice-Hall of India Pvt. Limited.

Potyondy, D. 'A Flat-Jointed Bonded-Particle Material for Hard Rock'. 2012. American Rock Mechanics Association. https://www.onepetro.org/conference-paper/ARMA-2012-501.

Potyondy, D. 'The Bonded-Particle Model as a Tool for Rock Mechanics Research and Application: Current Trends and Future Directions'. *Geosystem Engineering*, 2015, 18 (1): 1–28. https://doi.org/10.1080/12269328.2014.998346.

References

Potyondy, D. 'A Flat-Jointed Bonded-Particle Model for Rock'. 2018. American Rock Mechanics Association. https://www.onepetro.org/conference-paper/ARMA-2018-1208.

Potyondy, D. 'Technical Memorandum: Material-Modeling Support for PFC, PFC 6 Documentation Set', 2019. Itasca Consulting Group Inc.

Potyondy, D., Cundall, P.A. 'A Bonded-Particle Model for Rock'. *International Journal of Rock Mechanics and Mining Sciences*, Rock Mechanics Results from the Underground Research Laboratory, Canada, 2004, 41 (8): 1329–64. https://doi.org/10.1016/j.ijrmms.2004.09.011.

Rabczuk, T., Zi, G. 'A Meshfree Method Based on the Local Partition of Unity for Cohesive Cracks'. *Computational Mechanics*, 2007, 39 (6): 743–60. https://doi.org/10.1007/s00466-006-0067-4.

Rice, J.R. 'A Path Independent Integral and the Approximate Analysis of Strain Concentration by Notches and Cracks'. *Journal of Applied Mechanics*, 1968, 35 (2): 379–86. https://doi.org/10.1115/1.3601206.

Richardson, L.F., Glazebrook, R.T. 'IX. The Approximate Arithmetical Solution by Finite Differences of Physical Problems Involving Differential Equations, with an Application to the Stresses in a Masonry Dam'. *Philosophical Transactions of the Royal Society of London. Series A, Containing Papers of a Mathematical or Physical Character*, 1911, 210 (459–470): 307–57. https://doi.org/10.1098/rsta.1911.0009.

Sakai, M., Bradt, R.C. 'Graphical Methods for Determining the Nonlinear Fracture Parameters of Silica and Graphite Refractory Composites'. In *Fracture Mechanics of Ceramics: Volume 7 Composites, Impact, Statistics, and High-Temperature Phenomena*, edited by R. C. Bradt, A. G. Evans, D. P. H. Hasselman, and F. F. Lange, 127–42, 1986. Boston, MA, Springer US. https://doi.org/10.1007/978-1-4615-7023-3_10.

Schacht, C. *Refractories Handbook*, 2004. CRC Press.

Schlangen, E., Garboczi, E.J. 'New Method for Simulating Fracture Using an Elastically Uniform Random Geometry Lattice'. *International Journal of Engineering Science*, 1996, 34 (10): 1131–44. https://doi.org/10.1016/0020-7225(96)00019-5.

Schlangen, E., Mier, J.G.M. van. 'Experimental and Numerical Analysis of Micromechanisms of Fracture of Cement-Based Composites'. *Cement and Concrete Composites*, Special Issue on Micromechanics of Failure in Cementitious Composites, 1992, 14 (2): 105–18. https://doi.org/10.1016/0958-9465(92)90004-F.

Scholtès, L., Donzé, F.-V. 'Modelling Progressive Failure in Fractured Rock Masses Using a 3D Discrete Element Method'. *International Journal of Rock Mechanics and Mining Sciences*, 2012, 52: 18–30. https://doi.org/10.1016/j.ijrmms.2012.02.009.

Scholtès, L., Donzé, F.-V. 'A DEM Model for Soft and Hard Rocks: Role of Grain Interlocking on Strength'. *Journal of the Mechanics and Physics of Solids*, 2013, 61 (2): 352–69. https://doi.org/10.1016/j.jmps.2012.10.005.

Shao, Y., Duan, Q., Qiu, S. 'Consistent Element-Free Galerkin Method for Three-Dimensional Crack Propagation Based on a Phase-Field Model'. *Computational Materials Science*, 2020, 179: 109694. https://doi.org/10.1016/j.commatsci.2020.109694.

Sharafisafa, M., Nazem, M. 'Application of the Distinct Element Method and the Extended Finite Element Method in Modelling Cracks and Coalescence in Brittle Materials'. *Computational Materials Science*, 2014, 91: 102–21. https://doi.org/10.1016/j.commatsci.2014.04.006.

Slepetz, J.M., Carlson, L. 'Fracture of Composite Compact Tension Specimens'. *Fracture Mechanics of Composites*, 1975. https://doi.org/10.1520/STP34796S.

Spencer, B.W., Huang, H., Dolbow, J.E., Hales, J.D. 'Discrete Modeling of Early-Life Thermal Fracture in Ceramic Nuclear Fuel'. INL/CON-14-31355, 2015. Idaho National Lab. (INL), Idaho Falls, ID (United States). https://www.osti.gov/biblio/1177218.

References

Steinbrech, R., Khehans, R., Schaarwächter, W. 'Increase of Crack Resistance during Slow Crack Growth in Al2O3 Bend Specimens'. *Journal of Materials Science*, 1983, 18 (1): 265–70. https://doi.org/10.1007/BF00543834.

Tessier-Doyen, N., Glandus, J.C., Huger, M. 'Experimental and Numerical Study of Elastic Behavior of Heterogeneous Model Materials with Spherical Inclusions'. *Journal of Materials Science*, 2007, 42 (14): 5826–34. https://doi.org/10.1007/s10853-006-1386-8.

Tessier-Doyen, Nicolas. 'Etude Expérimentale et Numérique Du Comportement Thermomécanique de Matériaux Réfractaires Modèles'. *Http://Www.Theses.Fr*, 2003. Thesis, Limoges, France, University of Limoges. http://www.theses.fr/2003LIMO0030.

Tikhonov, A.N., Samarskii, A.A. 'Homogeneous Difference Schemes on Non-Uniform Nets'. *USSR Computational Mathematics and Mathematical Physics*, 1963, 2 (5): 927–53. https://doi.org/10.1016/0041-5553(63)90505-6.

Tinschert, J., Zwez, D., Marx, R., Anusavice, K.J. 'Structural Reliability of Alumina-, Feldspar-, Leucite-, Mica- and Zirconia-Based Ceramics'. *Journal of Dentistry*, 2000, 28 (7): 529–35. https://doi.org/10.1016/S0300-5712(00)00030-0.

Tschegg, E.K. Equipment and appropriate specimen shape for tests to measure fracture values. AT-390328, 1986, issued 1986.

Tucker, C., Liang, E. 'Stiffness Predictions for Unidirectional Short-Fiber Composites: Review and Evaluation'. *Composites Science and Technology*, 1999, 59–655.

Vallejos Javier Andres, Salinas José Matias, Delonca Adeline, Mas Ivars Diego. 'Calibration and Verification of Two Bonded-Particle Models for Simulation of Intact Rock Behavior'. *International Journal of Geomechanics*, 2017, 17 (4): 06016030. https://doi.org/10.1061/(ASCE)GM.1943-5622.0000773.

Ventura, G., Xu, J.X., Belytschko, T. 'A Vector Level Set Method and New Discontinuity Approximations for Crack Growth by EFG'. *International Journal for Numerical Methods in Engineering*, 2002, 54 (6): 923–44. https://doi.org/10.1002/nme.471.

Wang, X., Yang, J., Liu, Q., Zhang, Y., Zhao, C. 'A Comparative Study of Numerical Modelling Techniques for the Fracture of Brittle Materials with Specific Reference to Glass'. *Engineering Structures*, 2017, 152: 493–505. https://doi.org/10.1016/j.engstruct.2017.08.050.

Weibull, W. *The Phenomenon of Rupture in Solids*, 1939. Stockholm, Generalstabens litografiska anstalts förlag.

Weibull, W. 'A Statistical Distribution Function of Wide Applicability', 1951, 18: 293–97.

Yuan, R., Shi, B. 'Acoustic Emission Activity in Directly Tensile Test on Marble Specimens and Its Tensile Damage Constitutive Model'. *International Journal of Coal Science & Technology*, 2018, 5 (3): 295–304. https://doi.org/10.1007/s40789-018-0215-4.

Zerhouni, O., Tarantino, M.G., Danas, K. 'Numerically-Aided 3D Printed Random Isotropic Porous Materials Approaching the Hashin-Shtrikman Bounds'. *Composites Part B: Engineering*, 2019, 156: 344–54. https://doi.org/10.1016/j.compositesb.2018.08.032.

Zhang, F., Dontsov, E., Mack, M. 'Fully Coupled Simulation of a Hydraulic Fracture Interacting with Natural Fractures with a Hybrid Discrete-Continuum Method'. *International Journal for Numerical and Analytical Methods in Geomechanics*, 2017, 41 (13): 1430–52. https://doi.org/10.1002/nag.2682.

Zhou, C., Karakus, M., Xu, C., Shen, J. 'A New Damage Model Accounting the Effect of Joint Orientation for the Jointed Rock Mass'. *Arabian Journal of Geosciences*, 2020, 13 (7): 295. https://doi.org/10.1007/s12517-020-5274-3.

References

Zhou, C., Xu, C., Karakus, M., Shen, J. 'A Systematic Approach to the Calibration of Micro-Parameters for the Flat-Jointed Bonded Particle Model'. *Geomechanics and Engineering*, 2018, 16 (5): 471–82. https://doi.org/10.12989/gae.2018.16.5.471.

Zienkiewicz, O.C., Taylor, R.L., Zhu, J.Z. *The Finite Element Method: Its Basis and Fundamentals*, 2013. Butterworth-Heinemann.

Živcová, Z., Černý, M., Pabst, W., Gregorová, E. 'Elastic Properties of Porous Oxide Ceramics Prepared Using Starch as a Pore-Forming Agent'. *Journal of the European Ceramic Society*, 2009, 29 (13): 2765–71. https://doi.org/10.1016/j.jeurceramsoc.2009.03.033.

Abstract

This PhD is part of the Marie Skłodowska-Curie action ATHOR project (Advanced THermomechanical multiscale mOdelling of Refractory linings), supported by the European Commission. Refractories are heterogenous ceramics, resistant at high temperatures for which, in many cases, pre-existent microcracks within the microstructure play a key role in sustaining thermal shocks. The Discrete Element Method (DEM) is considered as a major numerical tool that can help, in future, to design high-performance microstructures. Thus, the present PhD is focused on numerical simulations of refractory ceramics by considering their microstructures, heterogeneities including cracks, and their influence on fracture mechanics. This work has been managed within a partnership with the company "ITASCA consultants". Within the Particle Flow Code (PFC), as main numerical framework, the Flat Joint Model (FJM) is chosen since this contact model can mimic the microstructure of interlocked grains, like the microstructure of refractories. To develop numerical models that can help to investigate the role played by the microstructure in the macroscopic thermomechanical behaviour, it is essential to have an accurate micro to macro multiscale approach of each key physical properties for thermal shocks, starting with elastic properties. In this way, as DEM is not, at this stage, as robust as FEM, a periodic homogenisation approach is proposed for such continuum media. This approach has been validated by comparing the obtained results to model materials, analytical and FEM models. At mesoscale, a DEM model using a statistical approach to mimic the mechanical influence of pre-existing microcracks is investigated. This technique has also been validated by experimental mechanical data. Subsequently, to check the proposed DEM model applicability, Wedge Splitting Test (WST) simulations are managed to investigate the fracturing process and qualitatively compared to DIC experimental outputs. In the end, a discrete/continuous hybrid model is proposed to optimise the WST simulations in order to save computational time. These key results open very interesting new ways to use DEM in predicting the thermomechanical behaviour of heterogeneous materials containing numerous microcracks that could propagate simultaneously.

Keywords: Refractories, Microcracks, DEM modelling, Periodic homogenisation, Fracture mechanics

Résumé

Cette thèse s'inscrit dans le cadre du projet Européen ATHOR (Advanced THermomechanical Multiscale Modelling of Refractory Linings). Les matériaux réfractaires sont des céramiques hétérogènes, résistantes à des températures élevées pour lesquelles, dans de nombreux cas, des microfissures préexistantes au sein de la microstructure jouent un rôle clé dans la résistance aux chocs thermiques. La Méthode des Eléments Discrets (MED) est aujourd'hui considérée comme un outil numérique majeur qui peut contribuer, à l'avenir, à concevoir des microstructures plus performantes. Ainsi, cette thèse est dédiée à la simulation numérique de matériaux réfractaires intégrant leur microstructure, leurs hétérogénéités, ainsi que la présence de fissures, et leur influence sur le comportement mécanique macroscopique. Ces travaux ont par ailleurs été réalisés dans le cadre d'un partenariat avec la société "ITASCA consultants". Au sein de l'outil Particle Flow Code (PFC), utilisé comme plateforme numérique MED, le model de contact Flat Joint Model (FJM) a été choisi car celui-ci permet de modéliser des microstructures de grains imbriqués, analogues à celles des matériaux réfractaires. Afin de développer des modèles numériques permettant de décrire les relations entre la microstructure et le comportement thermomécanique macroscopique, il est essentiel de mettre en œuvre une approche multi-échelles, micro à macro, précise pour chacune des propriétés physiques clés intervenant dans la tenue aux chocs thermiques, en commençant par les propriétés d'élasticité. Dans cet objectif, la MED n'étant pas, à ce stade, aussi robuste que la Méthode des Eléments Finis (MEF), une approche d'homogénéisation périodique est proposée pour des milieux continus. Cette approche a ici été validée en comparant les résultats obtenus à des matériaux modèles, des modèles analytiques et MEF. A l'échelle méso-scopique, un modèle MED utilisant une approche statistique pour imiter l'influence mécanique des microfissures préexistantes est mis en œuvre. Cette approche a également été validée par des données mécaniques expérimentales. Par la suite, afin de vérifier l'applicabilité du modèle MED proposé, des simulations de Wedge Splitting Test (WST) sont proposées pour étudier le processus de fissuration et le comparer qualitativement aux résultats expérimentaux obtenus en DIC. Finalement, un modèle hybride discret/continu (MED/MVF) est proposé pour optimiser ces simulations de WST et réduire les temps de calculs. Ces résultats clés ouvrent de nouvelles voies très intéressantes d'utilisation de la MED pour prédire le comportement thermomécanique de matériaux hétérogènes contenant de nombreuses microfissures pouvant se propager simultanément.

Mots clés: Réfractaires, Microfissures, Modélisation MED, Homogénéisation Périodique, Mécanique de la Rupture